1987

The Role of Horizontal Processes in Upper-Ocean Prediction: A Forecast Simulation in the Sea of Japan.

John M. Harding Jr
Louisiana State University and Agricultural & Mechanical College

Recommended Citation
Harding, John M. Jr, "The Role of Horizontal Processes in Upper-Ocean Prediction: A Forecast Simulation in the Sea of Japan." (1987). *LSU Historical Dissertations and Theses*. 4449.
https://digitalcommons.lsu.edu/gradschool_disstheses/4449

INFORMATION TO USERS

The most advanced technology has been used to photograph and reproduce this manuscript from the microfilm master. UMI films the original text directly from the copy submitted. Thus, some dissertation copies are in typewriter face, while others may be from a computer printer.

In the unlikely event that the author did not send UMI a complete manuscript and there are missing pages, these will be noted. Also, if unauthorized copyrighted material had to be removed, a note will indicate the deletion.

Oversize materials (e.g., maps, drawings, charts) are reproduced by sectioning the original, beginning at the upper left-hand corner and continuing from left to right in equal sections with small overlaps. Each oversize page is available as one exposure on a standard 35 mm slide or as a 17" × 23" black and white photographic print for an additional charge.

Photographs included in the original manuscript have been reproduced xerographically in this copy. 35 mm slides or 6" × 9" black and white photographic prints are available for any photographs or illustrations appearing in this copy for an additional charge. Contact UMI directly to order.

U·M·I

Accessing the World's Information since 1938

300 North Zeeb Road, Ann Arbor, MI 48106-1346 USA

Order Number 8811407

The role of horizontal processes in upper-ocean prediction: A forecast simulation in the Sea of Japan

Harding, John M., Jr., Ph.D.

The Louisiana State University and Agricultural and Mechanical Col., 1987

U·M·I
300 N. Zeeb Rd.
Ann Arbor, MI 48106

THE ROLE OF HORIZONTAL PROCESSES IN UPPER-OCEAN PREDICTION: A FORECAST SIMULATION IN THE SEA OF JAPAN

A Dissertation

Submitted to the Graduate Faculty of the
Louisiana State University
Agricultural and Mechanical College
in partial fulfillment of the
requirements for the degree of
Doctor of Philosophy

in

The Department Of Marine Sciences

by
John M. Harding, Jr.
B.S., University of Miami, 1970
M.S., University of California, San Diego, 1971
December 1987

ACKNOWLEDGMENTS

An effort of this type requires support of many types including financial, technical, bureaucratic, and personal. Funding for this effort was provided by the U.S. Navy Space and Naval Warfare Systems Command through the Air-Ocean Prediction program (program element 63207N).

Three individuals provided the major technical support for this project through their past and present scientific efforts and via fruitful discussion. I express my sincere appreciation to Bill Wiseman, Paul Martin, and Mike Clancy. Additional valuable advice on this work was provided by the various members of my graduate committee including Bob Thoms, Steve Murray, Bob Costanza and Harry Roberts. For providing the digitized frontal positions as well as the bulk of references on the Sea of Japan, I wish to thank Taebo Shim. For additional relevant comments, and/or references, I would like to recognize Jeff Hawkins, Harley Hurlburt, Masamichi Inouye, Peter Niiler, Ruth Preller, Michele Rienecker, and Dana Thompson. For final drafting and figure arrangement, I express my appreciation to Renee Edman, Linda Jenkins and the graphics support staff for helping complete this document on schedule. I especially thank Alex Warn-Varnas for lightening my non-technical work load over the past six months so that I could complete this

work. For his good-natured hectoring, through three different dissertation topics, I recognize Tom Kinder. Without his efforts, this paper might yet be in preparation. I also extend my gratitude to the patron saint of LSU marine sciences graduate students, Gerry Newman, for steering me through the bureaucratic maze of the graduate school office.

For personal support through the prolonged gestation of this effort, I extend my deepest appreciation to my entire family. I especially recognize my parents, Jack and Doady, and my wife, Therese, for their steadfast confidence and backing, both in word and deed. I also thank my children, Ventana, Soquel, and Jevon for providing the distractions which rarely hindered the creation of this work but kept me sane for the duration.

Finally, for inspiration, I dedicate this dissertation to my nonagenarian grandmother, Marjorie Eva Gillingham, who refuses to quit "as long as God has work for me here."

TABLE OF CONTENTS

LIST OF TABLES

LIST OF FIGURES

ABSTRACT

Present-day, operational, upper-ocean, thermal-structure forecast models consist of mixed-layer models with local wind-generated horizontal and vertical advection. To extend their applicability into dynamically active regions, e.g. western boundary current regions, the next generation models are envisioned to include mesoscale advection provided by high horizontal resolution circulation nowcast and, eventually forecast models. In this study, I consider the impact of this additional component of advection in a representative dynamic ocean region.

I perform four experiments using a modified version of an operational, upper-ocean, thermal prediction model. Each of the four experiments consists of a series of daily, 72-hr-duration, upper-ocean hindcasts. They were each conducted for four weeks during the warming season in the Sea of Japan. The first experiment uses an Nx1 dimensional mixed layer model with no horizontal processes included. The second experiment uses the same model with the addition of horizontal diffusion and local wind-generated horizontal and vertical advection. This model is comparable to present-day operational models. The third experiment repeats the second with the addition of a fixed geostrophic component to the horizontal advection.

The fourth experiment allows daily variation of the geostrophic component through each three day forecast.

A suite of statistical measures applied to the results indicates a small but statistically significant increase in forecast skill due to the addition of the nowcast mesoscale advection. The additional analysis of a representative individual forecast strengthens this result. The statistical plus individual analyses together lead to three conclusions. First, the addition of geostrophic flow can have a statistically significant impact, especially in frontal regions. Second, global statistical measures alone are not sufficient model comparison criteria since they can mask specific regions or times of significant change. Third, the use of forecast mesoscale circulation in future upper-ocean thermal forecast models will require care due to the potential for artificial cross-frontal advection.

1. INTRODUCTION

Upper-ocean thermal structure influences a range of man's activities. These include commercial fisheries, long-range weather forecasting, climate forecasting, and acoustic ocean surveillance and detection (ELSBERRY and GARWOOD, 1980; MOOERS, ROBINSON, and PIACSEK, 1982). Knowledge of both present and future locations of fronts, mixed layer depth, and upwelling zones, via their impact on nutrient distribution, can affect decisions on fisheries management. Heat storage and distribution in the upper-ocean both affect long-range weather and climate forecasting as the ocean acts as both heat source and sink for the lower atmosphere. Finally, upper-ocean thermal structure helps determine the path and strength of acoustic energy propagating in the ocean thus affecting the surveillance and detection of hostile submarines.

My primary goal in this study is to consider one aspect in the evolution of operational upper-ocean thermal structure prediction. In particular, I present an investigation into the role of horizontal advection on upper-ocean thermal structure forecasting. The unique aspect of this work lies in its comparison of present-day, operational models containing locally-generated wind-drift advection with proposed models containing the additional component of non-locally forced flow.

Upper-ocean thermal structure prediction, in particular, and dynamic ocean prediction, in general, rely on several prerequisites. ELSBERRY and GARWOOD(1980) advance several key features necessary in a dynamic ocean prediction system. First, driven by atmospheric forcing, it must respond on a wide range of time scales. Resolution of the oceanic response to the atmosphere must occur on time scales ranging from the diurnal and atmospheric synoptic scale (~2-5 days) out to the seasonal and beyond.

Second, the atmospheric forcing prediction for the system must be available and contain the variability and skill necessary for ocean prediction. To resolve the diurnal and synoptic time scales in the dynamic ocean prediction, for example, requires the atmospheric forcing prediction at time intervals capable of representing the atmospheric variability at these scales (e.g., several hours).

Third, the ocean forecast model must contain the ability to treat both advective and mixing processes as a prerequisite for treating phenomena such as ocean fronts.

Fourth, the forecast model should cycle with an analysis, the analysis providing initial/update conditions for the forecast and the forecast providing a first guess for the next analysis. The analysis can thus keep the forecast consistent with observations, while the forecast can provide a representation of the synoptic scale variability not present in the existing observational system, i.e. provide information in data sparse areas.

HURLBURT(1984, 1986) proposes an evolutionary approach to the development of such an ocean prediction system. This approach considers three general classes of response of the ocean to atmospheric forcing. Class I response is strong, rapid, and direct where the ocean is less sensitive to errors in initial conditions and more sensitive to errors in forcing functions. Time scales are comparable to those in the atmospheric forcing. Consequently, the predictability of these phenomena is limited to the time scales of atmospheric predictability which are presently 3 to 5 days (CULLEN, 1983). Surface waves, oceanic mixed layers, and upwelling events are examples.

Class II response is slow, indirect, and, while less sensitive to forcing errors, is more sensitive to errors in the initial state. Time scales are on the order of weeks to months. Predictability is envisioned beyond that of atmospheric predictability due to the indirect atmosphere/ocean coupling inherent in these oceanic phenomena. Examples of this class are mesosale flow instabilities, mesoscale eddies, meandering currents, and frontal locations.

The Class III response is slow and relatively direct. Time scales are weeks to years and result from responses to accumulated atmospheric forcing. Examples include equatorial circulation, El Nino, and gyre-scale circulations.

HURLBURT(1984, 1986) therefore suggests that the dynamic ocean prediction problem initially be separated and

approached as the requisite data (initialization, update, and forcing), models, and computing power become available for each class.

This evolutionary approach can be considered a generalization of the approach suggested by both ELSBERRY and GARWOOD(1980) and CLANCY and MARTIN(1981). Recognizing the limitations of the available data, model, and computer capabilities, ELSBERRY and GARWOOD(1980) propose that the first generation model consist of a non-advective, mixed-layer model. A variety of models have proven the predictability of the mixed layer (e.g., DENMAN and MIYAKE, 1973; MELLOR and DURBIN, 1975; THOMPSON, 1976; PRICE, MOOERS, and VAN LEER, 1978; WARN-VARNAS et al., 1982; DAVIS, DESZOEKE, and NIILER, 1981; MARTIN, 1982; MARTIN, 1985); thus the models exist. Computational power also exists to provide synoptic representations of the mixed layer since, without horizontal coupling, the forecast at each grid point can be computed separately and stored. Initialization and update data, while sparse, also exists (as discussed below). Finally, the forcing data is available from atmospheric general circulation models run operationally at the U.S. Navy's Fleet Numerical Oceanography Center (FNOC). These forcing functions have proven reasonable in comparison with buoy data (FRIEHE and PAZAN, 1978) and correctable, when necessary, for use in ocean simulations (GALLACHER, 1979; BUDD, 1980; WARN-VARNAS et al., 1982).

This first generation model predicts ocean thermal structure changes in response to atmospheric forcing on time scales of days to weeks. The rationale behind this approach is the separation in time scales between the impact of vertical mixing and horizontal advective effects. For forecasts of several days, vertical mixing effects dominate advective effects over much of the ocean (ELSBERRY and GARWOOD, 1980). A major fraction of atmospheric forcing of the ocean is concentrated in relatively short periods associated with the passage of extratropical cyclones (ELSBERRY and CAMP, 1978; ELSBERRY and RANEY, 1978). And a major fraction of ocean thermal structure modification during strong forcing can be explained in terms of non-advective mixed layer dynamics (CAMP and ELSBERRY, 1978). ELSBERRY and GARWOOD(1980) however propose this 1-D approach only as a first step. They call for the later necessary inclusion of both mixing and advective processes as data acquisition and models improve.

GARWOOD's review(1979) of air-sea interaction and mixed layer dynamics suggests that the inclusion of horizontal and vertical advection of the mean fields in mixed layer models is certainly mandated by the observations. Wind-driven horizontal advection strongly affects upper-ocean thermal structure in oceanic frontal regions (e.g., RODEN, 1976; RODEN and PASKAUSKY, 1978; DESZOEKE, 1980; CUSHMAN-ROISIN, 1981; HORTON, 1984; ADAMEC and GARWOOD, 1985). Even away from strong fronts, PADUAN and DESZOEKE(1986) indicate that the effect of horizontal

advection depends on the amount of cross-isotherm Ekman advection which is sensitive to storm structure and proximity. Geostrophic flow in their region of study was weak, non-divergent, and parallel to the surface isotherms and thus had little effect relative to the Ekman flow. CLANCY and POLLAK(1983) summarize these results saying that drift-current advection, air-sea heat exchange, solar absorption, and vertical mixing primarily control the large scale mixed-layer variablity in the upper ocean on the diurnal to seasonal time scales.

Consequently, the first-generation, operational, ocean-prediction system, expands on the general design proposed by ELSBERRY and GARWOOD(1980), and includes wind-driven advective effects. The forecast component of this system, the Thermodynamic Ocean Prediction System (TOPS), (CLANCY and MARTIN, 1979; CLANCY and MARTIN, 1981; CLANCY et al., 1981; CLANCY and POLLAK, 1983), includes horizontal diffusion and both horizontal and vertical wind-drift advection of the mean fields. It contains, as well, a simplified representation of the geostrophic advection based on climatological temperature and salinity fields. Figure 1 provides a schematic representation of how the TOPS forecast model blends into the overall operational analysis/prediction system at FNOC as described by CLANCY and POLLAK(1983).

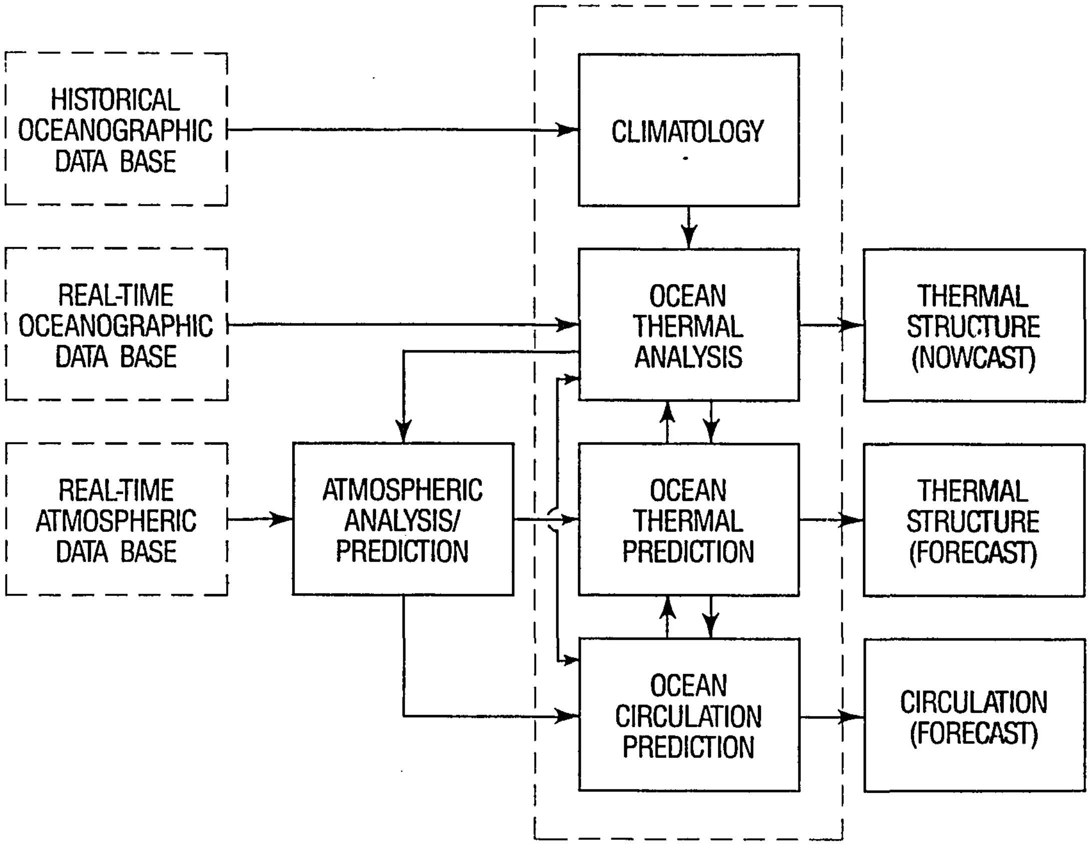

Figure 1. Schematic of an operational upper-ocean thermal analysis/prediction system.

An analysis scheme gathers all available in situ data (bathythermograph, surface ship observations, and satellite-derived, multichannel, sea-surface temperatures (Hawkins, 1985)) within a few-day time window. For the northern hemisphere, this data daily consists of approximately 150 XBT measurements, 1500 ship injection or bucket temperatures, and 50,000 - 100,000 multichannel sea-surface temperatures from the NOAA TIROS satellites.

The present operational objective analysis is the Expanded Ocean Thermal Structure (EOTS) analysis (MENDENHALL, CUMING, and HOLL, 1978; HOLL, CUMING, and MENDENHALL, 1979; CLANCY, 1982; CLANCY and POLLAK, 1983). Based on the Fields-By-Information Blending (FIB) methodology (HOLL and MENDENHALL, 1971), EOTS combines the data with available climatology to provide an ocean thermal nowcast in the upper 400 m of the ocean blended with climatology below. This analysis-only portion of the overall system presently provides regional, synoptic, thermal structure nowcasts on polar stereographic projections for selected oceanic regions (e.g., Gulf Stream, ~20 km resolution; Caribbean,~32 km; Kuroshio,~32 km; Mid-Pacific,~54 km; Indian Ocean,~80 km). In selected regions (e.g., Gulf Stream, Kuroshio), near real-time representations of fronts and eddies are included weekly into the analyses (HAWKINS et al., 1986). Personnel at the responsible Naval Oceanography Command regional center supply weekly estimates of surface front and eddy locations

and gradients obtained from available ship, aircraft, and satellite data.

The addition of the TOPS to the system allows for analysis/prediction cycling as proposed by ELSBERRY and GARWOOD(1980) and CLANCY and MARTIN(1981). In these cycling applications, the analysis is renamed TOPS-EOTS to distinguish it from the non-cycled analysis. TOPS-EOTS provides an initial condition to the TOPS module. TOPS, initialized from the TOPS-EOTS analysis and forced using atmospheric fields provided by the FNOC atmospheric general circulation models, provides up to 72 hr, upper-ocean forecasts of thermal structure. The 24 hr TOPS forecast results are used as first guess for the next day's analysis thus closing the analysis/forecast/analysis loop. Presently this cycling occurs operationally for the northern and southern hemisphere (~320 km resolution) and for the Norwegian Sea, the eastern Mediterranean and the western Mediterranean regions (~40 km resolution). The TOPS applied to these latter two regions contains no horizontal advection or diffusion and is therefore referred to as non-advective TOPS. The Norwegian Sea version, developed by this author, does.

The existing, operational, circulation module shown at the bottom of figure 1 presently provides a climatologically-derived geostrophic flow but only for the northern hemisphere region. Thus real-time effects of mesoscale advection (the HURLBURT(1984,1986) Class II phenomena) are not presently included. Several studies

however suggest that they should be, especially in dynamically active areas.

MULLER, GARWOOD, and GARNER(1984) and STEVENSON(1983) suggest the importance of mixed layer changes due to vertical motions induced by Rossby waves. These changes however are found to be important on the seasonal as opposed to the synoptic time scale. WELLER(1982) stresses the impact on the upper-ocean of inertial motions due to vertical motions induced by the divergence of the mesoscale flow. Heat budget studies in dynamically active regions also indicate the impact of mesoscale advection on the synoptic variability of the upper-ocean thermal structure. KURASAWA, HANAWA, and TOBA(1983), for example, considered the heat balance in the upper 200 m at Ocean Station T south of Japan. On time scales of a few days to a month, they found the variation of heat content depends on heat convergence. They infer the cause of this convergence to be the advection of water masses bounded by sharp fronts. ERIKSEN(1987), studying an eddy-energetic region southwest of the Gulf Stream, found mesoscale advection accounting for much of the density variability within the seasonal thermocline on time scales of a few days. JOYCE, KASE, and ZENK(1980) likewise found geostrophic advection important over a few day time scale in the seasonal thermocline during the Joint Air-Sea Interaction(JASIN) study in August and September 1978. Some changes in upper-ocean thermal structure appeared to be directly related to the local winds. However horizontal advection of spatially varying

temperature fields was the dominant process below the mixed layer.

Consequently, plans for the next generation models (CLANCY and POLLAK, 1983; HURLBURT, 1984; MARTIN et al., 1985; HAWKINS et al., 1986; CLANCY, POLLAK, and HARDING, 1986, HURLBURT, 1986; CLANCY, 1986) call for increased TOPS resolution (meshes to ~20 km) and for the replacement of the present circulation module. Initially, the mesoscale advection would be generated by a "geostrophic nowcast" calculated by applying a thermal wind equation to the initial temperature and salinity conditions for the thermal forecast. Following this would be the the use of mesoscale forecast horizontal and vertical advective fields provided by an eddy-resolving, global or regional, ocean circulation forecast model(e.g., HURLBURT and THOMPSON, 1980; PRELLER, 1986; ROBINSON, 1986). Initially the thermal and circulation forecasts would be coupled passively, that is the thermal models would not feed back information to the circulation module. When sufficient initialization data, models, and computer power arise, this system would eventually yield to a more complete ocean prediction system. This eventual system would likely consist of either an oceanic general circulation model with a completely embedded mixed layer or a fully three-dimensional hydrodynamic/thermodynamic model (e.g., ADAMEC et al.,1981; MOOERS, ROBINSON and THOMPSON, 1987).

This evolutionary process stems from the trade-offs required between providing improved operational models as

they become available and the capabilities of ocean forecasting as limited by available data, models and computers. Global eddy-resolving circulation models require sufficiently accurate altimetric data for initialization and update, a Class VII supercomputer (~1 gigaflop speed, ~250 million words memory), and adequately tested models (HURLBURT, 1984; 1986). These won't be operationally available for several years. ROBINSON(1986) and GLENN, ROBINSON, and SPALL(1987) describe a tactical scale (~1000 km x 1000 km) forecast scheme using intensive in situ data and/or feature models for limited areas such as the Gulf Stream. One such model is presently run quasi-operationally by personnel at the Navy Eastern Oceanography Command. However, the necessity for pre-knowledge of the boundary conditions appears to be a major limitation to these limited scale models and is an active area of research.

Increasing the physical complexity of the forecast system to better match the known ocean physics, we might expect improvements to present forecast skill. This expectation especially holds in dynamically active regions such as frontal zones and western boundary currents with active mesoscale advection. However, when one increases physical complexity in an evolutionary way as outlined above, the potential exists for pathological behavior. An example might be the simulation of frontal dynamics where, in reality, salinity compensates temperature with the resultant condition of no density front. A simple

persistence forecast would likely outperform a simulation containing the dynamics of only the temperature or salinity variability alone.

This research thus attempts to provide insight into the first steps of the evolutionary process described above in accordance with specific recommendations in MOOERS, ROBINSON, and THOMPSON(1986). Namely, what is the impact of nowcast mesoscale advection on a simulated operational forecast? Second, what are the implications of passive mesoscale advective forecasts with respect to upper-ocean thermal forecasts?

The next section (Section 2) describes how and why I approach the above questions using numerical simulation experiments focused on a specific regional area. Section 3 explains why I chose the Sea of Japan for the simulation area and provides an oceanographic review of the region. Section 4 gives a detailed description of the forecast model used for the simulations. Section 5 describes the source of the thermal fields used as initial conditions in the simulations and also provides some comparisons with the limited available data. Section 6 relates details of the the actual numerical experiments performed. Section 7 gives the results of the experiments along with accompanying discussion. Section 8 summarizes the results of this study providing conclusions and recommendations drawn from this work.

2. APPROACH

Determining the impact of increasing the physical complexity of a forecast system, as in the above-mentioned questions, falls into the general realm of determining model error estimates. The report of Working Group IV of the Ocean Prediction Workshop 1986, Phase II (MOOERS, ROBINSON and THOMPSON, 1986) provides insight into tackling such problems. Missing or inaccurate physics in a forecast model introduces some of the error in the physical accuracy of ocean models. Model/data comparisons can help estimate these errors but in addition (or in the absence of adequate data sets) model/model comparisons can be used. Parallel runs of models with differing levels of physical approximation are an example. These provide information as to whether increasing complexity is beneficial. The possibility also exists that an increasing yet incomplete level of physics may introduce pathological results. Given the result that increasing physics are beneficial, the comparisons provide information as to the significance or cost-effectiveness of the improvement. Finally, error levels in the forecast can be compared to those of other components in the forecast system. An improvement in model error of 0.01° C may not justify the computational cost of a more sophisticated model if the data input is only accurate to 0.5° C.

Note the cost/benefit judgment implied in this last statement is obviously application dependent. A minor increase in accuracy in an ocean search and rescue model might well be worth a major cost. A comparable accuaracy increase in a forecast model used for location of fish schools may not.

Appropriate data sets providing synoptic coverage, for a regional area, for a significant length of time, for mixed layer models do not exist (MARTIN, 1987). Therefore, following the ideas discussed above, I approach this study from a model/model comparison as opposed to a model/data comparison viewpoint. In addition, this study addresses the above questions in the context of operational forecast procedures albeit with certain simplifications in order to focus the study.

In this particular study, repeated, daily, 72-hour duration, simulated forecasts provide the basis for four separate experiments. These experiments are performed in a dynamically active region, during a four week period in May and June of 1984, The four experiments each use the operational TOPS model as a basis, but with four increasing levels of physical complexity describing the horizontal processes in each. These experiments are described in more detail in section 6.

My primary intent is to address the questions posed in the introduction as opposed to validating the prediction system as a whole. Therefore, my experiments try to isolate, as much as possible, the mixed layer forecast

module while still simulating the overall system. To accomplish this isolation, several simplifications are made. First, the forecast for any given day begins with essentially the same initial condition for each of the four experiments. I therefore look at differences occurring within three day forecast periods rather than at cumulative differences that might occur due to analysis/forecast cycling over time. This latter comparison would introduce complicating questions concerning skill in both the analysis scheme and the cycling mechanism, in addition to that of the TOPS component of the system. Studies of these cumulative analysis/forecast cycling effects await the presently unavailable validation data for a regional area sampled synoptically over an extended time. This simplification, however, is especially relevant to shipboard prediction systems (MARTIN, 1987), where extended cycling will not normally occur.

The second simplification in these experiments is the use of analyzed and short forecast (6 hr) atmospheric forcing for the TOPS. Existing operational ocean forecasts use 1-3 day FNOC atmospheric forecasts as forcing functions. This second simplification minimizes errors introduced into the experiments due to errors in the atmospheric forecast models.

Validation and testing of the present operational TOPS have, in the past, used one dimensional model studies (e.g., MARTIN, 1985) and large scale regional studies (e.g., WARN-VARNAS et al., 1982). However, the primary

validation of these models has been in the real-time operational context due to the lack of appropriate data sets (e.g., CLANCY, POLLAK, and HARDING, 1986). TOPS and TOPS-EOTS results are presently compared with available real-time data, prior to its assimilation, and daily and monthly cumulative statistics then compiled. High resolution (~20 km), repeated, synoptic, regional ocean thermal data are not readily available. Hence the validation of future high resolution forecast/analysis systems will likely be in a comparable, cumulative statistical, operational context as well.

Consequently, the questions addressed by this work concerning the impact of evolutionary inclusion of mesoscale advection were specifically chosen to minimize the necessity for extensive validation data and yet provide insight and direction for the near-term future of operational upper-ocean forecasting. The intercomparison between the experimental results, as they become more physically realistic, provide the primary results of this study. Comparisons with the limited available data provide interesting, additional, but non-critical results.

3. REGION

As reviewed in Section 1., drift-current advection, air-sea heat exchange, solar absorption, and vertical mixing primarily control the large scale mixed-layer variablity in the upper ocean on the diurnal to seasonal time scales. Therefore, the prime consideration in the choice of region for these experiments is that it be an area where mesoscale advective effects might also play a significant role.

The Tsushima Current flowing through the Sea of Japan provides just such a location. According to MORIYASU(1972a), the Tsushima current, though small in scale, provides hydrographic conditions similar to those east of Honshu in the dynamically active Kuroshio and Oyashio current systems. The Sea of Japan provides additional advantages as a simulation site.

First, the Japan Meteorological Agency, Hydrographic Department, and Fisheries Agency conduct regular surveys around the Japanese archipelago including repeated transects across the Tsushima Current (SONU, 1981; ICHIYE, 1983). While not providing the spatial and temporal coverage required for a validation study, these data can provide comparison data for some of the assumptions made in this particular work. This active interest in the region also holds promise for possible future survey/modeling

studies to validate real-time, synoptic, regional upper-ocean forecasts.

The second advantage to the choice of the Sea of Japan lies in size. The Sea of Japan, being about half the size of the Mediterranean, allows the application of existing TOPS on a ~20 km grid.

The third advantage to the Sea of Japan stems from its configuration. As a semi-enclosed sea with basically three active ports, the inflow/outflow configuration minimizes the introduction of open boundary problems. It also allows for future extensions of this work, through the application of dynamic ocean circulation models (e.g. HURLBURT and THOMPSON, 1980).

The fourth advantage of the Sea of Japan derives from the broad body of knowledge existing for the Sea of Japan, in general, and the Tsushima Current, in particular. This work goes back to 1928, with research continuing today (e.g., YASUI et al., 1967; MORIYASU, 1972a; SHUTO, 1982).

The Sea of Japan (figure 2) is a mid-latitude marginal sea connected to adjacent oceans by four shallow straits (SHUTO, 1982; CONLON, 1981). The Tsushima (Korea) and Tsugaru Straits join the Sea of Japan with the East China Sea and the Pacific Ocean respectively. The Soya (La Perouse) and Mamiya (Tatar) Straits connect the Sea of Japan to the Sea of Okhotsk. The Tsushima Strait is deepest with a sill depth of roughly 150 m.

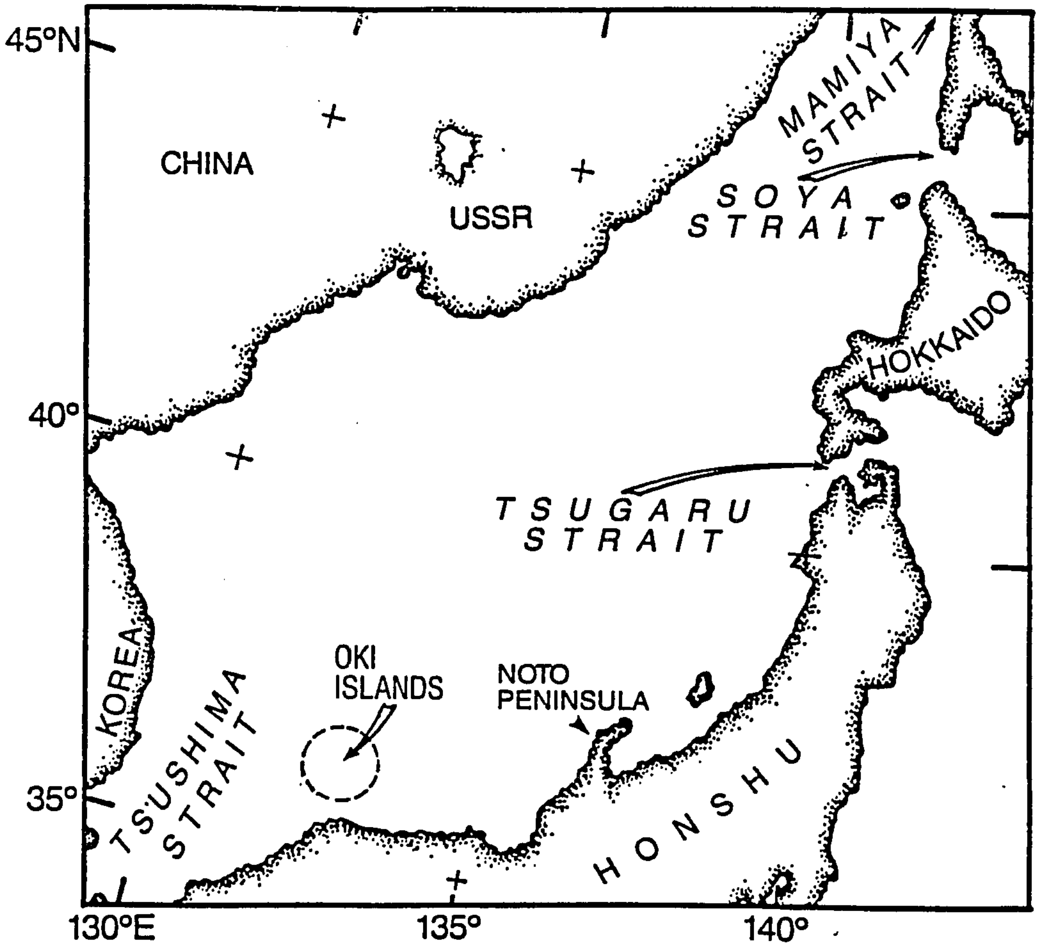

Figure 2. The Sea of Japan.

Characteristic features of the surface temperature on a seasonal time scale in the Sea of Japan include the following (MORIYASU, 1972a; YASUI et al., 1967). First, the temperature ranges from high in the south to low in the north with the isotherms running from WSW to ENE. This results from warm water entering via the Tsushima Strait mixing with the cooler Sea of Japan water as the flow progresses northeastward. Second, the north-south gradient ranges from 6° C in August to 15° C in December. Third, the highest temperatures occur in August with the lowest in February. Surface temperature values in the central region are approximately 4-6° C in February and 22-24° C in August. The second and third features result from strong cooling in the north in winter versus surface warming related to thermocline formation in the summer.

At 100 m, the seasonally averaged isotherms run SW to NE (YASUI et al., 1967). Temperatures in the north are 2-4° C throughout the year while those in the south range from 10-12° C in winter to 14-16° C in summer and autumn. At 100 m, the N-S gradient becomes stronger in summer in direct contrast to surface conditions. The N-S gradient in the central Sea of Japan indicates a frontal zone, the Polar Front, in the vicinity of 39 to 40 N. This implies, from geostrophic estimates, the location of a strong northeastward flowing current. North of this front is refered to as the cold current region, south of the front as the warm current region. At 400 m, temperatures appear

nearly homogeneous between 0 and 1° C throughout the year with no characteristic distribution.

The salinity distribution roughly follows that of temperature with high salinity water associated with the warm water flowing through the Tsushima Strait (YASUI et al., 1967). The exception is in summer when less saline East China Sea waters lower the salinity of the inflowing surface water. The change of salinity at 100 m associated with the polar front is approximately 0.5 with northern values of 34 and southern values of 34.5.

The Tsushima Current, the warm, saline flow indicated above, is the major feature in the hydrography of the Sea of Japan. Beginning as a branch of the Kuroshio which enters the East China Sea south of Kyushu, the Tsushima Current enters the Sea of Japan and flows north along the western side of Japan (SVERDRUP, JOHNSON, and FLEMING, 1942). The Tsushima Current exits the Sea of Japan primarily via the Tsugaru Strait (between Honshu and Hokkaido) and the Soya Strait (between Hokkaido and Sakhalin). The Tsugaru carries the bulk of the outflow with estimates ranging from 50-100% (MORIYASU, 1972a) to 70-90% (TOBA et al., 1982). The Soya Strait effectively takes the remainder.

More recent work has refined this description. HUH(1982) describes the origin of the Tsushima Current in the branching of the Kuroshio south of Honshu. The Kuroshio waters, mixing with East China Sea waters, then enter the Sea of Japan via the Tsushima Strait. An

interesting controversy however still exists about the nature of the flow once inside the Sea of Japan (MORIYASU, 1972a; CONLON, 1981; SONU, 1981; KAWABE, 1982a; ICHIYE, 1983). The originally accepted view (figure 3) was one of a three-branch Tsushima Current developing within or just to the east of the Tsushima Strait. These three branches supposedly rejoin east and north of the Noto peninsula (~37-40° N) flowing northward together.

The first branch (near-shore branch) begins in the eastern channel of the Tsushima Strait and flows northward in shallow water (< 150 m) along the Japanese coast. The second and third branches (offshore branch and Eastern Korean Current) begin in the deeper western channel of the Tsushima Strait. The second branch flows offshore of the first. The third branch flows northward along the Korean coast as a western boundary current veering offshore around 38-39° N to follow (or define) the Polar Front.

Marked meandering characterizes the flow north of the Oki Islands. This, in combination with an observed countercurrent east of the East Korean Current (TANIOKA, 1968), lends credence to the more recently accepted opinion that the second and third branches are just one meandering branch. ICHIYE(1983) supports this latter view dividing the Tsushima Current into eastern and western branches. His work demonstrates significant meandering in the western branch.

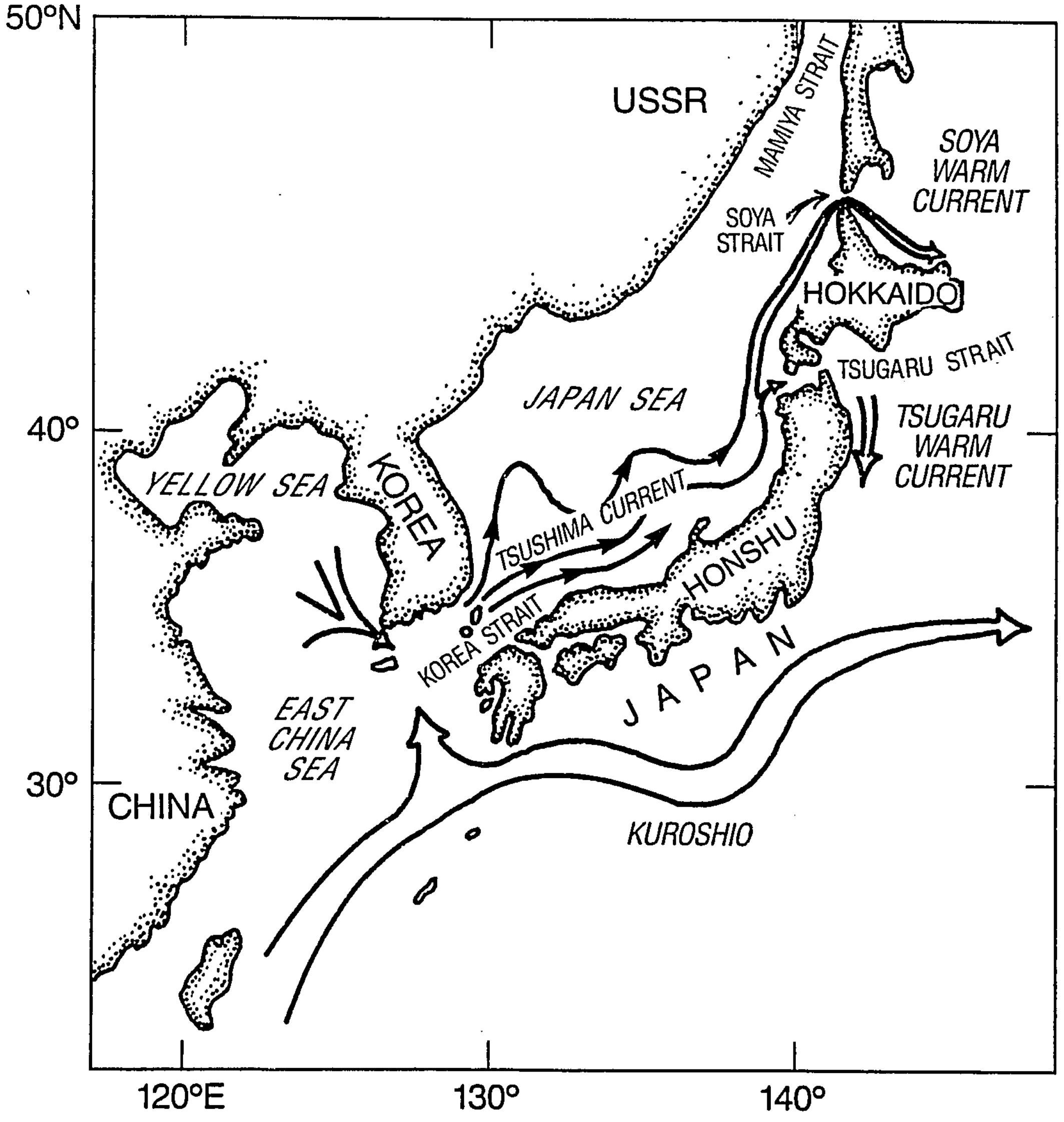

Figure 3. Schematic of flow in the Sea of Japan [adapted from CONLON(1981)].

ICHIYE(1983) further describes both branches as having width less than 100 km and depth less than 300 m. He suggests that the shallow nature of the current, combined with the sharp thermal boundary caused by the inflow of the warm water into the cooler Sea of Japan makes the synoptic surface temperature distribution useful for determining the current pattern. A 300 m maximum depth for the current agrees with previous work using a reference level of 300-400 m for geostrophic calculations in the Sea of Japan. MORIYASU(1972b) and CONLON(1981), in comparisons with current meter data, both demonstrate the suitability of the geostrophic approximation using these shallow reference levels.

Recent numerical modeling in the Sea of Japan has focused primarily on determining the nature of the flow of the Tsushima Current on seasonal and longer time scales (YOON, 1982a; YOON, 1982b; YOON, 1982c; KAWABE, 1982b). These studies suggest the inshore branch as a steady, bottom-controlled, current flowing along the continental shelf under the influence of the topographic β effect. The second branch exists only in the summer flowing offshore of the inshore branch. Its existence results from the increase of flow from June to August which forces the propagation of the two lowest modes of continental shelf waves. These also are a result of the topograhic β effect. The offshore branch which begins as the East Korean Warm Current, acts as a steady western boundary current resulting from the planetary β effect.

MORIYASU(1972a) summarizes estimates of annual transport for the Tsushima Current system of 1 Sv (1 Sv = 10^6 m^3/s). However, he also reports seasonally varying transport estimates at 40-41 N ranging from 2-7 Sv with summer being the period of strongest flow. SHUTO (1982) reports year to year variations, just in August, of 2-6.5 Sv. TOBA et al. (1982) indicate an annual average of 2 Sv with a range of variation of ±1.6 Sv. These estimates are primarily for the combination of all branches of the Tsushima Current system. Seasonally varying mean surface speeds in the East Korean Warm Current alone range from 17 cm/s in winter to 50 cm/s in summer (TANIOKA, 1968).

4. FORECAST MODEL

A modified version of the operational TOPS model (CLANCY and POLLAK, 1983) provides the basis for these experiments. Its complete description, including validation experiments, is thoroughly covered by CLANCY and POLLAK(1983) and CLANCY and MARTIN(1979, 1981). The model allows the modification of near-surface temperature and salinity stratification due to : (1) vertical mixing forced by both convection and wind-generated turbulence, and (2) surface heat and moisture fluxes. Advective effects can be incorporated via: (1) instantaneous Ekman curents, and (2) geostrophic currents calculated from the density field or provided externally from a circulation model. I review the model below including the variations added for these experiments.

4.1. Basic Equations

Four prognostic conservation equations, one each for temperature and salinity and two for momentum, comprise the heart of the TOPS. These take the following form with over bars ($\bar{\ }$) denoting ensemble means and primes($'$) indicating departures from these means,

$$\frac{\partial \overline{T}}{\partial t} = \frac{\partial}{\partial z}\left(-\overline{w'T'} + \nu\frac{\partial \overline{T}}{\partial z}\right) + \frac{1}{\rho_w c}\,\frac{\partial \overline{F}}{\partial z} - \frac{\partial}{\partial x}(u_a\overline{T}) - \frac{\partial}{\partial y}(v_a\overline{T})$$

$$- \frac{\partial}{\partial z}(w_a\overline{T}) + A\left(\frac{\partial^2 \overline{T}}{\partial x^2} + \frac{\partial^2 \overline{T}}{\partial y^2}\right) \qquad (1)$$

$$\frac{\partial \overline{S}}{\partial t} = \frac{\partial}{\partial z}\left(-\overline{w'S'} + \nu\frac{\partial \overline{S}}{\partial z}\right) - \frac{\partial}{\partial x}(u_a\overline{S}) - \frac{\partial}{\partial y}(v_a\overline{S})$$

$$- \frac{\partial}{\partial z}(w_a\overline{S}) + A\left(\frac{\partial^2 \overline{S}}{\partial x^2} + \frac{\partial^2 \overline{S}}{\partial y^2}\right) \qquad (2)$$

$$\frac{\partial \overline{u}}{\partial t} = f\overline{v} + \frac{\partial}{\partial z}\left(-\overline{w'u'} + \nu\frac{\partial \overline{u}}{\partial z}\right) - D\overline{u} \qquad (3)$$

$$\frac{\partial \overline{v}}{\partial t} = -f\overline{u} + \frac{\partial}{\partial z}\left(-\overline{w'v'} + \nu\frac{\partial \overline{v}}{\partial z}\right) - D\overline{v} \qquad (4)$$

with the variables as defined below,

T = temperature

S = salinity

u,v,w = x,y, and z components of current velocity relative to the grid

F = downward flux of solar radiation

ρ_w = reference density of seawater (1026.0 kg m^{-3})

c = specific heat of seawater (3901.4 J kg^{-1} $^\circ C^{1}$)

D = damping coefficient (1/864000. s^{-1})

ν = background eddy diffusion

f = Coriolis parameter

A = horizontal eddy diffusion coefficient (see below)

t = time

x,y,z = grid coordinates (z positive up)

u_a, v_a, w_a = x-, y-, z- components of advection current (see section 4.3).

The damping coefficient, D, in equations (1) and (4), represents the drag force due to radiation stress at the base of the mixed layer. This stress is associated with internal wave energy propagating both horizontally and vertically away from the wind forced region (POLLARD and MILLARD, 1970). The vertical diffusion coefficient, ν, in equations (1)-(4) represents a weak "background" eddy diffusion existing even below the surface mixed layer. Equations (3) and (4) only represent the wind drift (Ekman and inertial) component of the advection as discussed further in section 4.3.

The vertical eddy fluxes of temperature, salinity, and momentum in equations (1)-(4) are parameterized using the Level-2 turbulence closure theory of MELLOR and YAMADA(1974). The eddy flux parameterizations are,

$$\overline{w'T'} = -\ell q S_H \frac{\partial \overline{T}}{\partial z} \equiv -K_H \frac{\partial \overline{T}}{\partial z} \tag{5}$$

$$\overline{w'S'} = -\ell q S_H \frac{\partial \overline{S}}{\partial z} \equiv -K_H \frac{\partial \overline{S}}{\partial z} \tag{6}$$

$$\overline{w'u'} = -\ell q S_M \frac{\partial \overline{u}}{\partial z} \equiv -K_M \frac{\partial \overline{u}}{\partial z} \tag{7}$$

$$\overline{w'v'} = -\imath q S_M \frac{\partial \overline{v}}{\partial z} \equiv -K_M \frac{\partial \overline{v}}{\partial z} \tag{8}$$

where,

K_H, K_M = vertical eddy diffusion coefficients for heat and momentum, respectively

$\imath$ = turbulence length scale

q = square root of twice the turbulent kinetic energy

S_H, S_M = stability functions (functions of the gradient Richardson number, Ri).

The gradient Richardson number, Ri, represents the ratio between the vertical density gradient and the vertical shear,

$$Ri \equiv \frac{-\frac{g}{\rho_w} \frac{\partial \overline{\rho}}{\partial z}}{\left[\left(\frac{\partial \overline{u}}{\partial z}\right)^2 + \left(\frac{\partial \overline{v}}{\partial z}\right)^2\right]} \tag{9}$$

where,

g = acceleration of gravity (9.8 m s^{-2})

$\overline{\rho}$ = mean field density calculated using the non-linear FRIEDRICH and LEVITUS(1972) equation of state applied to $\overline{T}$ and $\overline{S}$.

The functional forms for the stability functions, S_H and S_M, are derived by MELLOR and YAMADA(1974) and presented in figure 4. Note that Ri = 0.23 implies a cutoff of the turbulence. This cutoff primarily determines the predicted mixing depth since the density stratification suppresses entrainment mixing when Ri exceeds 0.23.

A simplified version of the turbulent kinetic energy equation is used to calculate q in the Level-2 parameterization. This equation expresses the local balance of shear production, buoyancy production, and viscous dissipation of turbulent kinetic energy,

$$\ell q S_M\left[\left(\frac{\partial \bar{u}}{\partial z}\right)^2 + \left(\frac{\partial \bar{v}}{\partial z}\right)^2\right] + \ell q S_H\left(\frac{g}{\rho_w}\frac{\partial \bar{\rho}}{\partial z}\right) - \frac{q^3}{15\ell} = 0. \qquad (10)$$

The calculation of the turbulent length scale, ℓ, follows MELLOR and DURBIN(1975) and, with equations (5)-(10), closes the turbulence parameterization. The following equation defines ℓ,

$$\ell = \frac{0.1 \int_{-\infty}^{0} |z|\, q\, dz}{\int_{-\infty}^{0} q\, dz}. \qquad (11)$$

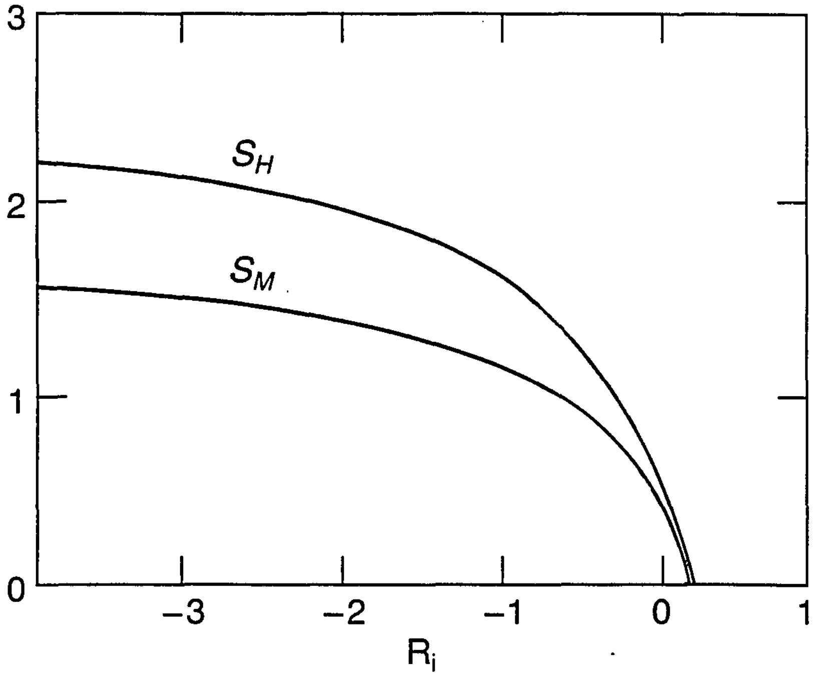

Figure 4. Stability functions, S_H and S_M, as a function of gradient Richardson number.

The horizontal diffusion coefficient, A, in the original TOPS is taken from HANEY(1974) as given below,

$$A = A_o \left(\frac{\Delta x}{\Delta x_o}\right)^{4/3} \qquad (12)$$

where,

Δx = horizontal grid spacing (~ 23 km)

A_o = reference horizontal diffusion coefficient

(3.0×10^3 m^2 sec^{-1})

Δx_o = reference horizontal grid spacing (275 km).

A comparable parameterization more closely related to available oceanic data is used in the TOPS model for this study. Taken directly from OKUBO and OZMIDOV(1970), the following "4/3 law" is used,

$$A = c\varepsilon^{1/3}\lambda^{4/3} \qquad (13)$$

where,

c = numerical constant of order 0.1

ε = turbulent energy flux

λ = scale of the phenomena in question.

Experimental data involving horizontal diffusion of tracer spots over a wide range of λ support the validity of this parameterization in the ocean. For scale ranges, λ, of 10

km to 1000 km, ε equals $10^{-5}cm^2s^{-3}$. Since A is required to dissipate energy from phenomena unresolved by the grid, λ is assumed to equal Δx. This formulation provides horizontal eddy diffusion coefficients of the same order of magnitude as equation (12) but smaller by a factor of 2 to 3.

Finally, the solar radiation flux divergence in 4.1.1. is parameterized using a Type IA extinction profile from data of JERLOV(1968).

4.2. Grid and Finite Differencing

The vertical grid consists of 17 levels from the surface to 500 m as shown in Table 1. $\overline{T}$, $\overline{S}$, $\overline{u}$, $\overline{v}$, u_a,and v_a are defined at these depths. The vertical eddy fluxes as well as w_a are defined midway between the above quantities. Horizontally, $\overline{T}$, $\overline{S}$, $\overline{u}$, $\overline{v}$, w_a, and the vertical eddy fluxes are defined at the points of the 63x63 polar stereographic grid shown in figure 5. This grid is a subset of the standard FNOC 63x63 Northern Hemisphere polar stereographic grid on which the present Northern Hemisphere operational TOPS runs. The subset grid covers the Sea of Japan with roughly a 23 km mesh spacing. The horizontal current components, u_a, v_a, are displaced one-half grid length in the x- and y- directions respectively in the manner of an Arakawa C grid (MESINGER and ARAKAWA, 1976).

TABLE 1. TOPS VERTICAL GRID

Level	Depth(m)
1	2.5
2	7.5
3	12.5
4	17.5
5	25.0
6	32.5
7	40.0
8	50.0
9	62.5
10	75.0
11	100.0
12	125.0
13	150.0
14	200.0
15	300.0
16	400.0
17	500.0

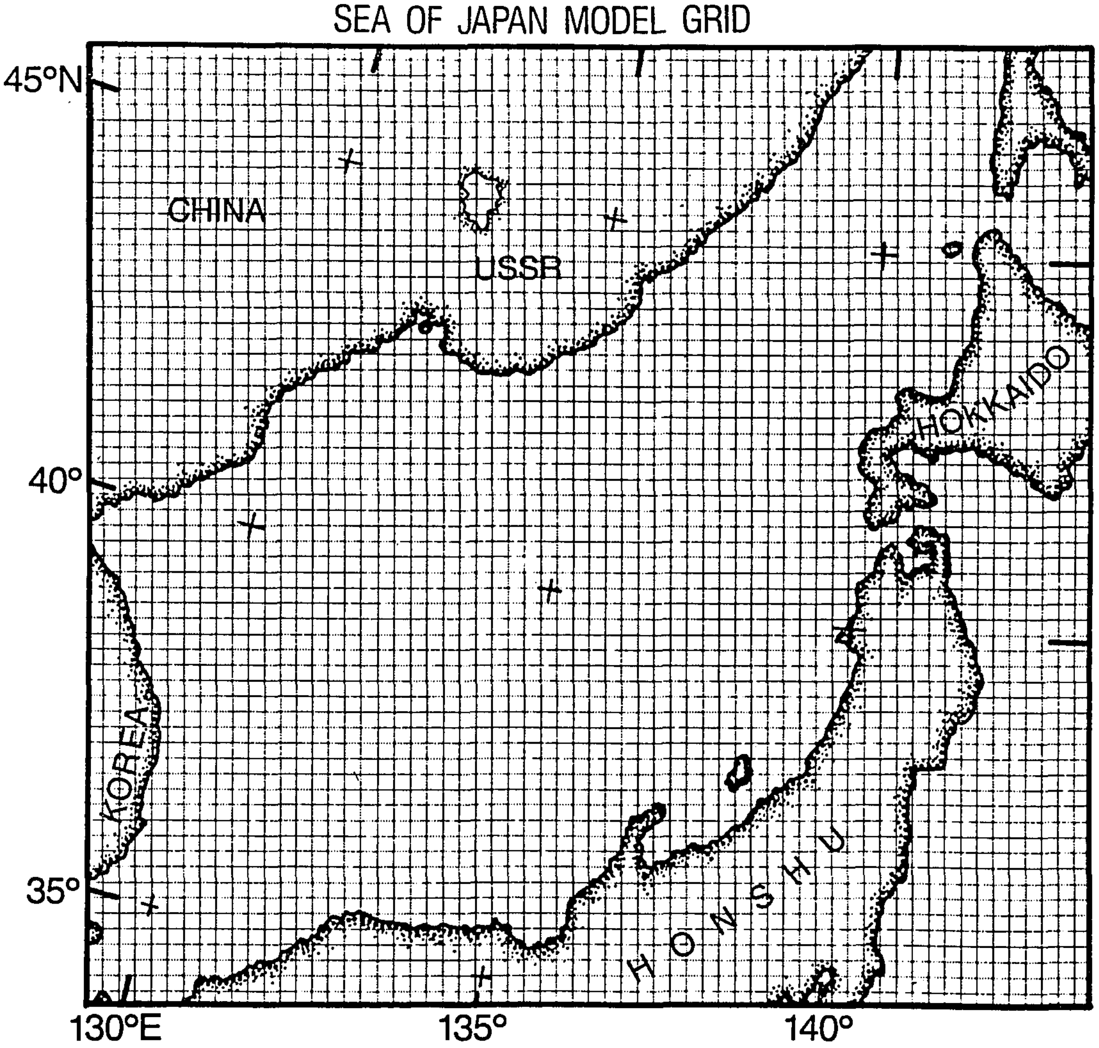

Figure 5. The Sea of Japan model grid.

Spatial derivatives are all centered in space. In equations (1)-(4), time differencing is trapezoidal for the Coriolis and vertical advection terms, backward for the vertical eddy flux terms, and forward for all other terms. Appendix A provides representations of equations (1)-(4) in finite difference form.

4.3. Treatment of Advection

Equations (3) and (4) contain no horizontal pressure gradient terms and therefore represent only the Ekman and inertial or wind-drift components of the current. This stems from the assumption that the non-linear terms can be neglected in the full momentum equations. I present scaling arguments supporting this assumption in Appendix B. Neglect of the non-linear terms allows the application of the principle of superposition (POND and PICKARD, 1978) where motions associated with vertical friction can be calculated separately from those associated with horizontal pressure gradients. Neglect of the pressure terms in equations (3) and (4) has the advantage of allowing initialization of the model by an analysis of sparse data since it eliminates spurious wave motions due to an unbalanced initial state. Geostrophic flow can contribute to the advection of temperature and salinity nonetheless, via its role in the u_a and v_a equations defined,

$$u_a = u_i + u_g^* \qquad (14)$$

$$v_a = v_i + v_g^* \qquad (15)$$

where,

u_i, v_i = x- and y-components of the instantaneous wind drift current

u_g^*, v_g^* = x- and y-components of the total current not included in u_i, v_i.

As discussed in the introduction, these latter components of the current, u_g^* and v_g^*, will eventually represent the mesoscale flow from eddy-resolving hydrodynamic models. For this study, I provide this input via the proposed interim technique of nowcast geostrophic advection. I discuss the derivation of this below.

The wind drift components, u_i and v_i, result from the interpolation of $\bar{u}$ and $\bar{v}$ each time step to the staggered grid. The geostrophic components, u_g^* and v_g^*, are calculated from a density field derived, for this study, from the daily temperature analysis fields described in Section 5 and an assumed constant salinity. The thermal wind equations (Pond and Pickard,1978), shown below, integrated upward from a specified level of no motion and

applied to this density field, provide the raw geostrophic flow components, u_g, v_g,

$$\frac{\partial(\rho f v_g)}{\partial z} = -g \frac{\partial \rho}{\partial x} \qquad (16)$$

$$\frac{\partial(\rho f u_g)}{\partial z} = g \frac{\partial \rho}{\partial y}. \qquad (17)$$

These raw geostrophic currents are then used to solve for the stream function, ψ, via the following equation,

$$\frac{\partial^2 \psi}{\partial x^2} + \frac{\partial^2 \psi}{\partial y^2} = \frac{\partial v_g}{\partial x} - \frac{\partial u_g}{\partial y}. \qquad (18)$$

The boundary conditions on ψ are prescribed such that the net outflow through the Tsugaru and Soya Straits balances the net inflow through the Tsushima Strait. The Tsugaru Strait takes 75% of the outflow and the Soya Strait the rest, consistent with present knowledge of the Tsushima Current system (section 3). The resultant, non-divergent geostrophic flow components then result from the following standard definitions,

$$u_g^* = - \frac{\partial \psi}{\partial y} \qquad (19)$$

$$v_g^* = \frac{\partial \psi}{\partial x}. \qquad (20)$$

The purpose for eliminating the horizontal divergence of the geostrophic flow field in this way lies in the nature of the divergence calculation (CLANCY and MARTIN, 1979). Calculating the divergence involves small terms resulting from the differences between large terms. Thus small errors in the horizontal flow field (from noise in the density field) can cause large errors in the vertical motion field calculated from the divergence of the horizontal field. Note the use of the non-divergent components of the geostrophic flow precludes investigation of the effects on the upper-ocean forecast of the vertical component of the mesoscale flow (WELLER, 1982).

Consequently, the vertical advection, w_a, results from Ekman pumping/suction calculated from the following,

$$w_a(z) = \int_z^o \left(\frac{\partial u_i}{\partial x} + \frac{\partial v_i}{\partial y}\right) dz. \tag{21}$$

4.4. Initial Conditions

For this study, a synthesis of available operational objective upper-ocean analyses (TOPS-EOTS) and subjective surface analyses provide the daily temperature fields for the TOPS initial conditions (see Section 5). These synthesized initial conditions provide the initial temperatures at the levels shown in Table 2.

TABLE 2. TOPS-EOTS VERTICAL GRID

Level	Depth(m)
1	0.0
2	25.0
3	50.0
4	75.0
5	100.0
6	125.0
7	150.0
8	200.0
9	250.0
10	300.0
11	400.0

Note that all fixed depths in the analysis system except 0 and 250 m are shared by TOPS (Table 1) but that TOPS provides better resolution in the upper 75 m. An initialization algorithm is applied to preserve this information during the daily TOPS temperature update process. This algorithm tends to retain the TOPS profile shape while matching temperatures at shared levels.

Synoptic salinity analyses do not exist since salinity observations are not routinely made. Initial conditions for salinity therefore are deduced from a daily interpolation of monthly Northern Hemisphere climatology for depths 0, 25, 50, 100, 150, 200, 400, and 600 m interpolated to the Sea of Japan grid. An algorithm is then applied to the profile to eliminate regions of unstable density stratification in the initial state.

The initial conditions for momentum are handled in two ways. For the initial forecast in a multiple forecast sequence, $\bar{u}$ and $\bar{v}$ are set to 0 below the mixed layer. Within the mixed layer, they are set equal to the steady state solution to equations (3) and (4), resulting from the initial wind stress. Subsequent forecasts in the sequence use the previous day's, 24 hr forecast $\bar{u}$ and $\bar{v}$. This approach helps minimize inconsistencies between the wind stress and the inertially varying surface current at the beginning of each forecast within a sequence.

The initial conditions for turbulent length scale, ι, are handled in a similar two phase approach. The first day

of the simulations initializes ι to 2.5 m. Subsequent initial daily values are calculated from the previous day's 24 hr forecast.

4.5. Boundary Conditions

Surface boundary conditions for the temperature, salinity, and momentum equations (1)-(4) are given below,

$$\left[-\overline{w'T'} + \nu\frac{\partial\overline{T}}{\partial z}\right]_{z=0} = -\frac{(B_0+H_0+LQ_0)}{\rho_w c} \qquad (22)$$

$$\left[-\overline{w'S'} + \nu\frac{\partial\overline{S}}{\partial z}\right]_{z=0} = \frac{(Q_0-P_0)\overline{S}_0}{\rho_w} \qquad (23)$$

$$\left[-\overline{w'u'} + \nu\frac{\partial\overline{u}}{\partial z}\right]_{z=0} = \frac{\tau^x}{\rho_w} \qquad (24)$$

$$\left[-\overline{w'v'} + \nu\frac{\partial\overline{v}}{\partial z}\right]_{z=0} = \frac{\tau^y}{\rho_w} \qquad (25)$$

where,

B_0 = surface infrared radiative heat flux

H_0 = surface sensible heat flux

Q_0 = surface evaporation rate

L = heat of vaporization (2.453×10^6 J kg^{-1})

P_0 = surface precipitation rate

$\overline{S}_o$ = surface salinity

τ_x, τ_y = x- and y-components of the surface wind stress.

The wind stress terms are calculated as follows,

$$\tau^x = \rho_a C_D U(U^2 + V^2)^{1/2} \tag{26}$$

$$\tau^y = \rho_a C_D V(U^2 + V^2)^{1/2} \tag{27}$$

where,

U,V = x- and y- components of the wind velocity at 10 m reference level

ρ_a = reference density for air (1.17 kg m^{-3})

C_D = drag coefficient.

The drag coefficient, C_D, is calculated from the wind speed dependent formulation of GARRAT(1977) assuming U, V in cgs units,

$$C_D = 0.00075 + 6.7 \times 10^{-7}(U^2 + V^2)^{1/2}. \tag{28}$$

U and V are calculated from available 19.5 m reference level winds, $U_{19.5}$ and $V_{19.5}$. Assuming a constant drag

coefficient of 0.001 and neutral stratification in the atmospheric boundary layer, the 19.5 meter winds are multiplied by 0.943 to approximate the 10 m winds. For this study, C_D ranged from 0.00075 to 0.00175.

$U_{19.5}$ and $V_{19.5}$, $(B_0+H_0+LQ_0)$, and Q_0 are interpolated to the grid shown in figure 5 from fields provided at 6 hr intervals by the FNOC global atmospheric prediction models. The Global Surface Contact Layer Interface model (GSCLI) provides the wind components. The GSCLI is basically a global version of the earlier northern hemisphere planetary boundary layer model described by MIHOK and KAITALA(1976). The other terms are provided by the Naval Operational Global Atmospheric Prediction System (NOGAPS), a global general circulation model (GCM) derived from the UCLA GCM (ARAKAWA and LAMB, 1977; ROSMOND, 1981).

The values of τ_x, τ_y, $(B_0+H_0+LQ_0)$, and Q_0 are linearly interpolated to each time step from the 6 hr values. NOGAPS provides a 12 hr, predicted, accumulated precipitation and from this the precipitation rate, P_0, is derived. Although TOPS has the capability to use P_0, it is currently set to 0 both in the operational models and for these experiments due to questions of the precipitation forecast skill of NOGAPS (CLANCY, personal communication).

The upper boundary condition for the radiational heating calculations requires the surface solar radiative heat flux at each timestep, F_0, as determined by,

$$F_o = I_o\cos(\alpha)[0.651 + 0.349(1 - 0.27(w^{*}\sec(\alpha)^{0.303})] \quad (29)$$

where,

I_o = amplitude of solar flux computed as described below

α = instantaneous zenith angle of the sun

w^{*} = non-dimensional reference water vapor mass(3.5).

I_o, the solar flux amplitude for a given six hour interval is calculated as a weighted sum of six-hourly, instantaneous, solar flux amplitudes,

$$I_o = \frac{b_1 I_1 + b_2 I_2}{b_1 + b_2} \quad (30)$$

where,

I_1, I_2 = instantaneous amplitude of solar flux at initial and final times of given six-hour interval available from NOGAPS (see below for derivation)

b_1, b_2 = weighting factors as defined below.

NOGAPS provides six hourly instantaneous surface solar flux values, F_1 and F_2 which include the effects of NOGAPS predicted cloud cover. These are convertible to cloud

corrected solar flux amplitudes, I_1 and I_2 by means of modified versions of equation (29),

$$I_1 = \frac{F_1}{\cos\alpha_1[0.651 + 0.349(1-0.271(w^* \sec\alpha_1)^{0.303})]} \tag{31}$$

$$I_2 = \frac{F_2}{\cos\alpha_2[0.651 + 0.349(1-0.271(w^* \sec\alpha_2)^{0.303})]} \tag{32}$$

where,

α_1, α_2 = instantaneous zenith angle of sun at the beginning and end of a given six hour interval.

The weighting parameters b_1, b_2 likewise for the beginning and end of a given six hour interval are given by,

$$b_1 = \begin{cases} (\cos\alpha_1 - \cos\alpha_C)^2 & \text{for } \alpha_1 < \alpha_C \\ 0 & \text{for } \alpha_1 \geq \alpha_C \end{cases} \tag{33}$$

$$b_2 = \begin{cases} (\cos\alpha_2 - \cos\alpha_C)^2 & \text{for } \alpha_2 < \alpha_C \\ 0 & \text{for } \alpha_2 \geq \alpha_C \end{cases} \tag{34}$$

where,

α_C = cutoff zenith angle (80°).

Thus, a weighted combination of solar flux amplitudes from the beginning and end of each six-hour period provides the value for I_0. The weighting functions provide that values at high zenith angles have low or no weight since cloud cover estimates from F_1 and F_2 are unreliable at high zenith angles.

The lower boundary conditions on equations (1)-(4) are that temperature, salinity, and momentum are held constant throughout each forecast.

For the experiments described in this report, two special lateral boundary conditions are considered, land-sea and open. At land-sea boundaries, horizontal diffusion as well as the normal component of both wind-drift and geostrophic advection are set to 0. Consequently, neither temperature nor salinity advect or diffuse across land-sea boundaries. Open boundaries are treated as non-advective TOPS points as suggested by MILLER (unpublished report,1983). Thus one-grid point inside an open boundary, both salinity and temperature can advect or diffuse in from the exterior points while temperature and salinity at the exterior points remain unaffected by horizontal influences. This open-boundary condition is new to TOPS and has performed satisfactorily in tests in the Norwegian Sea. For these experiments, this condition will have little influence due to the semi-enclosed configuration of the Sea of Japan.

5. ANALYSIS COMPONENT

Sufficient data does not presently exist to perform the repeated, daily, upper-ocean, synoptic, objective analyses suitable for initializing the proposed experiments. Consequently, to simulate realistic initial conditions for these experiments, I merge three pieces of information: (1) daily, operational, coarse-resolution, upper-ocean objective analyses available from FNOC, (2) high horizontal resolution, weekly, subjective sea surface temperature (SST) analyses available from the Naval Oceanography Command Center (NOCC) in Guam, and (3) subjective knowledge about the Sea of Japan (Section 3).

5.1 Derivation of Synthetic Initial Conditions

In this study, archived fields from the operational Northern Hemisphere TOPS-EOTS analysis provide the basis for the daily initial conditions for temperature. As described in the introduction, the TOPS-EOTS analysis combines all available data as well as the synoptic, upper-ocean, variabiliity due to atmospheric forcing. These daily analyses, interpolated from the FNOC, Northern Hemisphere, polar stereographic grid to the Sea of Japan grid, provide the basic 0-400 m temperature fields.

Figures 6-13 provide examples at 0 m of these interpolated fields for May 8-15, 1984.

These interpolated fields are modified to reflect the frontal structure available from the weekly NOCC maps. These modifications can be summarized in three steps. First, I form gridded, daily SST maps interpolated from the weekly, subjective NOCC analyses. Second, I warp each daily, TOPS-EOTS SST field to conform to the appropriate, NOCC-derived, gridded SST field. Third, I warp the subsurface, TOPS-EOTS, temperature fields using the transformation required for the SST. I describe this three-step process in more detail below.

The NOCC in Guam provides weekly, subjective, SST maps for the western Pacific region covering the Kuroshio, Oyashio, and Tsushima Current systems. Naval personnel at the NOCC create these maps using all available ship, aircraft, and satellite information available to them (AG1 MIKE ADAMS, 1984, personal communication). The data is compiled weekly with more recent data given higher weight in the subjective analysis. Two examples for May 8 and May 15, 1984 are shown in figures 14 and 15. SHIM(1986) digitized the location of the polar front from these maps. He defined the frontal position as the line following the center of the high, SST gradient region as seen in figures 14 and 15.

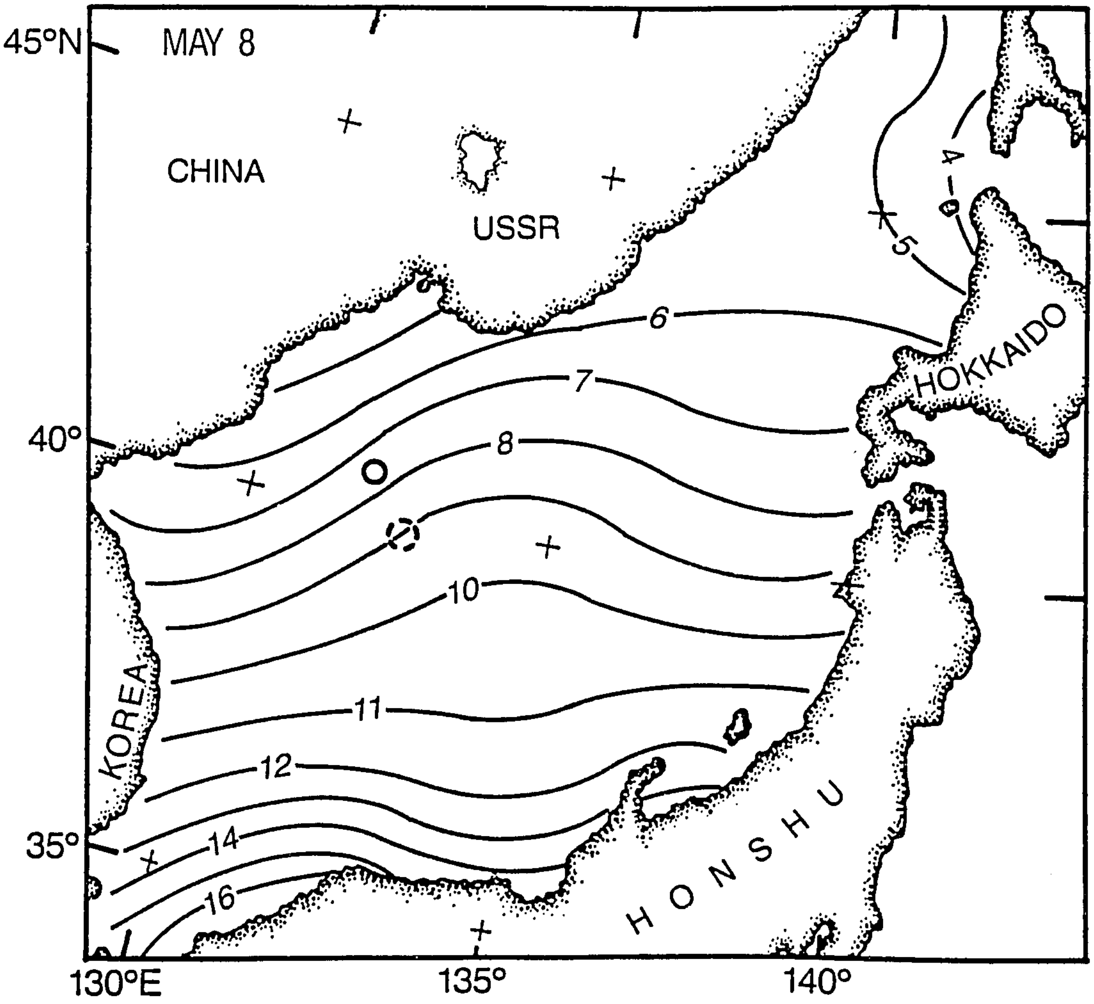

Figure 6. Zoomed EOTS SST (°C) for May 8, 1984.

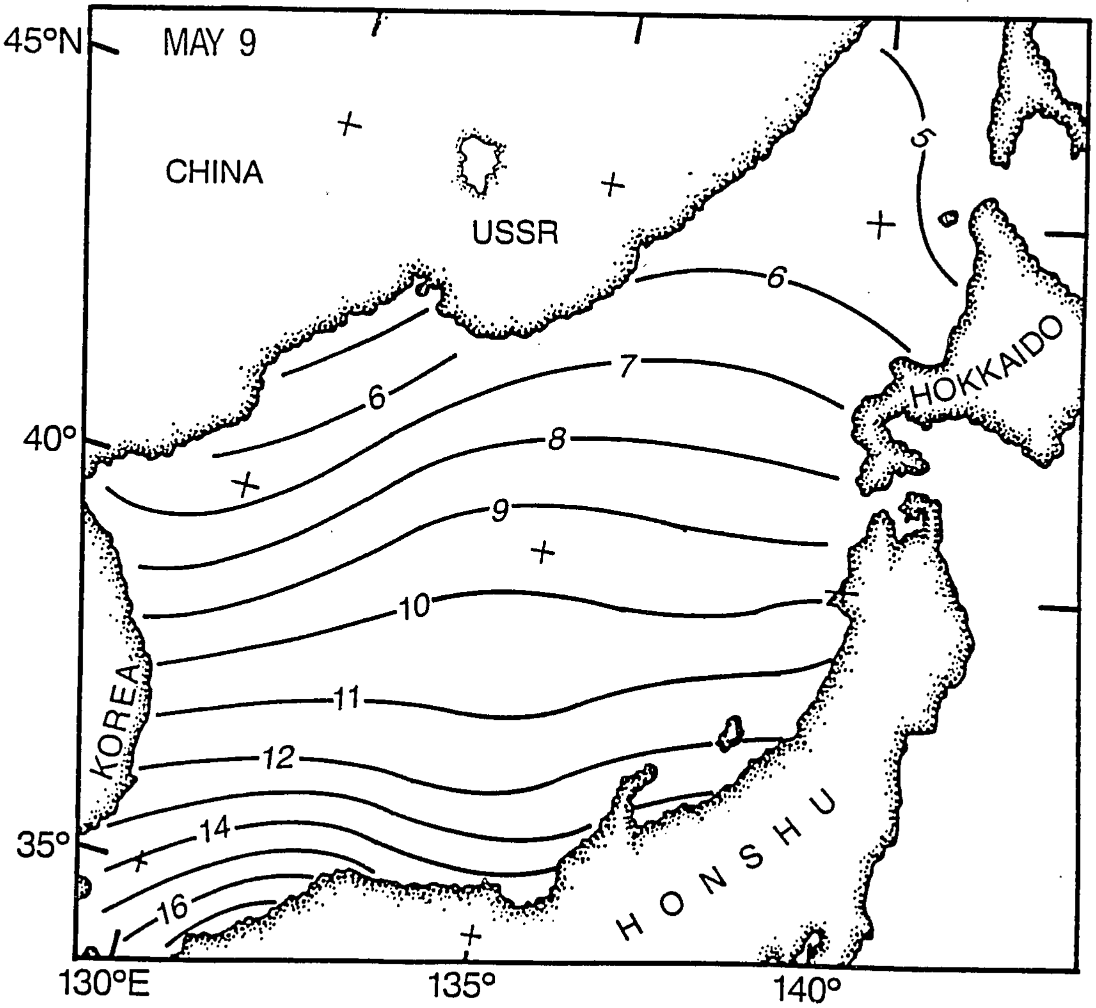

Figure 7. Zoomed EOTS SST (°C) for May 9, 1984.

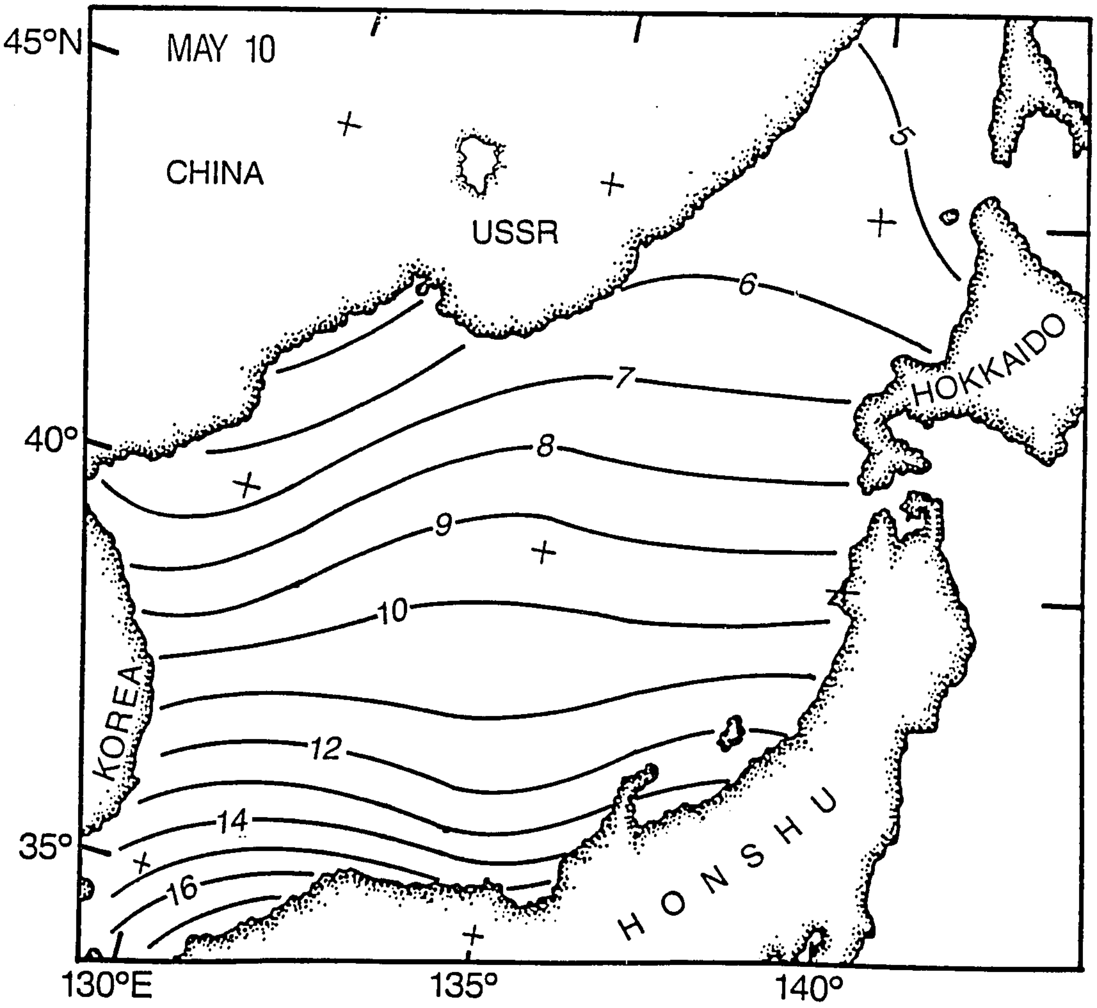

Figure 8. Zoomed EOTS SST (°C) for May 10, 1984.

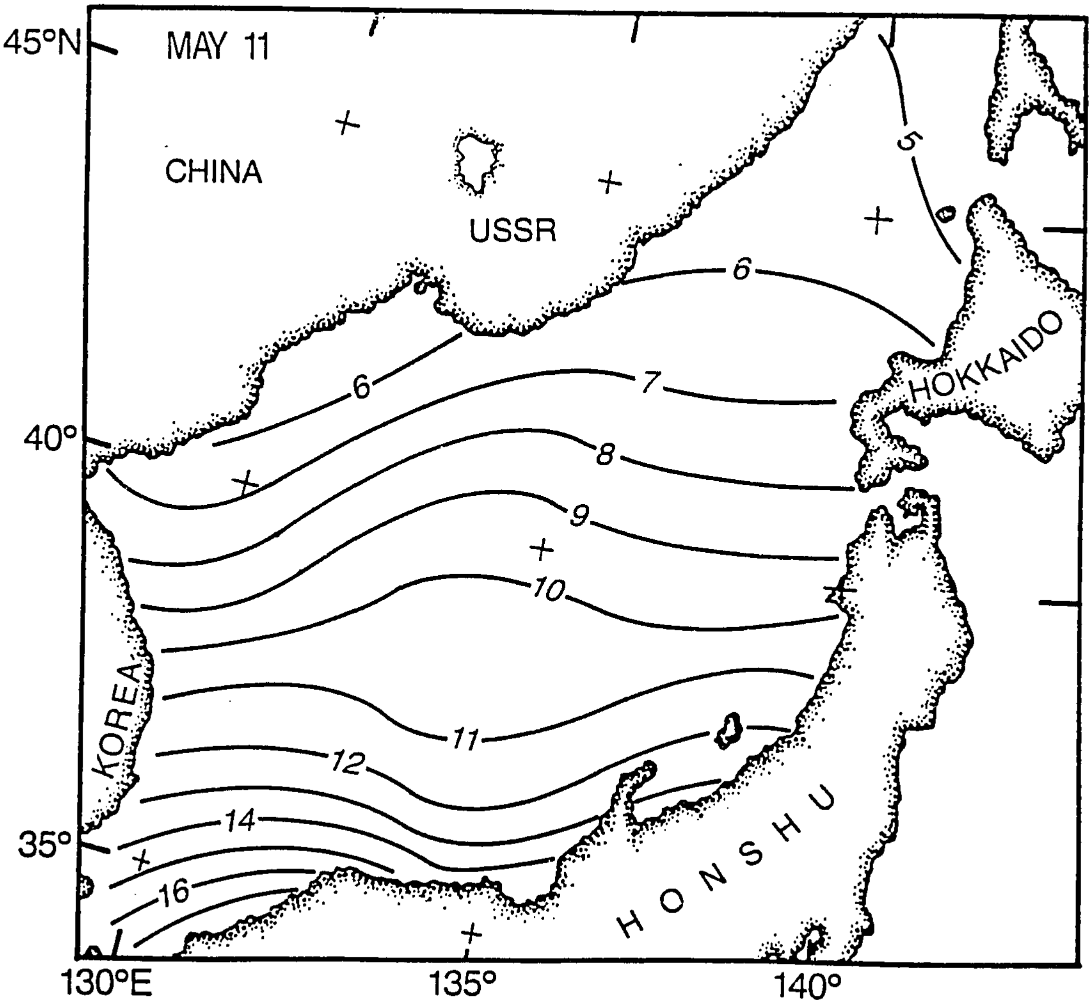

Figure 9. Zoomed EOTS SST (°C) for May 11, 1984.

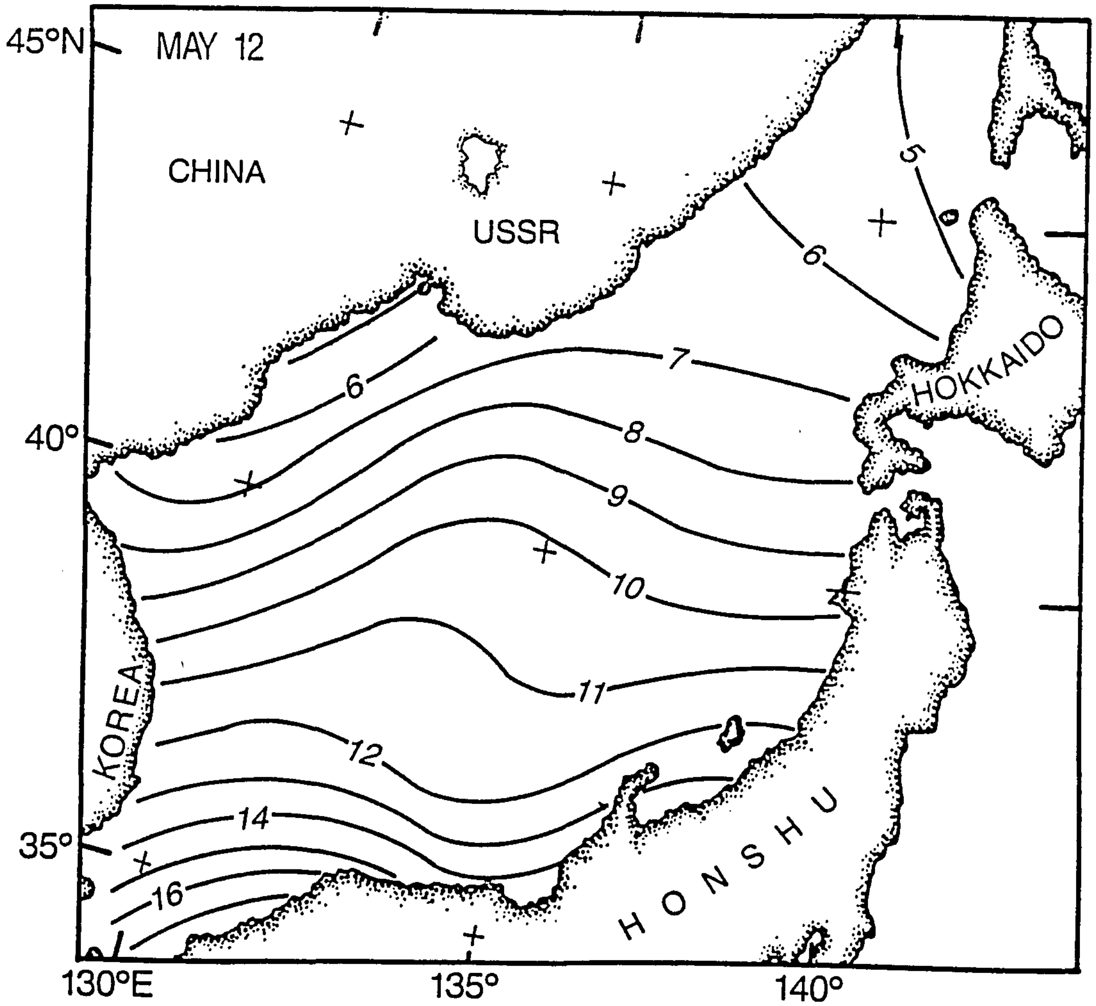

Figure 10. Zoomed EOTS SST (°C) for May 12, 1984.

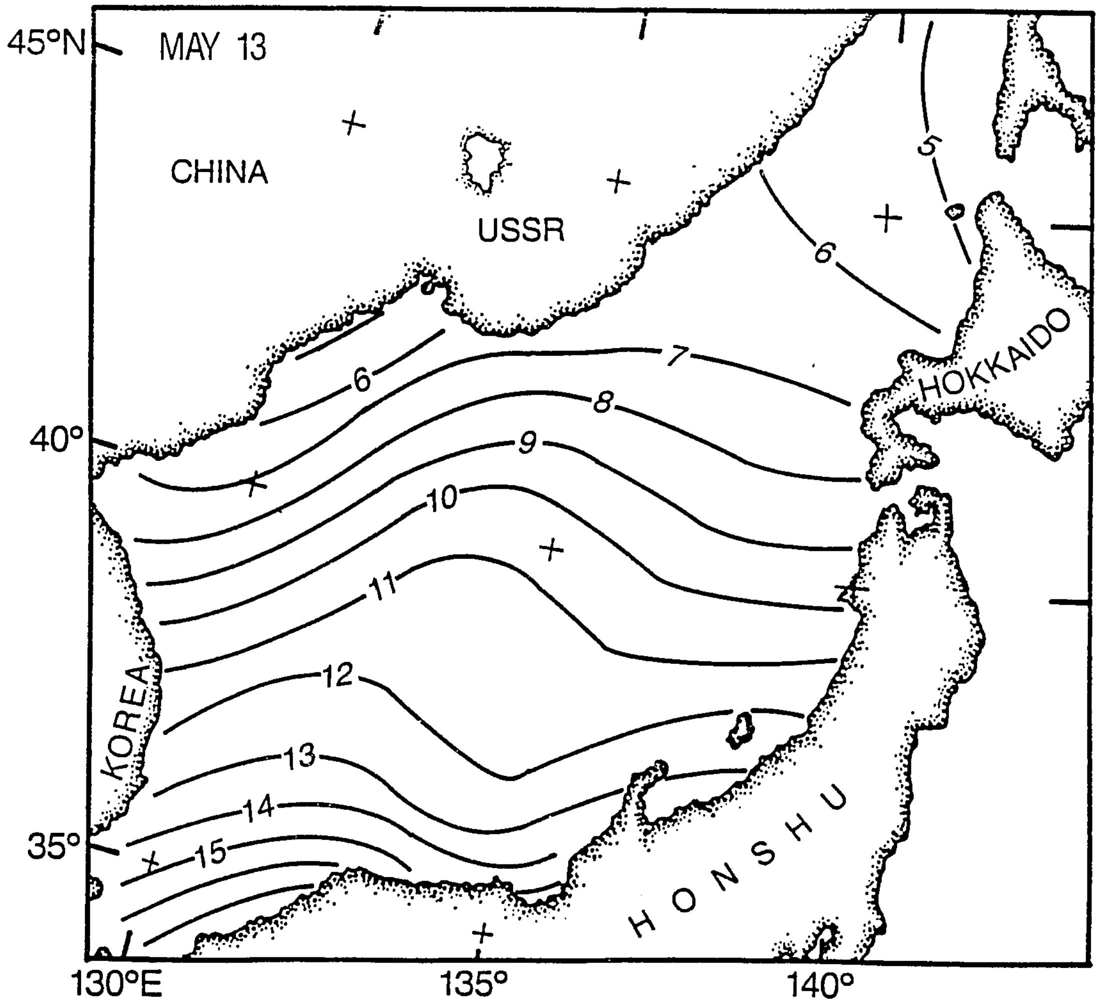

Figure 11. Zoomed EOTS SST (°C) for May 13, 1984.

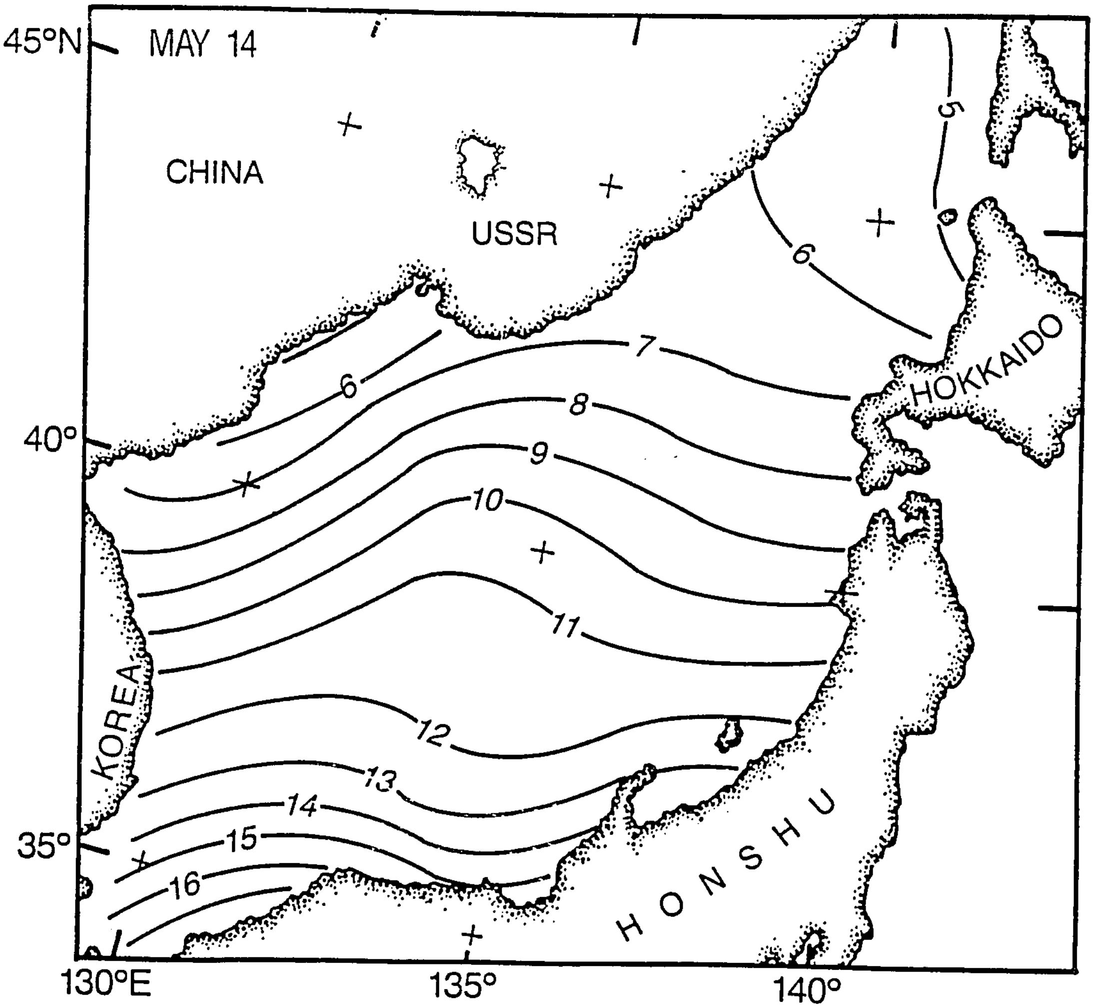

Figure 12. Zoomed EOTS SST (°C) for May 14, 1984.

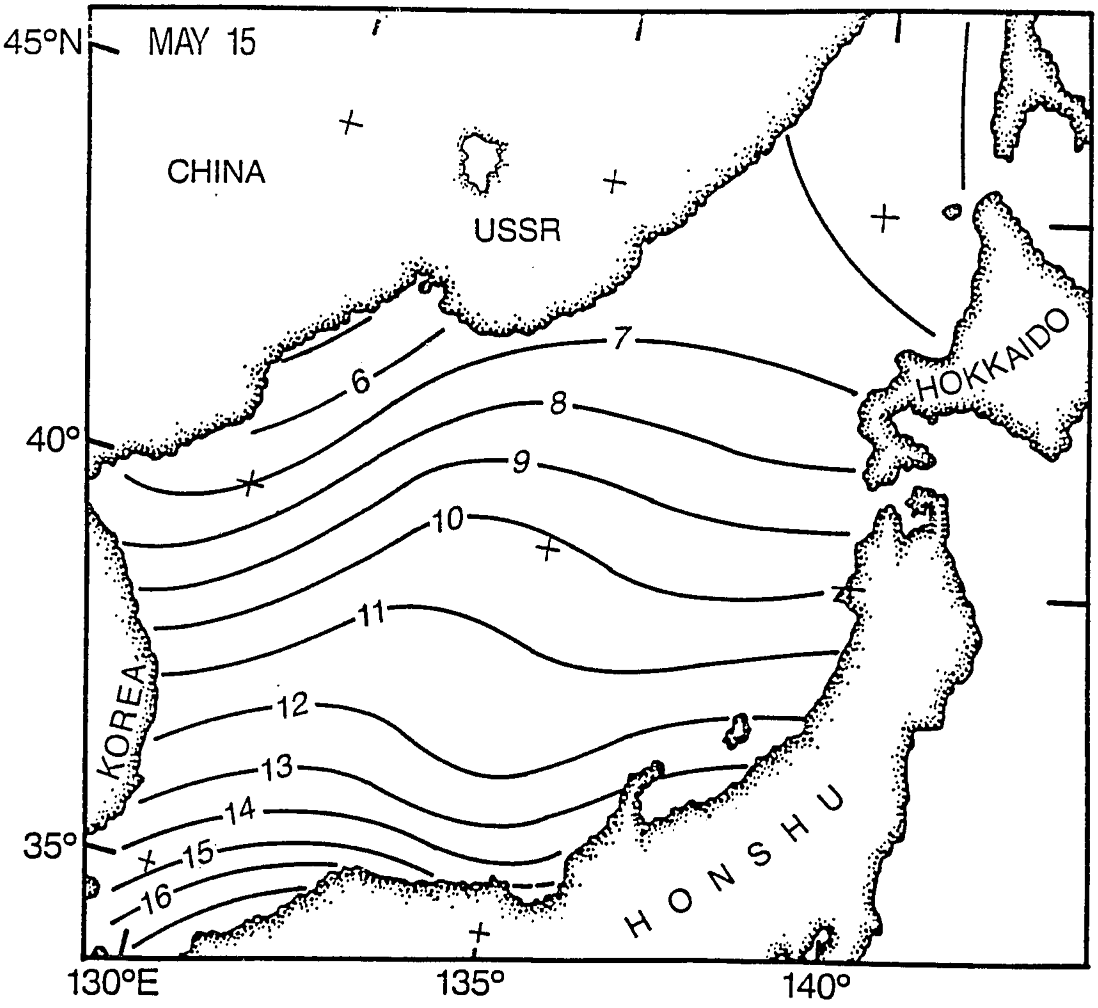

Figure 13. Zoomed EOTS SST (°C) for May 15, 1984.

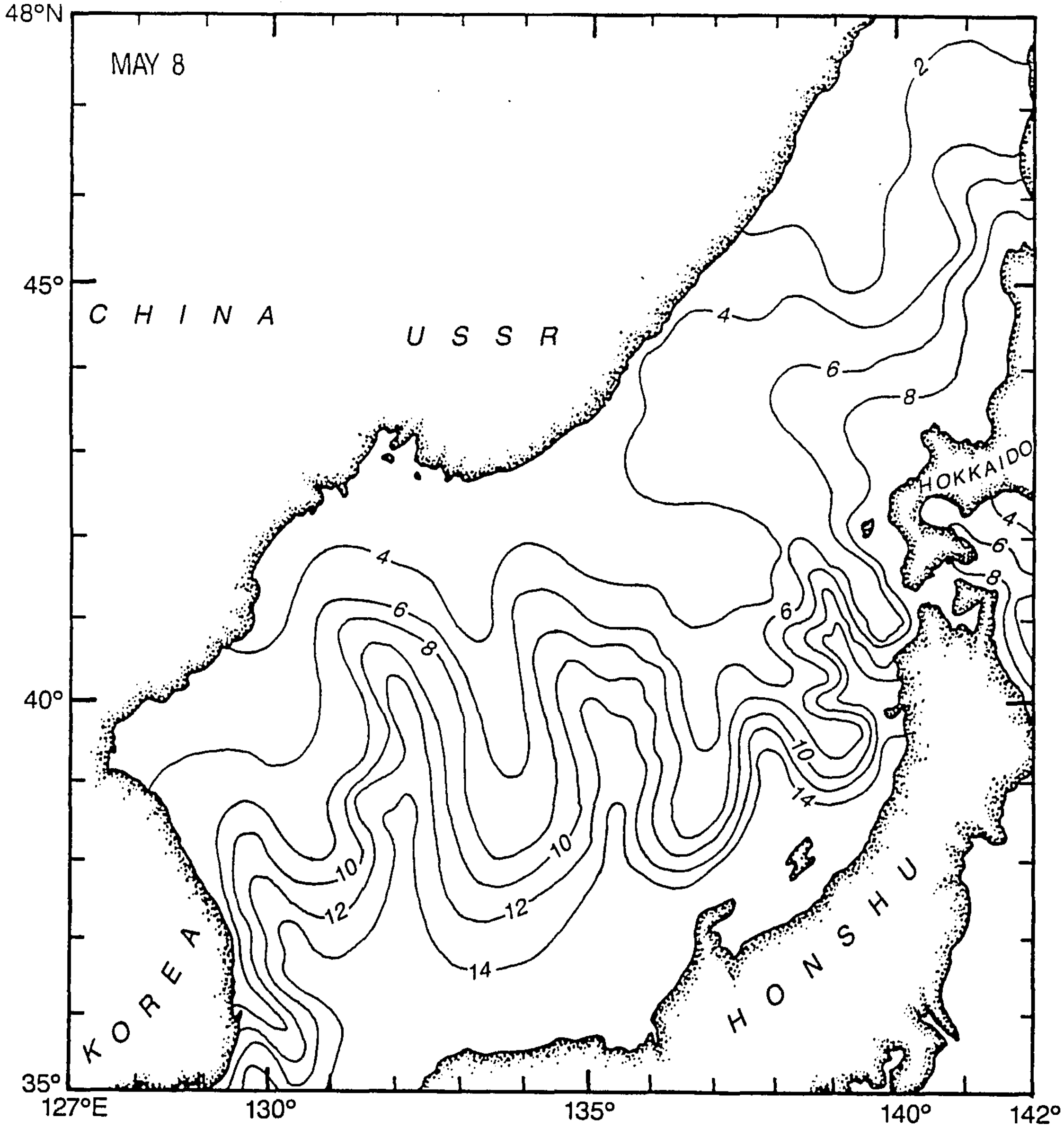

Figure 14. Sea of Japan subset of NOCC Guam weekly Pacific Ocean SST (°C) analysis for May 8, 1984.

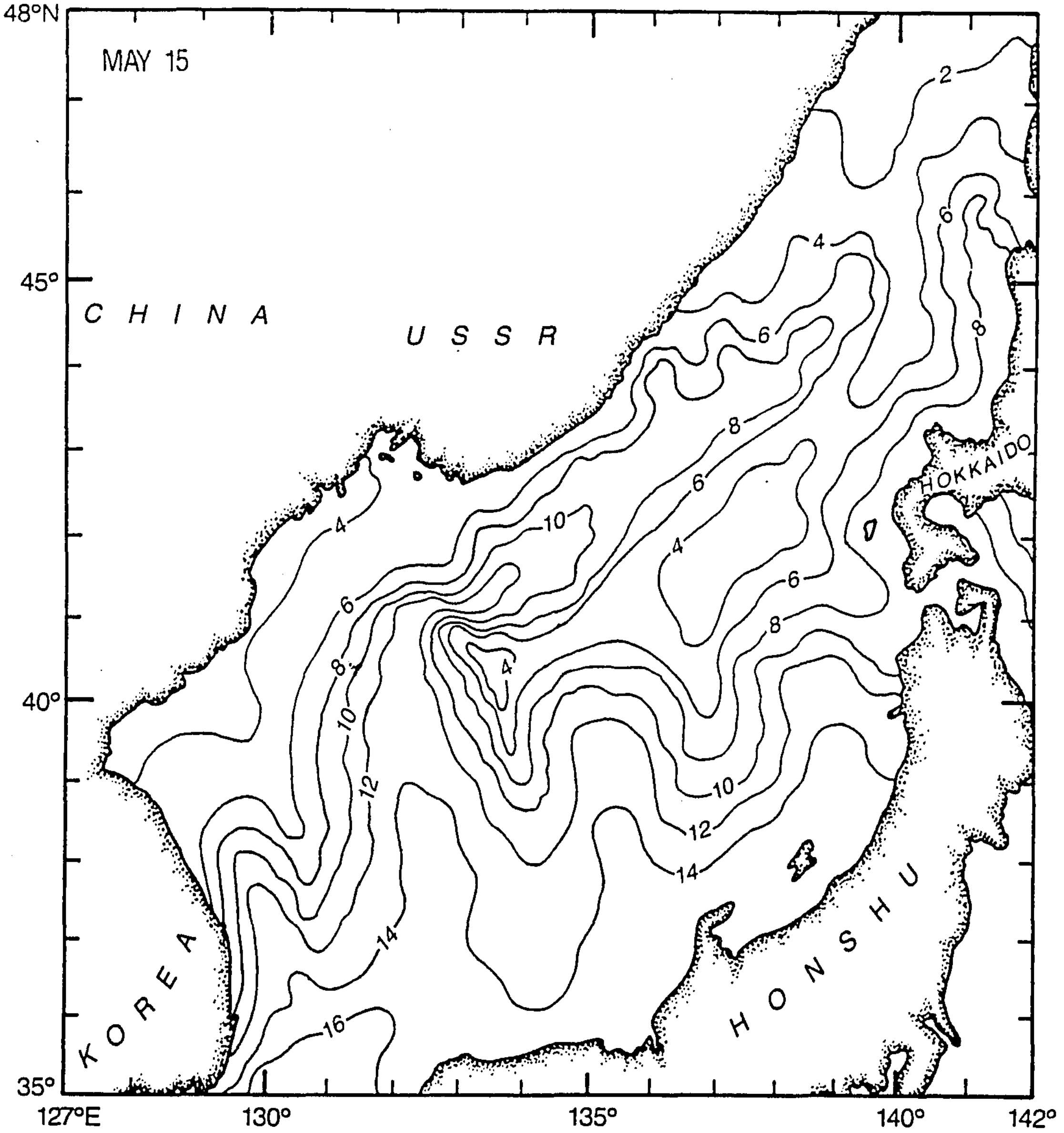

Figure 15. Sea of Japan subset of NOCC Guam weekly Pacific Ocean SST (°C) analysis for May 15, 1984.

From these weekly frontal locations, I interpolate daily frontal positions. First, the positions of six major inflection points on the front, which are consistent week to week, are located on the weekly maps. The resultant five frontal segments, defined by the inflection points for the beginning and end of each week, are then used to linearly interpolate to daily frontal locations. Examples of the daily frontal locations are shown in figures 16a-b again for the May 8-15 time period. As illustration, the six inflection points (which include the end points) are marked by circles on figures 16a for May 8 and 16b for May 15.

Frontal temperatures, cross-frontal temperature range, and cross-Sea-of-Japan temperature extremes are also extracted from the each of the weekly NOCC maps. For definition of these terms, I refer back to figures 14 and 15. I define the frontal temperature as the isotherm which approximately follows the frontal position. For both, May 8 and May 15, this value is 9°C. The cross-frontal temperature range represents the temperature change across the ~100 km width of the high SST-gradient region. For the May-June period covered in this work, I used a constant value of 6°C. Finally, I define the cross-basin temperature extremes as follows. The warmest temperature is the approximate value at a location at 35°N on the Japanese coast.

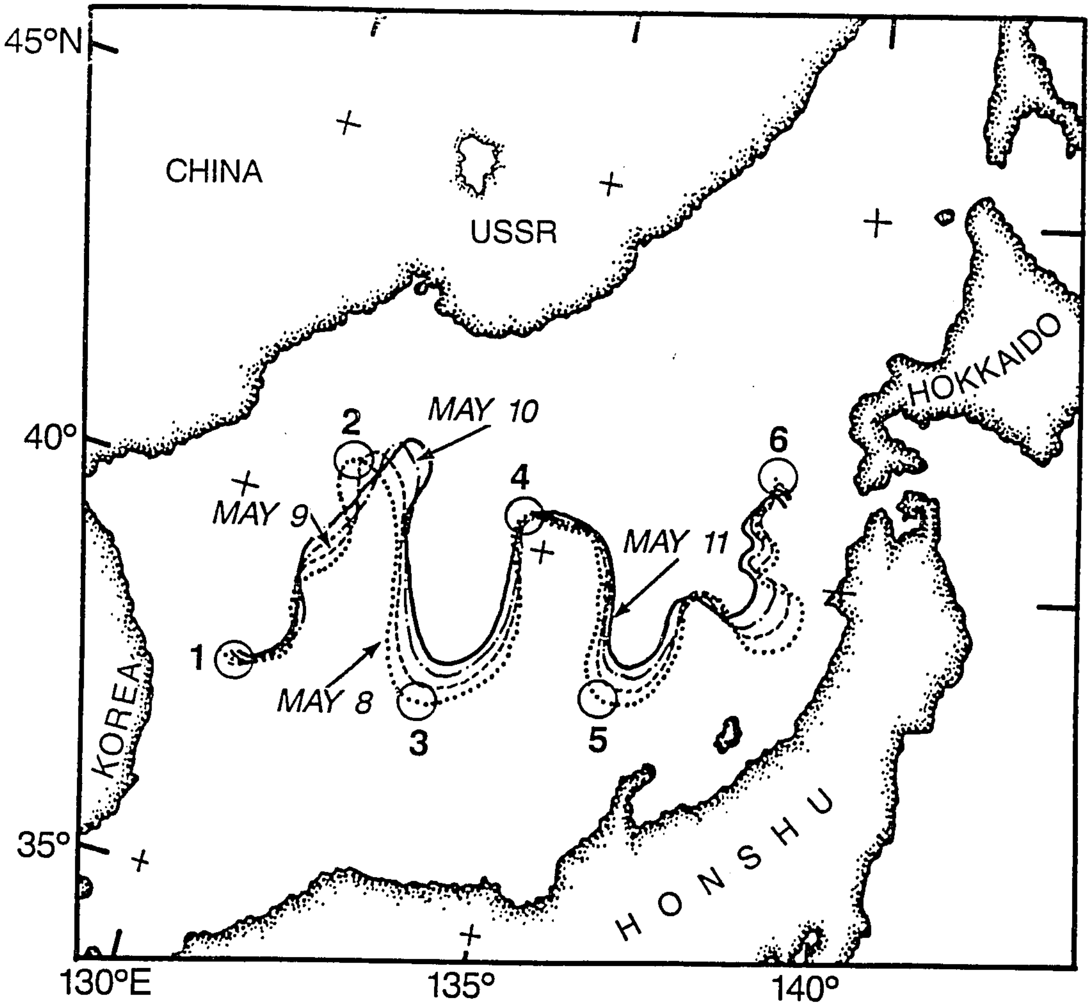

Figure 16a. Interpolated polar front location in the Sea of Japan for May 8-11, 1984.

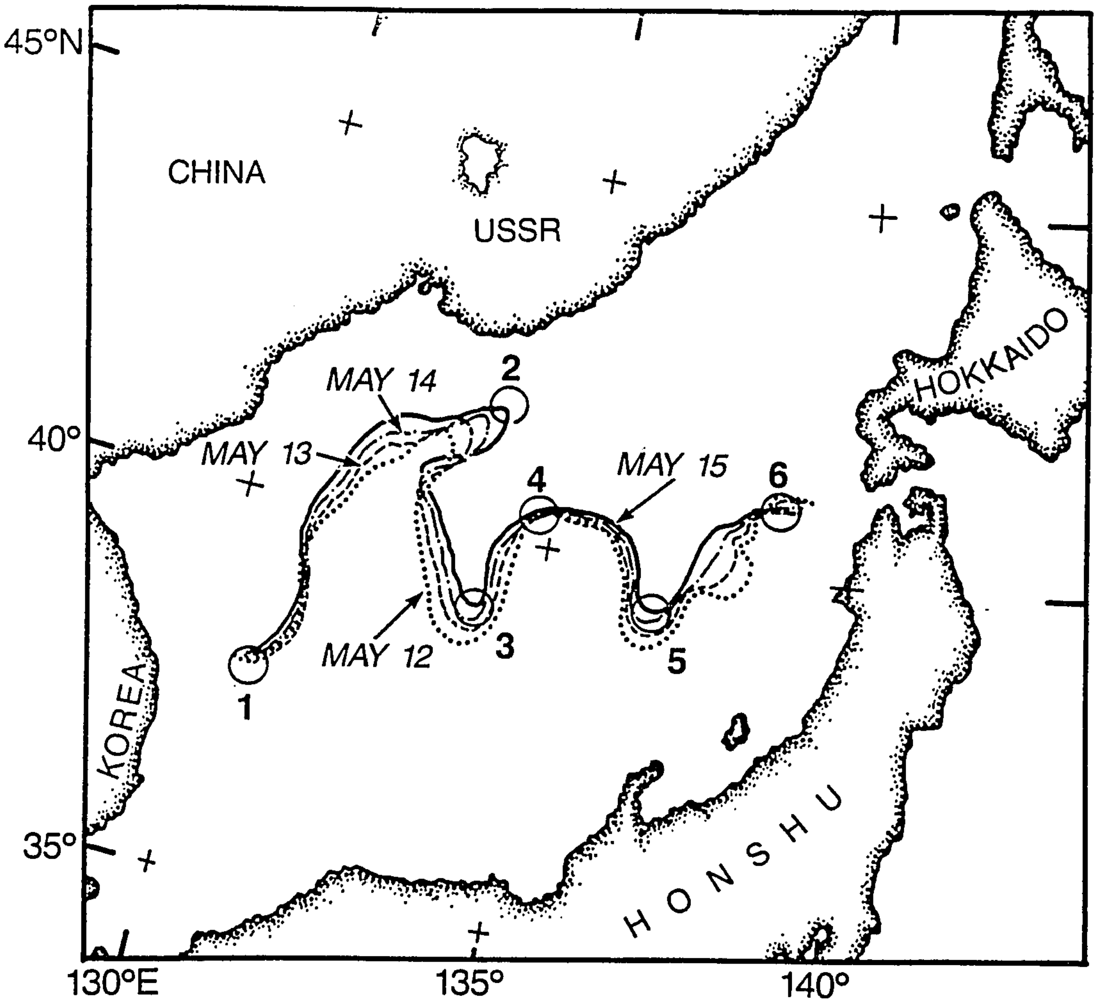

Figure 16b. Interpolated polar front location in the Sea of Japan for May 12-15, 1984.

The coldest is defined as the value at 43°N, 132°E. As illustration, these temperatures were 3°C and 15°C for May 8 and 4°C and 16°C for May 15. All of the above parameters are then linearly interpolated to daily values. Deriving the daily gridded SST field is then a multistep process.

First the grid south of the front is set to the frontal temperature plus half the frontal temperature difference. North of the front, the grid is set to the frontal temperature minus half the frontal temperature difference. I then smooth the field by applying a 9-point, running, block average to generate a realistic gradient across the front. For these experiments, this value is about 6°C/100 m. At this stage, the gridded field now has a frontal region qualitatively equivalent to the NOCC maps. However, away from the front the values are constant and equivalent to the temperature at the appropriate frontal edge (i.e., the frontal temperature ± 3°C). To remedy this, all points below a line beginning at grid point (1,1) and running east northeast (ENE) across the grid are set equivalent to the warmest basin temperature as defined above. Comparably, all points above a line beginning about (1,40) and running ENE across the grid are set to the appropriate, daily, basin-temperature minimum. Recall from section 3 that WSE to ENE is the orientation of the seasonally averaged isotherms through the central Sea of Japan. Grid point falling between the southern boundary region and the southern frontal edge are then linearly

interpolated in the y grid- direction. Similarly, points located between the northern boundary region and the northern front edge are also linearly interpolated. Figures 17-24, for May 8-15, demonstrate that the resultant synthetic SST fields compare favorably with the NOCC weekly maps.

The corresponding daily EOTS sub-surface analyses are subsequently modified using the above SST fields such that the TOPS-EOTS SST's are consistent in form and value with the subjective analyses. This is accomplished by identifying the surface isotherm on the TOPS-EOTS SST fields that most closely corresponds in position with the frontal position. For May 8, the isotherm is 9°C, for May 15, 10°C (figures 6 and 13). Any difference between this temperature and the daily mid-front temperature from the NOCC-derived SST are added to the entire TOPS-EOTS SST field so that the frontal temperatures, as defined for each, are equivalent. A transform grid is then created which contains the grid index of the closest TOPS-EOTS point which matches each synthetic SST grid point.

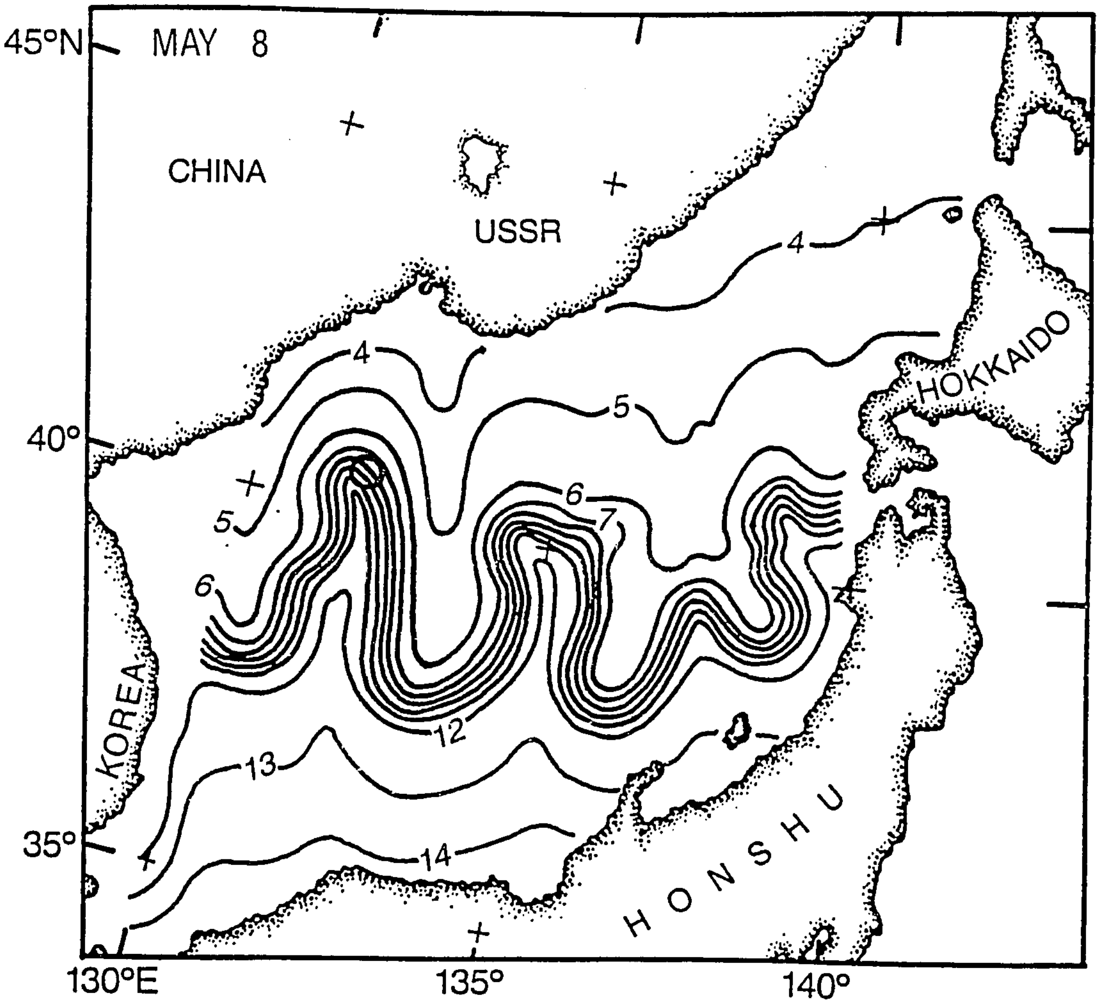

Figure 17. Synthetic SST (°C) field for May 8, 1984.

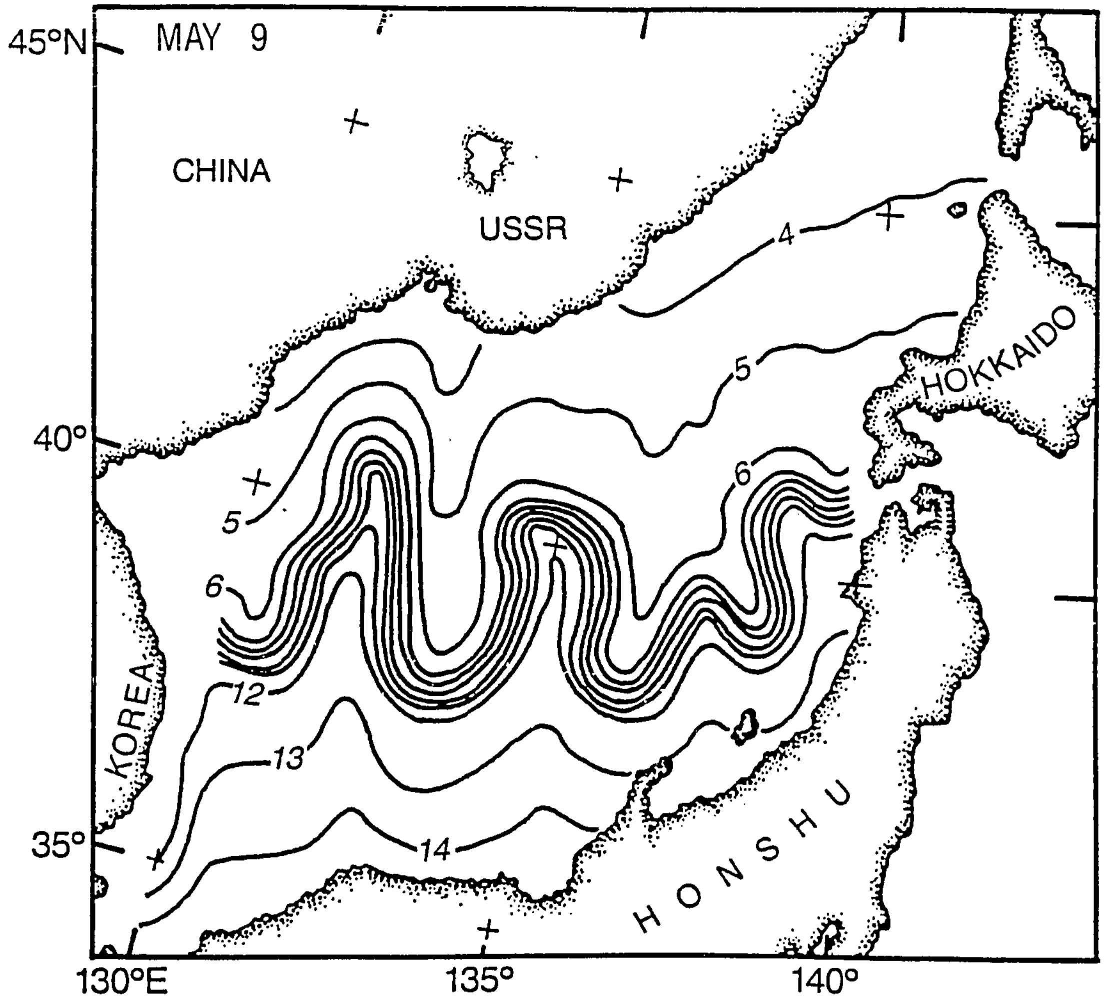

Figure 18. Synthetic SST (°C) field for May 9, 1984.

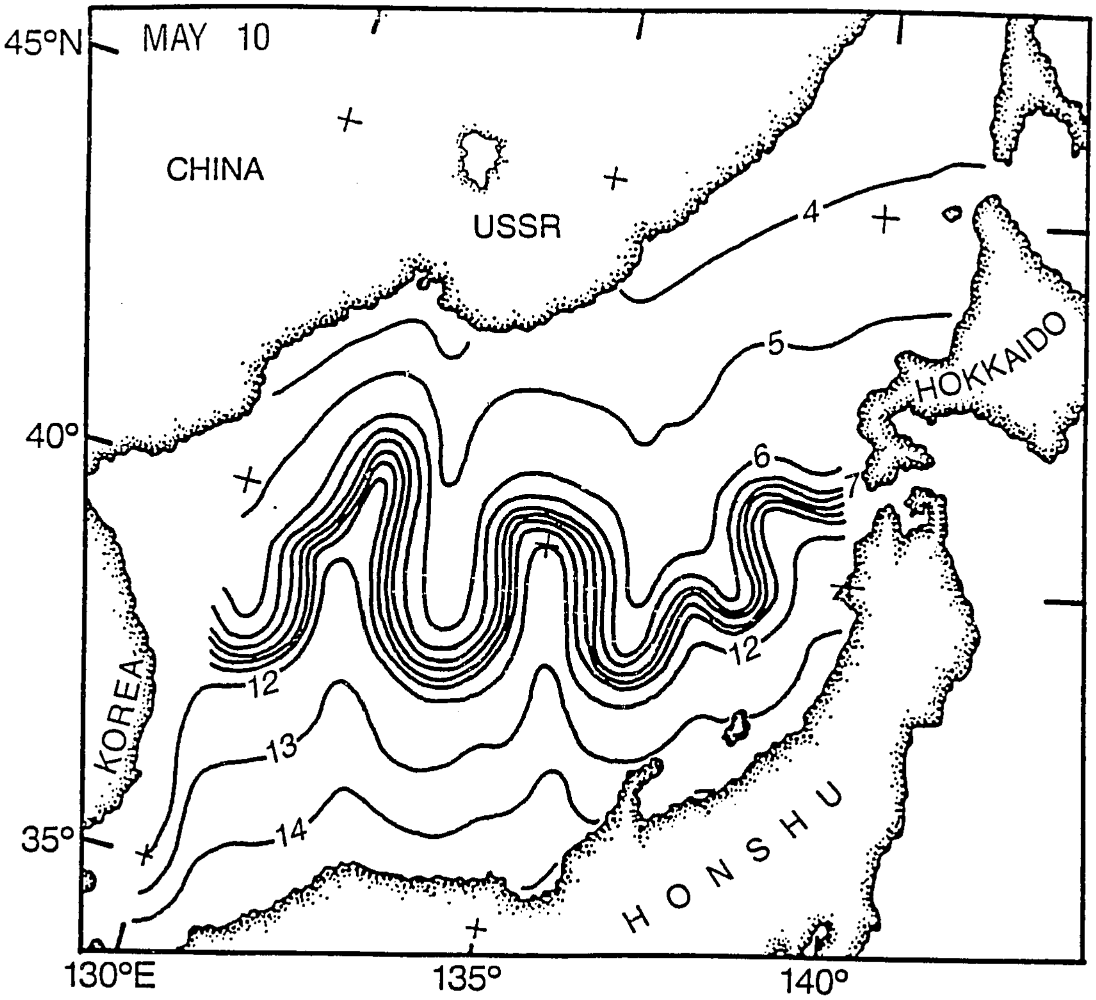

Figure 19. Synthetic SST (°C) field for May 10, 1984.

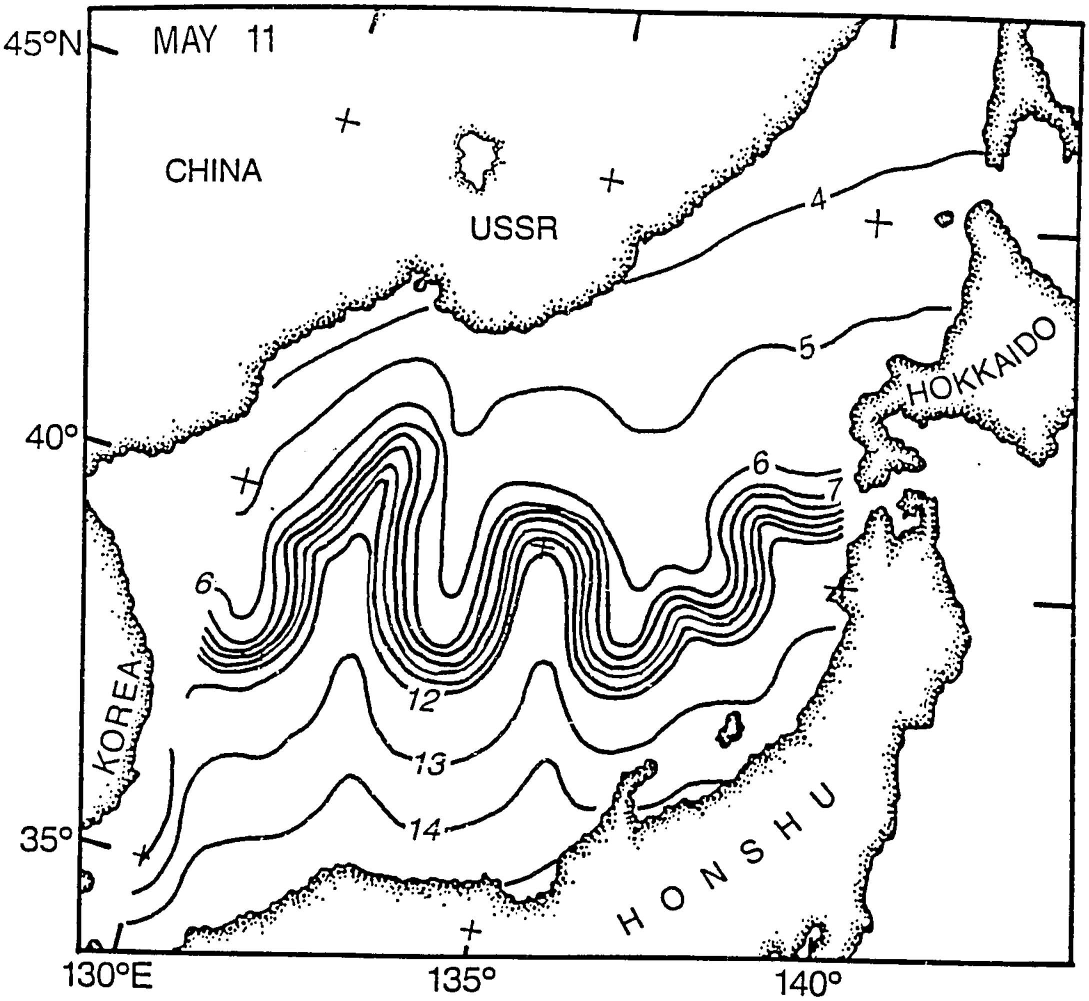

Figure 20. Synthetic SST (°C) field for May 11, 1984.

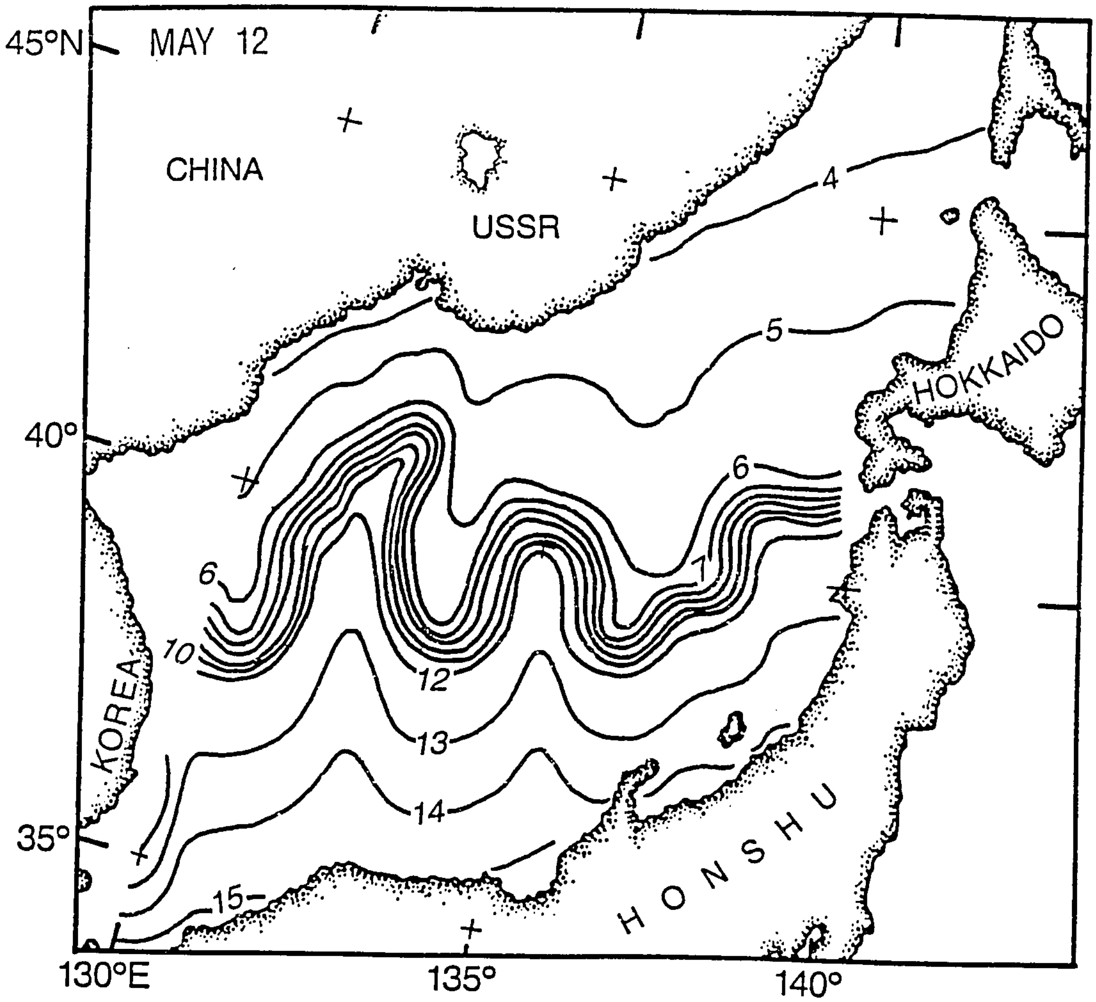

Figure 21. Synthetic SST (°C) field for May 12, 1984.

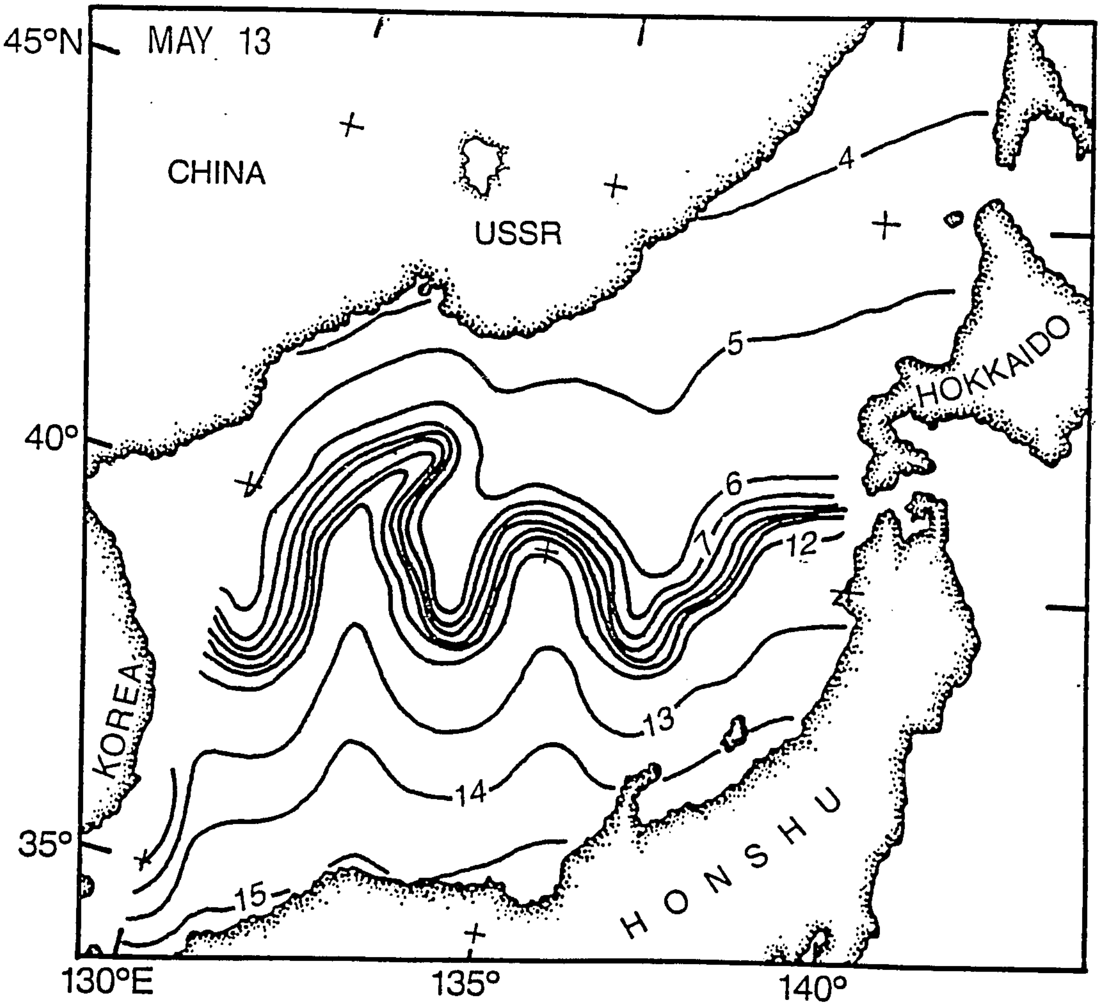

Figure 22. Synthetic SST (°C) field for May 13, 1984.

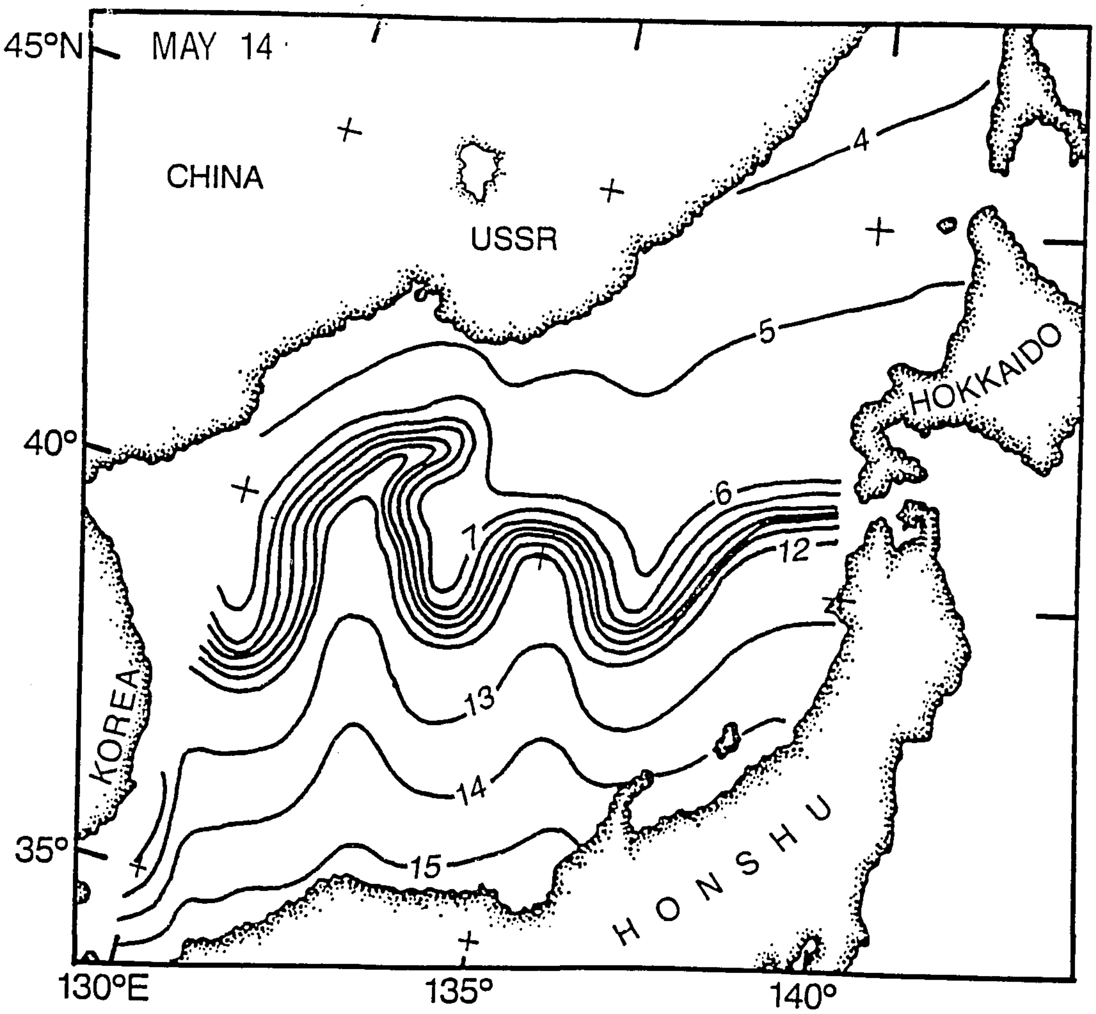

Figure 23. Synthetic SST (°C) field for May 14, 1984.

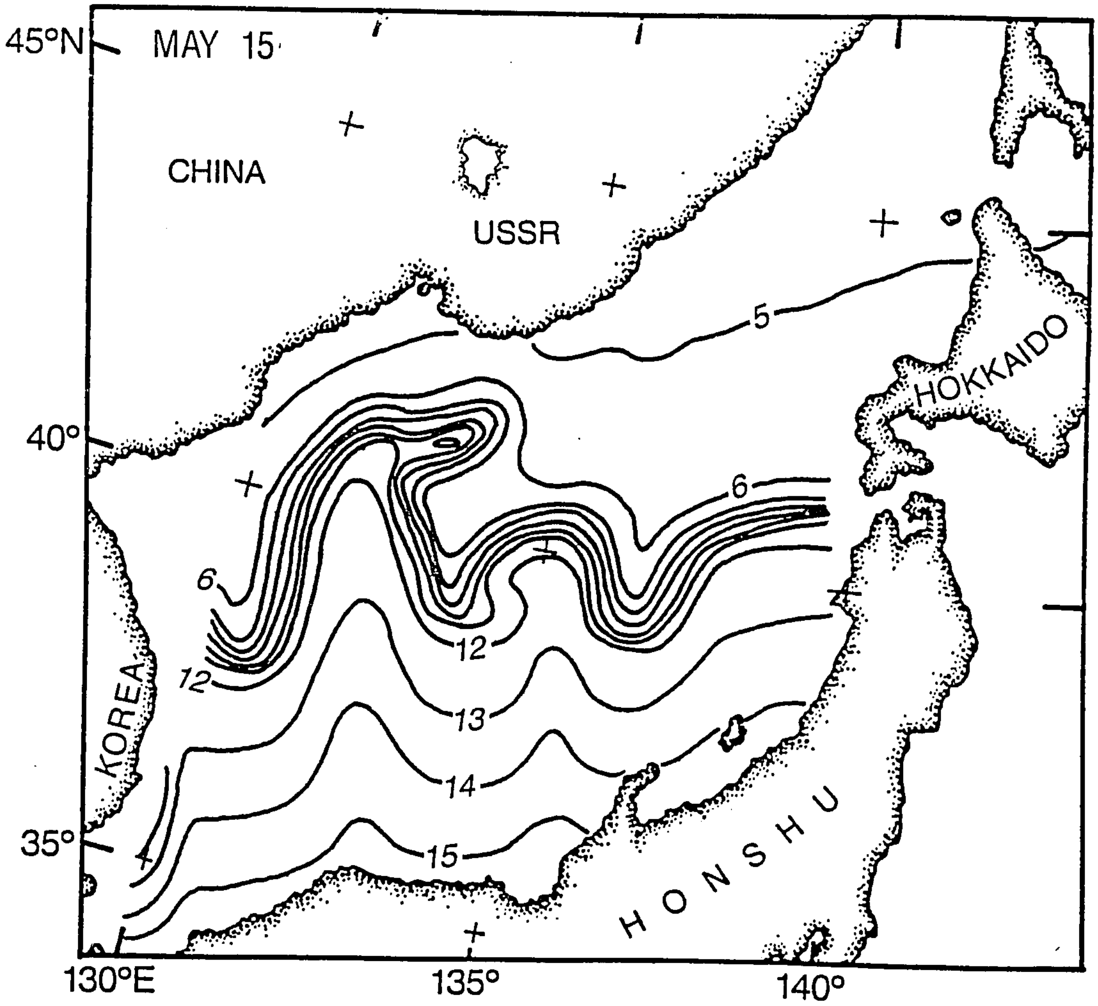

Figure 24. Synthetic SST (°C) field for May 15, 1984.

For example, consider a point (16,32) on the NOCC-derived SST gridded field for May 8 (marked by a circle on figure 17). (Note that both the NOCC-derived SST and TOPS-EOTS SST fields have equivalent mid-frontal temperatures for this date. Thus no additive adjustment is required as discussed above). This is a mid-front point with temperature 9°C. This same point on the TOPS-EOTS SST field (marked by a circle on figure 6) is about 7.5°C. If I position myself, at (16,32) on this latter grid and search radially for the nearest 9°C point, the result is point (18,28) (see dashed circle on figure 6). Point (16,32) on the transform grid is then given the position value (18,28). That is, to transform the TOPS-EOTS SST at (16,32) to match the NOCC-derived SST, I need to use the TOPS-TEOTS value from point (18,28). I continue this process for the entire grid until the entire transform grid is created.

The subsurface TOPS-EOTS fields are then modified in point-to-point correspondence with those changes required to modify the surface field. Note in this process, that changes of frontal position or orientation with depth are neglected. Below 100 m the TOPS-EOTS profiles were set to an exponential function to better reflect the known shallow temperature structure variability in the Sea of Japan. This last approximation is inconsequential to the experiments since the mixed layer variability during the period of the experiments is all above 100 m. Examples of the vertical variability in the final synthetic fields are

shown in figures 25-31 for 13 May, 1984 at 25, 50, 100, 150, 200, 300, and 400 m, respectively.

5.2 Comparisons With Available Data

The experimental design does not critically depend on absolute realism for these fields. They are used only to provide quasi-realistic yet uniform initial thermal conditions for each three-day forecast within the four different experiments. Yet it is informative to compare these constructed analyses to actual available bathythermograph data to have a sense of how reasonable they are. Data extracted from the FNOC, archived, unclassified data base, provides sub-surface, temperature information for three cruises in this region during the May-June period of the experiments. These measurements were all taken during the standard bi-monthly transects performed by the Japanese Meteorological Agency aboard the Seifu Maru (SONU, 1981). Only thermal profiles were available from the FNOC data base. I first consider the position of the polar front to determine if the interpolated positions used in the synthetic analyses are consistent with those observed in the cruise transects.

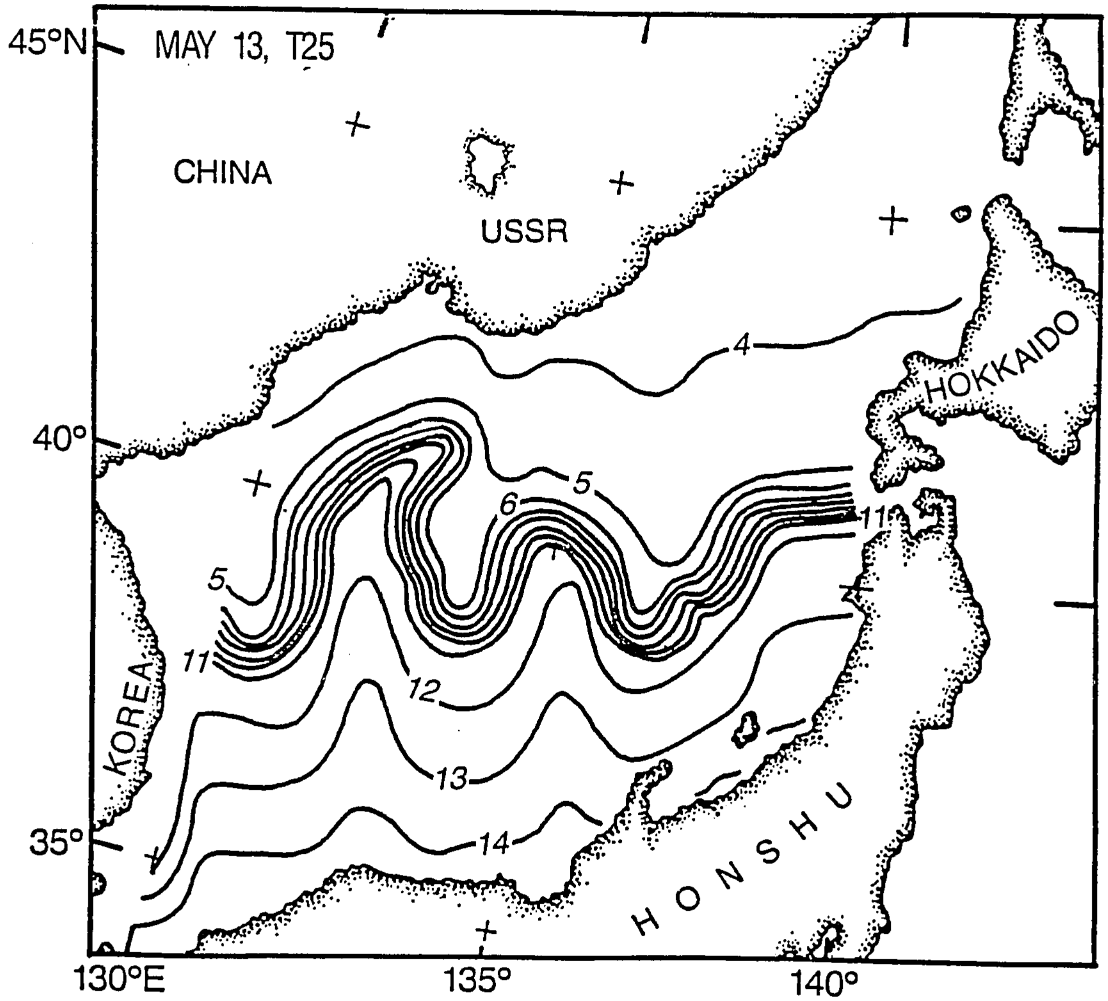

Figure 25. Frontally modified, daily, EOTS temperature (°C) at 25 m for May 13, 1984.

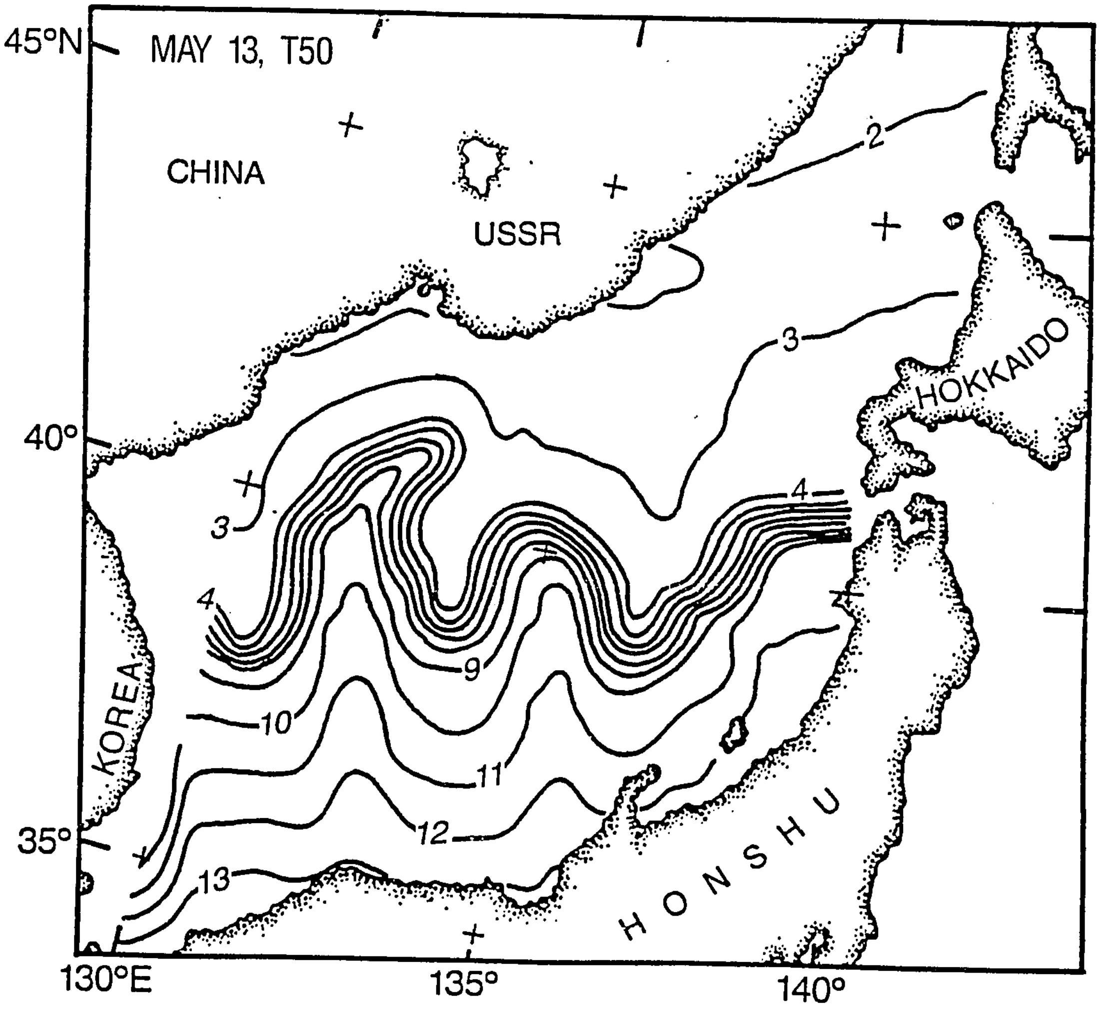

Figure 26. Frontally modified, daily, EOTS temperature (°C) at 50 m for May 13, 1984.

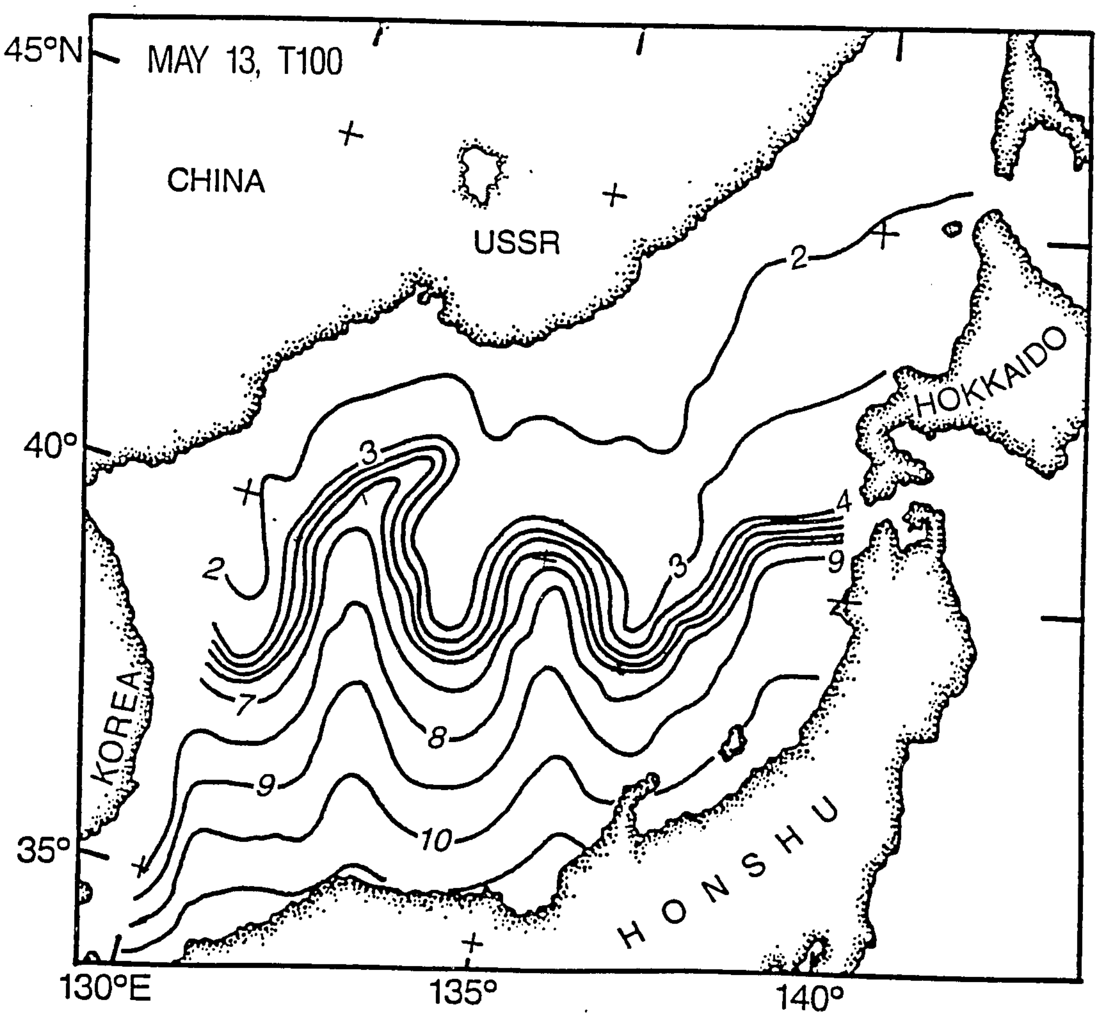

Figure 27. Frontally modified, daily, EOTS temperature (°C) at 100 m for May 13, 1984.

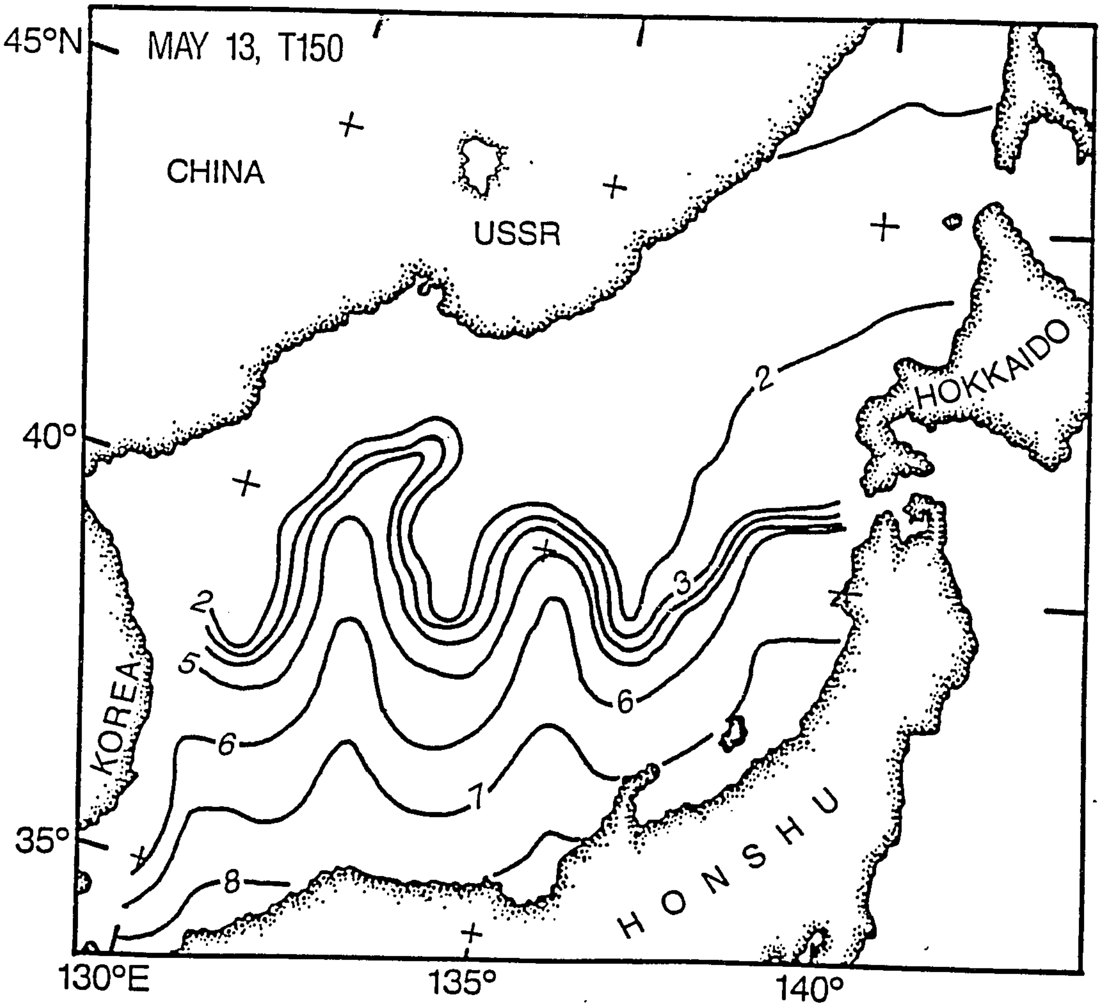

Figure 28. Frontally modified, daily, EOTS temperature (°C) at 150 m for May 13, 1984.

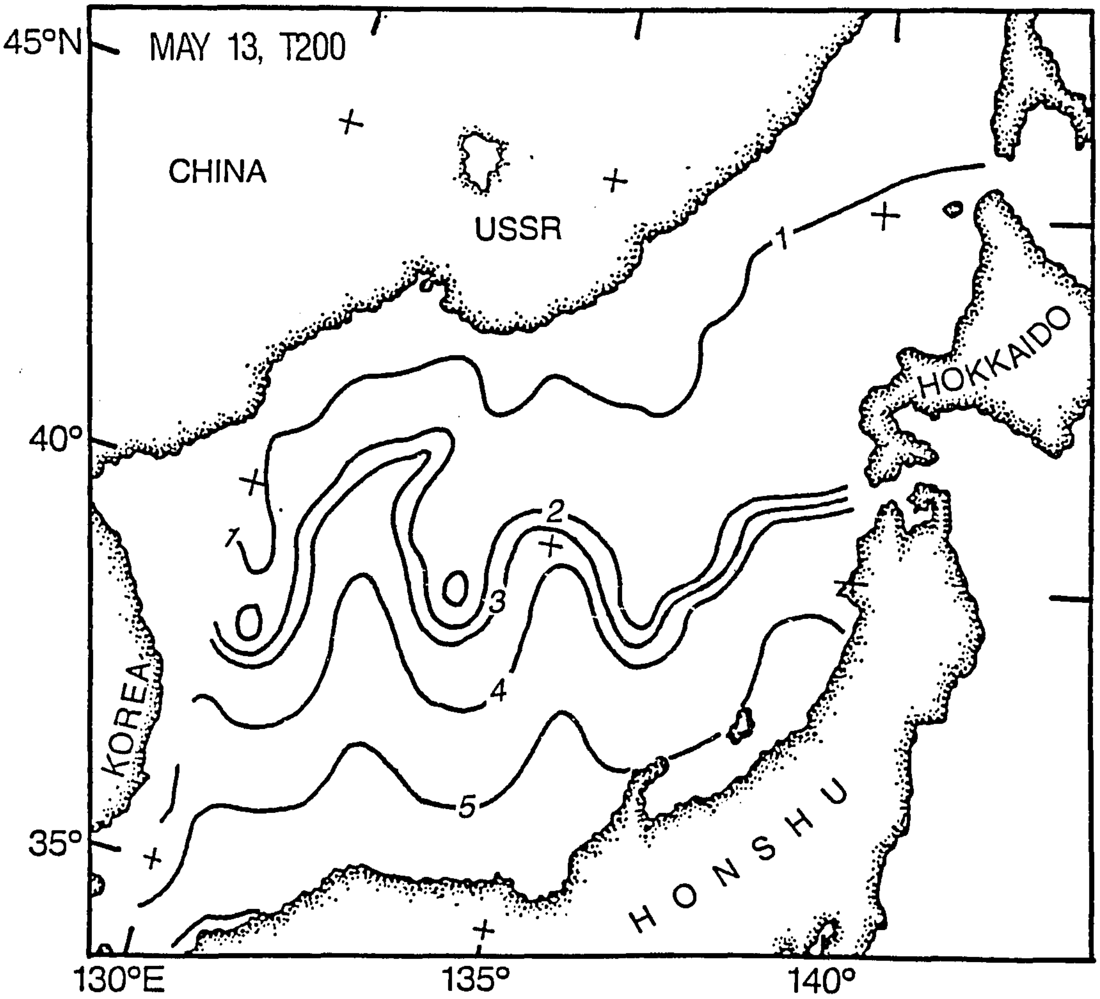

Figure 29. Frontally modified, daily, EOTS temperature (°C) at 200 m for May 13, 1984,

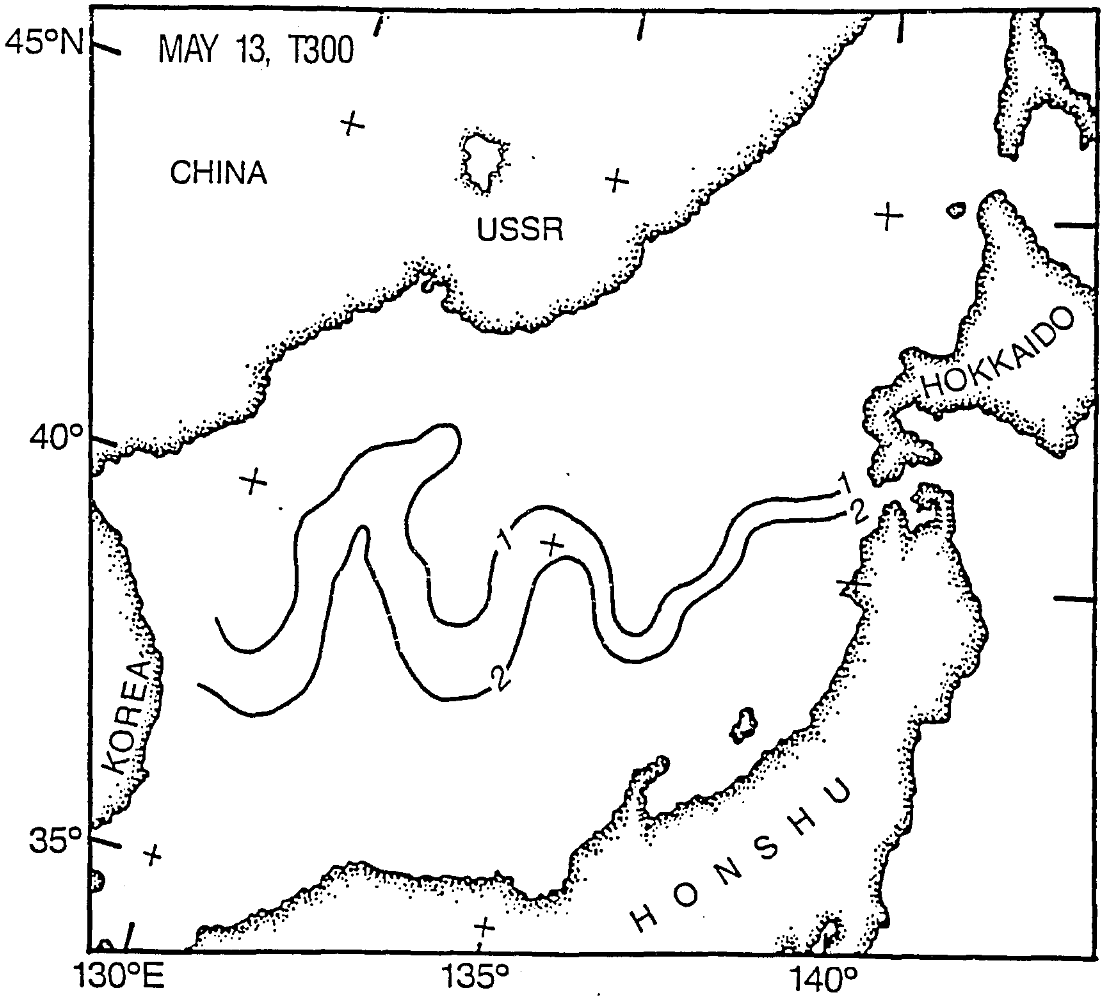

Figure 30. Frontally modified, daily, EOTS temperature (°C) at 300 m for May 13, 1984.

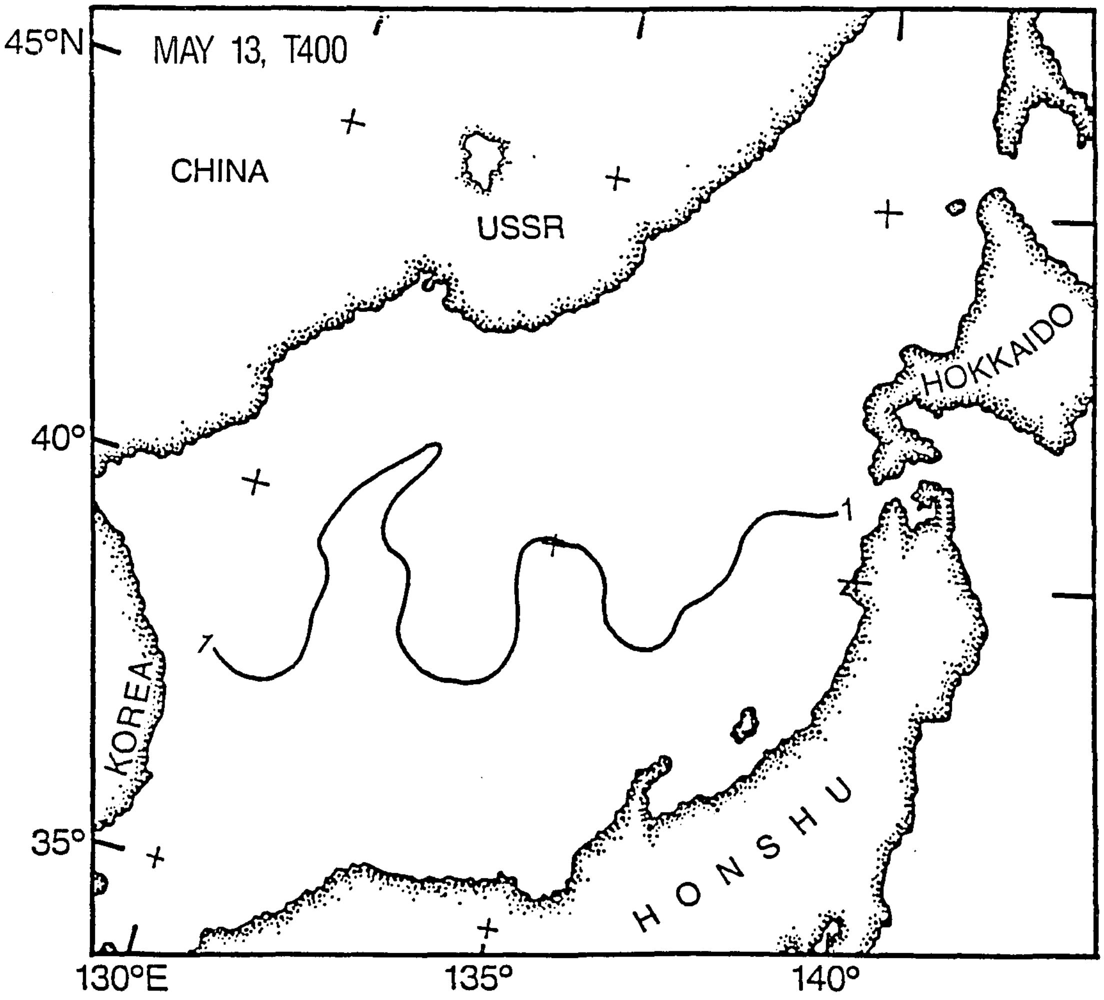

Figure 31. Frontally modified, daily, EOTS temperature (°C) at 400 m for May 13, 1984.

The first cruise occurred from May 9-12, 1984 in three legs. Figure 32 illustrates the station locations occupied in order from 1-28. The NOCC derived, interpolated frontal position for May 11 is also included. The boxes and arrows indicated inferred flow direction perpendicular to those transects crossing the frontal position.
Referring to equations 16 and 17, one notes that flow will progress with the less dense (warmer) fluid to the right of the flow direction. Assuming the temperature is not salinity compensated, the arrows in figure 32 show flow direction inferred from the thermal profiles shown in figures 33 a, b and c.

The first striking feature to note from profiles 1-8 (figure 33a) is the apparent manifestation of the inshore branch of the Tsushima Current as described in section 3. Note the NOCC maps don't depict this as a surface feature and my synthetic analyses thus cannot contain it.

The confused nature of the profiles in the immediate frontal vicinity is more unsettling (figure 33b). Flow reversals, both horizontally and vertically, indicated by the profile plots, suggest active meander and/or eddy activity or possibly aliasing due to inadequate sampling in time and/or space. (The dashed arrow in figure 32 represents the inferred flow suggested by the deeper parts of the profiles.) Figure 34 indicates this confusion could be consistent with the NOCC frontal positions.

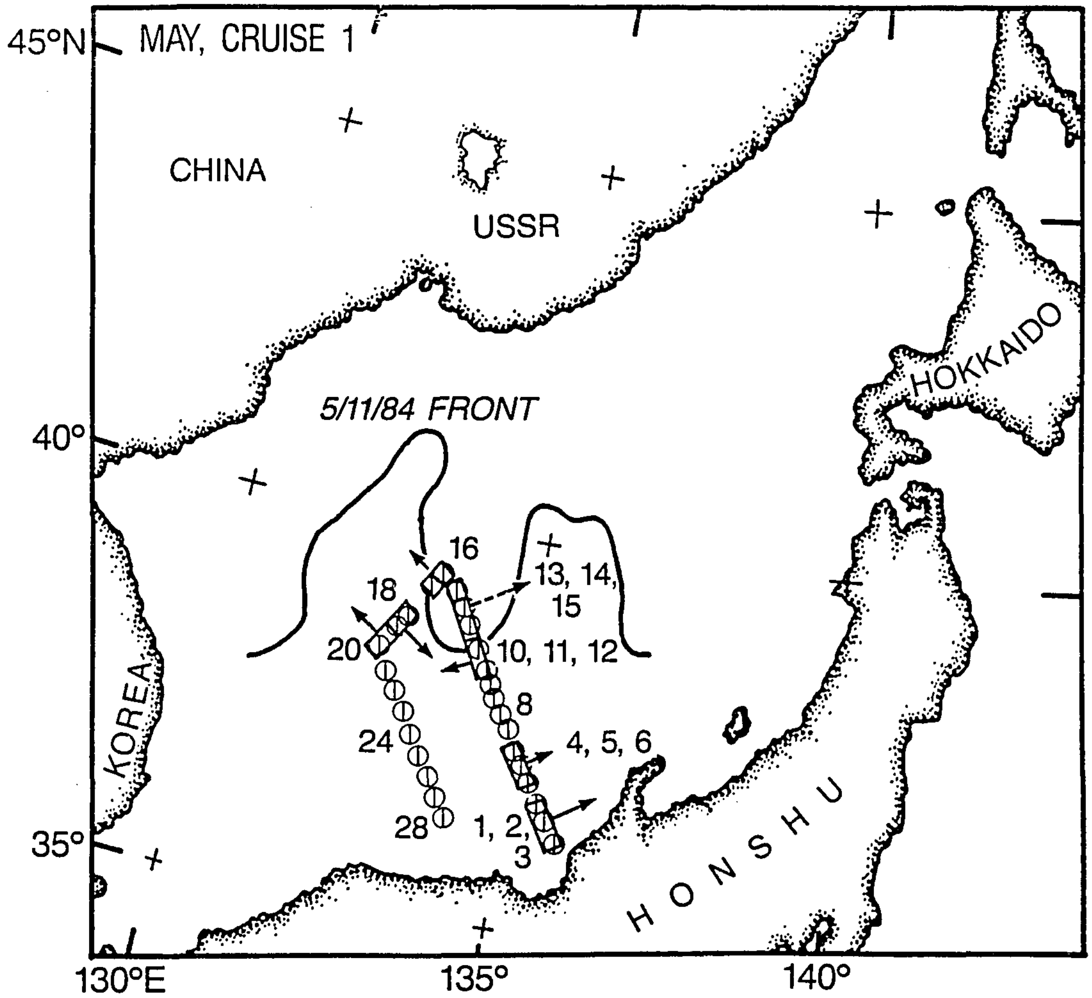

Figure 32. Stations occupied and resultant inferred flow during May 9-12, 1984, cruise of the Seifu Maru. May 11 interpolated frontal location superimposed.

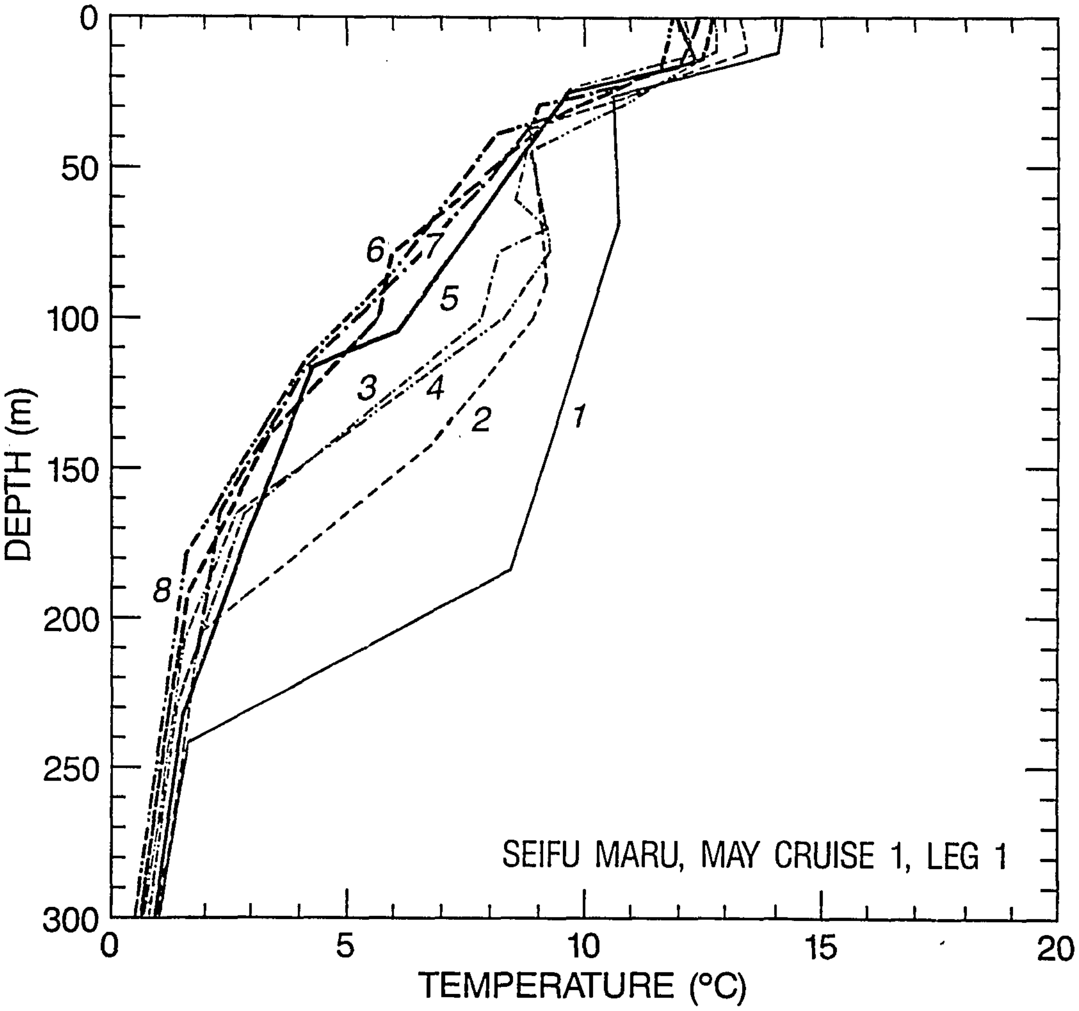

Figure 33a. Temperature profiles for first half of leg 1 of May 9-12, 1984, Seifu Maru cruise.

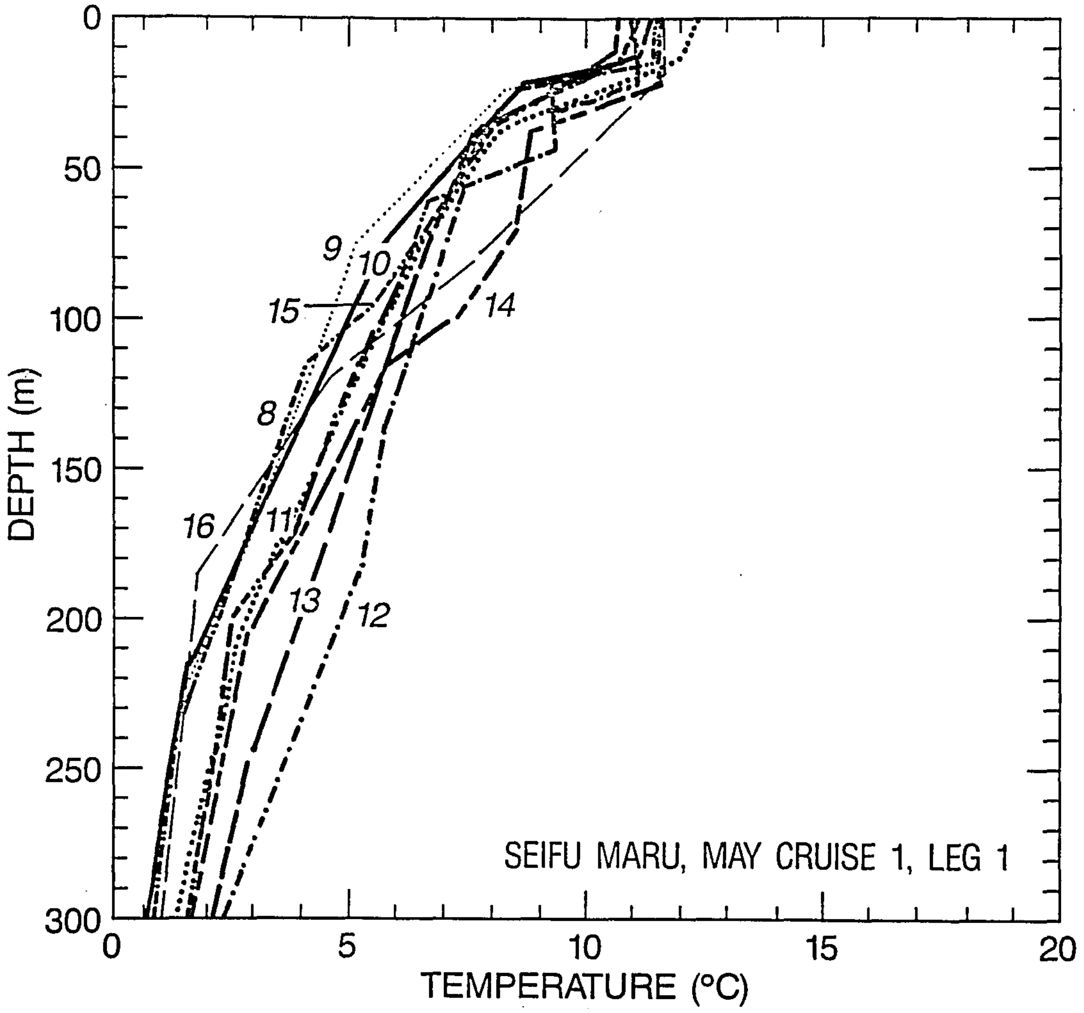

Figure 33b. Temperature profiles for second half of leg 1 of May 9-12, 1984, Seifu Maru cruise.

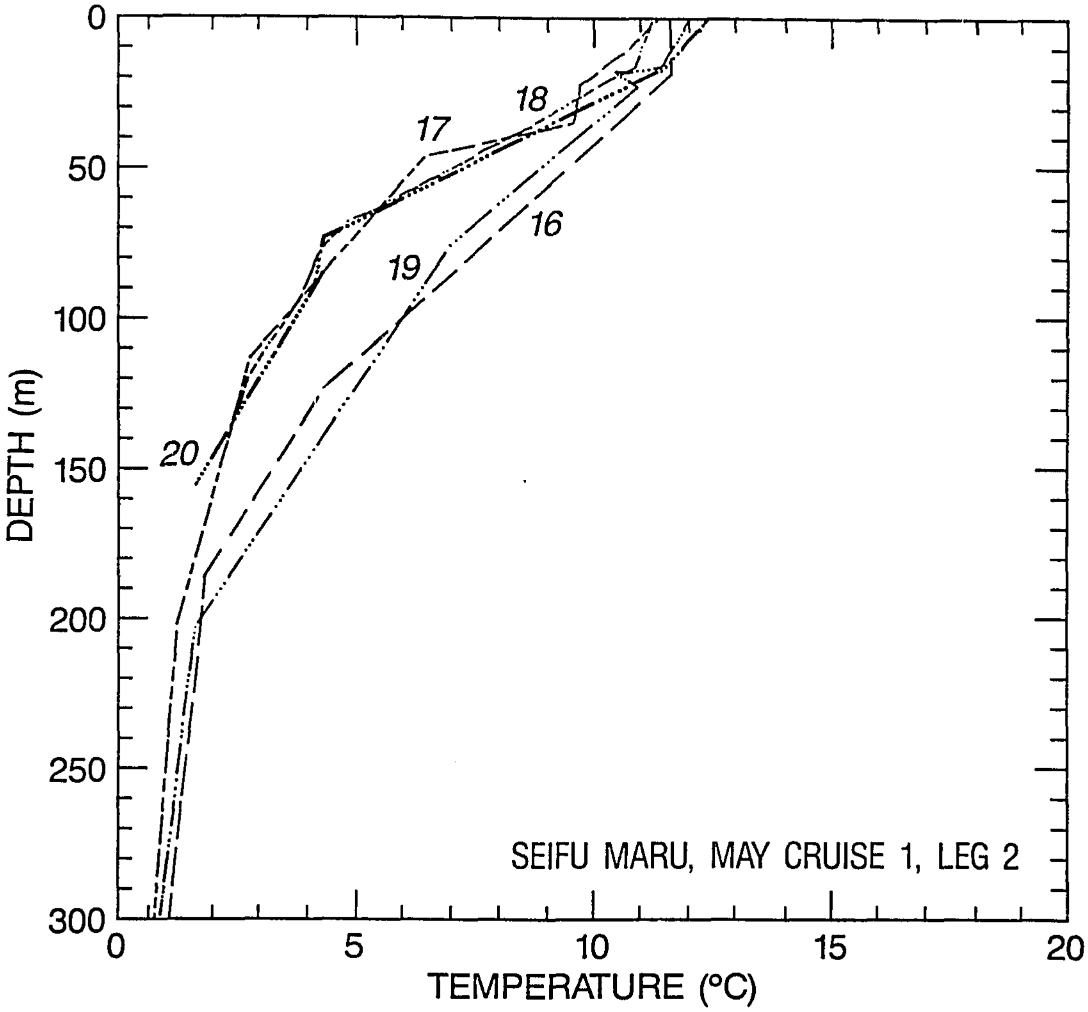

Figure 33c. Temperature profiles for leg 2 of May 9-12, 1984, Seifu Maru cruise.

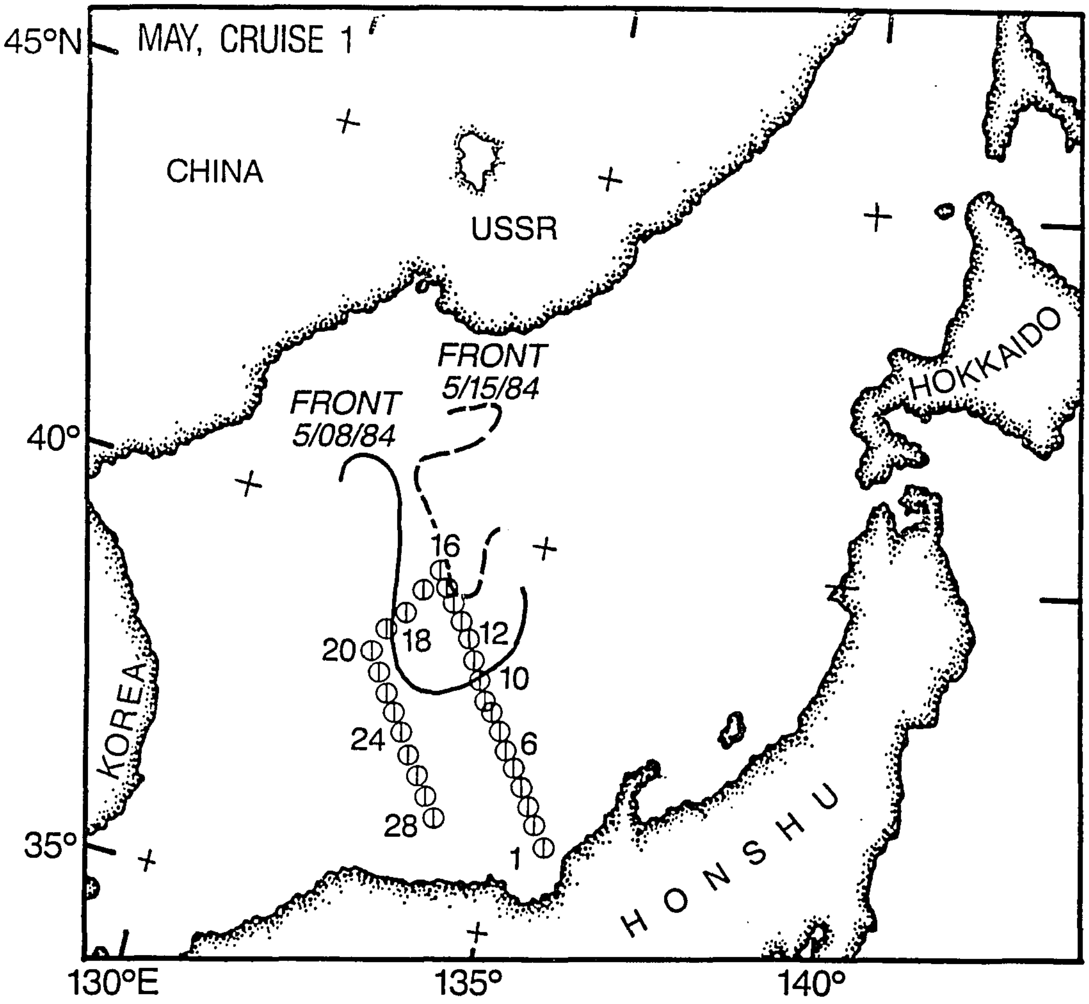

Figure 34. Stations occupied during May 9-12, 1984, cruise of the Seifu Maru. May 8 and 15, 1984, frontal locations superimposed.

From May 8-15, the NOCC analyses point to a rapid northward retreat of the particular meander crossed by the Seifu Maru transects. This frontal excursion (if it actually exists) could account for the apparent confusion.

The next two cruises occurred during more frontally quiescent times. The second Seifu Maru cruise sampled 21 stations nearer to the Tsushima Strait on the 17-19 of May (figure 35). The interpolated frontal position from May 19 is superimposed. The arrows again indicate inferred flow derived from thermal profiles shown in figures 36 a and b. The inshore branch again seems evident in profiles 19-21. However, the near frontal flow now appears consistent with the interpolated frontal orientation and location.

The final cruise sampled north of the Noto Peninsula on the 25-27 of May as indicated in Figure 37. The superimposed interpolated front is that for 27 May. The arrows again denote inferred flow from profiles depicted in figures 38a, b and c. Flow derived from stations 5-7 is consistent with the local frontal position and orientation. Stations 12-14 are also consistent. Stations 15-19 confuse the interpretation somewhat. Stations 14-16, in profile shape, appear either as a return flow from stations 12-14 or as part of a detached eddy coupled with stations 17-19. Thermal profile characteristics support the former however, stations 1-4 suggest the latter. As discussed in section 3 the branches of the Tsushima Current may rejoin in this vicinity adding to the interpretive confusion.

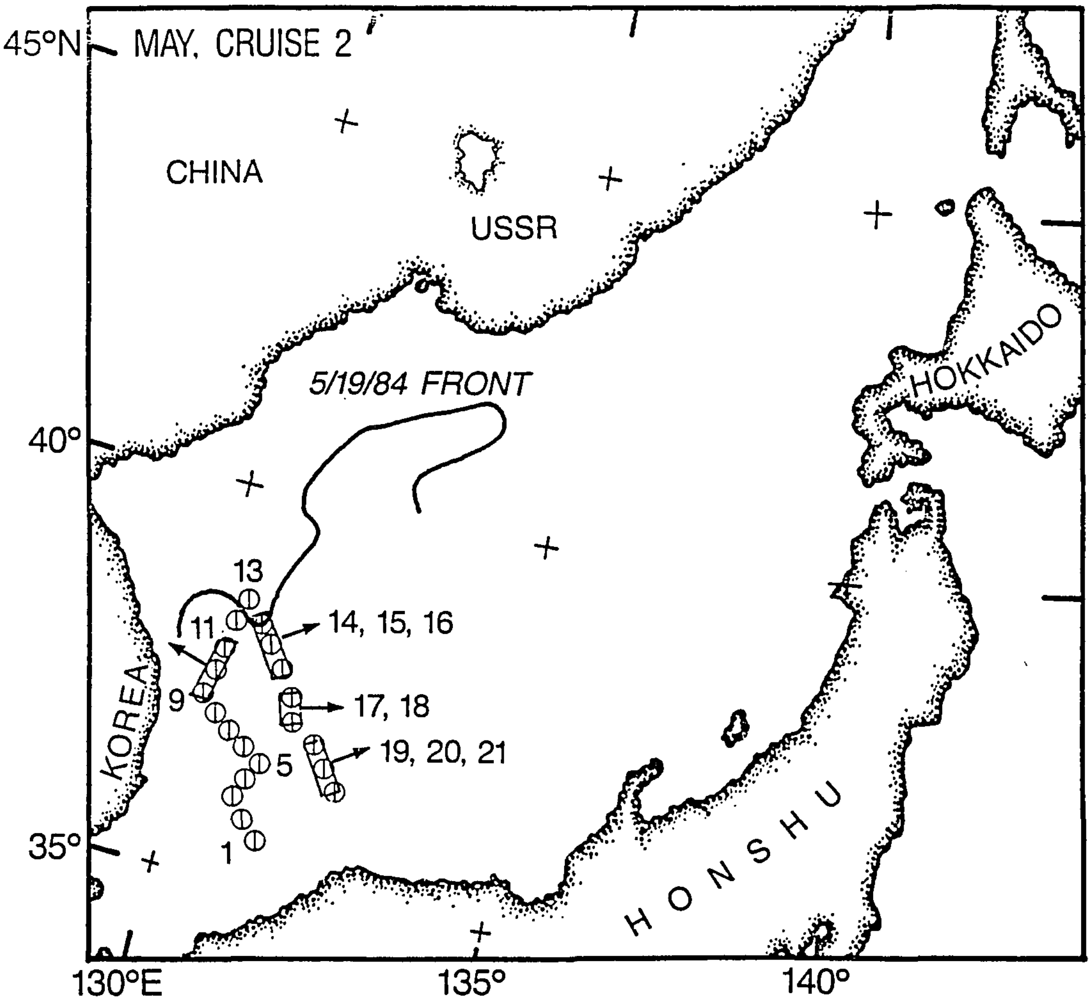

Figure 35. Stations occupied and resultant inferred flow during May 17-19, 1984, cruise of the Seifu Maru. May 19 interpolated frontal location superimposed.

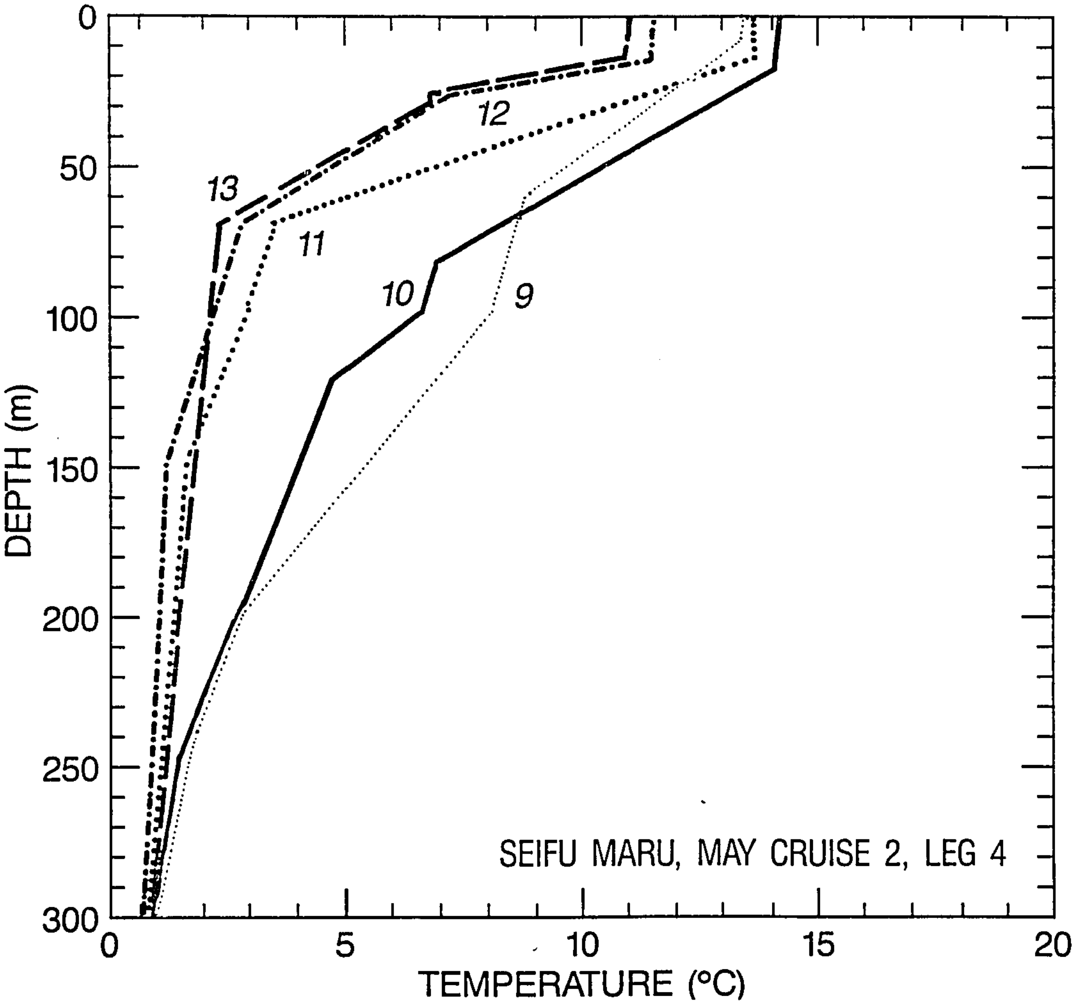

Figure 36a. Temperature profiles for leg 4 of May 17-19, 1984, Seifu Maru cruise.

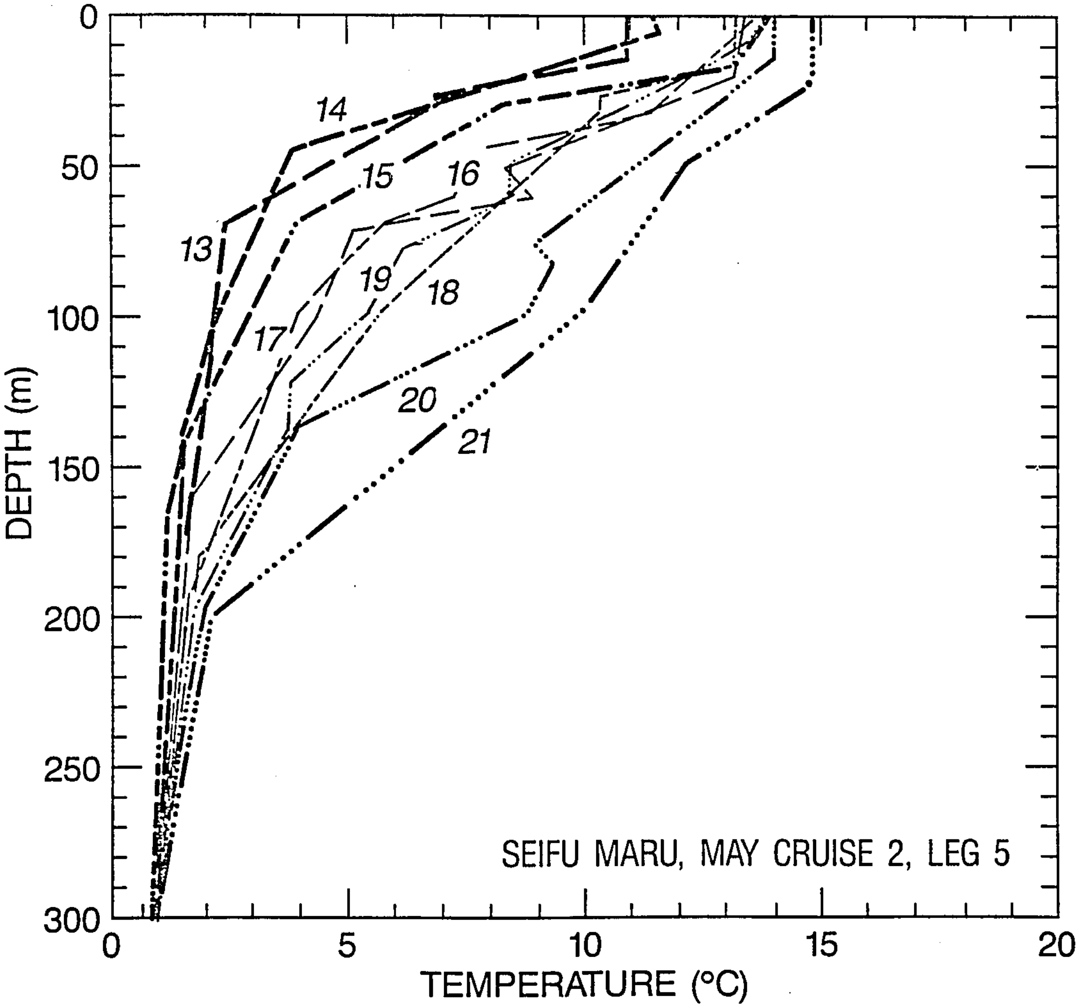

Figure 36b. Temperature profiles for leg 5 of May 17-19, 1984, Seifu Maru cruise.

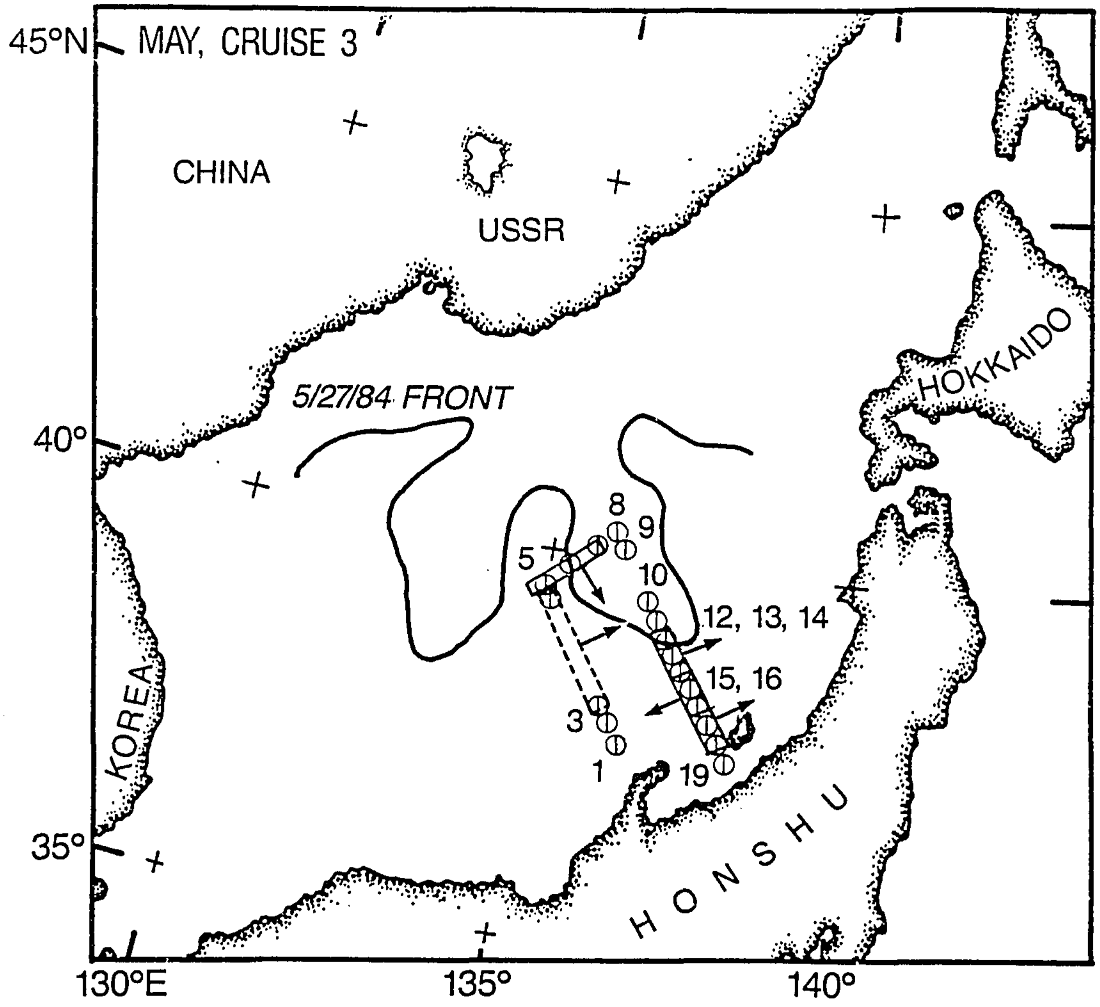

Figure 37. Stations occupied and resultant inferred flow during May 25-27, 1984, cruise of the Seifu Maru. May 27 interpolated frontal location superimposed.

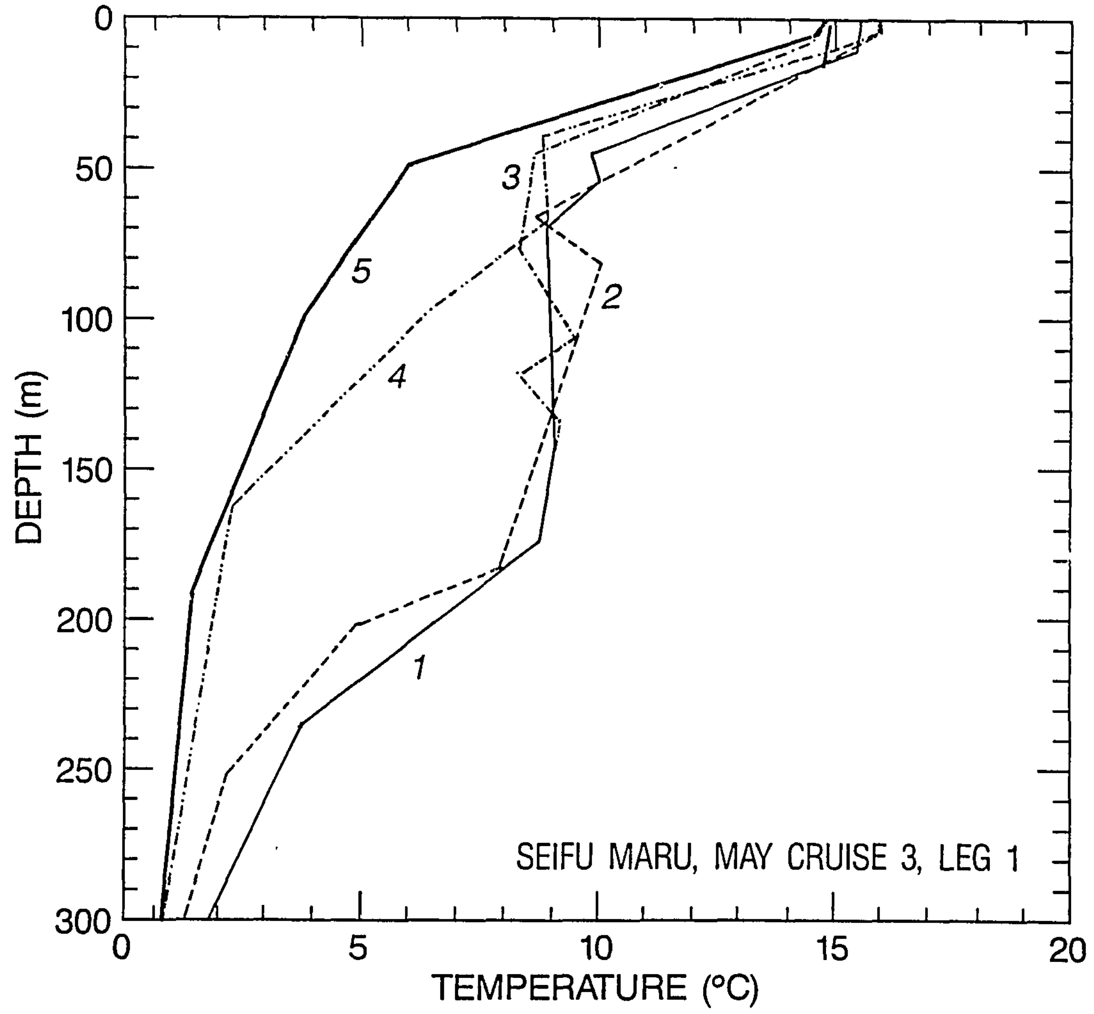

Figure 38a. Temperature profiles for leg 1 of May 25-27, 1984, Seifu Maru cruise.

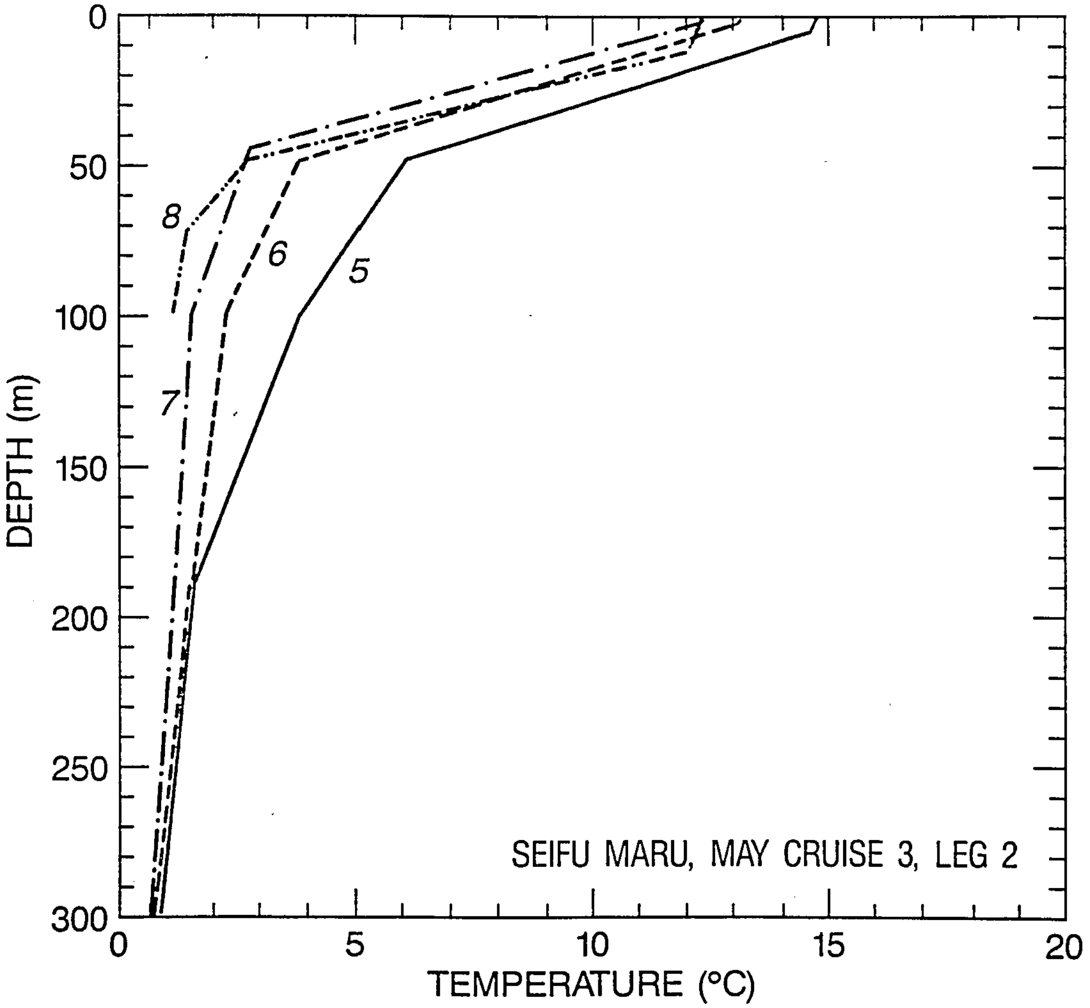

Figure 38b. Temperature profiles for leg 2 of May 25-27, 1984, Seifu Maru cruise.

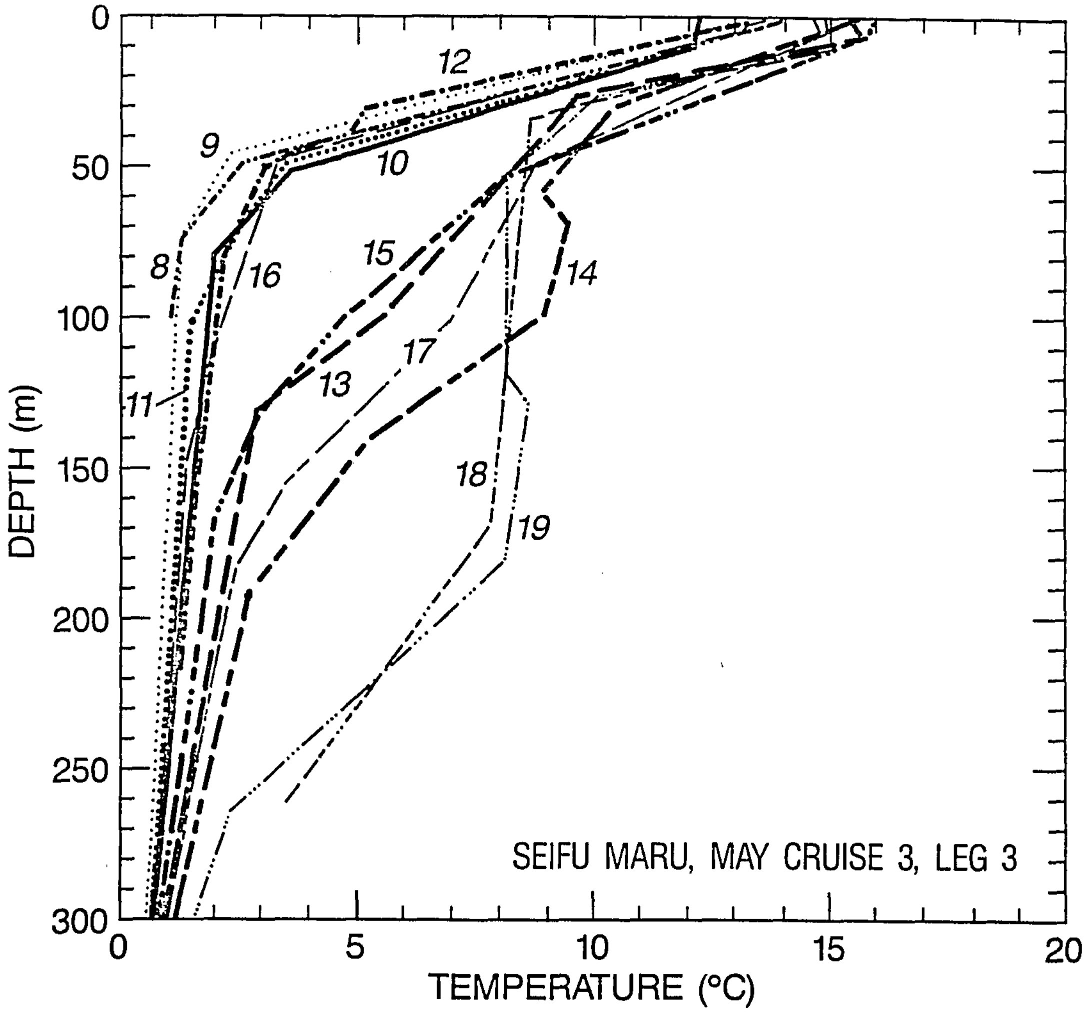

Figure 38c. Temperature profiles for leg 3 of May 25-27, 1984, Seifu Maru cruise.

The resolution in the *Seifu Maru* transects does not adequately resolve the structure of the Tsushima Current yielding some confusion in the interpretation of the flow field. I conclude that these three *Seifu Maru* cruises do not contradict the proposition that the NOCC-derived frontal positions roughly represent the position of the offshore branch of the Tsushima Current.

I carry the comparison one step further by comparing profiles from two *Seifu Maru* frontal transects with corresponding profiles from the appropriate synthetic analysis. Figure 39 shows the position of stations 5, 6, 7 and 12, 13, 14 for the May 25-27 *Seifu Maru* cruise. Recall that these profiles yielded flow directionally consistent with the NOCC derived frontal position also shown in figure 39. The points denoted A1-A5 are model grid point locations with profiles available for May 26. The profiles corresponding to stations 5, 6, 7 and 12, 13, 14 are shown in figures 40a and b. The profiles for the synthetic analysis points A1-A5 are outlined in figure 41.

The synthetic frontal profiles of figure 41 are generally within the envelope of frontal profiles sampled by the *Seifu Maru*. They will thus suffice for the purposes of this study. As an aside however, several differences between the measured and synthetic frontal representations are notable.

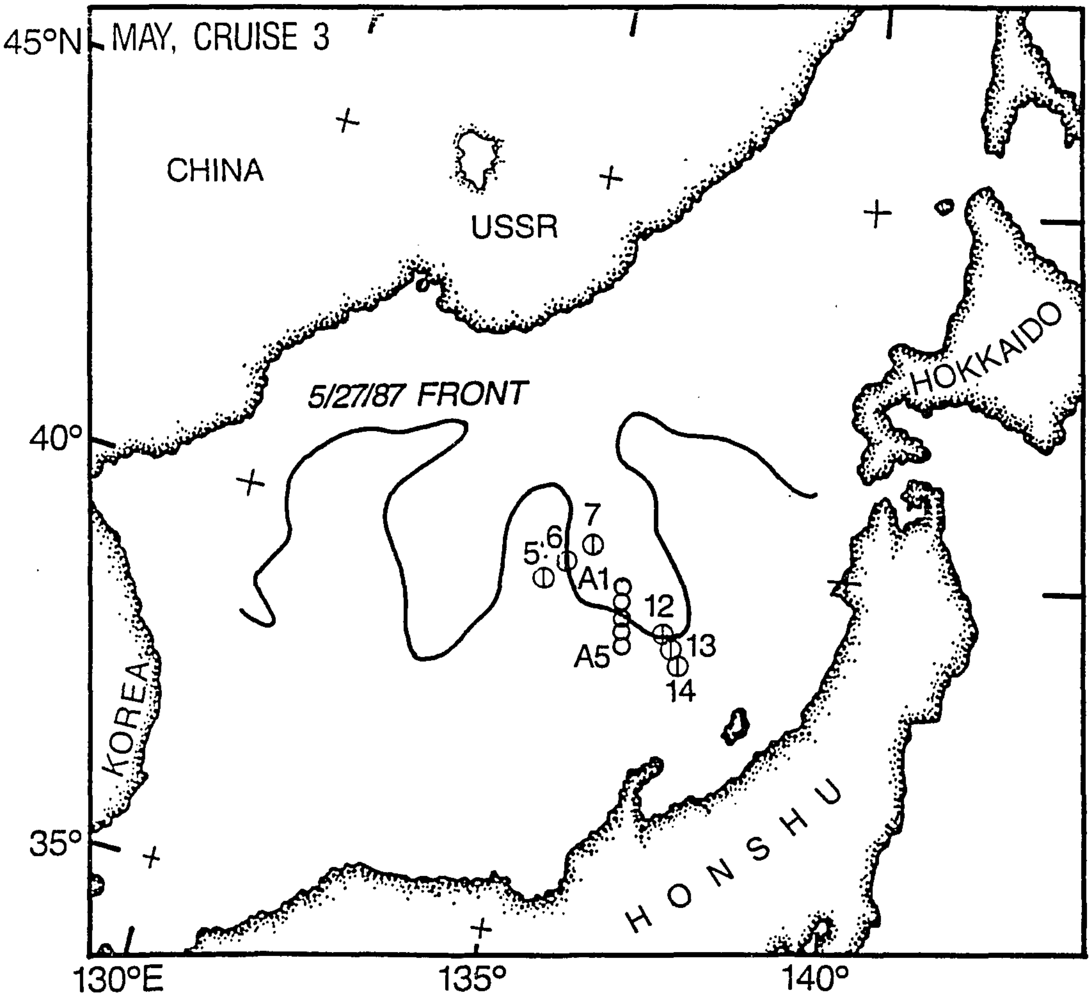

Figure 39. May 27, 1984, interpolated frontal position with appropriate *Seifu Maru* cross-frontal stations marked. A1-A5 denote model cross-frontal grid points.

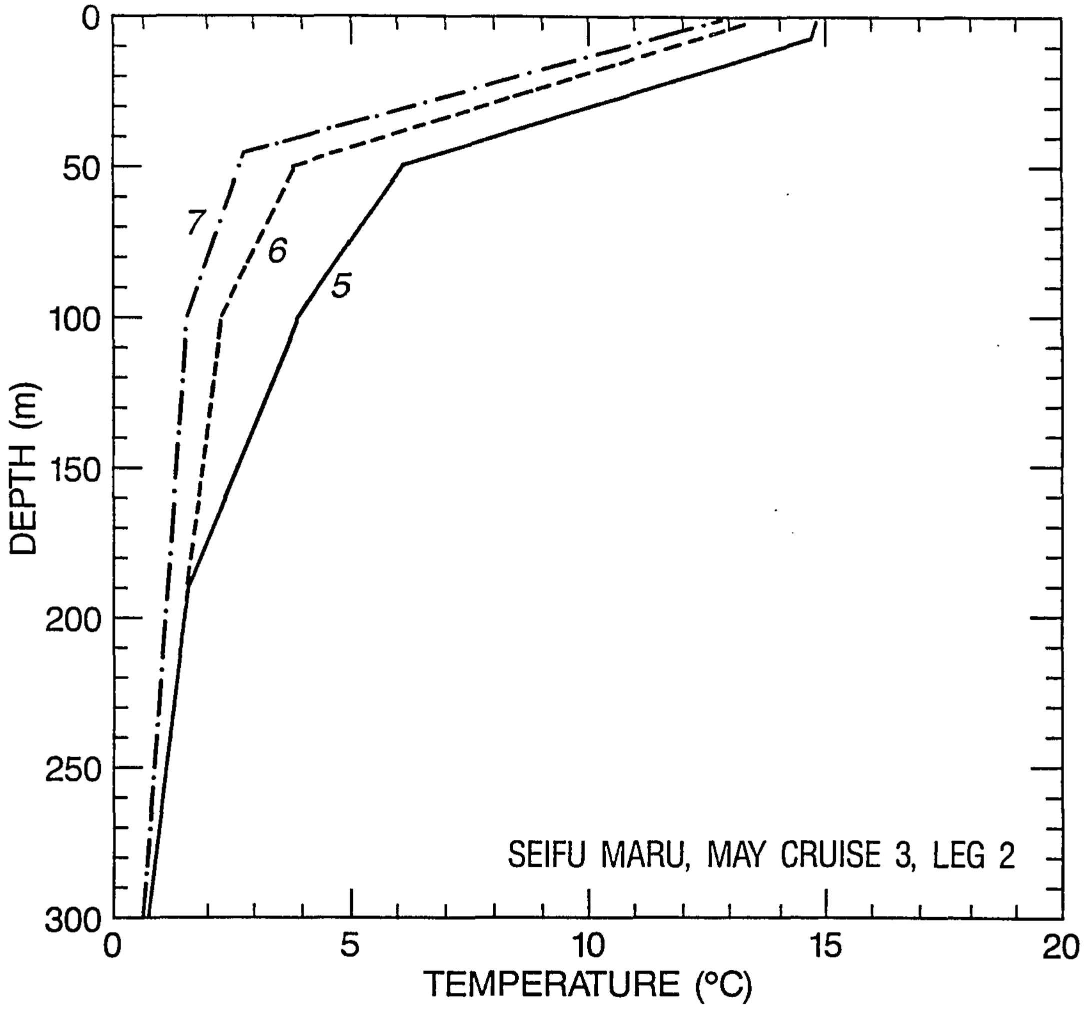

Figure 40a. Temperature profiles for stations 5-7 of May 25-27, 1984, Seifu Maru cruise.

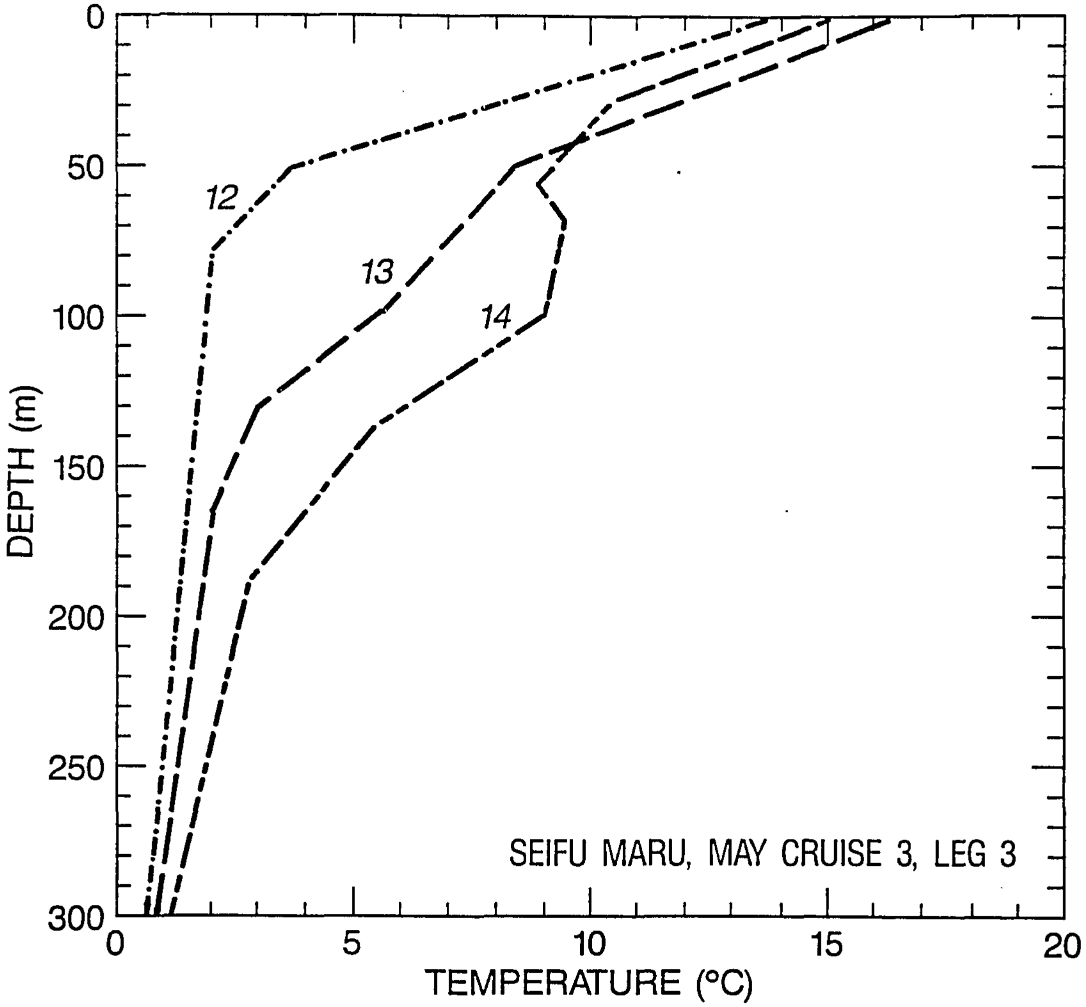

Figure 40b. Temperature profiles for stations 12-14 of May 25-27, 1984, Seifu Maru cruise.

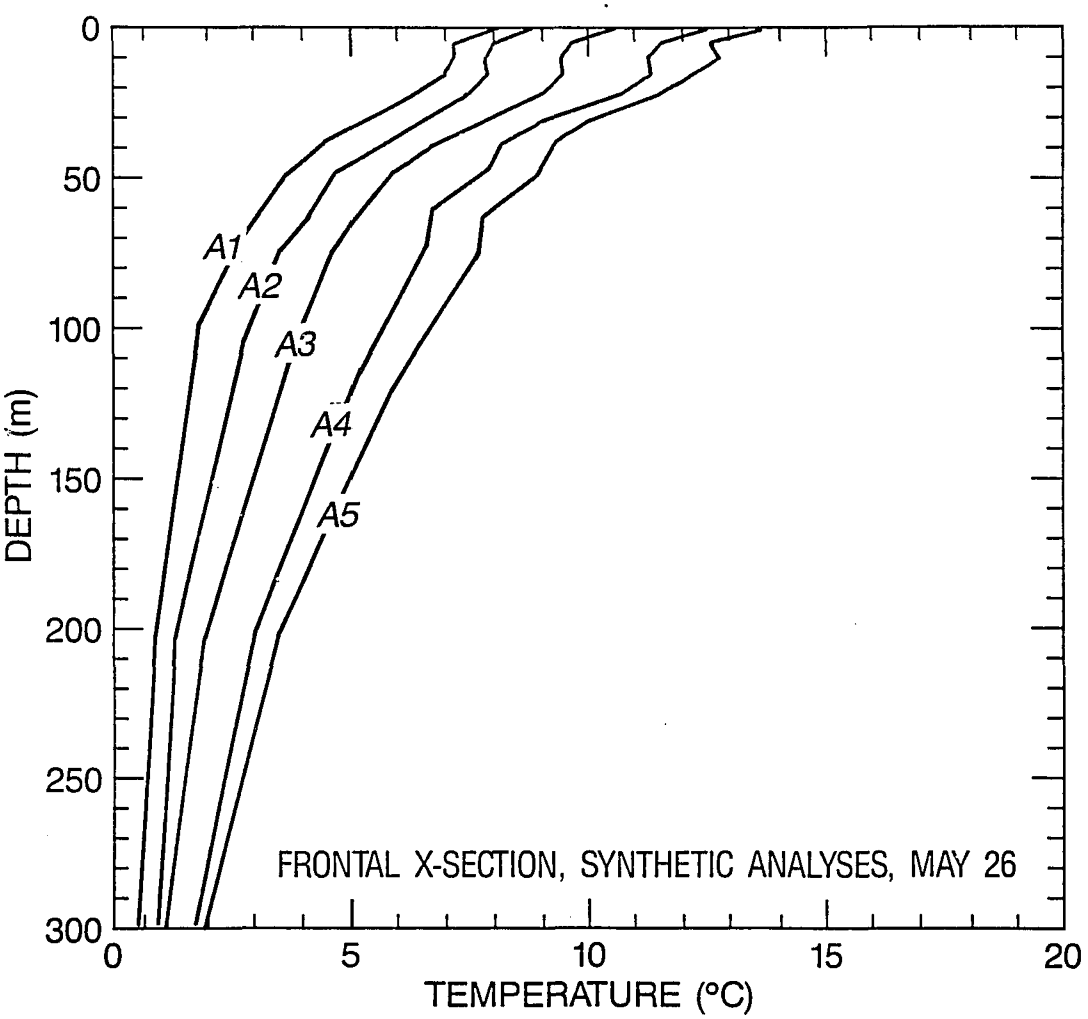

Figure 41. Temperature profiles from model initial conditions for May 26, 1984, for positions A1-A5 shown in figure 39.

The measured surface frontal temperature difference is order 2°C with maximum differences at depth of 3.5°C and 7°C for the two different frontal crossings. The synthetic profiles indicate a 6°C surface difference, decreasing to 5°C at 100 m decreasing to 1.5°C at 300 m. Also the warmest observed temperatures are 15-16°C whereas the warmest synthetic temperature is 14°C.

This latter discrepancy probably arises from the weekly composite performed to derive a single weekly analysis. As noted previously the data entering the subjective NOCC analysis is weighted more heavily with proximity to the analysis date. However in a warming season the dependence on the previous week's data might be expected to yield a cold bias when compared to actual data. What is puzzling is why NOCC surface frontal temperature differences tend to agree with the large subsurface temperature differences seen in the actual data.

The relatively high temperature of the synthetic analysis (1.5°C) relative to the data (.2°C-.5°C) at 300 m simply suggests that the exponential tail in the contructs should have been forced to converge faster.

The final discrepancy occurs near the surface where the synthetic analyses indicate some remnant mixed layer structure while the data indicates strong negative temperature gradients. Note that figure 41 shows the actual initial condition for the May 26 forecast since the synthetic initial condition would only contain the 0 and 25 m temperature (Table 2). Also recall from section 4.4,

that the actual initial condition contains the temperature values from the synthetic analysis for those levels denoted in Table 2, but also contains the previous forecast's profile shape in the near-surface region. Therefore the detail in the upper 25 m results from the previous day's forecast. The likely interpretation is that the kink in the upper 25 m results from residual mixed layer deepening remaining from previous forecasts. Given that the 0 to 25 m stratification in the synthetic analysis is weaker than that measured, it is reasonable that the 26 May initial condition might contain the remnants of previous model-forecast, mixed layers which the actual stratification might not allow to form.

6. EXPERIMENTAL DESIGN

The four experiments of this study cover a four week period beginning May 8, 1984 and continuing through June 4, 1984. As described in the approach, the four experiments consist of four increasingly complex versions of regional TOPS applied to daily, 72 hour duration forecasts for the above time period.

6.1. Experiments

Experiment 1 performs the forecasts using regional TOPS with the horizontal diffusion and advection of mean fields shut off. Thus the Sea of Japan is covered with a grid of one-dimensional mixed layer models.

Experiment 2 repeats the above forecasts in a manner closest to present day operational forecasts. Horizontal advection and diffusion plus vertical advection of the thermal and salinity fields are included in the mixed layer formulation but only for the wind-drift advection. The horizontal advection results from the local wind-forced Ekman and inertial components while the vertical advection arises from Ekman pumping and Ekman suction.

Experiment 3 repeats the above daily forecasts adding the geostrophic component of the horizontal advection applicable at the initial state of the forecast and derived

from the synthetic analyses. Thus persistence of the geostrophic component is assumed.

Experiment 4 extends experiment 3 by simulating the availability of predicted mesoscale circulation fields albeit in a limited way. The known synthetic analysis fields for each day within each three-day forecast are used to calculate daily geostrophic advection. These advection fields are then used to update the geostrophic flow field daily within each forecast period. However, the thermal field does not necessarily evolve consistently with the mesoscale flow field. Figure 42 provides an example. Consider an eastward propagating meander along a temperature front centered on and parallel to stream line a at time n. Neglect any surface forcing. Experiment 4 might have the geostrophic flow change to streamline b at the beginning of day n+1. Artificial cross-stream advection of temperature would thus occur at the intersection of a and b since the time evolution of the flow is imposed rather than derived from the coupled conservation equations for temperature, salinity, and momentum.

As a consequence, although experiment 4 is more physically complex, experiment 3 is more physically consistent and should thus be expected to provide the most physically correct result of the four. I include experiment 4 specifically because it does contain the potential for artificial, cross-stream temperature advection.

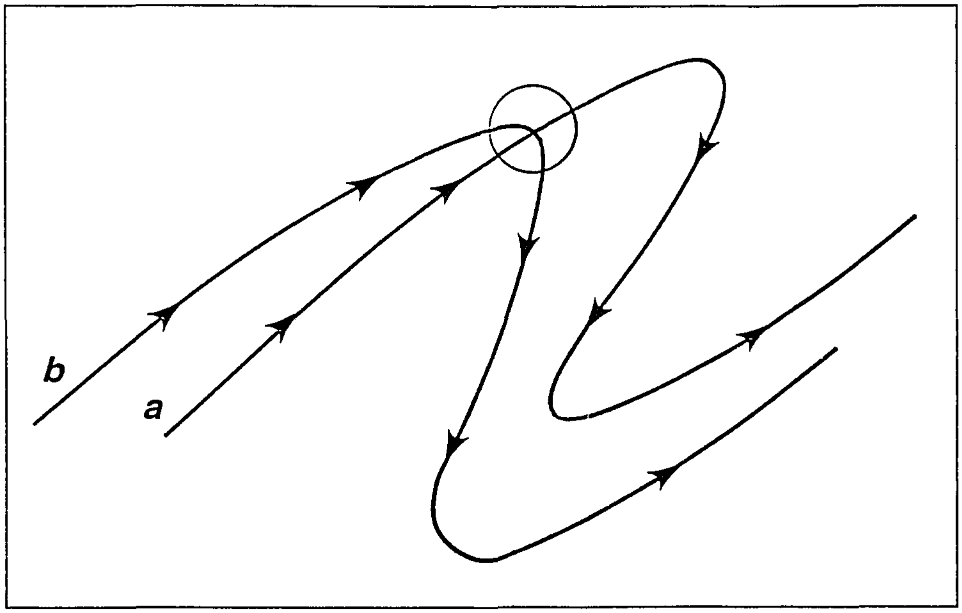

Figure 42. Schematic illustrating potential for artificial cross-frontal advection in experiment 4.

I wish to illustrate, if not exactly simulate, a potential problem in the application of passive mesoscale advection to upper-ocean thermal forecasts. I will return to this issue in section 7.

When referring individually to these experiments through the remainder of this report, I refer either to the above experiment numbers or as follows. Experiment 1 is the non-advective forecast, experiment 2 is the Ekman forecast, experiment 3 is the geostrophic nowcast, and experiment 4 is the geostrophic forecast.

6.2. Time Period

I choose the period from May 8 to June 4 for several reasons. First, it covers the essential period of spring transition for the Sea of Japan in 1984. Rapid upper-ocean warming and mixed layer shallowing, associated with a marked decrease in the wind, characterize this time (ELSBERRY and RANEY, 1978). Figure 43 illustrates the SST change for the time before, during and after the experimental period. The upper curve shows the measured daily temperature warming at 37.7°N ,134.3°E. These SST measurements, designated 21002 in the FNOC archives, are assumed to be from a data buoy operated by the Japanese.

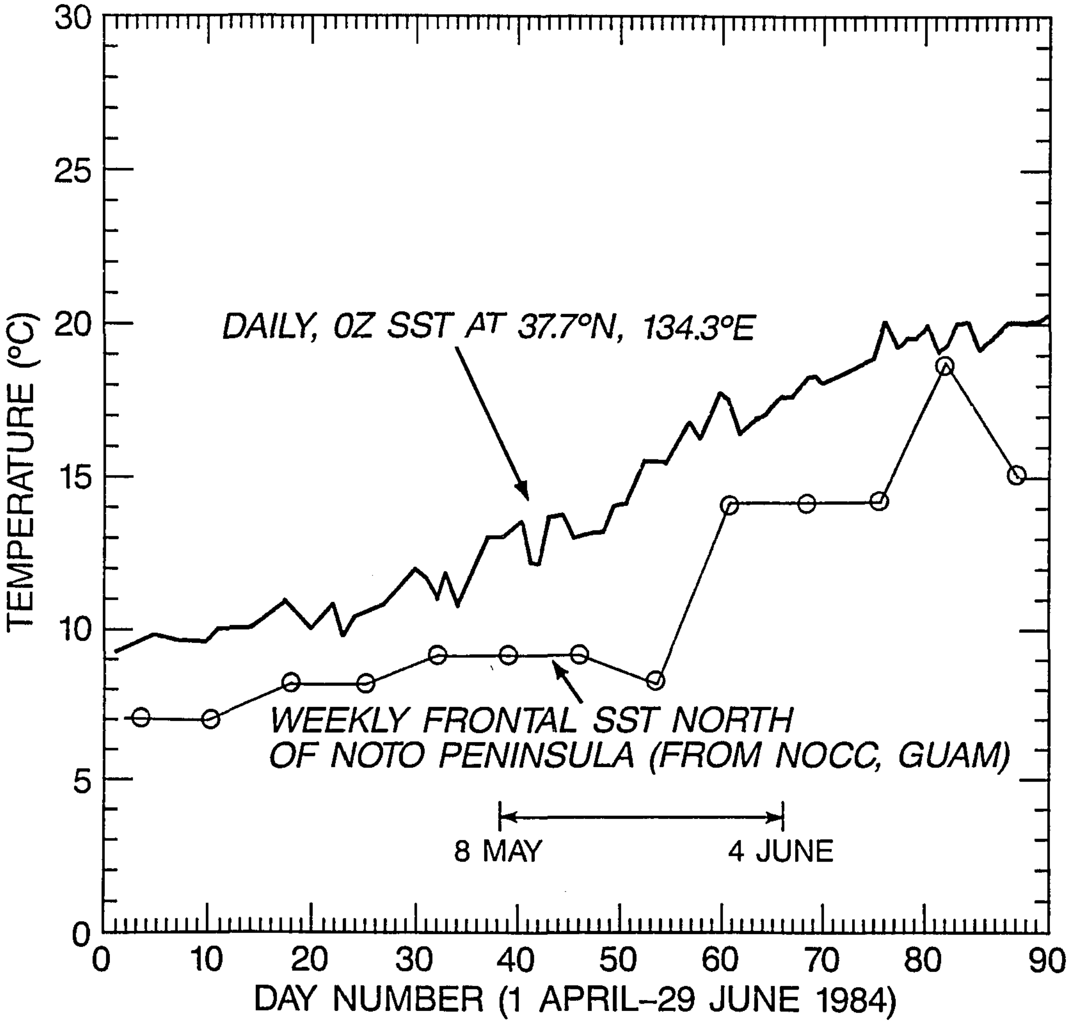

Figure 43. SST (°C) vs. time (days) for period before, during and after experimental period of May 8 - June 4, 1984. Upper curve for buoy 21002 (33.7°N, 134.3°E). Lower curve for weekly midfrontal SST north of Noto Peninsula extracted from NOCC Guam analyses.

The lower curve denotes the weekly temperature extracted from the NOCC subjective analyses at a mid-frontal location directly north of the Noto peninsula. The warming is evident in both curves though more noticeably for the frontal location. Figure 44 illustrates the corresponding evolution of square of the wind speed from NOGAPS limited to the experimental period itself. I use the square of the speed since it directly relates to wind stress (eqs. 26 and 27) and thus better reflects the wind influence on the model. The three curves represent cold (41.4°N, 134.5°E), warm (37.7°N, 135.4°E), and near-frontal (39.6°N, 135.0°E) locations in the Sea of Japan. One can thus expect this time period to provide model responses during both active and inactive local wind forcing.

Another advantage to this period is the shallow nature of the mixed layer. Mixed layer variability is expected only within the upper 25 m at this time (figures 33, 36 and 38) where the model resolution (Table 1) can most accurately resolve it (MARTIN, 1986).

Finally this period covers a time of significant evolution in frontal position as derived from the NOCC subjective analyses. Figure 45 illustrates this variability within a limited area in the middle of the model grid. I limit the experiments to this 28 day period to contain the computational cost in time and mass storage for both the experiments and subsequent analysis.

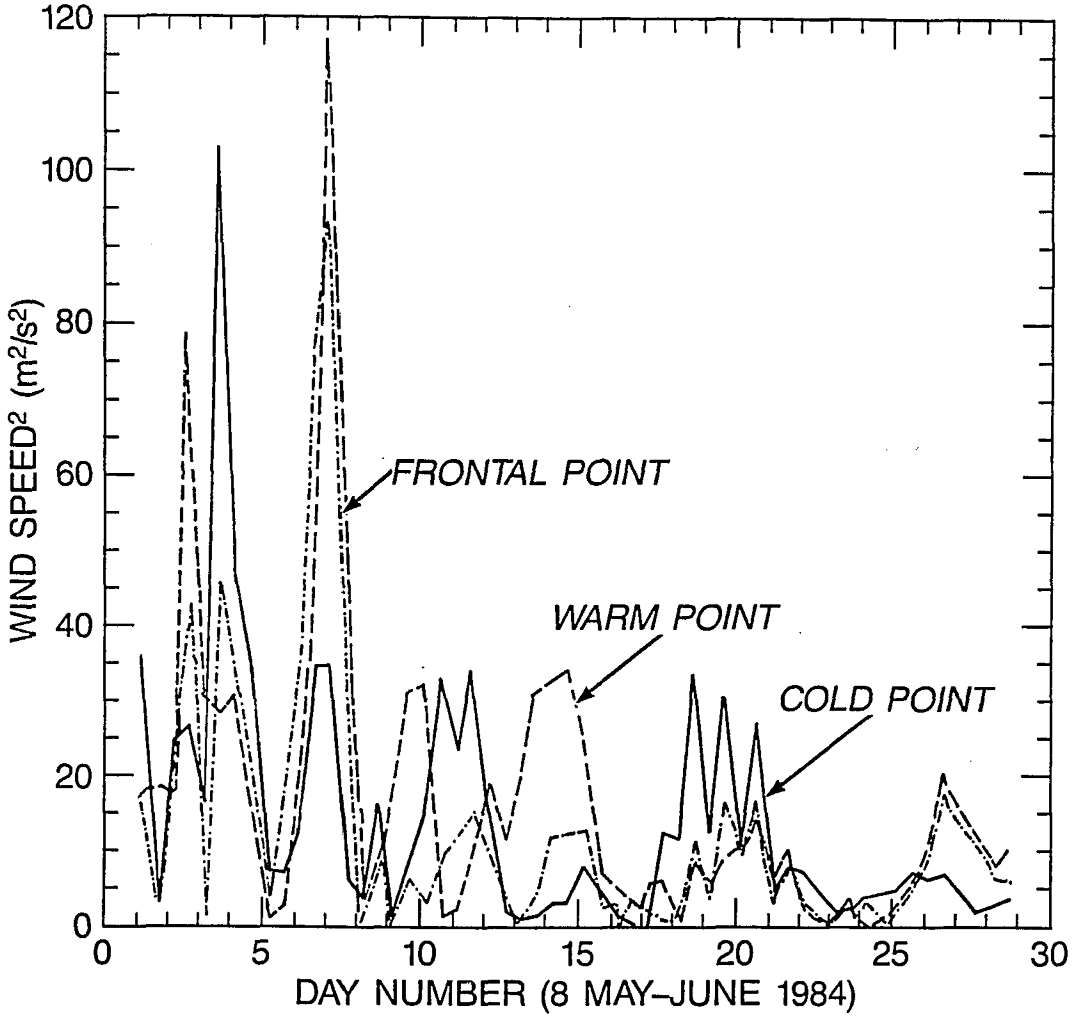

Figure 44. NOGAPS derived (wind speed)^2 vs. time for May 8 - June 4, 1984, at three locations. (--) indicates warm side at 37.7°N, 135.4°E. (-·-) indicates near-frontal position, 39.6°N, 135.0°E. (—) indicates cold side at 41.4°N, 134.5°E.

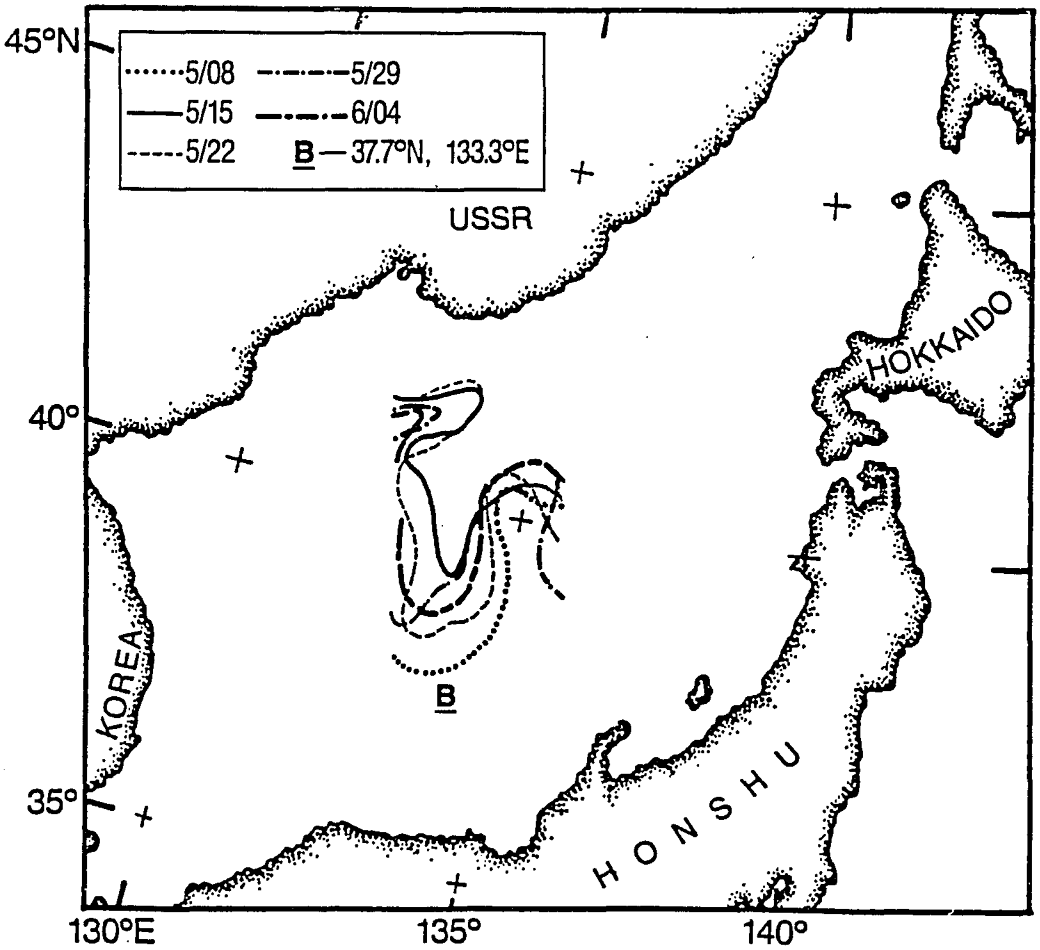

Figure 45. Weekly frontal positions derived from the NOCC Guam subjective SST analyses for May 8 - June 4, 1984. Rectangular area denotes model subregion over which section 7 statistical analyses are performed.

6.3. Computational Requirements

I performed all the experiments on computers at FNOC. Each experiment was set up and submitted to FNOC from the Institute for Naval Oceanography's (INO) VAX 8800 via 9600 baud dedicated phone line. This line terminates at FNOC in a Control Data Corporation (CDC) CYBER 855. The set-up calculations for each forecast are performed on this machine. These include the gathering and reformatting of restart, forcing, and initial thermal fields from tape. Those experiments requiring geostrophic currents (experiments 3 and 4) had these calculated on the 855's. All this information is subsequently forwarded to the FNOC CDC CYBER 205 supercomputer for the actual forecast calculation and preliminary output organization. The output then returns to the 855 where it is stored on tape and other mass storage clean up occurs. Table 3 summarizes, for each experiment, the central processor time required for each of these steps on the given machine. The final printed output then returns to the INO VAX via the dedicated phone line. Selected portions of the forecast data are later recovered from FNOC tape and transferred to the INO VAX for final analysis, interpretation and plotting purposes.

TABLE 3. CENTRAL PROCESSOR TIMES (S)
REQUIRED PER 3-DAY FORECAST

Step(Machine)	1(855)	2(205)	3(855)
Experiment			
1	25	111	16
2	25	127	16
3	57	128	16
4	113	128	16

Table 3 does not indicate actual wall-clock time required for the FNOC runs. FNOC computers are primarily operational and allow research and development runs only during designated, non-operational periods. This limits the time available to run these experiments. Data storage on tape requires operator intervention also slowing the job processing. The combined effect of the above two factors results in a total time requirement of approximately 6 weeks (including evenings and weekends) necessary to run all four experiments for the 28 day period.

7. RESULTS AND DISCUSSION

7.1. Statistical Analysis

I initially address the evaluation and comparison between these experiments using statistical measures proposed by WILLMOTT(1981, 1982) and WILLMOTT et al(1985) for operational model evaluation. These measures provide an evaluation of model accuracy which determines how well model-predicted events match with corresponding, independently obtained, reliable observations. Other methods are available (e.g., PREISENDORFER and BARNETT, 1983), however Willmott's suite of statistics are more widely used and thus more readily interpreted. The recommended statistics include: the means ($\bar{O},\bar{P}$) and standard deviations (s_o,s_p) of the observed and predicted variates respectively, the intercept (a) and slope (b) of a least squares regression between the variates, errors described by the root mean squared error (RMSE), systematic RMSE ($RMSE_s$), unsystematic RMSE ($RMSE_u$), and the index of agreement (d_2). Additionally, the mean error, ME, is also derived ($ME=\bar{P}-\bar{O}$) and also reported. Appendix C provides a description and derivation of the various statistical measures advanced by WILLMOTT et al(1985) as used in this study. In conjunction with the appropriate data display

graphics (primarily scatterplots, time series and histograms), WILLMOTT et al(1985) suggests one can "comprehensively accomplish the operational evaluation of one or more models."

As mentioned previously, the observational data do not exist to adequately evaluate regional, synoptic, upper-ocean, thermal structure forecasts. Consequently, I compare each 72 hr forecast from each of the various experiments with the 72 hr forecast of experiment 3. Recall from section 6, I expect experiment 3 to be the most physically consistent. I compute the statistics separately for selected vertical levels within the model. The observations, o_i, are the experiment 3, 72-hr forecast temperatures at each grid point within some horizontal subset of the grid. The set of observations consists of the individual o_i, accumulated over this horizontal subset as well as over the 28 days of the total experimental period for the specified vertical level. The predictions, p_i, are the corresponding, 72-hour forecast temperatures from each of the other experiments. Since my observations are model results instead of measured data, I replace "error" with "deviation" in my statistical notation when discussing the results. Thus, for instance, RMSE becomes RMSD.

Simply comparing the statistics of one model relative to experiment three with a second model relative to experiment 3 provides one measure with which to

intercompare models and their performance. For instance, one model may show an RMSD of 1°C for SST relative to another showing 0.5°C thus suggesting a 50% improvement when using the second model. However, one needs to also consider this relative error in the context of the entire forecast system within which the forecast model is but a single component.

The error of the data used in creating an operational initial condition is one source of additional error. The accuracy of the atmospheric forcing provides another source of error. The sensitivity of the model to these related components determines how this error is passed through the system to the end product. In the feed-back system outlined in figure 1, the determination of total system error becomes extremely complicated. One can see that a small improvement in model forecast error might result in growing improvements to subsequent forecasts as they feel the result of positive feedback (with the analysis scheme for example). Note the converse of this is of substantial concern whenever various components of a forecast system are modified. Addressing the unknown effects of all the various error sources, their impact on and feedback with the upper-ocean forecast is a task beyond the scope of this paper. I will however, include a reference error level into my statistical comparisons. I use an error level of 0.5°C as a known minimum level of error which enters the operational upper-ocean forecasts. This is the known RMSE of the highest density and quality data source presently

entering the operational thermal analyses (HAWKINS, 1985; HAWKINS et al., 1986). These data are the satellite-derived, multi-channel, sea-surface temperatures (MCSST).

A third consideration when comparing relative error levels is necessarily application dependent. I alluded to one aspect of this briefly in section 2. A statistically significant yet minimal decrease in forecast error may be worth the cost in life or death applications such as search and rescue. Another aspect involves the final user's specific sensitivity to the forecast output. In acoustics applications (e.g., URICK, 1983), the end user is someone using the temperature and salinity profiles to arrive at sound speed. Acoustic propagation is more sensitive to actual changes in profile shape due to vertical variability in temperature as opposed to the actual temperatures themselves. Sound speed minima tend to focus or channel sound waves for instance. The temperature gradient at and depth of the base of a surface mixed layer are more important to this end user than the absolute temperature of the layer itself. At low frequencies, the sound waves experience little effect due to the variability of the upper-ocean profile. This results from the vertical scales of this variability being small relative to the wavelengths at low frequencies. At mid- to high frequencies however, small changes in surface temperature gradient can determine if a surface duct (sound channel) exists or not, suggesting the potential for extreme sensitivity to small forecast errors. Application specific error sensitivities are

also beyond the immediate scope of this paper. I leave application specific interpretations of error sensitivity to the reader. Consequently, I confine my statistical comparisons to the actual statistics with consideration given only to the 0.5°C reference level discussed above.

In addition to the four experiments, I include a persistence forecast in the comparisons as well. The 72 hr persistence forecast is simply the initial condition for each 72 hr forecast period. I add a persistence comparison since little difference noted between persistence and experiment 3 might suggest that the forecast models are not needed at all. All points for these comparisons come from the rectangular subset of the model domain as shown in figure 45. This subset encompasses approximately 300 points but is far from the open boundary regions. Accumulated over the 28 day period, approximately 9000 points are compared.

Figures 46 a,b,c,d provide the SST scatter plots for (a) persistence, (b) experiment 1, (c) experiment 2, and (d) experiment 4, all relative to experiment 3. The persistence scatter plot shows the most variability with a notable cold tendency. Note the least squares line fitting the persistence forecast (figure 46a),is almost 1°C colder than the 1:1 line expected of a perfect forecast. The persistence forecast also shows more scatter than do experiments 1,2 and 4. Experiment 1 shows somewhat more scatter than experiments 2 and 4. The corresponding statistical summaries (Tables 4a,b,c,d) calculated as

described in Appendix C support this visual interpretation. A comparison of mean deviation, which represents a simple difference between the means, shows the persistence forecast to be 0.86°C colder than experiment 3. The corresponding mean deviation for experiments 1,2, and 4 are much smaller at -0.14, 0.08, and 0.00, respectively. There is a question whether these last three differences are even significant since the 95% confidence bounds overlap each other.

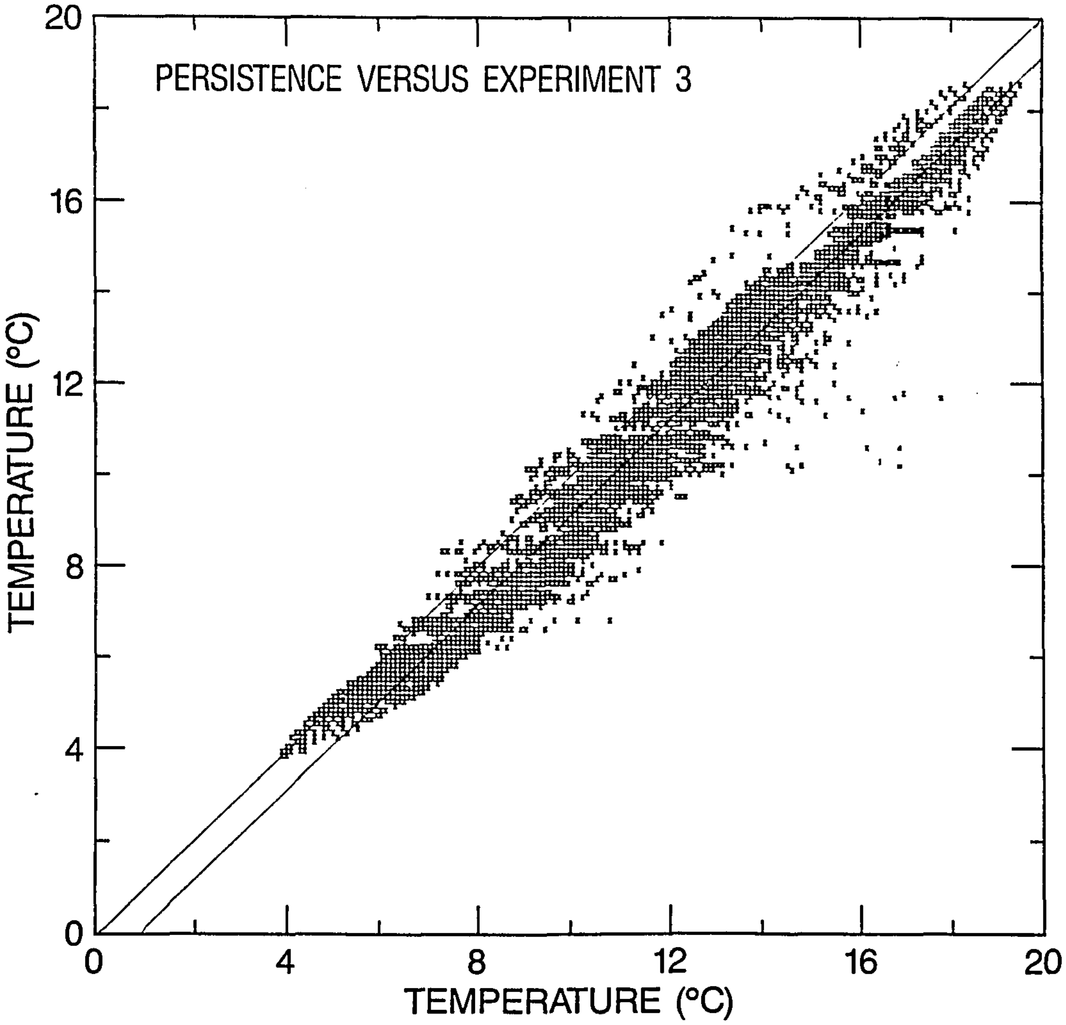

Figure 46a. Scatter plot of TAU 72 SST (°C) forecasts covering May 8 - June 4, 1984, for persistence vs. experiment 3.

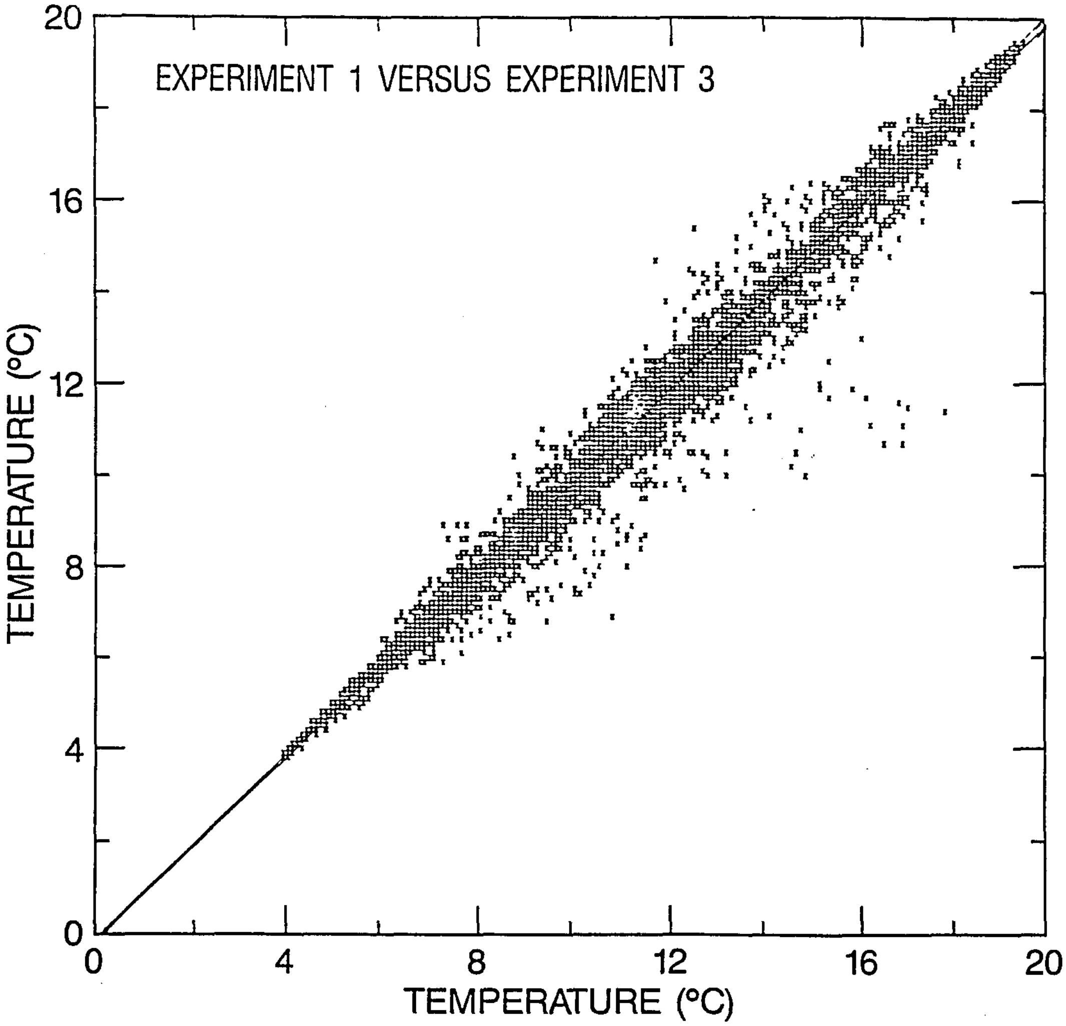

Figure 46b. Scatter plot of TAU 72 SST (°C) forecasts covering May 8 - June 4, 1984, for experiment 1 vs. experiment 3.

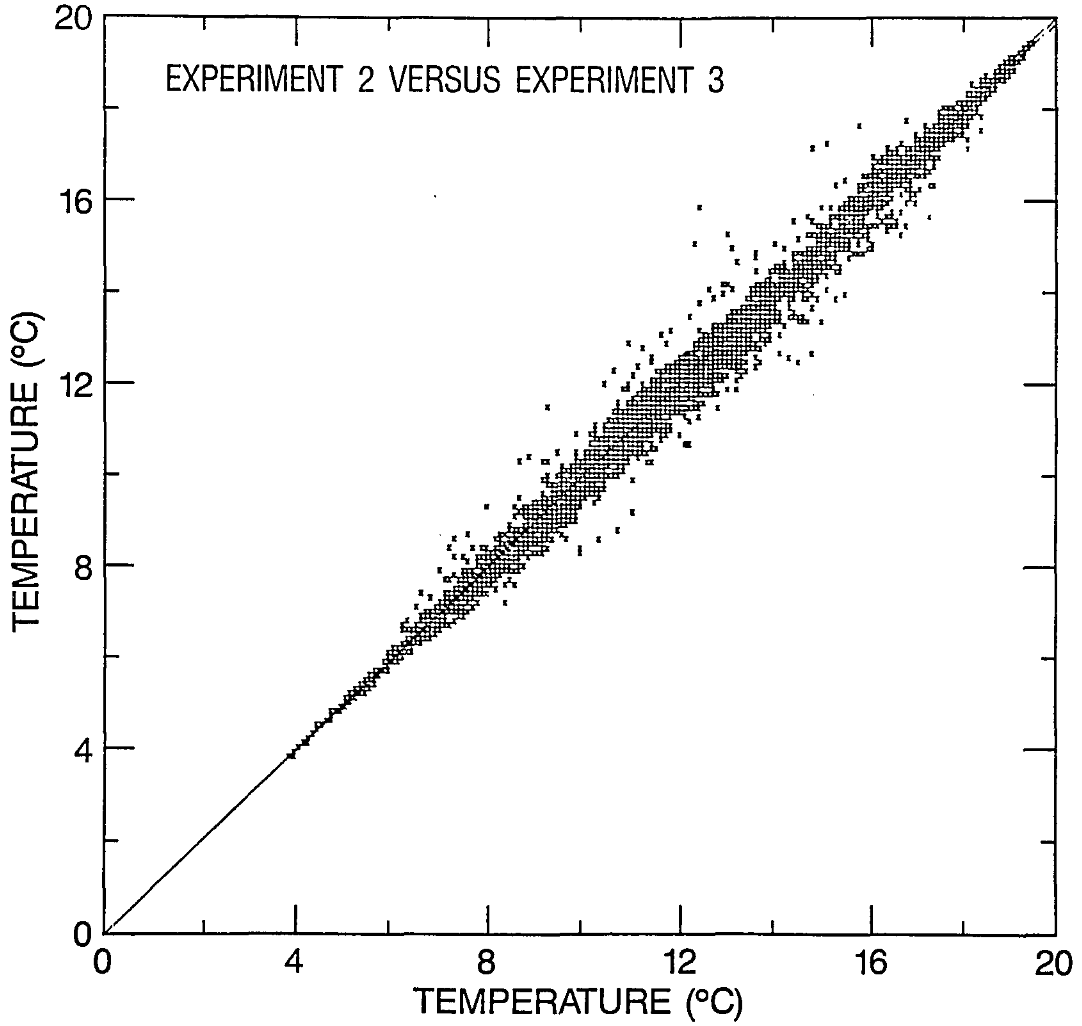

Figure 46c. Scatter plot of TAU 72 SST (°C) forecasts covering May 8 - June 4, 1984, for experiment 2 vs. experiment 3.

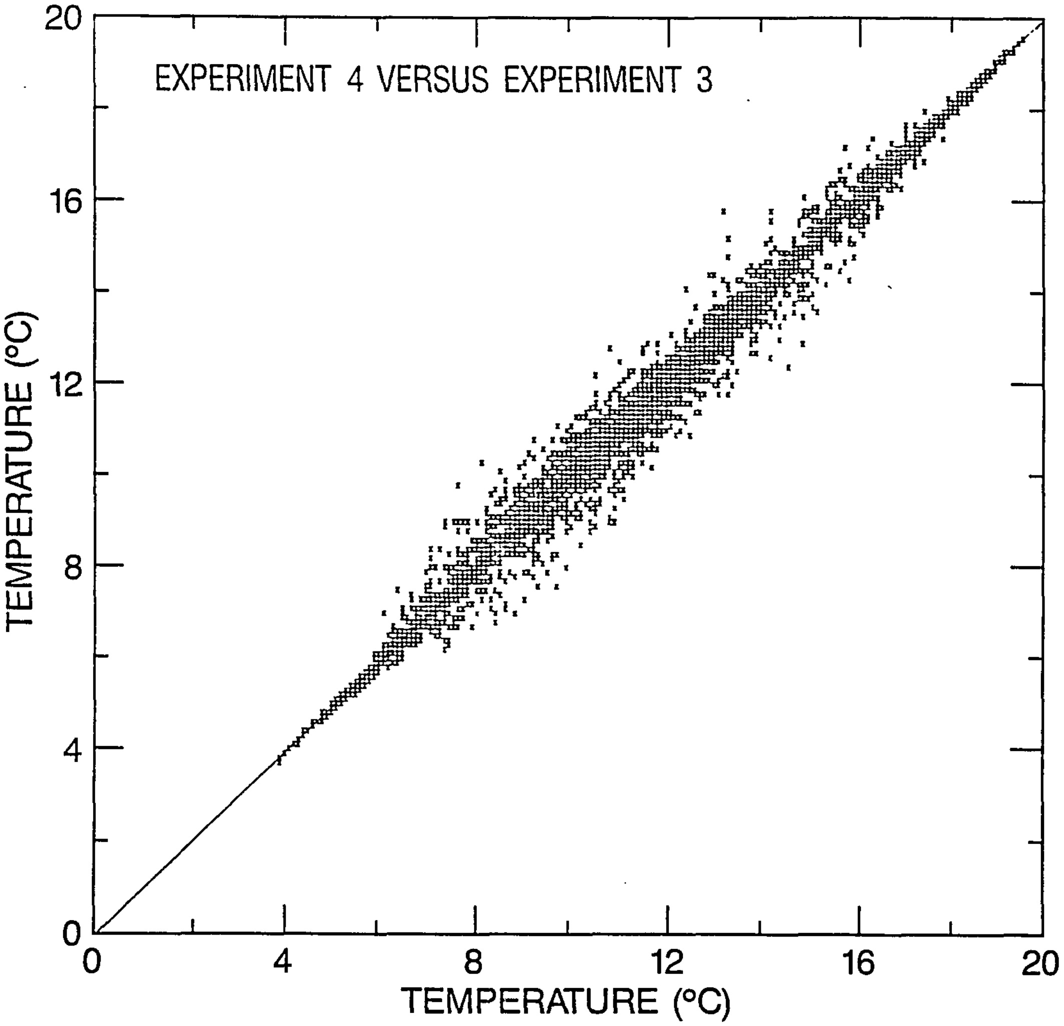

Figure 46d. Scatter plot of TAU 72 SST (°C) forecasts covering May 8 - June 4, 1984, for experiment 4 vs. experiment 3.

TABLE 4a STATISTICAL SUMMARY:
TAU 72 SST (°C), PERSISTENCE VS. EXPERIMENT 3

	PERSISTENCE	EXPERIMENT 3
NUMBER OF POINTS (N)	9072	9072
MEAN ($\overline{P}$, $\overline{O}$)	10.88	11.74
95% CONFIDENCE BOUNDS	(10.80, 10.96)	(11.66, 11.82)
STANDARD DEVIATION	3.66	3.60
95% CONFIDENCE BOUNDS	(3.63, 3.70)	(3.56, 3.63)

....

MEAN DEVIATION	-0.86
RMS DEVIATION (RMSD)	1.09
95% CONFIDENCE BOUNDS	(1.08, 1.11)
SYSTEMATIC RMS DEVIATION (RMSD$_s$)	0.86
UNSYSTEMATIC RMS DEVIATION (RMSD$_u$)	0.68
INDEX OF AGREEMENT (d_2)	0.98
95% CONFIDENCE BOUNDS	(0.98, 0.98)
LINEAR REGRESSION LINE	Y = 1.00X - 0.87

TABLE 4b STATISTICAL SUMMARY:
TAU 72 SST (°C), EXPERIMENT 1 VS. EXPERIMENT 3

	EXPERIMENT 1	EXPERIMENT 3
NUMBER OF POINTS (N)	9072	9072
MEAN ($\overline{P}$, $\overline{O}$)	11.60	11.74
95% CONFIDENCE BOUNDS	(11.52, 11.68)	(11.66, 11.82)
STANDARD DEVIATION	3.60	3.60
95% CONFIDENCE BOUNDS	(3.56, 3.63)	(3.56, 3.63)

....

MEAN DEVIATION	-0.14
RMS DEVIATION (RMSD)	0.47
95% CONFIDENCE BOUNDS	(0.44, 0.49)
SYSTEMATIC RMS DEVIATION (RMSD$_s$)	0.14
UNSYSTEMATIC RMS DEVIATION (RMSD$_u$)	0.44
INDEX OF AGREEMENT (d_2)	1.00
95% CONFIDENCE BOUNDS	(1.00, 1.00)
LINEAR REGRESSION LINE	Y = 0.99X - 0.05

TABLE 4c STATISTICAL SUMMARY:
TAU 72 SST (°C), EXPERIMENT 2 VS. EXPERIMENT 3

	EXPERIMENT 2	EXPERIMENT 3
NUMBER OF POINTS (N)	9072	9072
MEAN ($\overline{P}$, $\overline{O}$)	11.66	11.74
95% CONFIDENCE BOUNDS	(11.58, 11.73)	(11.66, 11.82)
STANDARD DEVIATION	3.59	3.60
95% CONFIDENCE BOUNDS	(3.55, 3.62)	(3.56, 3.63)

....

MEAN DEVIATION	0.08
RMS DEVIATION (RMSD)	0.29
95% CONFIDENCE BOUNDS	(0.28, 0.30)
SYSTEMATIC RMS DEVIATION ($RMSD_s$)	0.09
UNSYSTEMATIC RMS DEVIATION ($RMSD_u$)	0.27
INDEX OF AGREEMENT (d_2)	1.00
95% CONFIDENCE BOUNDS	(1.00, 1.00)
LINEAR REGRESSION LINE	Y = 0.99X - 0.02

TABLE 4d STATISTICAL SUMMARY:
TAU 72 SST (°C), EXPERIMENT 4 VS. EXPERIMENT 3

	EXPERIMENT 4	EXPERIMENT 3
NUMBER OF POINTS (N)	9072	9072
MEAN ($\overline{P}$, $\overline{O}$)	11.74	11.74
95% CONFIDENCE BOUNDS	(11.67, 11.82)	(11.66, 11.82)
STANDARD DEVIATION	3.60	3.60
95% CONFIDENCE BOUNDS	(3.57, 3.64)	(3.56, 3.63)

....

MEAN DEVIATION	0.00
RMS DEVIATION (RMSD)	0.29
95% CONFIDENCE BOUNDS	(0.28, 0.29)
SYSTEMATIC RMS DEVIATION ($RMSD_s$)	0.01
UNSYSTEMATIC RMS DEVIATION ($RMSD_u$)	0.29
INDEX OF AGREEMENT (d_2)	1.00
95% CONFIDENCE BOUNDS	(1.00, 1.00)
LINEAR REGRESSION LINE	Y = 1.00X + 0.02

The RMSD decreases from 1.09°C for persistence, to 0.47°C for experiment 1, to 0.29°C for both experiments 2 and 4. Note the accompanying 95% confidence bounds are all less than ± 0.03°C indicating these differences are statistically significant.

As discussed further in Appendix C, the $RMSD_s$ represents the difference of the least squares line from the 1:1 line in an additive and multiplicative sense. The $RMSD_u$ represents the uncorrellated part of the error, namely the scatter about the least squares line. Models with large systematic errors can be improved by using the additive and multiplicative factors inherent in the least squares line. Large unsystemmatic errors cannot be corrected. Consider the persistence forecast with $RMSE_s$ of 0.86°C. Since the least squares line and 1:1 line are nearly parallel, (i.e.,a=1.00, figure 46a), the $RMSE_s$ is primarily additive and basically equal to the absolute value of the mean error, -0.86°C. The persistence "model" could thus be improved for this forecast period simply by adding 0.86°C to all the persistence SST's. The improvements to experiments 1, 2, 1nd 4 would not be nearly as dramatic since their $RMSD_s$ are relatively small: 0.14°C, 0.09°C, and 0.01°C, respectively. In addition, their $RMSD_s$'s are a smaller proportion of their total RMSD's. The $RMSD_u$ for persistence, experiment 1, 2, and 4 are 0.68°C, 0.44°C, 0.27°C, and 0.29°C. These last statistics

support the previous, qualitative, visual interpretation of the scatter in figures 46 a,b,c,d. The statistic, d_2, (a WILLMOTT(1981) invention) reflects the degree that a simulated variate accurately estimates the observed. The values encountered in these experiments suggest all the experiments do this well with persistence the worst with d_2 of 0.98.

By the above statistical measures, persistence stands out as performing notably worse than the other experiments even when considering the reference MCSST error of 0.5°C. This interpretation holds even if one assumes all of the systematic error could be removed from the persistence forecast. This is heartening, in that it demonstrates the utility of ocean modeling as a forecast tool.

One might suggest that persistence forecast skill might fare better when compared against actual data as opposed to experiment 3 results. In reply, one can first note that during this warming period (see figure 43), the observed persistence forecast error should be expected. During rapid surface warming, one expects three-day-old temperatures (the persistence forecast) colder than the verifying temperatures.

One can go further and calculate a measure of persistence error at buoy 21002 (33.7°N,134.3°E) where we have SST data for the experimental period. Buoy 21002, daily SST's (sampled at 9 A.M. local time) are used as the observations. Buoy temperatures from three days prior comprise the predictions. Table 5 summarizes the results.

TABLE 5 STATISTICAL SUMMARY:
TAU 72 SST (°C), BUOY PERSISTENCE VS. BUOY TEMPERATURE

	BUOY PERSISTENCE	BUOY TEMPERATURE
NUMBER OF POINTS (N)	25	25
MEAN ($\overline{P}$, $\overline{O}$)	14.77	15.33
95% CONFIDENCE BOUNDS	(14.08, 15.38)	(14.63, 15.96)
STANDARD DEVIATION	1.81	1.84
95% CONFIDENCE BOUNDS	(1.49, 2.07)	(1.47, 1.98)

....

MEAN ERROR	-0.56
RMS ERROR (RMSE)	0.94
95% CONFIDENCE BOUNDS	(0.79, 1.10)
SYSTEMATIC RMS ERROR ($RMSE_s$)	0.59
UNSYSTEMATIC RMS ERROR ($RMSE_u$)	0.73
INDEX OF AGREEMENT (d_2)	0.93
95% CONFIDENCE BOUNDS	(0.89, 0.95)
LINEAR REGRESSION LINE	Y = 0.90X + 1.02

Note that the RMSE of 0.94°C with 95% confidence bounds of 0.79°C and 1.10°C, the RMSE_s of 0.59°C, and the RMSD_u of 0.73°C all compare favorably with the statistics of the persistence forecast given in Table 4a. That the buoy statistics tend to show slightly lower errors than the persistence forecast above is also consistent. The buoy location lies primarily south of the front throughout the experimental period while the persistence forecast relative to experiment 3, contains frontal activity as well. This location effect appears in the mean temperatures as well. The mean buoy temperature is ~15°C while the persistence forecast mean is ~11°C.

Figure 47 provides vertical profiles of RMSD for the persistence forecast, experiment 1, 2, and 4. For these experiments the RMSD decreases fairly rapidly with depth. Note that the largest differences occur in the upper 20 m where the mixed layer variability is expected. Thus, for these experiments the SST statistics provide the most dramatic differences.

While it is satisfying that the TOPS forecasts appear to out-perform persistence in a measurable way, it is interesting that the relative differences between the other experiments are not large. One might expect that spatially partitioning the subregion into warm, frontal and cold subregions and then recalculating the statistics might yield more dramatic results.

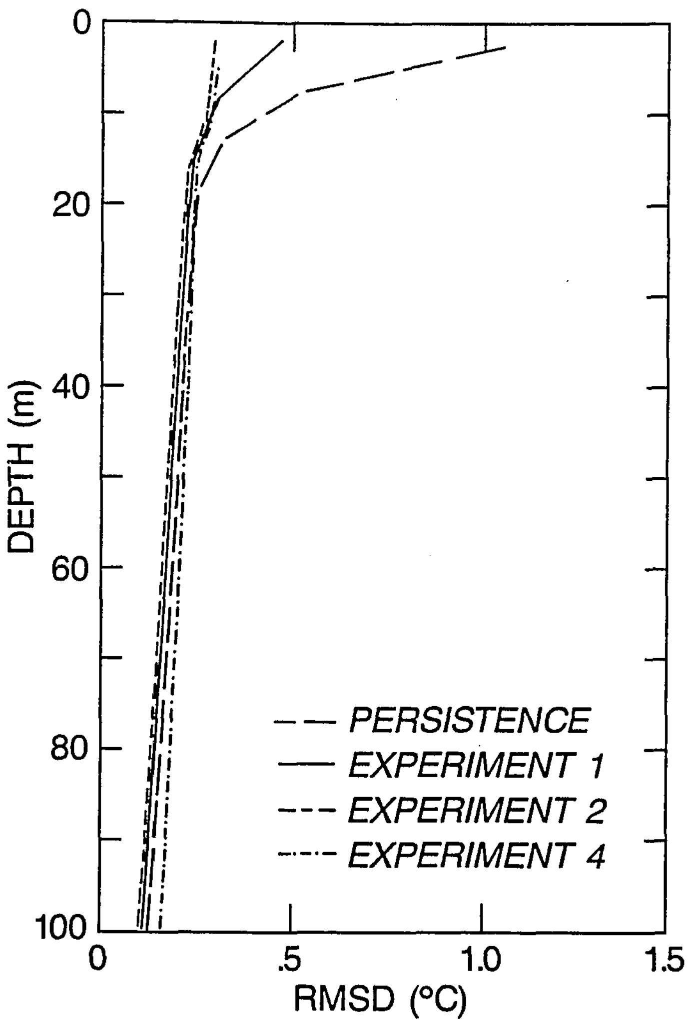

Figure 47. RMSD temperature (°C) vs. depth (m) for TAU 72 forecasts of persistence, experiment 1, experiment 2, and experiment 4, all vs. experiment 3, May 8 - June 4, 1984.

The statistical variability in the frontal region, for instance, would not be masked by the other two relatively quiescent regions. To check this, I mask each three-day forecast result into warm, frontal and cold regions for the rectangular region shown in figure 45. I base the mask on the initial condition used for each forecast. The frontal region is that area encompassed by the defined frontal temperature ± 3°C for the particular day (see section 5). The warm region is the area warmer than this, the cold region, the area colder. For ease of interpretation, table 6 summarizes the statistics, RMSD, $RMSD_s$,$RMSD_u$, and d_2. For reference, Appendix D contains the associated scatterplots, statistical tables, and vertical RMSD profiles for these cases.

In general, the results are as expected. The frontal region shows larger errors than the warm and cold sides for most cases. (I discuss the one exception to this below.) Persistence performs poorly, relative to the other experiments, in warm, frontal, and cold regions.

Ekman advection and horizontal diffusion appears to have had little impact on the warm side since the RMSD for experiment 1 (0.13°C) is comparable to that for experiment 2 (0.12°C). This is in direct contrast to both frontal and cold regions where experiment 1 had RMSD of 0.56°C and 0.40°C respectively. These are compared to the corresponding experiment 2 values of 0.38°C and 0.17°C.

TABLE 6. SUMMARY CORE STATISTICS

SUBREGION: FORECAST:	TOTAL	WARM	FRONT	COLD
PERSISTENCE				
RMSD	1.09	0.56	1.14	1.20
95% BOUNDS	1.08,1.11	0.55,0.55	1.12,1.16	1.17,1.23
RMSD$_s$	0.86	0.49	0.90	1.06
RMSD$_u$	0.68	0.28	0.70	0.56
d_2	0.98	0.98	0.95	0.91
EXPERIMENT 1				
RMSD	0.47	0.13	0.56	0.40
95% BOUNDS	0.44,0.49	0.13,0.14	0.53,0.58	0.33,0.46
RMSD$_s$	0.14	0.08	0.17	0.18
RMSD$_u$	0.44	0.10	0.53	0.36
d_2	1.00	1.00	0.99	0.99
EXPERIMENT 2				
RMSD	0.29	0.12	0.38	0.17
95% BOUNDS	0.28,0.30	0.11,0.12	0.36,0.39	0.15,0.20
RMSD$_s$	0.09	0.07	0.11	0.05
RMSD$_u$	0.27	0.09	0.36	0.17
d_2	1.00	1.00	0.99	1.00
EXPERIMENT 4				
RMSD	0.29	0.06	0.39	0.13
95% BOUNDS	0.28,0.29	0.05,0.06	0.38,0.41	0.11,0.16
RMSD$_s$	0.01	0.01	0.01	0.01
RMSD$_u$	0.29	0.06	0.39	0.13
d_2	1.00	1.00	0.99	1.00

The mesoscale component of advection which is included in experiment 3 shows its primary impact in the frontal area, as expected. The experiment 2 results show this since as the basis of the comparisons, the experiment 3 error has been assumed 0. The warm and cold side RMSD of 0.12°C and 0.17°C are relatively small compared to the 0.5 reference MCSST error level and more importantly when compared against the frontal RMSD of 0.38°C. The experiment 4 results are comparable with experiment 2.

I return to the exception noted above where the frontal RMSD was not the largest. The single exception is the cold side persistence forecast with RMSD of 1.20 relative to 1.14 for the frontal region. These differences appear significant since the RMSD, 95% confidence bounds do not overlap. With the exception of week 2, the frontal position generally moves toward the cold side (figure 45). Thus the frontal region defined at the beginning of a forecast will tend to be to the south of the actual front at the end. That is, the actual frontal position for the verifying analysis will tend to be toward or in the initially defined cold region. Consequently, the cold side statistics for the persistence forecast tend to contain frontal variability.

Consider the results presented to this point. Also consider that WILLMOTT (1981, 1982) and WILLMOTT et al(1985) assert that these sorts of analyses are not only necessary but also sufficient for the operational evaluation of models. One might therefore conclude two

things with respect to the evolutionary development of an upper-ocean forecast system. First, the forecast models appear to provide a significant improvement over a persistence forecast. Second, the succesive addition of wind-drift advection (experiment 2), and nowcast mesoscale advection (experiment 3) do provide statistically measurable improvements to the forecast.

Given that these measures supposedly provide comprehensive model evaluation criterion, however, one might be tempted to base cost/benefit decisions on such statistics. For instance, one might decide that the cost of additional physical processes beyond the wind drift advection of experiment 2, may not appear justified. In the next subsection, I present results that suggest that while necessary, this sort of analysis may not be sufficient when comparing model results for operational applications. Temporal and spatial variability in the error may not be adequately resolved by the available validation statistics.

7.2. Individual Forecast Comparison

Consider the primary causes of variability one might expect in a three-day, upper-ocean forecast. First would be the diurnal cycle associated with the earth's rotation and resultant rising and setting of of the sun. Second would be the synoptic variability associated primarily with extratropical cyclones. Third is the mesoscale variability

associated with meandering and eddy shedding in dynamically-active frontal areas. Of these three, the last two are aperiodic in time and space. That is, storms of identical strength do not pass over a particular location at a fixed interval. Likewise meandering and eddy-shedding in a dynamically active region can occur at different times at different locations (except where topographically constrained) along a front. The solar signal at the ocean's surface is actually a combination of periodic and aperiodic events since cloud cover modulates it.

Further, oceanic responses to these particular aperiodic events are of likely interest to the user of the forecasts. It is the unexpected which we need to forecast. Therefore, unless the independent verification data is sufficient to run the validation statistics for these high variability places and times, I suggest that the statistical analyses alone are not sufficent descriptors when comparing model results.

I present results from a single forecast for the May 12, 1984 to illustrate the point. Recall this is the period early in the experimental period when a strong increase in the wind speed occurred (figure 44). Figure 48 shows the initial condition for SST on May 12; this is also how a 72 hr persistence forecast would appear. Figures 49a-d illustrate the 72 hr SST forecast for experiments 1-4 respectively. Note the contour interval for figures 48 and 49 is 1°C. Experiment 1, the non-advective forecast, shows little obvious change.

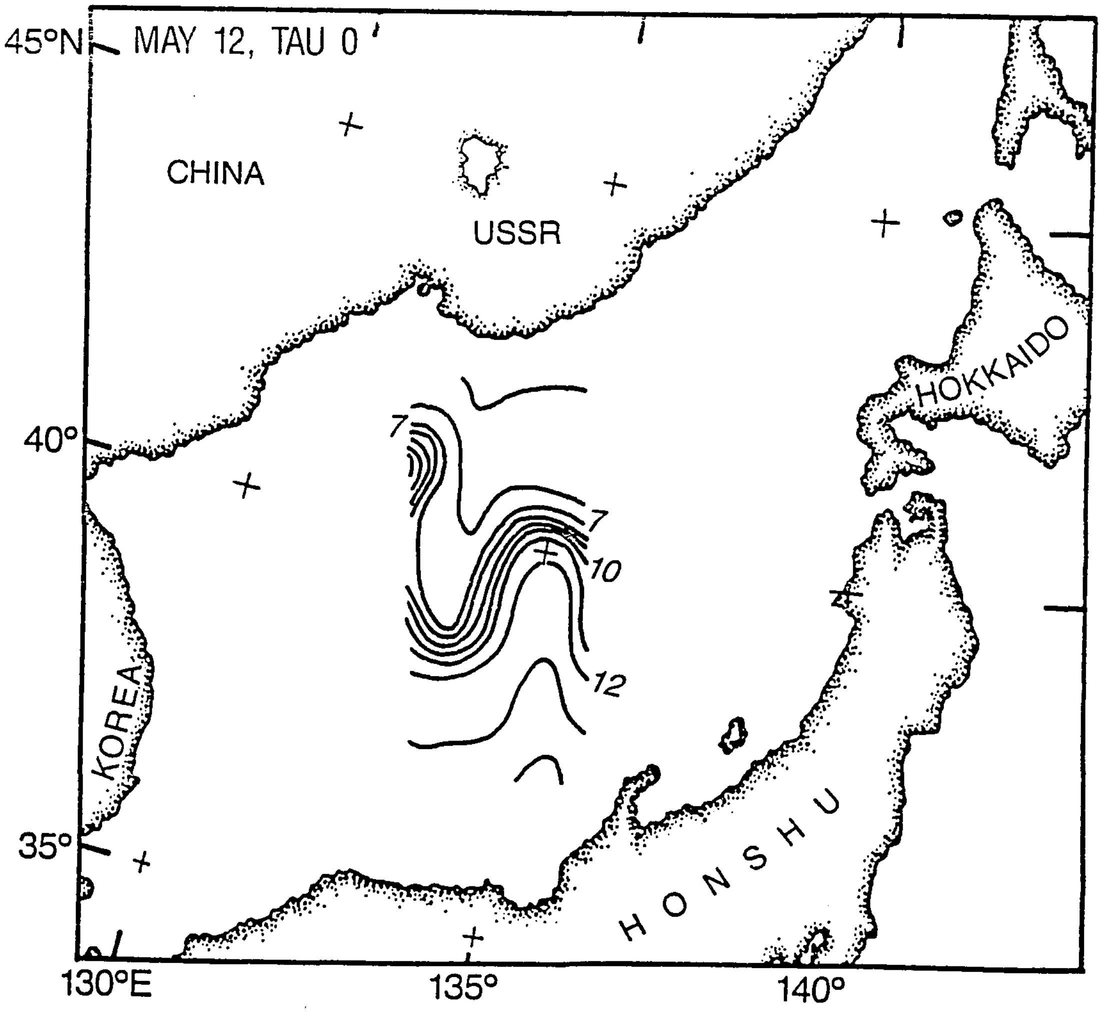

Figure 48. Initial condition SST (contour interval = 1°c), for May 12, 1984, forecast.

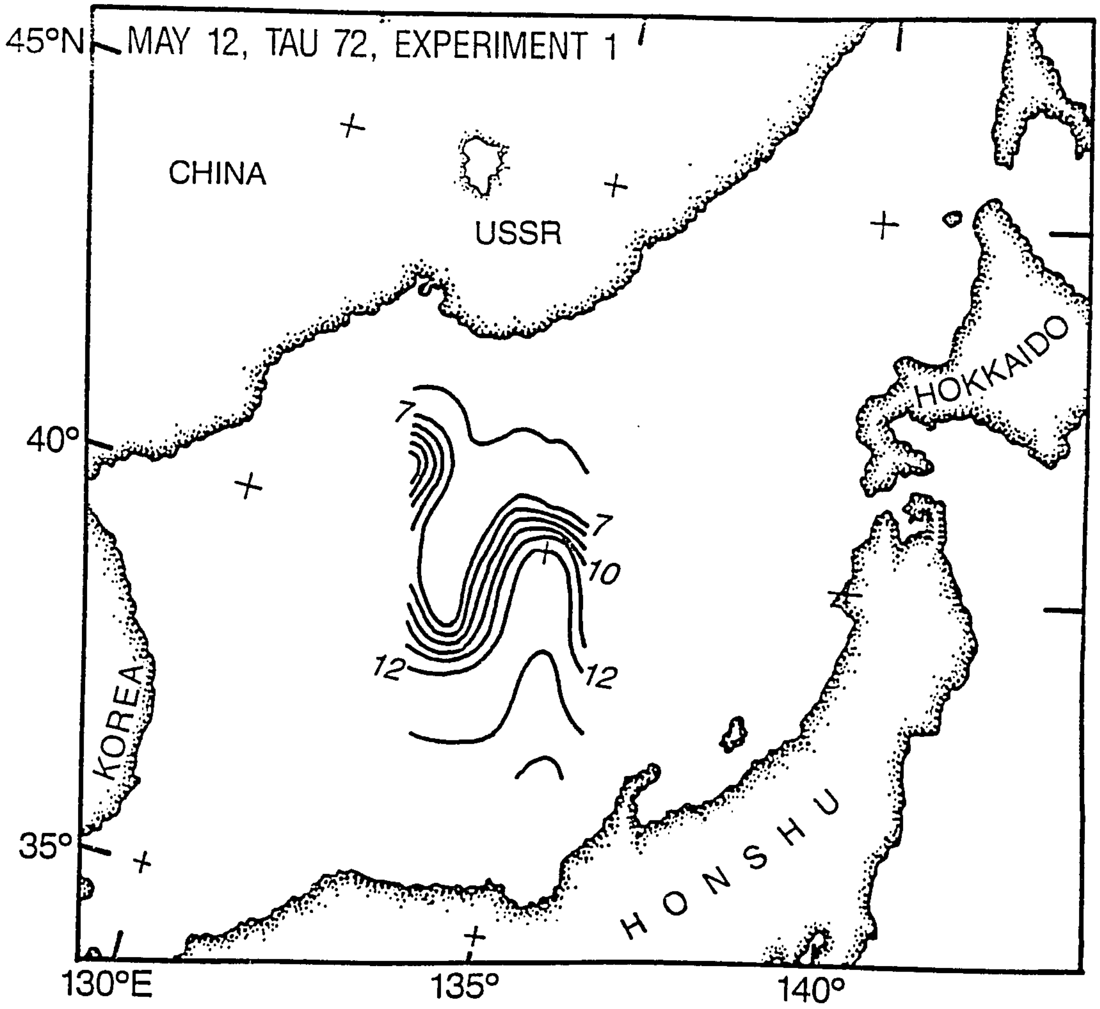

Figure 49a. Forecast SST (°C), experiment 1, May 12, 1984, TAU 72.

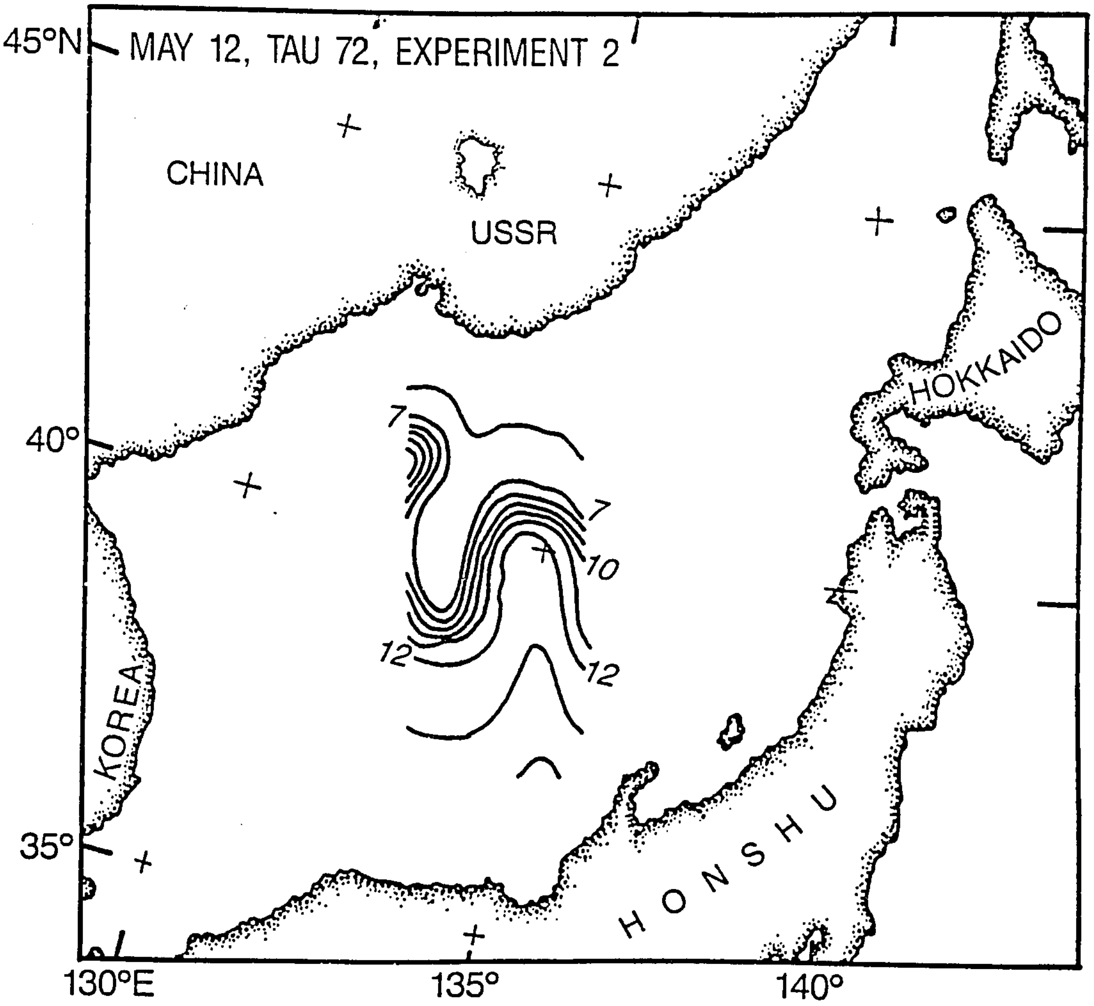

Figure 49b. Forecast SST (°C), experiment 2, May 12, 1984, TAU 72.

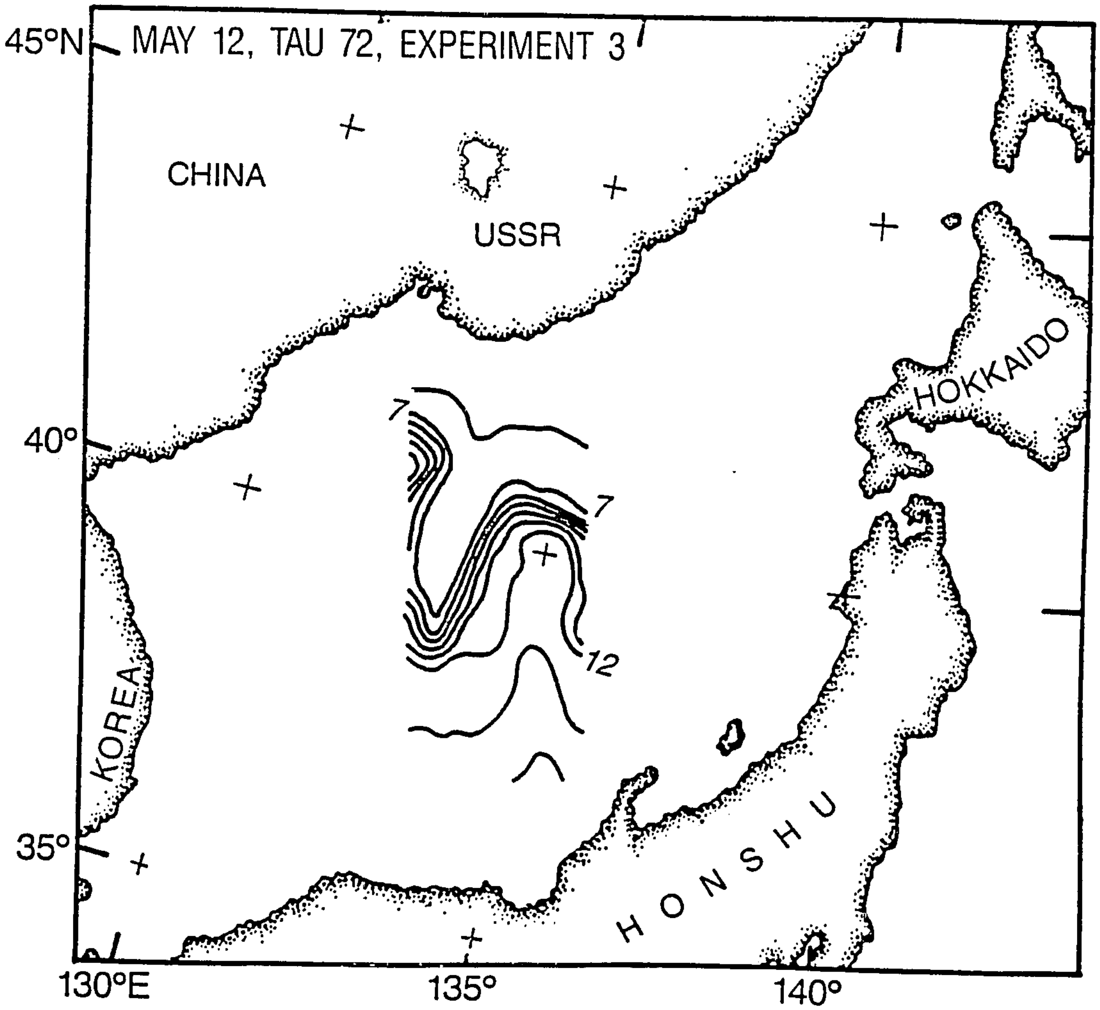

Figure 49c. Forecast SST (°C), experiment 3, May 12, 1984, TAU 72.

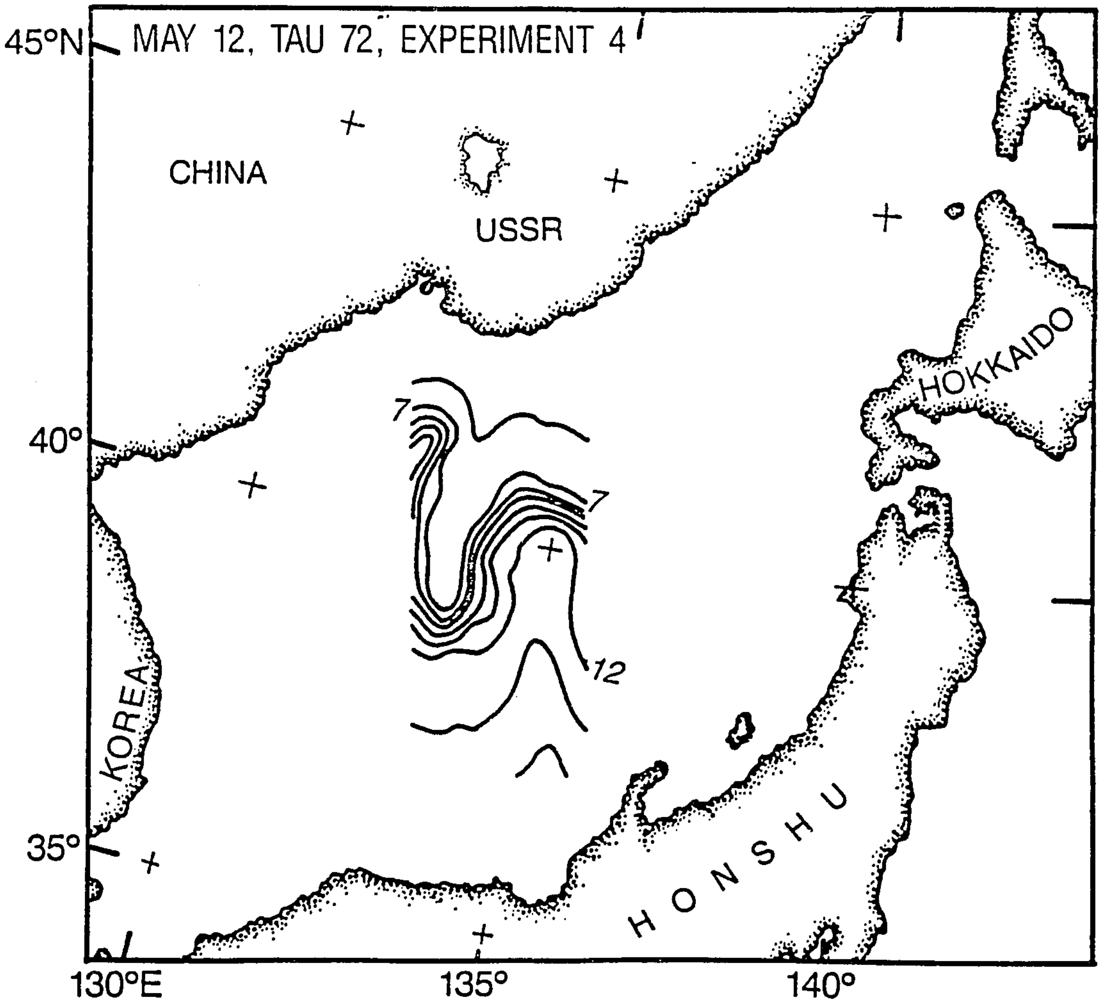

Figure 49d. Forecast SST (°C), experiment 4, May 12, 1984, TAU 72.

Experiment 2, which includes wind-drift advection and diffusion shows some packing of the isotherms at the front primarily in the center portion of our field of view. Figures 50a-d illustrate the surface pressure and wind speed and direction from NOGAPS used for this forecast. Note the extratropical cyclone that passes from the southwest toward the northeast through the lower portion of the grid during this period. This provides a wind field capable of driving Ekman flow causing the isotherm packing seen in figure 49b. The addition of nowcast advection accentuates this packing via the advection of warmer water from the south. Recall that the streamlines from the nowcast advection will basically appear as the isotherms do in figure 48. Figure 49d shows the effect of the forecast advection not so much by packing the isotherms relative to the Ekman forecast, but by causing kinks in the surface isotherms.

Figures 51a-d accentuate and support the above description by presenting the 72 hr SST change fields for experiments 1-4 respectively. Note the contour interval for these figures is 0.5°C.

Continuing in this vein, I present a series of vertical profiles for this same forecast period. Figure 52 again illustrates the May 12 initial SST field with four locations where I extract vertical temperature profiles.

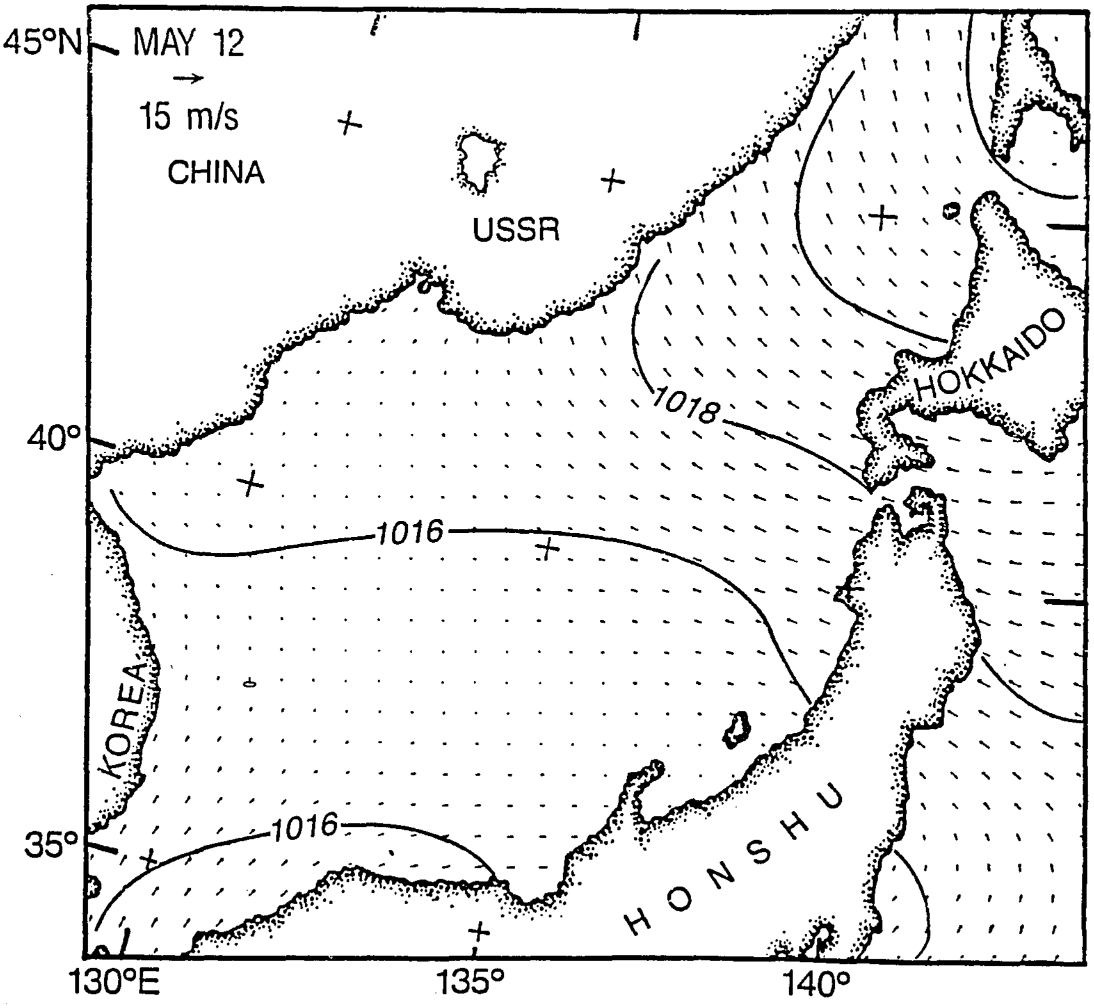

Figure 50a. Wind vectors (ms^{-1}) and sea level pressure (mb) from NOGAPS, May 12, 1984.

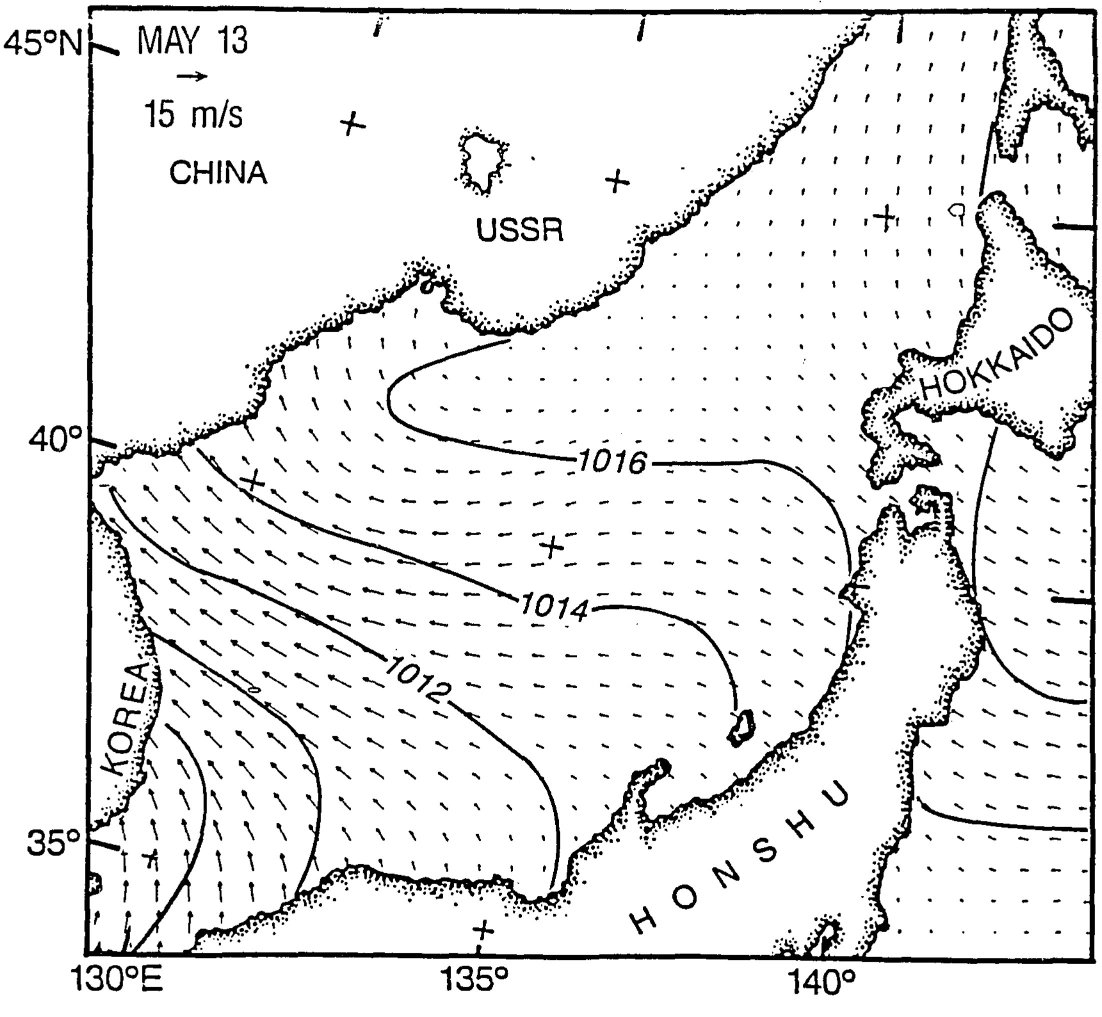

Figure 50b. Wind vectors (ms^{-1}) and sea level pressure (mb) from NOGAPS, May 13, 1984.

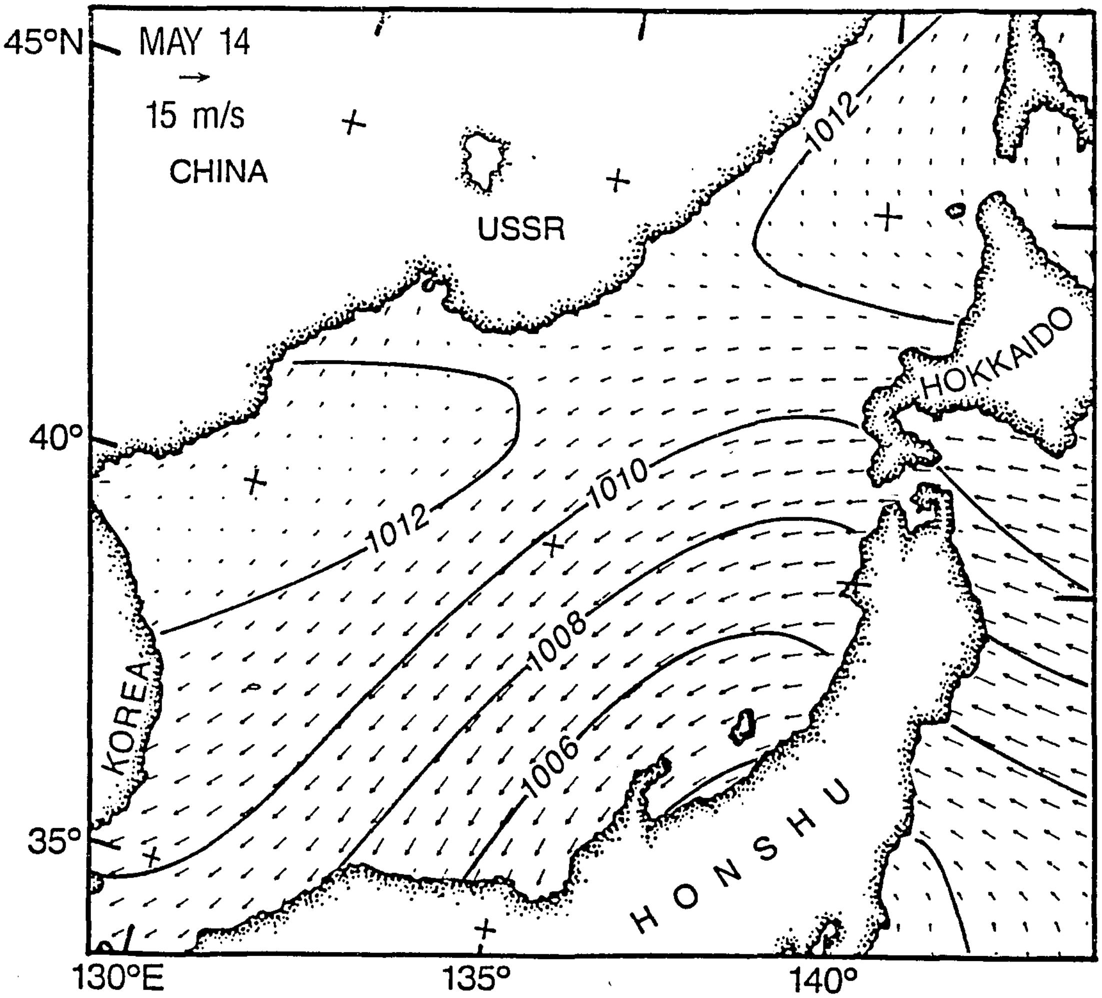

Figure 50c. Wind vectors (ms^{-1}) and sea level pressure (mb) from NOGAPS, May 14, 1984.

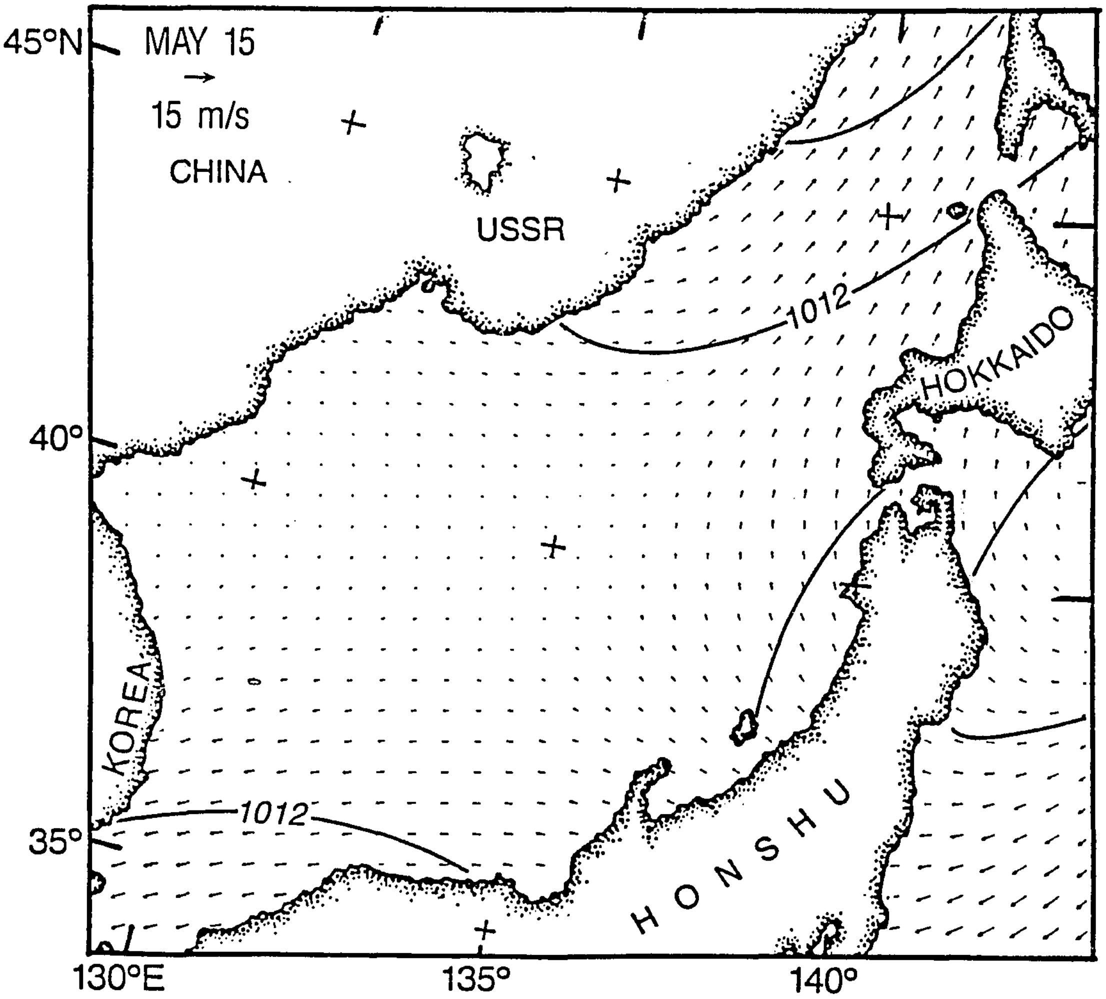

Figure 50d. Wind vectors (ms^{-1}) and sea level pressure (mb) from NOGAPS, May 15, 1984.

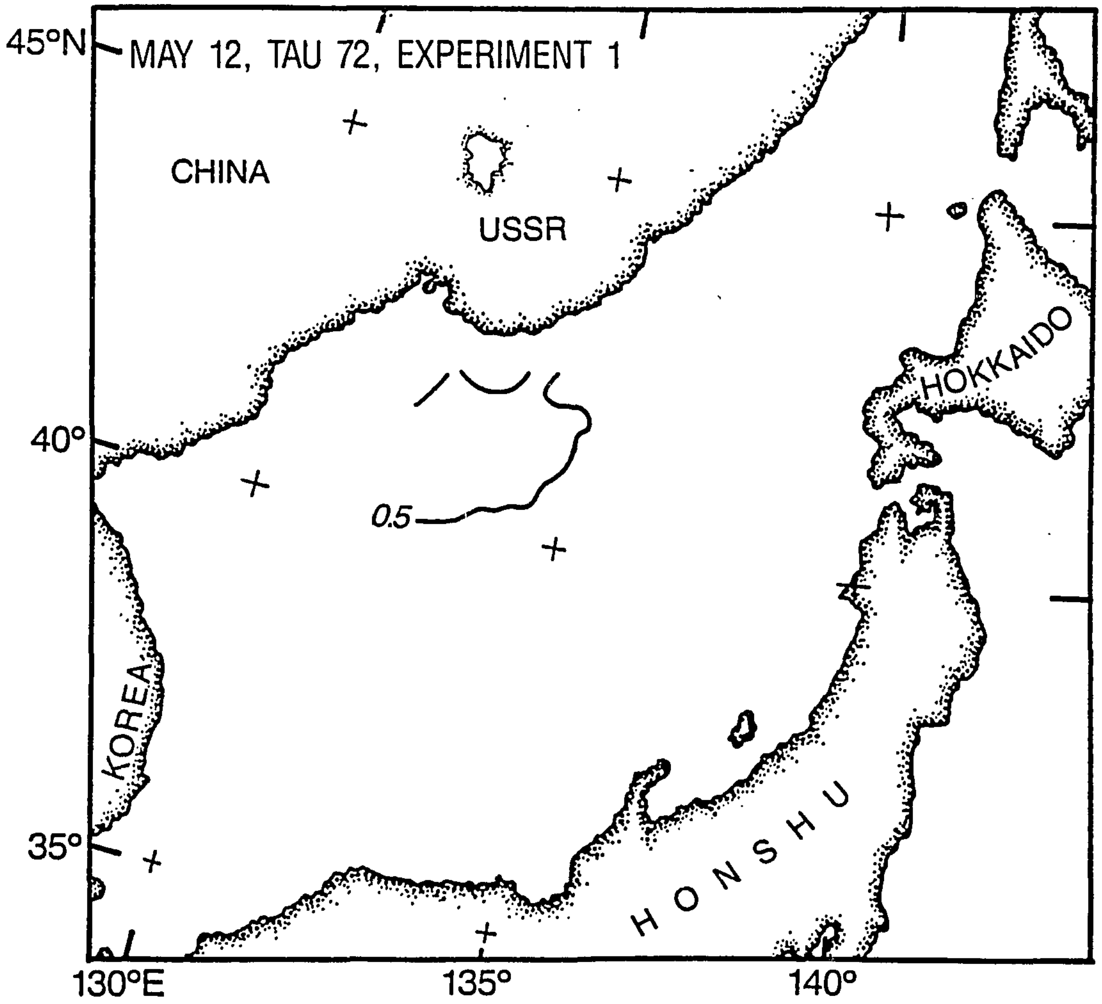

Figure 51a. Forecast SST change (contour = 0.5°C), experiment 1, May 12, 1984, TAU 72.

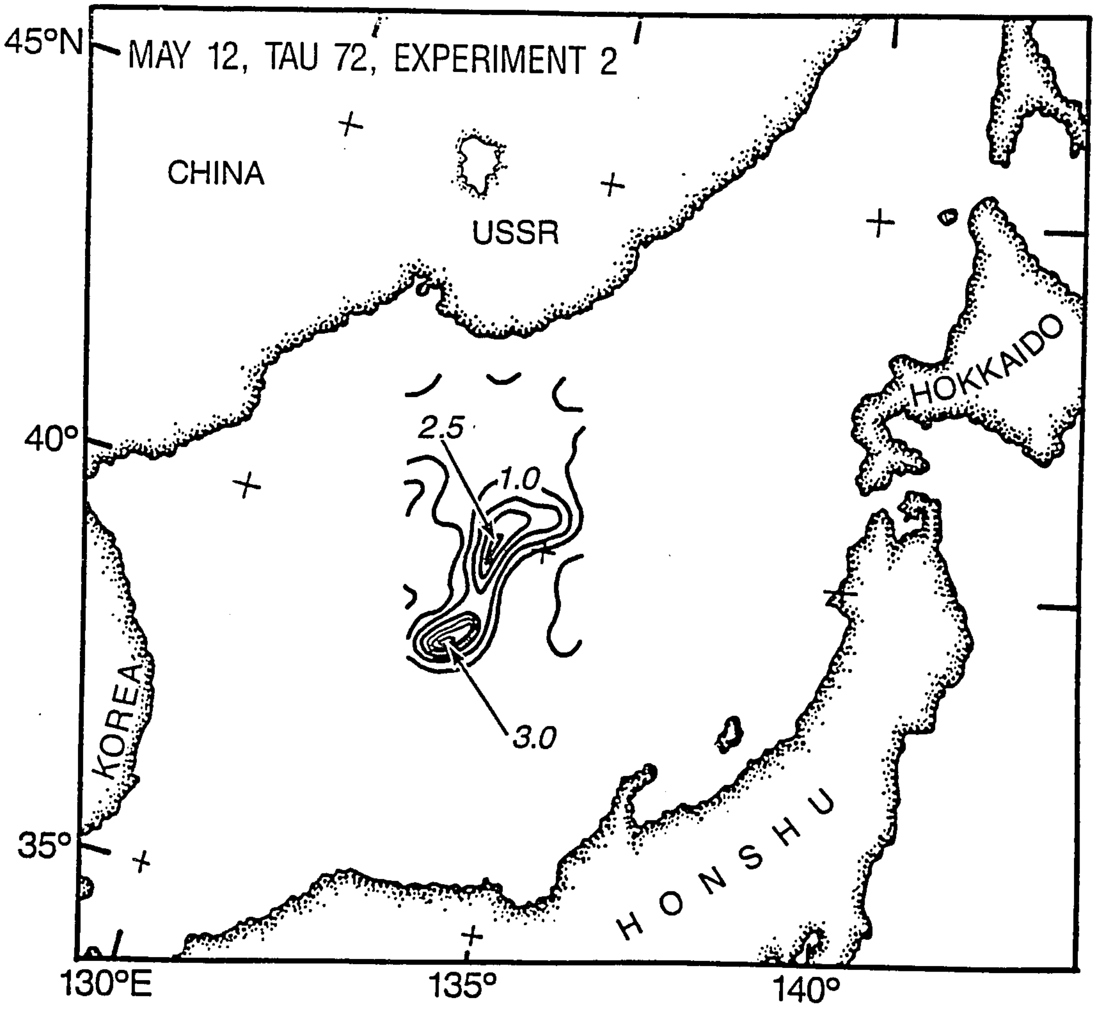

Figure 51b. Forecast SST change (contour = 0.5°C),
experiment 2, May 12, 1984, TAU 72.

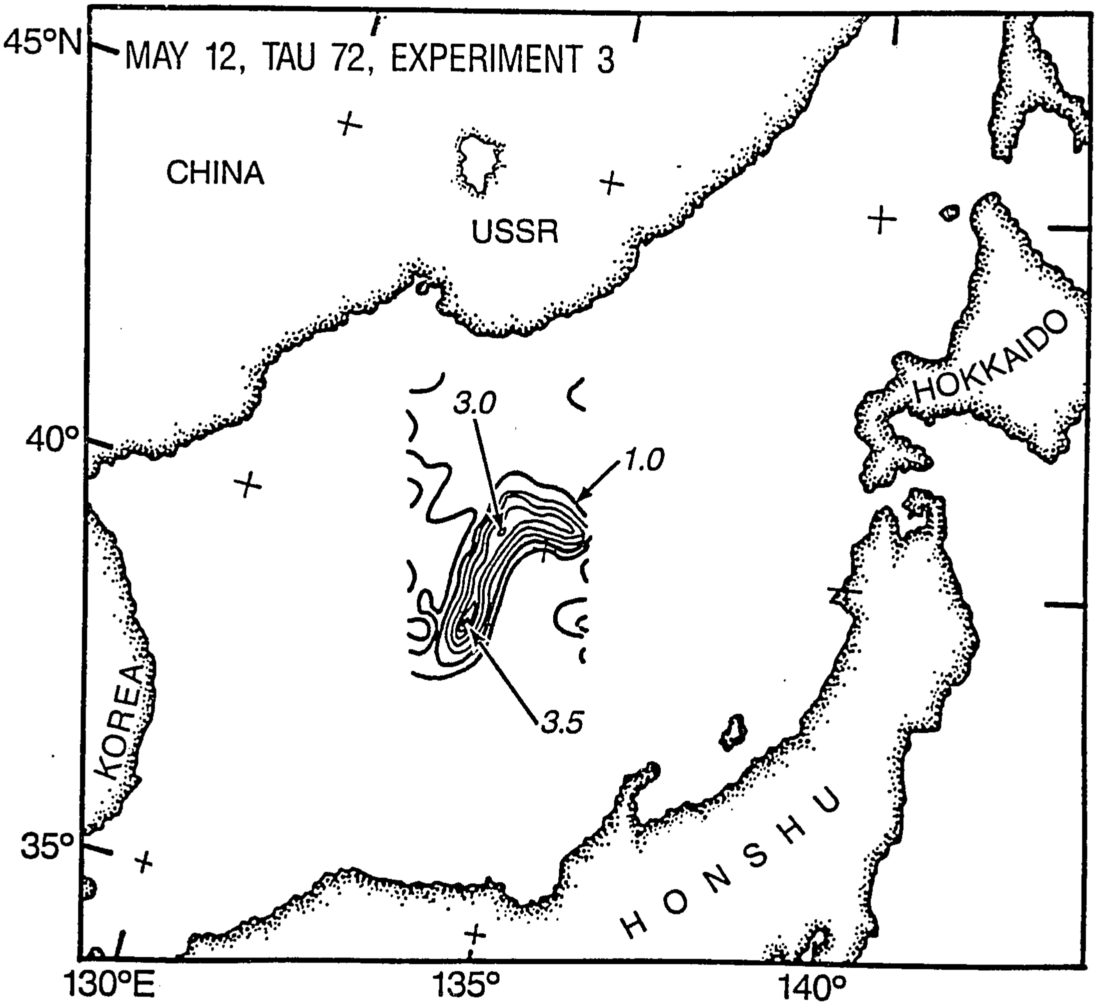

Figure 51c. Forecast SST change (contour = 0.5°C), experiment 3, May 12, 1984, TAU 72.

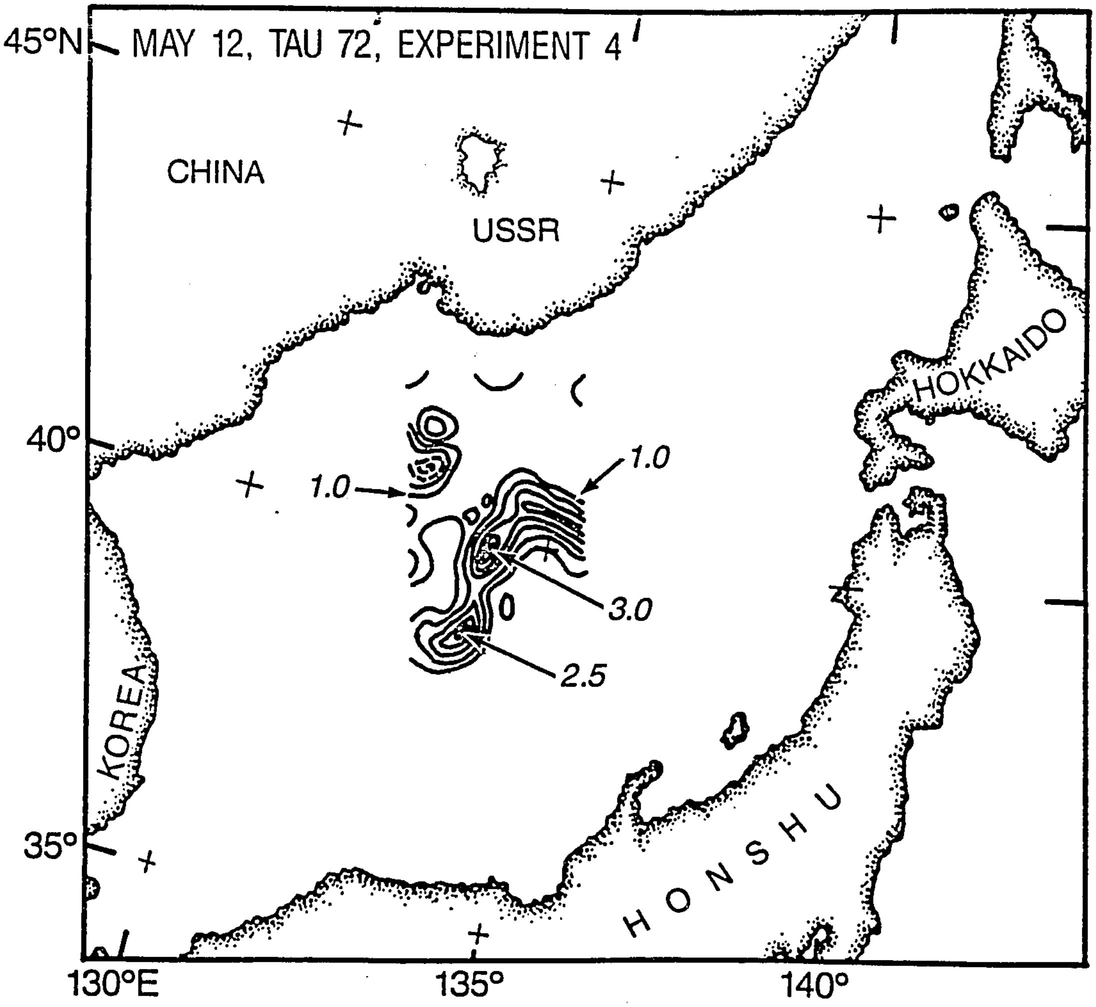

Figure 51d. Forecast SST change (contour = 0.5°C), experiment 4, May 12, 1984, TAU 72.

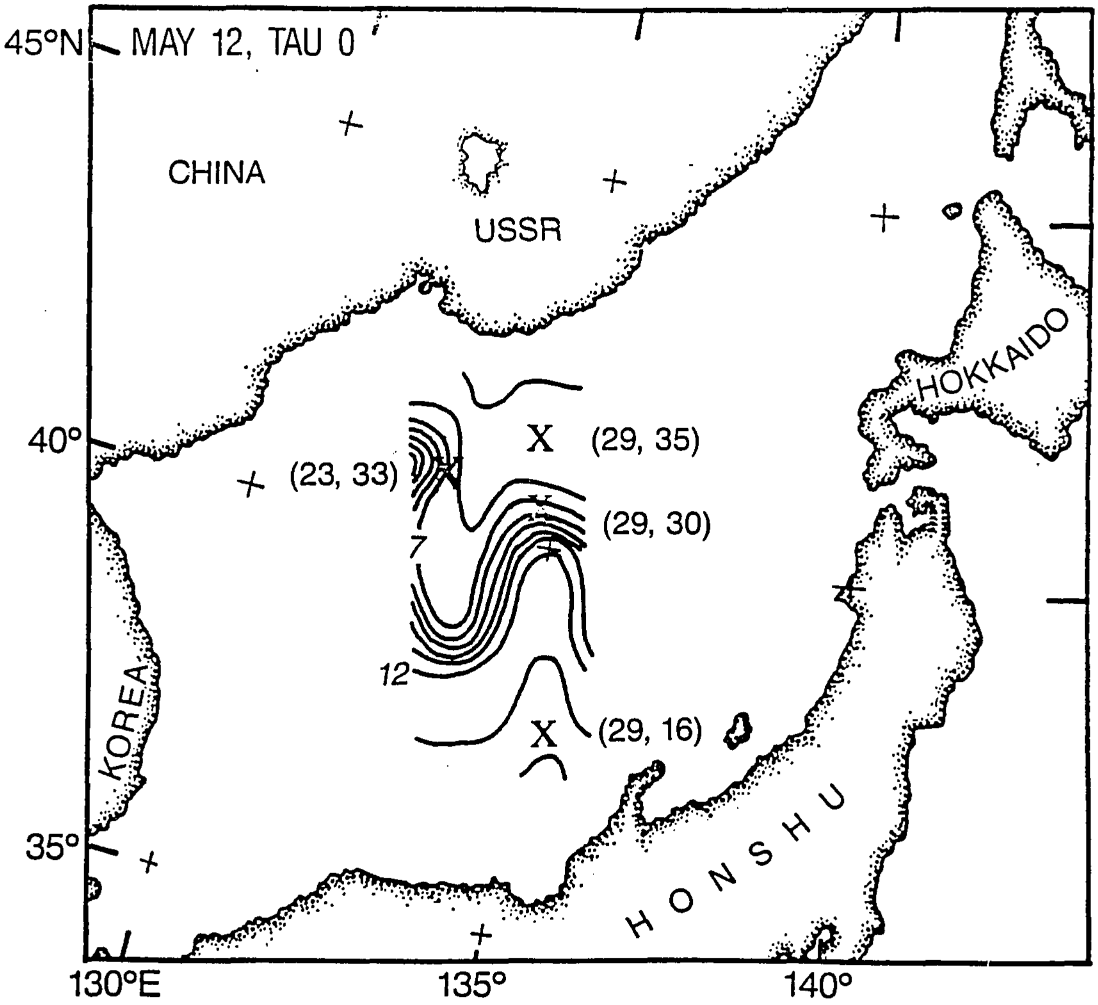

Figure 52. Initial condition SST (°C) for May 12, 1984, forecast identifying four specific grid point locations.

The profiles are denoted by model grid point where (29,16) is on the warm side, (29,35) is on the cold side, and (29,30) and (23,33) are in the frontal region. Consider first the warm side.

Figure 53 shows the evolution of the experiment 1 forecast through the 72 hr period. The forecast times (TAU) for 24, 48 and 72 hr are all shown with the TAU 0 profile superimposed on each. The forecasts are marked by (0), the TAU 0 profile by (x). The effects of the storm passage are evident. Surface warming occurs in the first 24 hours, warming continues through the second 24 hours but the increased wind is now beginning to mix it vertically. By 72 hr the warmed surface water has been mixed down to 17 m. The surface water has now cooled back to the initial temperature due to the entrainment of cooler, deeper water. Given that point (29,16) is away from the front, only weak horizontal temperature gradients exist and minimal geostrophic flow occurs. Given the weak horizontal temperature gradients, even an Ekman flow associated with the increased wind stress should make little difference to the forecast. Likewise, with minimal geostrophic flow, the geostrophic nowcast and forecasts should also be little changed. Figure 54 bears out this supposition demonstrating that the 72 hr experiment 2,3 and 4 vertical temperature profiles respectively, are little different from that for experiment 1.

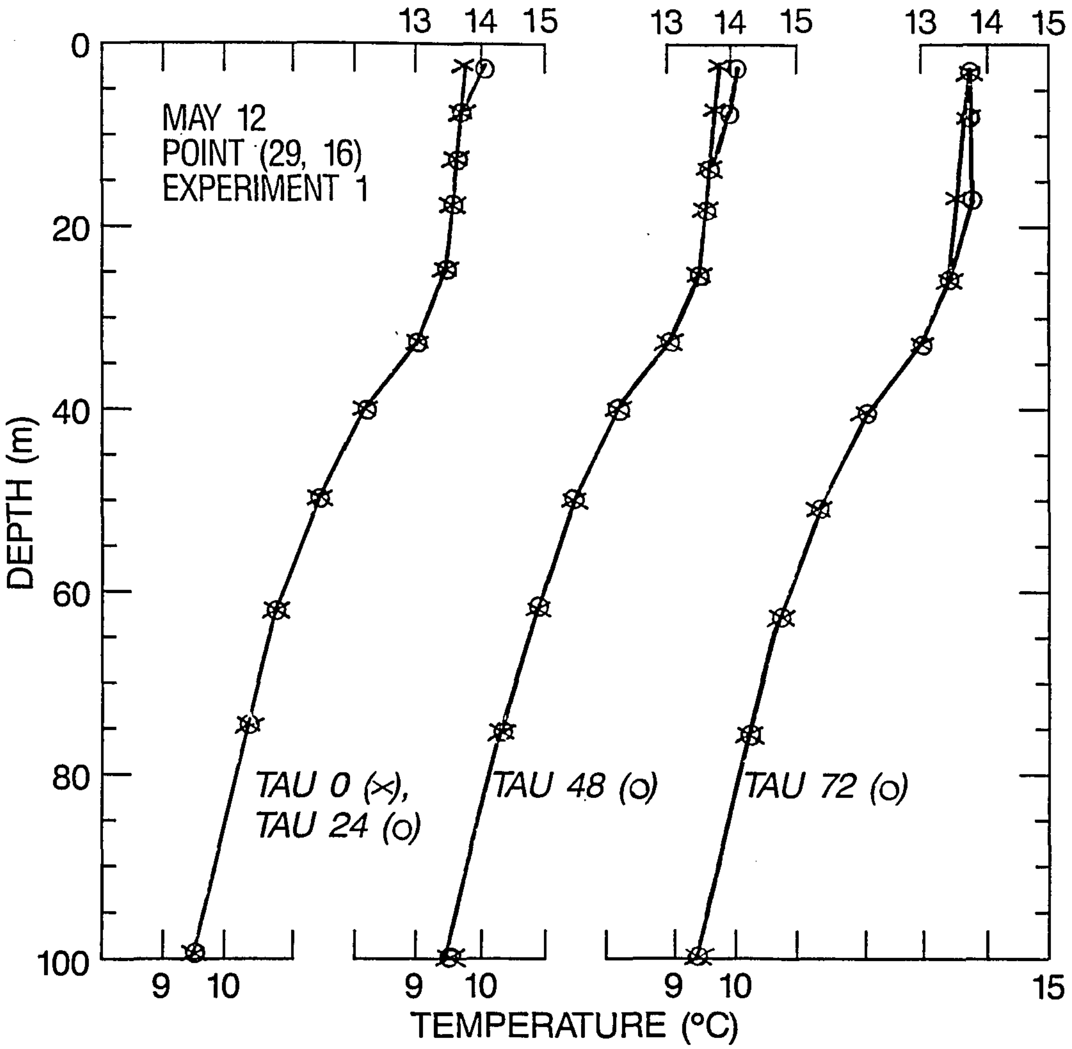

Figure 53. Experiment 1 temperature (°C) vs. depth (m) for May 12, 1984, warm side point (29,16), (x) TAU 0, (o) TAU 24, Tau 48, and TAU 72.

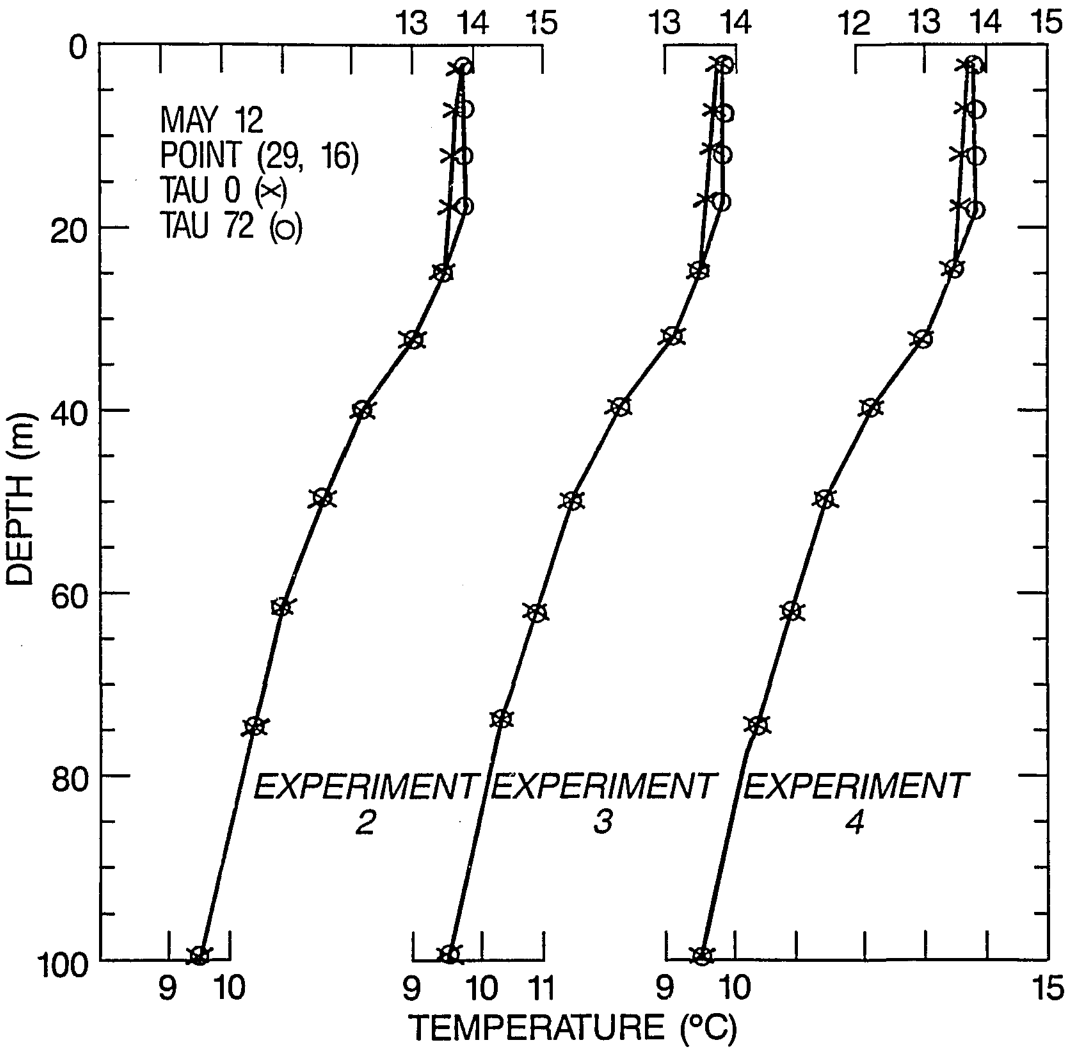

Figure 54. Experiment 2, experiment 3, and experiment 4 temperature (°C) vs. depth (m) for May 12, 1984, warm side point (29,16), (x) TAU 0, (o) TAU 72.

Bypassing the front for now, a similar result might also be expected at point (29,35) on the cold side of the front. Figure 55 shows the May 12, TAU 24, 48 and 72 hr forecasts for experiment 1. Here, however, only surface warming occurs with no apparent vertical mixing associated with the storm. Refering back to figure 44, one sees that the storm had a minimal effect this far north on the grid. Looking at figure 56 which gives the vertical temperature profiles for the May 12 TAU 72 hr forecast for experiments 2-4, they look similar to the experiment 1, TAU 72 profile on the previous figure. The one slight difference seems to be the slight warming at depth apparent in experiments 2-4. Since it occurs below the region of expected Ekman influence, this warming results from the horizontal diffusion common to these last three experiments. Proceeding to the frontal points, both the temperature gradients and geostrophic flows occur which one might expect to alter the different forecast profiles. Figure 57 shows the vertical profiles for TAU 24, 48 and 72 for the May 12 forecast but now at (29,30). The warming and vertical mixing again occur as at (29,16) but not as dramatically. This likely results from the combination of stronger vertical stratification at (29,30) relative to (29,16) in addition to the decreased wind forcing at (29,30) as well (again see figure 44).

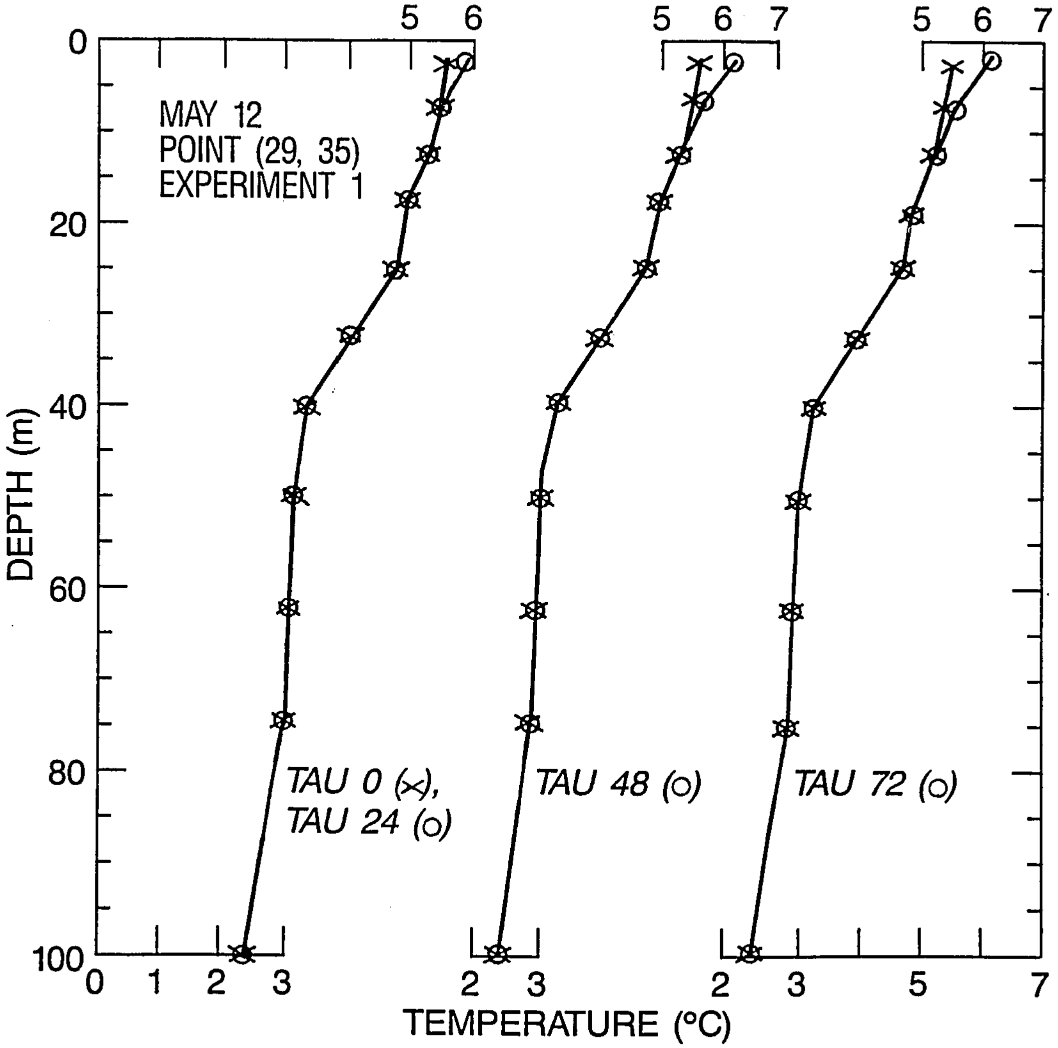

Figure 55. Experiment 1 temperature (°C) vs. depth (m) for May 12, 1984, cold side point (29,35), (x) TAU 0, (o) TAU 48, and TAU 72.

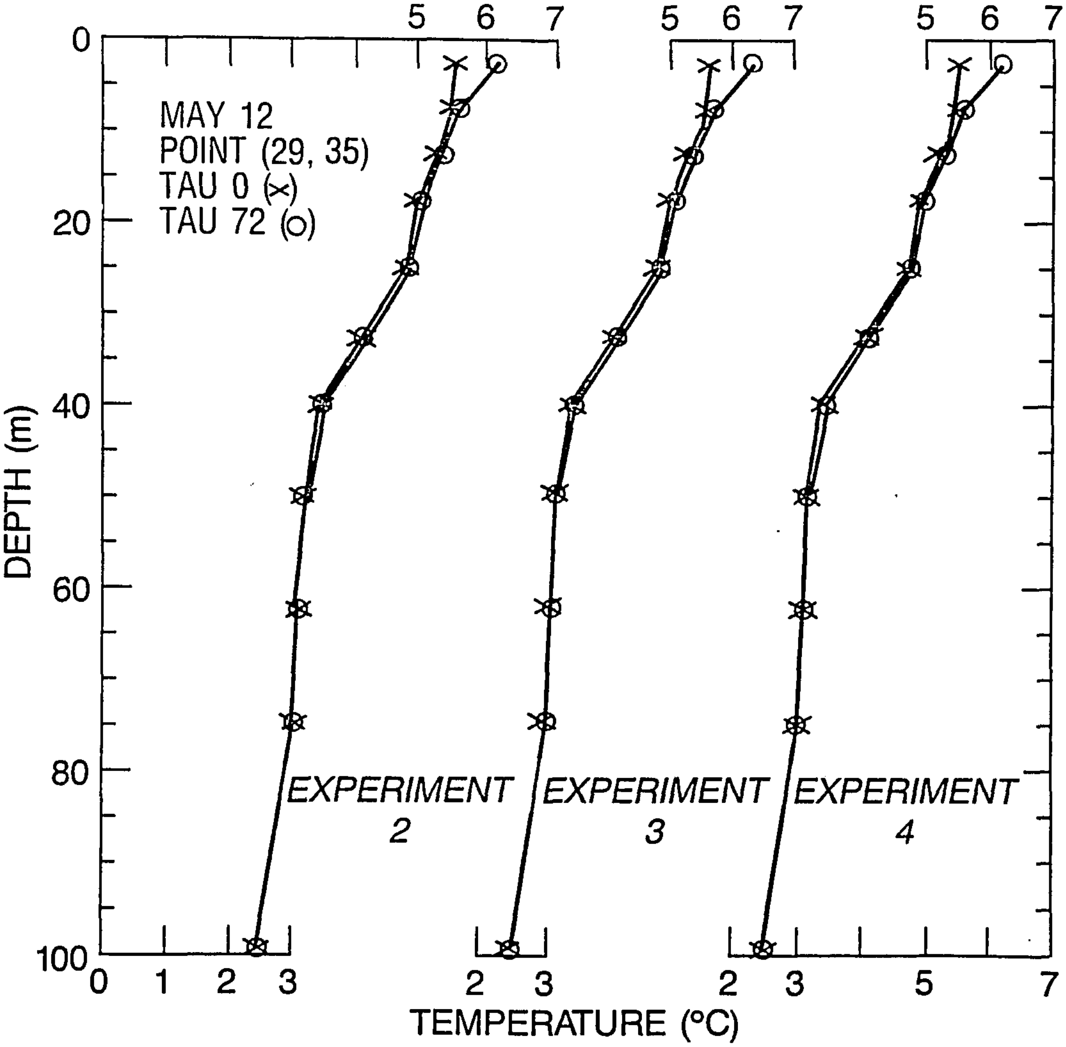

Figure 56. Experiment 2, experiment 3, and experiment 4 temperature vs. depth for May 12, 1984, cold side point (29,35), (x) TAU 0, (o) TAU 72.

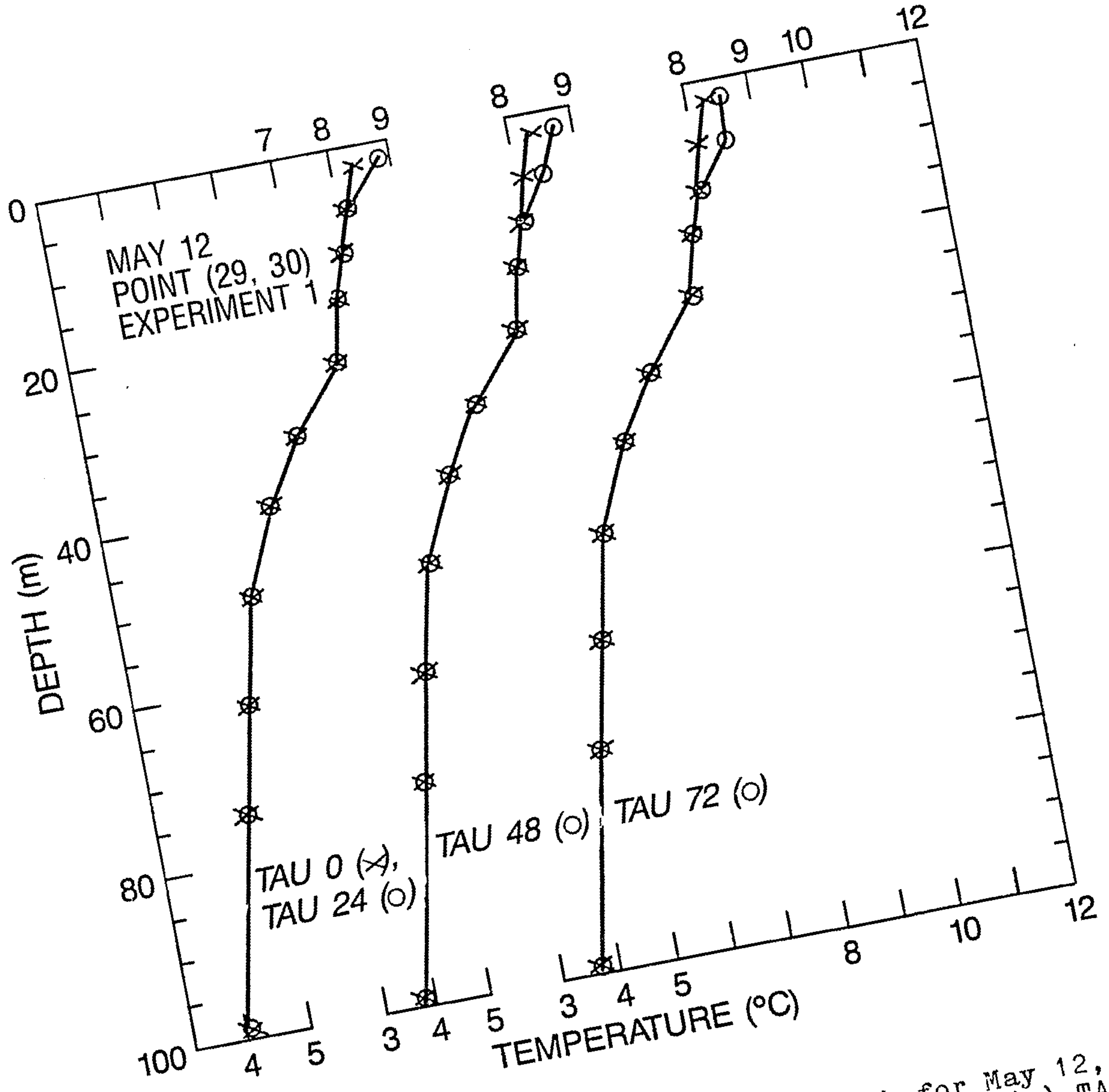

Figure 57. Experiment 1 temperature vs. depth for May 12, 1984, frontal point (29,30), (x) TAU 0, (o) TAU 24, TAU 48, and TAU 72.

Given the strong, horizontal, thermal gradient here, the comparable TAU 72 for experiment 2 shows a dramatic 2°C surface warming (figure 58). Adding the geostrophic nowcast shows the same surface warming with the addition of warming throughout the profile resulting from the geostrophic advection. Experiment 4 shows that the geostrophic forecast basically accentuates this warming throughout the profile.

Consider a final frontal point, (23,33), which provides a more dramatic example of differences between the different experiments. Figure 59 again provides the appropriate TAU 24, 48, and 72 hr forecast profiles for experiment 1. This evolution of the temperature structure appears quite similar to the cold water point (29,35) with simple surface warming. On figure 60, the experiment 2, TAU 72 forecast for this point shows an additional warming at depth due to horizontal diffusion. The direction of the temperature change (i.e. warming) is correct since this point is at the cold edge of the front. However, at the surface, less warming is observed relative to that for experiment 1 indicating the effects at the surface of Ekman advection. Experiment 3 (figure 60) shows that the addition of the geostrophic advection results in quite a different profile shape from experiment 2. The geostrophic flow apparently advects water from a slightly colder region which counteracts the diffusive warming effects at depth.

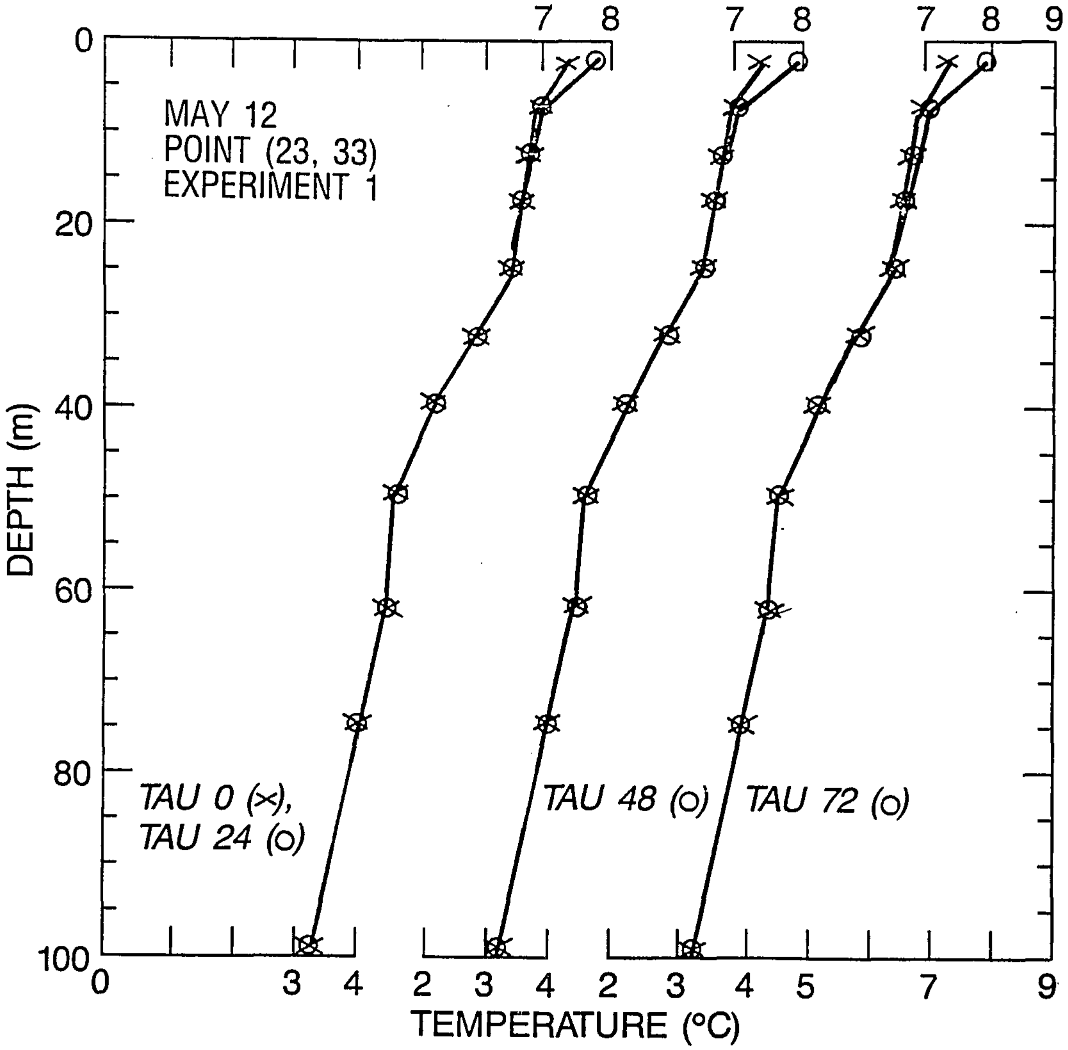

Figure 58. Experiment 2, experiment 3, and experiment 4 temperature vs. depth for May 12, 1984, frontal point (29,30), (x) TAU 0, (o) TAU 72.

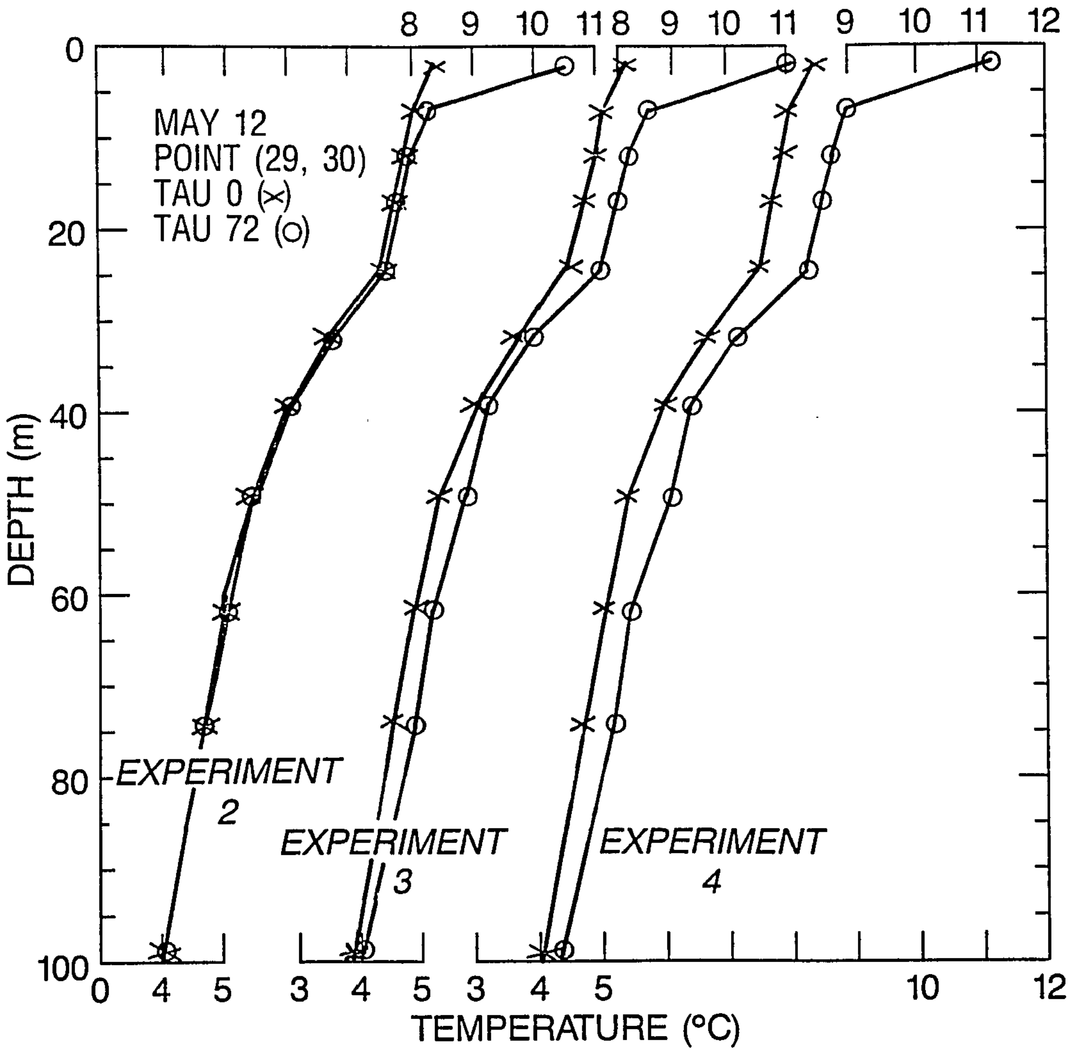

Figure 59. Experiment 1 temperature vs. depth for May 12, 1984, frontal point (23,33), (x) TAU 0, (o) TAU 24, TAU 48, and TAU 72.

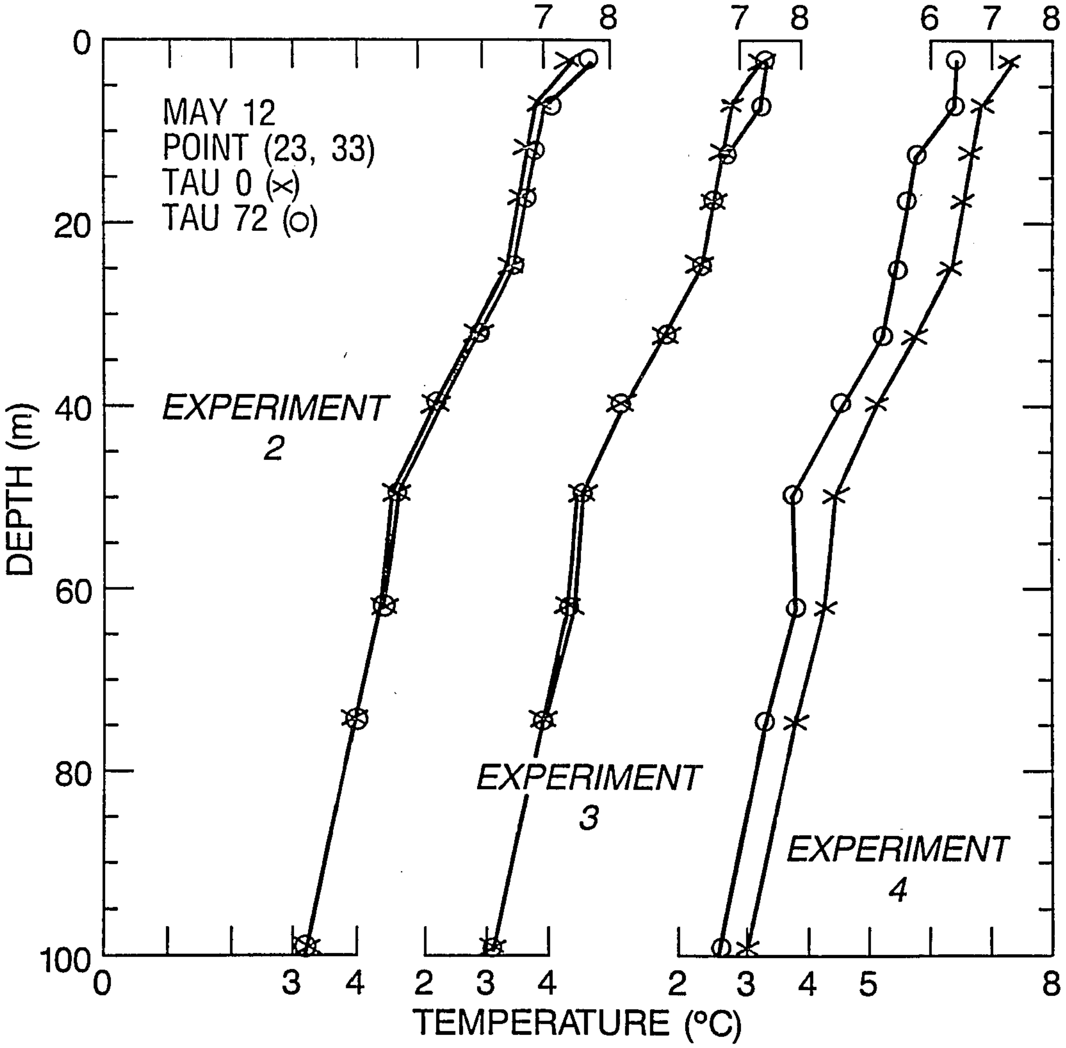

Figure 60. Experiment 2, experiment 3, and experiment 4 temperature vs. depth for May 12, 1984, frontal point (23,33), (x) TAU 0, (o) TAU 72.

At the surface, the combined effects of Ekman and geostrophic flow bring in a water mass that experienced some mixing. The TAU 72 forecast for experiment 4 shows a dramatic cooling relative to the other experiments throughout the profile. This is a result of unrealistic cross-stream advection. (I shall return to this point in a moment.)

To summarize, this entire sequence of figures, illustrating the variability within a single forecast, points out the difficulty of using overall or even regionally specific statistical calculations as sufficient measures in model comparisons. As I suggested earlier, the forecast user may be interested in specifically those features that appear in different places at different times which may become masked in statistical analyses of specific space and/or time groupings. Consider someone attempting to compute a high-frequency acoustic forecast. The 72-hr geostrophic nowcast at point (23,33) suggests the formation of a shallow surface duct during the three days. Neither the non-advective nor Ekman forecasts show this. Therefore, when performing operationally applicable model comparisons, one needs to consider if such aperiodic events are important and if so include some individual consideration of the outliers appearing on the scatterplots.

7.3. Potential Problem With Passive Advection

Recall figure 45 which demonstrates the variability of frontal position throughout the 28 day experimental period. In particular note that the change in frontal position from May 8 to May 15 indicates a large (order 100 km) eastward excursion in the northwest corner of the subgrid shown. Now consider figure 52 once again and note the position of (23,33). For the geostrophic forecast, the flow would initially follow the isotherms shown here. Through the duration of the forecast, however the flow (not the isotherms) would extend eastward in the northwest corner of the subgrid, just as the week 2, frontal excursion in figure 45. Therefore by the end of the May 12 forecast period, the geostrophic forecast would be advecting cold water toward (23,33). That is, an unrealistic cross-frontal advective flow is introduced in the experiment 4 results by not including the true dynamics for the geostrophic flow. Figure 51d and the experiment 4 profile on figure 60 illustrate the result. As noted in section 6, I included experiment 4 specifically to demonstrate the effects of unrealistic cross-frontal flow.

Experiment 4 does not truly simulate the passive mesoscale advective field available from the dynamic ocean models as outlined in the introduction. These dynamic models will provide the cross-isotherm flow allowing the thermal field to be advected. However, in the future,

operational upper-ocean, thermal forecasts will continue to rely heavily on thermal analyses for initial conditions. These thermal analyses will continue to rely on the combination of in-situ, satellite, and surface gradient information data as described in the introduction. Feature models and subsurface, altimeter-derived temperatures will likely also be included. Feature models are idealized front and eddy constructs inserted at the known locations of the surface gradients (BENNETT, CARNES and RIEDLINGER, 1987). The altimeter-derived subsurface temperatures will be derived and used as described by CLANCY (1986) and WILLIAMS, INNIS, and WHITE (1985). In these techniques, existing bathythermograph data will have extended usefulness in time due to altimetrically inferred changes in subsurface thermal structure.

The global, eddy-resolving, ocean circulation models will also use altimetric data but not necessarily as above. This is for two reasons. First these models don't require as much vertical resolution to describe the vertical structure required for accurate dynamic forecasts. Second, these models forecast HURLBURT (1984) Class 2 phenomena. Therefore, these models are more sensitive to initial conditions. This model sensitivity to initial conditions requires a less noisy initial condition than that used for the thermal forecast models above (HURLBURT, 1984). These global circulation forecasts will therefore tend to rely on the ocean models to dynamically assimilate the altimetrically-derived surface height into subsurface

information (HURLBURT, 1986). Other data sources (e.g., bathythermograph) should not be used for initialization and update unless it is quantitatively adequate to resolve the dynamic features (HURLBURT, 1984). On large regional or global domains, only altimetric data will likely provide the necessary subsurface information.

As a consequence, regional, upper-ocean, thermal forecasts and global and basin-scale, eddy-resolving, circulation forecasts will likely use different, not necessarily consistent initial conditions. An analagous result to that in figure 60 is thus possible unless one takes care that the thermal fields and initial circulation fields are consistent. One solution to this dilemma is to assure consistency by using the circulation model initial conditions (or forecast fields) to initialize the front and eddy locations in the thermal analysis.

Note that smaller regional models (order 1000 km x 1000 km) may not have as much of a problem since adequate data coverage, at times, may be available. Using dynamic data assimilation of both bathythermograph and infrared satellite imagery, ROBINSON(1986) and GLENN, ROBINSON, and SPALL(1987), have reported promising results. As noted earlier, the specification of the boundary conditions for these limited area models throughout the forecast remains a difficulty. For operational applications, the need for consistency between the circulation and the upper-ocean thermal structure at the initiation of the upper-ocean thermal forecast still stands.

8. SUMMARY AND CONCLUSIONS

8.1 Summary

In this study, I have attempted to evaluate one aspect in the evolutionary development of upper-ocean thermal forecast models. Specifically, I consider the impact of nowcast, geostrophic advection on upper-ocean thermal prediction in a frontal area. I carried out this work by means of a model comparison involving forecast simulations in the Sea of Japan.

Statistical comparisons for these particular simulations indicate that the inclusion of wind-drift advection plus horizontal diffusion provides (1) notable improvement relative to persistence forecasts and (2) moderate improvement over 1-dimensional, non-advective forecasts. In the immediate vicinity of the front, the inclusion of nowcast advection also improves the forecast further.

Subsequent individual forecast comparisons suggest that relying totally on a statistical comparison may not be sufficient when comparing models for operational applications. The needs of the forecast user must be considered since his interest may involve those events which are aperiodic in space and time and which thus may be masked by the statistical analysis.

One needs to include the individual examination of selected outlying points on the scatter plots.

A geostrophic forecast included in experiment 4 provides temporal changes to the flow but excludes the cross-frontal flow necessary to advect the thermal field consistently with the flow field. Unrealistic cross-frontal flow results. The results of this experiment, recommend caution in the future use of passive advection in upper-ocean forecasts. One must assure that the initial conditions for the thermal forecast are consistent with the passively provided mesoscale flow to avoid analogous artificial cross-frontal flow.

Where, in a general sense, are the next improvements and applications of upper-ocean forecast models expected? Beyond nowcast advection, the coupling (or merging) of upper-ocean thermal forecast models with eddy-resolving ocean circulation models will provide the next major advance in the capability of operational ocean forecast models. The impact on both high and low frequency acoustics should be considerable in regions of mesoscale variability. In atmospheric prediction, the merging of upper-ocean thermal forecast models and atmospheric general circulation models is a logical next step (Tom Rosmond, Naval Environmental Prediction Research Facility, personal communication). This atmosphere-ocean model can contain the direct coupling necessary to provide the interactive, ocean-atmosphere feedback expected on the diurnal to 5-day time scale. Finally, the potential exists to couple the

upper-ocean forecast models with biological models such as phytoplankton response models (e.g., DITORO et al, 1977). The capability to forecast regions of high primary productivity could significantly aid real-time fisheries by locating probable accumulations of predator species higher in the food chain. A secondary benefit to the ocean models themselves would be a potential source of validation data tied to satellite resources such as the Ocean Color Imager (Satellite Planning Committee of Joint Oceanographic Institutions Incorporated, 1985).

8.2 Recommendations

This study contains several shortcomings. The lack of adequate verification data forces reliance on synthetic initial conditions. This lack also forces the study into model/model versus model/data comparisons. Additionally, the model itself does not contain all the necessary physics nor resolution which might be desirable in this sort of study. In future studies addressing potential directions in the evolutionary development of upper-ocean forecast systems, what route should one take?

The first recommendation is for the execution of a series of data collection efforts specifically designed to test and evaluate upper-ocean thermal forecast models. Previous efforts have not provided the combination of spatial and temporal coverage necessary for just such tests. As a general experimental design, one might

consider a sequence of air-expendable bathythermograph surveys in a dynamically active region. These surveys would attempt to synoptically sample boxes of from 200 to 1000 km on a side with 10-20 km horizontal spacing. These surveys would also try to closely bracket several of the aperiodic events (e.g., storm passage, eddy-shedding) where the upper-ocean models are expected to have an impact. These surveys would be complemented by in-situ instrumentation providing long-term (˜ year) time series of oceanic temperature, salinity and current as well as surface fluxes, all at several locations within the survey area. Satellite infrared and sea-surface height data could provide important additional information as to front and eddy locations as well as SST validation data.

Given the cost of such surveys, adequate verification data for regional, several-day, upper-ocean forecasts will likely always be limited. Thus the development of a state-of-the-art fully hydrodynamic/thermodynamic model should also be a goal. One should not, however, expect this model to be the operational model for two reasons. The real-time data base will probably never support it and the operational computer power will likely not support full global coverage for such a model. Note that the evolutionary approach was initially adopted for the same reasons. This model could be applied, however, to existing semi-enclosed regions (Sea of Japan, Gulf of Mexico, Bering Sea, Mediterranean Sea) where it can fit on existing research computers allowing many test runs. This model

would be evaluated with all existing data sets. This model could then generate benchmark data sets required to test those ideas and models proposed for operational use under simulated operational forecast conditions.

REFERENCES

ADAMEC, D., R. L. ELSBERRY, R. W. GARWOOD and R. L. HANEY (1981) An embedded mixed-layer-ocean circulation model. Dynamics of Atmospheres and Oceans, 6, 69-96.

ADAMEC, D. and R. W. GARWOOD, JR. (1985) The simulated response of an upper-ocean density front to local atmospheric forcing. Journal of Geophysical Research, 90, 917-928.

ARAKAWA, A. and V. R. LAMB (1977) Computational design of the basic dynamical processes of the UCLA general circulation model. In Methods in Computational Physics, Vol. 17, Academic Press, Inc., New York.

BENNETT, T. J., M. J. CARNES and L. M. RIEDLINGER (1987) Incorporation of a front and eddy map into optimal estimation-based thermal analyses: Preliminary results. NORDA Technical Report, in preparation.

BUDD, B.W. (1980) Prediction of the spring transition,and related sea-surface temperature anomalies. M. S. thesis, Naval Postgraduate School, Monterey, CA, 95 pp.

CAMP, N. T. and R. L. ELSBERRY (1978) Oceanic thermal response to strong atmospheric forcing. II. The role of one-dimensional processes. Journal of Physical Oceanography, 8, 215-224.

CLANCY, R. M. (1982) The expanded ocean thermal structure (EOTS) analysis: Description, critique, and outlook. In: Ocean Prediction: The Scientific Basis and the Navy's Needs. Proceedings of the Ocean Prediction Workshop, Monterey, CA, Edited by and available from C. N. K. MOOERS, S. A. PIACSEK and A. R. ROBINSON, 229-235.

CLANCY, R. M. (1986) An overview of present and planned ocean thermal products at Fleet Numerical Oceanography Center. In: A Status and Prospectus Report on the Scientific Basis and the Navy's Needs. Proceedings of the Ocean Prediction Workshop, Phase I, Cambridge, MA, Phase II, Long Beach, MS, Edited by C. N. K. MOOERS, A. R. ROBINSON and J. D. THOMPSON. Available from the Institute for Naval Oceanography, NSTL, MS 39529, 335-343.

CLANCY, R. M. and P. J. MARTIN (1979) The NORDA/FLENUMOCEANCEN thermodynamical ocean prediction system (TOPS): A technical description. NORDA Technical Note 54, Naval Ocean Research and Development Activity, NSTL Station, MS, 28 pp.

CLANCY, R. M. and P. J. MARTIN (1981) Synoptic forecasting of the oceanic mixed layer using the Navy's operational environmental data base: Present capabilities and future applications. Bulletin of the American Meteorological Society, 62, 770-784.

CLANCY, R. M., P. J. MARTIN, S. A. PIACSEK and K. D. POLLAK (1981) Test and evaluation of an operationally capable synoptic upper-ocean forecast system. NORDA Technical Note 92, Naval Ocean Research and Development Activity, NSTL Station, MS, 66 pp.

CLANCY, R. M. and K. D. POLLAK (1983) A real-time synoptic ocean thermal analysis/forecast system. Progress in Oceanography, 12, 383-424.

CLANCY, R. M., K. D. POLLAK and J. M. HARDING (1983) Validation of ocean thermal models at Fleet Numerical Oceanography Center. In MDS '86, Proceedings of the Marine Data Systems International Symposium, New Orleans, LA, 332-337.

CONLON, D. M. (1981) Dynamics of flow in the region of the Tsugaru Strait. Technical Report No. 312, Coastal Studies Institute, Louisiana State University, Baton Rouge, LA, 62 pp.

CULLEN, M. J. P. (1983) Current progress and prospects in numerical techniques for weather prediction models. Journal of Computational Physics, 50, 1-37.

CUSHMAN-ROISIN, B. (1981) Effects of horizontal advection on upper ocean mixing: A case of frontogenesis. Journal of Physical Oceanography, 11, 1345-1356.

DAVIS, R. E., R. DESZOEKE and P. NIILER (1981) Variability in the upper ocean during MILE. Part II: Modeling the mixed layer response. Deep Sea Research, 28A, 1453-1475.

DENMAN, K. L. and M. MIYAKE (1973) Upper layer modification at Ocean Station Papa: Observations and simulation. Journal of Physical Oceanography, 3, 185-186.

DESZOEKE, R. A. (1980) On the effects of horizontal variability of wind stress on the dynamics of the ocean mixed layer. Journal of Physical Oceanography, 10, 1439-1454.

DITORO, D. M., R. V. THOMANN, D. J. O'CONNER and J. L. MANCINI (1977) Estuarine phytoplankton biomass models _ Verification analyses and preliminary applications. In, The Sea. Edited by E. D. Goldberg, J. N. McCave, J. J. O'Brien, and J. H. Steele,Wiley-Interscience, New York, pp. 969-1020.

DIXON, W. L., and F. J. MASSEY, JR. (1969) _Introduction to statistical analysis_. McGraw-Hill, 638 pp.

ELSBERRY, R. L. and N. T. CAMP (1978) Oceanic thermal response to strong atmospheric forcing. I. Characteristics of forcing events. _Journal of Physical Oceanography_, 8, 206-214.

ELSBERRY, R. L. and R. W. Garwood (1980) Numerical ocean prediction models- Goals for the 1980s. _Bulletin of the American Meteorological Society_, 61, 1556-1566.

ELSBERRY, R. L. and S. D. RANEY (1978) Sea surface temperature response to variations in atmospheric wind forcing. _Journal of Physical Oceanography_, 8, 881-887.

ERIKSEN, C. C. (1987) Observations of the seasonal cycle of upper ocean structure and the roles of advection and diapycnal mixing. _Journal of Geophysical Research_, 92, 5354-5368.

FRIEDRICH, H. and S. LEVITUS (1972) An approximation to the equation of state for sea water, suitable for numerical ocean models. _Journal of Physical Oceanography_, 2, 514-517.

FRIEHE, C. A. and S. E. PAZAN (1978) Performance of an air-sea interaction buoy. Journal of Applied Meteorology, 17, 1488-1497.

GALLACHER, P. C. (1979) Preparation of ocean model forcing parameters from FNWC atmospheric analysis and model predictions. Technical Report NPS63-79-005, Naval Postgraduate School, Monterey, CA, 24 pp.

GARRATT, J. R. (1977) Review of drag coefficients over oceans and continents. Monthly Weather Review, 105, 915-929.

GARWOOD, R. W., JR. (1979) Air-sea interaction and dynamics of the surface mixed layer. Reviews of Geophysics and Space Physics 17, 1507-1524.

GLENN, S., A. ROBINSON, and M. SPALL (1987) Recent results from the Harvard Gulf Stream forecasting program. Oceanographic Monthly Summary, 7, 3 and 12-13.

HANEY, R. L. (1974) A numerical study of the response of an idealized ocean to large-scale surface heat and momentum flux. Journal of Physical Oceanography, 4, 145-167.

HAWKINS, J. D. (1985) Multichannel sea surface temperature retrievals for Navy utilization. NORDA Technical Note 312, Naval Ocean Research and Development Activity, NSTL Station, MS, 10 pp.

HAWKINS, J. D., J. M. HARDING, J. R. CHASE, R. M. CLANCY and B. L. SAMUELS (1986) The impact of satellite infrared sea surface temperatures on FNOC ocean thermal analyses. NORDA Technical Report 142, Naval Ocean Research and Development Activity, NSTL Station, MS, 38 pp.

HOLL, M. M. and B. R. MENDENHALL (1971) Fields by information blending, sea-level pressure version. Technical Report M-167, Meteorology International Incorporated, Monterey, CA, 71 pp.

HOLL, M. M., M. J. CUMING and B. R. MENDENHALL (1979) The expanded ocean thermal structure analysis system: A development based on the fields by information blending methodology. Technical Report M-241, Meteorology International Incorporated, Monterey, CA, 216 pp.

HORTON, C. (1984) Surface front displacement in the Gulf Stream by Hurricane/Tropical Storm Dennis. Journal of Geophysical Research, 89, 2005-2012.

HUH, O. K. (1982) Spring season flow of the Tsushima Current and its separation from the Kuroshio: Satellite evidence. Journal of Geophysical Research, 87, 9687-9693.

HURLBURT, H. E. (1984) The potential for ocean prediction and the role of altimeter data. Marine Geodesy, 8, 17-66.

HURLBURT, H. E. (1986) Dynamic transfer of simulated altimeter data into subsurface information by a numerical ocean model. Journal of Geophysical Research, 91, 2372-2400.

HURLBURT, H. E. (1986) The ocean prediction problem and its diversity: Some issues and possible solutions. In: A Status and ProspectusReport on the Scientific Basis and the Navy's Needs. Proceedings of the Ocean Prediction Workshop, Phase I, Cambridge, MA, Phase II, Long Beach, MS, Edited by C. N. K. MOOERS, A. R. ROBINSON and J. D. THOMPSON. Available from the Institute for Naval Oceanography, NSTL, MS 39529, 192-226.

HURLBURT, H. E. and J. D. THOMPSON (1980) A numerical study of Loop Current intrusions and eddy shedding. Journal of Physical Oceanography, 10, 1611-1651.

KURASAWA, Y., K. HANAWA and Y. TOBA (1983) Heat balance of the surface layer of the sea at coean weather station T. Journal of the Oceanographical Society of Japan, 39, 192-202.

JERLOV, N. G. (1968) Optical oceanography. Elsevier, 352 pp.

JOYCE, T. M., R. H. KASE and W. ZENK (1980) Horizontal advection of temperature in the seasonal thermocline during JASIN 1978. Journal of Physical Oceanography, 10, 1686-1690.

KAWABE, M. (1982a) Branching of the Tsushima Current in the Japan Sea: Part I. Data analysis. Journal of the Oceanographical Society of Japan, 38, 95-107.

KAWABE, M. (1982b) Branching of the Tsushima Current in the Japan Sea: Part II. Numerical Experiment. Journal of the Oceanographical Society of Japan, 38, 183-192.

MARTIN, P. J. (1982) Mixed-layer simulation of buoy observations taken during Hurricane Eloise. Journal of Geophysical Research, 87, 409-427.

MARTIN, P. J. (1985) Simulation of the mixed layer at OWS November and Papa with several models. Journal of Geophysical Research, 90, 903-916.

MARTIN, P. J. (1987) Testing of a shipboard thermal forecast model. In preparation.

MARTIN, P. J., J. M. HARDING, J. D. HAWKINS and R. M. CLANCY (1985) The FNOC TOPS/TEOTS ocean thermal forecast/analysis system. Naval Research Reviews, 37, 3-7.

MELLOR, G. L. and P. A. DURBIN (1975) The structure and dynamics of the ocean surface mixed-layer. Journal of Physical Oceanography, 5, 718-725.

MELLOR, G. L. and T. YAMADA (1974) A heirarchy of turbulence closure models for planetary boundary layers. Journal of the Atmospheric Sciences, 31, 1791-1806.

MENDENHALL, B. R., M. J. CUMING and M. M. HOLL (1978) The expanded ocean thermal-structure analysis system users manual. Technical Report M-232, Meteorology International Incorporated, Monterey, CA, 110 pp.

MESINGER, F. and A. ARAKAWA (1976) Numerical methods used in numerical models. GARP Publication Series No. 17. World Meteorological Organization, Geneva, Switzerland, 64 pp.

MIHOK, W. F. and J. E. KAITALA (1976) U.S. Navy Fleet Numerical Weather Central operational five-level global fourth-order primitive-equation model. Monthly Weather Review, 104, 1527-1550.

MOOERS, C. N. K., S. A. PIACSEK and A. R. ROBINSON (1982) Ocean Prediction: The Scientific Basis and the Navy's Needs. Proceedings of the Ocean Prediction Workshop, Monterey, CA, 320 pp.

MOOERS, C. N. K., A. R. ROBINSON and J. D. THOMPSON (1986) Ocean Prediction Workshop 1986: A Status and Prospectus Report on the Scientific Basis and the Navy's Needs. Proceedings of the Ocean Prediction Workshop, Phase I, Cambridge, MA, Phase II, Long Beach, MS, 494 pp.

MORIYASU, S. (1972a) The Tsushima Current. In, Kuroshio-Its physical aspects. Edited by H. STOMMEL and K. YOSHIDA, Univ. Tokyo Press, Tokyo, pp.353-369.

MORIYASU, S. (1972b) On short-term fluctuations of the Tsushima Current to the northwest of the Noto Peninsula in October 1969. The Oceanographical Magazine, 24, 1-23.

MULLER, P., R. W. GARWOOD and J. P. GARNER (1984) Effect of vertical advection on the dynamics of the oceanic surface mixed layer. Annales Geophysicae, 2, 387-398.

OKUBO, A. and R. V. OZMIDOV (1970) Empirical dependence of the coefficient of horizontal turbulent diffusion in the ocean on the scale of the phenomenon in question. Bulletin (Izvestiya), Academy of Sciences, USSR, Atmospheric and Oceanic Physics, 6, No.5, 534-536.

PADUAN, J. D. and R. A. DESZOEKE (1986) Heat balances in the upper ocean at 50 N, 140 W during November 1980 (STREX). Journal of Physical Oceanography, 16, 25-38

POLLARD, R. T. and R. C. MILLARD (1970) Comparison between observed and simulated wind-generated inertial oscillations. Deep Sea Research, 17, 813-821.

POND, S. and G. L. PICKARD (1978) Introductory dynamic oceanography. Pergamon Press, Oxford, p 241.

PRELLER, R. H. (1986) A numerical model study of the Alboran Sea gyre. Progress in Oceanography, 16, 113-146.

PRICE, J. F., C. N. K. MOOERS and J. C. VAN LEER (1978) Observations and simulation of storm-induced mixed-layer deepening. Journal of Physical Oceanography, 8, 582-599.

ROBINSON, A. R. (1986) Recent experiments with Harvard open ocean model. In: A Status and Prospectus Report on the Scientific Basis and the Navy's Needs. Proceedings of the Ocean Prediction Workshop, Phase I, Cambridge, MA, Phase II, Long Beach, MS, Edited by C. N. K. MOOERS, A. R. ROBINSON and J. D. THOMPSON. Available from the Institute for Naval Oceanography, NSTL, MS 39529, 227-250.

RODEN, G. I. (1976) On the structure and prediction of oceanic fronts. Naval Research Reviews, 29, 18-35.

RODEN, G. I. and D. F. PASKAUSKY (1978) Estimation of rates of frontogenesis and frontolysis in the north Pacific Ocean using satellite and surface meteorological data from January 1977. Journal of Geophysical Research, 83, 4545-4550.

ROSMOND, T. E. (1981) NOGAPS: Navy operational global atmospheric system. Preprint Volume, Fifth Conference on Numerical Weather Prediction, Monterey, Published by the American Meteorological Society, Boston, 74-79.

SATELLITE PLANNING COMMITTEE (1985) Oceanography from space: A research strategy for the decade 1985-1995. Joint Oceanographic Institutions Incorporated, 2100 Pennsylvania Avenue, N.W., Washington, D.C., p. 15-20.

SHIM, T. (1986) The spatial and temporal variability of the Polar Front in the Sea of Japan. PhD. dissertation, Coastal Studies Institute, Louisiana State University, Baton Rouge, LA, 123 pp.

SHUTO, K. (1982) A review of sea conditions in the Japan Sea. La mer, 20, 119-124.

SONU, C. J. (1981) Survey of sea strait data around Japan. Technical Report No. 1, Tekmarine, Inc., Sierra Madre, CA, 700 pp.

STEVENSON, J. W. (1983) The seasonal variation of the surface mixed-layer response to the vertical motion of linear Rossby waves. Journal of Physical Oceanography, 13, 1255-1268

SVERDRUP, H. U., M. W. JOHNSON and R. H. FLEMING (1962) The oceans, their physics, chemistry, and general biology. Prentice Hall, New York, p 734.

TANIOKA, K. (1968) On the East Korean Warm Current (Tōsen Warm Current). The Oceanographical Magazine, 20, 31-38.

THOMPSON, R. O. (1976) Climatological numerical models of the surface mixed layer of the ocean. Journal of Physical Oceanography, 6, 496-503.

TOBA, Y., K. TOMIZAWA, Y. KURASAWA and K. HANAWA (1982) Seasonal and year-to-year variability of the Tshushima-Tsugaru warm current system with its possible cause. La mer, 20, 41-51.

URICK, R. J. (1983) Principles of underwater sound. Mcgraw-Hill, 423 pp.

WARN-VARNAS, A. W., R. M. CLANCY, M. L. MORRIS, P. J. MARTIN and S. HORTON (1982) Studies of large-scale thermal variability with a synoptic mixed-layer model. NORDA Technical Note 156, Naval Ocean Research and Development Activity, NSTL Station, MS, 34 pp.

WELLER, R. A. (1982) The relation of near-inertial motions observed in the mixed layer during JASIN (1978) experiment to the local wind stress and to the quasi-geostrophic flow field. Journal of Physical Oceanography, 12, 1122-1136.

WILLIAMS, G. O., G. E. INNIS and W. B. WHITE (1985) Role of GEOSAT altimetry in improving the performance of OTIS/TOPS at FNOC. Technical Report SAIC-85-1955, Science Applications International Corp., 1200 Prospect St., P.O. Box 2351, La Jolla, CA 92038, 65 pp.

WILLMOTT, C. J. (1981) On the validation of models. Physical Geography, 2, 184-194.

WILLMOTT, C. J. (1982) Some comments on the evaluation of model performance. Bulletin American Meteorological Society, 63, 1309-1313.

WILLMOTT, C. J., S. G. ACKLESON, R. E. DAVIS, J. J. FEDDEMA, K. M. KLINK, D. R. LEGATES, J. O'DONNELL, and C. M. ROWE (1985) Statistics for the evaluation and comparison of models. Journal of Geophysical Research, 90, 8995-9005.

YASUI, M., T. YASUOKA, K. TANIOKA and O. SHIOTA (1967) Oceanographic studies of the Japan Sea (1) Water characteristics. The Oceanographical Magazine, 19, 177-192.

YOON, J. H. (1982a) Numerical Experiment on the circulation in the Japan Sea, Part I. Formation of the East Korean Warm Current. Journal of the Oceanographical Society of Japan, 38, 43-51.

YOON, J. H. (1982b) Numerical Experiment on the circulation in the Japan Sea, Part II. Influence of seasonal variations in atmospheric conditions on the Tsushima Current. Journal of the Oceanographical Society of Japan, 38, 81-94.

YOON, J. H. (1982c) Numerical Experiment on the circulation in the Japan Sea, Part III. Mechanism of the nearshore branch of the Tsushima Current. Journal of the Oceanographical Society of Japan, 38, 125-130.

APPENDIX A

FINITE DIFFERENCE EQUATIONS

In the finite differencing of TOPS, spatial derivatives are all centered in space. In equations (1)-(4), time differencing is trapezoidal for the Coriolis and vertical advection terms, backward for the vertical eddy flux terms, and forward for all other terms. I now provide a more detailed outline of the differencing. I will present the differenced forms of equations (1) and (3) only since (2) and (4) can be directly inferred from them. I rewrite equations (1) and (3) below. I eliminate the overbars and use the turbulence parameterizations of equations 5 and 7 in order to simplify the notation. Variable definitions are given in section 4.1.

$$\overset{(a)}{\frac{\partial T}{\partial t}} = \overbrace{\frac{\partial}{\partial z}\left(K_H\frac{\partial T}{\partial z} + \nu\frac{\partial T}{\partial z}\right)}^{(b)} + \overset{(c)}{\frac{1}{\rho_w c}\,\frac{\partial F}{\partial z}} \overbrace{- \frac{\partial}{\partial x}(u_a T) - \frac{\partial}{\partial y}(v_a T)}^{(d)}$$

$$\overset{(e)}{- \frac{\partial}{\partial z}(w_a T)} + \overbrace{A\left(\frac{\partial^2 T}{\partial x^2} + \frac{\partial^2 T}{\partial y^2}\right)}^{(f)} \qquad \text{(A.1)}$$

(a) (b) (c) (d)

$$\frac{\partial u}{\partial t} = fv + \frac{\partial}{\partial z}\left(K_M\frac{\partial T}{\partial z} + \nu\frac{\partial u}{\partial z}\right) - Du \qquad (A.2)$$

Before I write out the finite difference forms of these equations, I present some details of the vertical and horizontal numerical grids in figures A1 and A2, respectively.

Vertical grid indices are denoted by the subscript k, x and y direction, horizontal grid indices by the subscripts i and j, respectively. From figure A1, note that T, S, u, and v are defined at the center of each slab with vertical grid positions designated ZM. The vertical eddy diffusion coefficients (K_M, K_H), vertical velocities (w), and downward fluxes of solar radiation (F) are defined at slab boundary points denoted by ZB. With the aid of figure A2, recall from section 4 that all of the above quantities are defined at the horizontal grid points shown on figure 5. Recall also that the u_a, v_a are defined on a staggered grid (shown dotted in figure A2).

For notational convenience, the absence of an i,j subscript implies the i,j location. Similarly in the vertical, the absence of a k subscript implies the k th vertical index. Time indexing is denoted by the superscript n; Δt represents the timestep used in the numerical integration. Note for the polar sterographic grid used for these experiments the lateral grid spacing is not exactly uniform.

.
.
.
.

ZB_{k-1} - - - - - - - - $K_{M_{k-1}}, K_{H_{k-1}}, w_{k-1}, F_{k-1}$ - - - - - - - -

ZM_{k-1} $T_{k-1}, S_{k-1}, u_{k-1}, v_{k-1}$

ZB_{k} - - - - - - - - $K_{M_{k}}, K_{H_{k}}, w_{k}, F_{k}$ - - - - - - - -

ZM_{k} $T_{k}, S_{k}, u_{k}, v_{k}$

ZB_{k+1} - - - - - - - - $K_{M_{k+1}}, K_{H_{k+1}}, w_{k+1}, F_{k+1}$ - - - - - - - -

ZM_{k+1} $T_{k+1}, S_{k+1}, u_{k+1}, v_{k+1}$

.
.
.
.

Figure A1 Vertical grid used in numerical solution of equations (1)-(4).

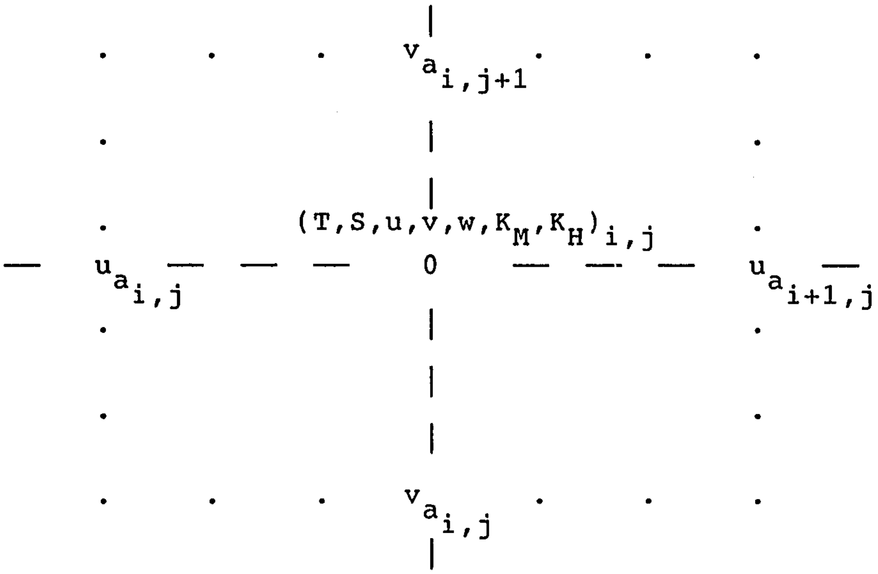

Figure A2 Horizontal grid at grid point (i,j), used in the numerical solution of equations (1)-(4).

This variability is included in TOPS but in order to simplify the notation, I use Δx and Δy to represent the x and y grid spacings. In finite difference form, equation A.1 then translates to the following at depth level ZM_k and horizontal position (i,j).

$$\frac{T^{n+1} - T^n}{\Delta t} = \tag{A.3a}$$

$$\frac{1}{(ZB_{k+1} - ZB)} \left[(\nu + K_{H_{k+1}}^{\;n+1}) \frac{(T_{k+1}^{n+1} - T^{n+1})}{(ZM_{k+1} - ZM)} - (\nu + K_H^{\;n+1}) \frac{(T^{n+1} - T_{k-1}^{n+1})}{(ZM_k - ZM_{k-1})} \right] \tag{A.3b}$$

$$+ \frac{1}{\rho_w c} \left[\frac{F_{k+1}^n - F^n}{(ZB_{k+1} - ZB)} \right] \tag{A.3c}$$

$$- \frac{1}{\Delta x} \left[u_{a_{i+1}}^{\;n} \frac{(T_{i+1}^n + T^n)}{2} - u_a^{\;n} \frac{(T^n + T_{i-1}^n)}{2} \right]$$

$$- \frac{1}{\Delta y} \left[v_{a_{j+1}}^{\;n} \frac{(T_{j+1}^n + T^n)}{2} - v_a^{\;n} \frac{(T^n + T_{j-1}^n)}{2} \right] \tag{A.3d}$$

$$- \frac{0.5}{(ZB_{k+1} - ZB)} \left[w_{a_{k+1}}^{\;n+1} \frac{(T_{k+1}^{n+1} + T^{n+1})}{2} - w_a^{\;n+1} \frac{(T^{n+1} + T_{k-1}^{n+1})}{2} + w_{a_{k+1}}^{\;n} \frac{(T_{k+1}^n + T^n)}{2} - w_a^{\;n} \frac{(T^n + T_{k-1}^n)}{2} \right] \tag{A.3e}$$

$$+ \frac{A}{\Delta x} \left[\frac{(T_{i+1}^n - T^n)}{\Delta x} - \frac{(T^n - T_{i-1}^n)}{\Delta x} \right]$$

$$+\frac{A}{\Delta y}\left[\frac{(T^{n}_{j+1}-T^{n})}{\Delta y}-\frac{(T^{n}-T^{n}_{j-1})}{\Delta y}\right] \qquad \text{(A.3f)}$$

The terms a-f in equation A.3 correspond to the similarly labeled terms in equation A.1. Term A.3b, the vertical diffusion term is computed using a backward time differencing scheme (MESINGER and ARAKAWA, 1976). This implicit differencing is used to improve the stability of the solution. Term A.3e, the vertical advection term, is also differenced implicitly but using a trapezoidal differencing which combines both time levels in the solution. All other terms use Euler or forward differencing. Forward differencing is explicit since all terms are at time level n. Equation A.2 can similarly be rewritten.

$$\frac{u^{n+1}-u^{n}}{\Delta t}= \qquad \text{(A.4a)}$$

$$\frac{f}{2}\,(v^{n+1}+v^{n}) \qquad \text{(A.4b)}$$

$$+\frac{1}{(ZB_{k+1}-ZB)}\left[(\nu+K_{M}{}^{n+1}_{k+1})\frac{(u^{n+1}_{k+1}-u^{n+1})}{(ZM_{k+1}-ZM)}\right.$$

$$\left.-(\nu+K_{M}{}^{n+1})\frac{(u^{n+1}-u^{n+1}_{k-1})}{(ZM_{k}-ZM_{k-1})}\right] \qquad \text{(A.4c)}$$

$$-Du^{n} \qquad \text{(A.4d)}$$

Trapezoidal time differencing appears in the Coriolis term, A.4b. For the oscillitory behavior induced by this term (i.e., inertial motions), trapezoidal differencing allows numerical stability without numerical damping (MESINGER and ARAKAWA, 1976). Backward time differencing is used in A.4c

to maintain stability of the friction term. The damping term, A.4d, uses simple forward differencing.

APPENDIX B

SCALING JUSTIFICATION FOR SEPARATION OF WIND-DRIFT AND GEOSTROPHIC FLOW

The assumption that the non-linear terms may be neglected in the equations of motion allows the separation of the momentum into wind-drift and geostrophic components. This assumption is fundamental to the current formulation of TOPS. In this appendix, I justify the above assumption via scaling arguments. I begin with the Reynolds equation for the mean motion in the x-direction (POND and PICKARD, 1978).

$$\overset{(a)}{\frac{\partial u}{\partial t}} = \overset{(b)}{- \frac{1}{\rho}\frac{\partial P}{\partial x}} + \overbrace{fv + 2\Omega\cos(\phi)w}^{(c)} + \overbrace{A_x\frac{\partial^2 u}{\partial x^2} + A_y\frac{\partial^2 u}{\partial y^2} + A_z\frac{\partial^2 u}{\partial z^2}}^{(d)} - \overbrace{u\frac{\partial u}{\partial x} - v\frac{\partial u}{\partial y} - w\frac{\partial u}{\partial z}}^{(e)} \qquad (B.1)$$

with the variables as defined below,

u,v,w = x,y, and z components of current velocity relative to the grid

ρ = density of seawater

A_x, A_y = horizontal eddy diffusion coefficient (see section 4.1, equations 12 and 13)

A_z = vertical eddy diffusion coefficient (see section 4.1, equations 7 and 8, $A_z = K_m$)

P = pressure

t = time

Ω = the rotation rate of the earth (2π radians/ 86400 s)

ϕ = latitude

f = Coriolis parameter ($2\Omega\sin(\phi)$)

x, y, z = earth-located coordinates (u positive eastward, v positive northward, and z positive up)

For notational convenience, I have omitted the overbars designating the mean properties of this equation.

Terms (a) and (e) in equation B.1, together represent the total rate of change of u with time. Term (a) is the local rate of change due to time variation. The terms in (e) represent the advective rates of change due to the motion. Term (b) represents the forces due to the distribution of mass which determine the pressure field. The forces relating to the earth's rotation (Coriolis forces) appear in (c). The terms in (d) represent forces due to the horizontal and vertical turbulent friction. Note the vertical friction term is directly related to the

wind via the surface boundary condition (equations 24 and 25).

As suggested above, two causative forces are at work. These are the pressure (derived from the mass distribution) and the surface wind stress. One might then consider two components of u, u_g associated with the pressure forcing, and u_e associated with the wind stress. One can then rewrite equation B.1 in terms of these components.

$$\begin{aligned}\frac{\partial}{\partial t}(u_e+u_g) = &- \frac{1}{\rho}\frac{\partial P}{\partial x} + f(v_e+v_g) + 2\Omega\cos(\phi)(w_e+w_g) \\ &+ A_x\frac{\partial^2(u_e+u_g)}{\partial x^2} + A_y\frac{\partial^2(u_e+u_g)}{\partial y^2} + A_z\frac{\partial^2(u_e+u_g)}{\partial z^2} \\ &- (u_e+u_g)\frac{\partial(u_e+u_g)}{\partial x} - (v_e+v_g)\frac{\partial(u_e+u_g)}{\partial y} \\ &- (w_e+w_g)\frac{\partial(u_e+u_g)}{\partial z} \qquad \text{(B.2)}\end{aligned}$$

Using knowledge of the oceanography in the Sea of Japan for the time period of the experiments (section 3), one can then designate appropriate magnitudes for the various terms in B.2 and evaluate their relative importance.

I first specify the time and space scales of interest. As discussed in the introduction, experiments suggest that local wind-forcing dominates the upper-ocean away from dynamically active regions. I therefore confine my scaling arguments below to the frontal region. Consequently, I consider the horizontal space scale, X, as the frontal

scale of 100 km. The vertical scale of interest, Z, is the upper-ocean mixed-layer scale for the period of the experiments, 10 m.

I present a range for the time scale, T, from hours out to the 3-day forecast period. I consider 0.25 of the inertial period, T_i, a relevant minimum. This is the time for the u-component of the inertial current to advance from its minimum to maximum absolute value. T_i is computed as follows,

$$T_i = \frac{2\pi}{f} . \tag{B.3}$$

At 40°N, $f \approx 10^{-4} s^{-1}$. Therefore $T_i \approx 6 \times 10^4$s and 0.25 $T_i \approx 1.5 \times 10^4$s. I therefore consider the scaling timescale, T, with the range of 10^4 to 10^5s.

The wind-drift current magnitude, U_e, is expected to be comparable to the geostrophic current magnitude, U_g, in the Sea of Japan. Values for the East Korean Warm Current are about 0.3 to 0.5 m s^{-1}. I therefore take $U_e(X) = U_g(X) = 10^{-1}$m s^{-1}. I specify these values as functions of X since they are appropriate with respect to X. They are not necessarily appropriate with respect to T or Z as discussed below relative to U_g. $U_e(T)$, responding to the time-scale of the wind variability, is expected to be comparable to $U_e(X)$ for the specified range of T. Similarly, over the mixed layer, $U_e(Z)$ is also of comparable order to $U_e(X)$. I

therefore set $U_e(T) = U_e(Z) = U_e(X)$. The variability of U_g with T should be smaller than $U_e(T)$ especially for $T = 10^4$. This is consistent with the research reviewed in the introduction suggesting that mesoscale circulations have little influence on the mixed layer on time scales shorter than a day. I therefore specify $U_g(T)$ with the range 10^{-2} to 10^{-1}m s^{-1} associated with the hours to days range of T. Finally, since the vertical scale of the geostrophic flow in the Sea of Japan is 100 m and the vertical scale of interest, Z, is 10 m, $U_g(Z)$ is taken as 10^{-2}m s^{-1}. That is, the horizontal geostrophic flow decreases from 10^{-1}m s^{-1} to 0 in the upper 100 m so the vertical variability of U_g for the 10 m scale is considered to be 10% of that for the 100 m scale.

I calculate the corresponding vertical scales of motion, W_e and W_g, using continuity. Assuming incompressibility of the fluid, the continuity equation may be written as follows.

$$\frac{\partial u}{\partial x} + \frac{\partial v}{\partial y} + \frac{\partial w}{\partial z} = 0 \qquad (B.4)$$

Equation B.4 can be expanded in similar fashion to B.2, to yield the following.

$$\frac{\partial(u_e+u_g)}{\partial x} + \frac{\partial(v_e+v_g)}{\partial y} + \frac{\partial(w_e+w_g)}{\partial z} = 0 \qquad (B.5)$$

In the absence of non-linear terms, the principle of superposition can be directly applied to yield separate

equations for the wind-forced and pressure-forced components. The wind-forced equation appears as follows.

$$\frac{\partial(u_e)}{\partial x} + \frac{\partial(v_e)}{\partial y} + \frac{\partial(w_e)}{\partial z} = 0 \qquad (B.6)$$

Applying the scaling parameters described above yields the following scaled equation.

$$\frac{U_e(X)}{X} + \frac{U_e(X)}{X} + \frac{W_e(Z)}{Z} = 0 \qquad (B.7)$$

Solving for $W_e(Z)$ yields the following.

$$W_e(Z) \simeq \frac{U_e(X)Z}{X} = \frac{10^{-1}10}{10^5} = 10^{-5} \qquad (B.8)$$

Note that since, $U_g(X)$ is assumed the same order as $U_e(X)$ that $W_g(Z) = W_e(Z)$.

The horizontal change in pressure is an unknown quantity and will addressed later. Table B1 summarizes the scaling parameters. One can take these quantities and apply them to an expanded equation B.2 to evaluate the relative importance of the various terms. I present these results in table B.2.

Note that the non-linear terms (terms 14-25 in table B.2) are all 10^{-7} or smaller relative to 10^{-5} for the dominant terms. As a first order approximation, the application of the principle of superposition thus appears justified for the experiments discussed in this report.

TABLE B1

VALUES FOR UPPER-OCEAN SCALING PARAMETERS IN THE SEA OF JAPAN

X: x, y, frontal scale, 100 km,	10^5m
Z: z, mixed layer scale,	10 m
T: t, time scale, hours to days,	10^4–10^5s
$U_e(X)$: u_e, v_e scaling relative to X,	10^{-1}m s^{-1}
$U_e(Z)$: u_e, v_e scaling relative to Z,	10^{-1}m s^{-1}
$U_e(T)$: u_e, v_e scaling relative to T,	10^{-1}m s^{-1}
$U_g(X)$: u_g, v_g scaling relative to X,	10^{-1}m s^{-1}
$U_g(Z)$: u_g, v_g scaling relative to Z,	10^{-2}m s^{-1}
$U_g(T)$: u_g, v_g scaling relative to T,	10^{-2}–10^{-1}m s^{-1}
$W_e(Z)$: w_e, derived via continuity (see above),	10^{-5}m s^{-1}
$W_g(Z)$: w_g, derived via continuity (see above),	10^{-5}m s^{-1}
A_x, A_y: (section 4.1),	10^2m^{2}s^{-1}
A_z: $10^{-5}$to 10^{-1}m^{2}s^{-1}(POND and PICKARD, 1978),	10^{-2}m^{2}s^{-1}
f: $2\Omega\sin(\phi)$ where ϕ = 40N,	10^{-4}s^{-1}
: $2\Omega\cos(\phi)$ where ϕ = 40N,	10^{-4}s^{-1}
ρ: reference density of sea water,	10^3kg m^{-3}
P(X): unknown pressure term,	? Pa

TABLE B.2

SCALING OF U-MOMENTUM EQUATION

	TERM	SCALING(m s^{-2})		RESULT(m s^{-2})
1	$\frac{\partial}{\partial t}(u_e)$	$\frac{U_e(T)}{T}$	$\frac{10^{-1}}{10^4} - \frac{10^{-1}}{10^5}$	$10^{-5} - 10^{-6}$
2	$\frac{\partial}{\partial t}(u_g)$	$\frac{U_g(T)}{T}$	$\frac{10^{-2}}{10^4} - \frac{10^{-1}}{10^5}$	10^{-6}
3	$\frac{1}{\rho}\frac{\partial P}{\partial x}$	$\frac{1}{\rho}\frac{P(X)}{X}$	$\frac{10^0 \; ?}{10^3 10^5}$	?
4	$f(v_e)$	$f\ U_e(X)$	$10^{-4} 10^{-1}$	10^{-5}
5	$f(v_g)$	$f\ U_g(X)$	$10^{-4} 10^{-1}$	10^{-5}
6	$2\Omega\cos(\phi)(w_e)$	$2\Omega\cos(\phi)W_e(Z)$	$10^{-4} 10^{-5}$	10^{-9}
7	$2\Omega\cos(\phi)(w_g)$	$2\Omega\cos(\phi)W_g(Z)$	$10^{-4} 10^{-5}$	10^{-9}
8	$A_x\frac{\partial^2(u_e)}{\partial x^2}$	$A_x \frac{U_e(X)}{X^2}$	$\frac{10^2 10^{-1}}{10^{10}}$	10^{-9}
9	$A_x\frac{\partial^2(u_g)}{\partial x^2}$	$A_x \frac{U_g(X)}{X^2}$	$\frac{10^2 10^{-1}}{10^{10}}$	10^{-9}
10	$A_y\frac{\partial^2(u_e)}{\partial y^2}$	$A_y \frac{U_e(X)}{X^2}$	$\frac{10^2 10^{-1}}{10^{10}}$	10^{-9}
11	$A_y\frac{\partial^2(u_g)}{\partial y^2}$	$A_y \frac{U_g(X)}{X^2}$	$\frac{10^2 10^{-1}}{10^{10}}$	10^{-9}
12	$A_z\frac{\partial^2(u_e)}{\partial z^2}$	$A_z \frac{U_e(Z)}{Z^2}$	$\frac{10^{-2} 10^{-1}}{10^2}$	10^{-5}
13	$A_z\frac{\partial^2(u_g)}{\partial z^2}$	$A_z \frac{U_g(Z)}{Z^2}$	$\frac{10^{-2} 10^{-2}}{10^2}$	10^{-6}
14	$(u_e)\frac{\partial(u_e)}{\partial x}$	$U_e(X)\ \frac{U_e(X)}{X}$	$\frac{10^{-1} 10^{-1}}{10^5}$	10^{-7}
15	$(u_e)\frac{\partial(u_g)}{\partial x}$	$U_e(X)\ \frac{U_g(X)}{X}$	$\frac{10^{-1} 10^{-1}}{10^5}$	10^{-7}
16	$(u_g)\frac{\partial(u_e)}{\partial x}$	$U_g(X)\ \frac{U_e(X)}{X}$	$\frac{10^{-1} 10^{-1}}{10^5}$	10^{-7}
17	$(u_g)\frac{\partial(u_g)}{\partial x}$	$U_g(X)\ \frac{U_g(X)}{X}$	$\frac{10^{-1} 10^{-1}}{10^5}$	10^{-7}

TABLE B.2 (continued)

	TERM	SCALING($m\ s^{-2}$)		RESULT($m\ s^{-2}$)
18	$(v_e)\frac{\partial(u_e)}{\partial y}$	$U_e(X)\ \frac{U_e(X)}{X}$	$\frac{10^{-1}10^{-1}}{10^{5}}$	10^{-7}
19	$(v_e)\frac{\partial(u_g)}{\partial y}$	$U_e(X)\ \frac{U_g(X)}{X}$	$\frac{10^{-1}10^{-1}}{10^{5}}$	10^{-7}
20	$(v_g)\frac{\partial(u_e)}{\partial y}$	$U_g(X)\ \frac{U_e(X)}{X}$	$\frac{10^{-1}10^{-1}}{10^{5}}$	10^{-7}
21	$(v_g)\frac{\partial(u_g)}{\partial y}$	$U_g(X)\ \frac{U_g(X)}{X}$	$\frac{10^{-1}10^{-1}}{10^{5}}$	10^{-7}
22	$(w_e)\frac{\partial(u_e)}{\partial z}$	$W_e(Z)\ \frac{U_e(Z)}{Z}$	$\frac{10^{-5}10^{-1}}{10^{1}}$	10^{-7}
23	$(w_e)\frac{\partial(u_g)}{\partial z}$	$W_e(Z)\ \frac{U_g(Z)}{Z}$	$\frac{10^{-5}10^{-2}}{10^{1}}$	10^{-8}
24	$(w_g)\frac{\partial(u_e)}{\partial z}$	$W_g(Z)\ \frac{U_e(Z)}{Z}$	$\frac{10^{-5}10^{-1}}{10^{1}}$	10^{-7}
25	$(w_g)\frac{\partial(u_g)}{\partial z}$	$W_g(Z)\ \frac{U_g(Z)}{Z}$	$\frac{10^{-5}10^{-2}}{10^{1}}$	10^{-8}

Assembling terms of order 10^{-5} yields a wind-drift equation comparable to equation 3.

$$\frac{\partial}{\partial t}(u_e) = -f(v_e) + A_z \frac{\partial^2(u_e)}{\partial z^2} \qquad (B.9)$$

For the pressure-related terms, no other term remains to balance the Coriolis term fv_g, thus implying the unknown pressure term is necessarily of like magnitude. The resulting equation is the time-independent geostrophic equation.

$$fv_g = -\frac{1}{\rho}\frac{\partial P}{\partial x} \qquad (B.10)$$

Equation B.10 is the basis of the thermal wind equation 16.

APPENDIX C

DESCRIPTION OF STATISTICAL PARAMETERS

In this appendix, I provide description of statistical parameters suggested by WILLMOTT(1981, 1982) and WILLMOTT et al(1985) for the evaluation of forecast models. The recommended statistics include: the means ($\bar{O},\bar{P}$) and standard deviations (s_o,s_p) of the observed and predicted variates respectively, the intercept (a) and slope (b) of a least squares regression between the variates, errors described by the root mean squared error (RMSE), systematic RMSE ($RMSE_s$), unsystematic RMSE ($RMSE_u$), and the index of agreement (d_2). The means and standard deviations are defined using standard definitions (e.g., DIXON and MASSEY, 1969). The RMSE is defined as follows.

$$RMSE = \left[N^{-1} \sum_{i=1}^{N} (p_i-o_i)^2 \right]^{0.5} \qquad (C.1)$$

where,

N = sample size

o_i = the i-th observation

p_i = the i-th prediction.

The sources or types of error cannot be directly deduced from RMSE alone and thus WILLMOTT(1981) recommends additional calculations which allow the separation (in a linear sense) of RMSE into systematic and unsystematic components. The square root in RMSE clarifies the error measure in the sense of providing a metric with the same units as the o_i and p_i. In the following discussion however, I remove the square root to clarify the derivation of the systematic and unsystematic components of the error. I discuss these statistics in terms of the mean squared error (MSE) and its systematic (MSE_s) and unsystematic (MSE_u) components.

$$MSE = MSE_s + MSE_u \qquad (C.2)$$

The systematic part of the error, MSE_s, is itself comprised of three components.

$$MSE_s = MSE_a + MSE_p + MSE_i \qquad (C.3)$$

These three components are the additive systematic error (MSE_a), the proportional systematic error (MSE_p), and the interdependent systematic error (MSE_i). The additive part of the error results from the constant over- or underprediction of the observed.

$$MSE_a = a^2 \qquad (C.4)$$

On a scatterplot, this error appears as a linear regression line parallel to the 1:1 line. The constant difference between the two lines then represents the error (a). The proportional part of the systematic error gives a measure

of the difference in slope of the regression line and the 1:1 line.

$$MSE_p = (b-1)^2 \left[N^{-1} \sum_{i=1}^{N} o_i{}^2\right] \qquad (C.5)$$

The additive and proportional parts of the error are not independent but are related via the covariation of the additive error (a) and proportionality error (b-1).

$$MSE_i = 2a\ (b-1)\ \overline{O} \qquad (C.6)$$

WILLMOTT(1981) provides the following example of the utility of decomposing the error into systematic and unsystematic components. An RMSE of an acceptable level (to a given investigator) might prompt one to accept a given forecast model as it is. If, however, the MSE is dominated by MSE_s, minor changes may enhance model performance at minimal cost. Conversely, given MSE dominated by MSE_u, the model may be performing as well as it can without major modification.

The index of agreement, d_2, is a descriptive statistic introduced by WILLMOTT(1981) to measure the degree to which a model's predictions are error free. It is defined as follows.

$$d_2 = 1 - \frac{\sum_{i=1}^{N} (p_i - o_i)^2}{\sum_{i=1}^{N} [\,|P_i'| + |O_i'|\,]^2} \qquad (C.7)$$

where,

$P_i' = p_i - \overline{O}$, and $O_i' = o_i - \overline{O}$. This statistic thus describes, in magnitude and sign, how observed deviations with respect to $\overline{O}$, correspond with the predicted deviations about $\overline{O}$. The measure, d_2, was not an especially sensitive statistic in the experiments of this report.

This concludes the discussion of WILLMOTT's(1981) recommended core statistics required in a model evaluation. In this and his 1982 work, he additionally recommmends against the use of the concept of statistical significance in the evaluation of models. Significance levels depend on continuous distributions and it is usually unknown to what extent the underlying assumptions have been violated. WILLMOTT et al (1985) modify this position somewhat. They suggest that quantitative estimates of reliability may now be determined via non-parameteric statistical measures.

The recommended technique for determining confidence bounds is called the "bootstrap." I refer the reader to the above reference for the details of this procedure. It basically creates an empirical distribution function for the statistic of interest from which the specified confidence limits may be derived. The "bootstrap" creates this empirical function by randomly sampling (with replacement) the given N-member data set to create a "bootstrap" sample of size N. The various statistical measures (e.g., $\overline{O}$, $\overline{P}$, s_o, s_p, RMSE, d_2) can then be calculated for this "bootstrap" sample. This procedure is

repeated many times until one has a frequency distribution for the given statistical parameter based on many "bootstrap" samples. The confidence limits can then be directly determined from the frequency distribution by stripping the appropriate percentage of N from both ends.

The 95% confidence bounds I report in this work, for instance, are calculated first by creating 200 "bootstrap" samples from each of the p_i and o_i data sets. The $\overline{O}$, $\overline{P}$, s_o, s_p, RMSE, d_2 are then calculated for each of these "bootstrap" samples. The confidence bounds for a given statistical parameter are then determined by removing 10 values from each end of the frequency distribution for that parameter.

APPENDIX D

ADDITIONAL STATISTICAL PLOTS AND TABLES

The following plots and tables provide supplemental information relative to the statistical comparisons of section 7.1. Figures D1 through D4 present scatterplots of TAU 72 SST forecasts for the May 8 - June 4, 1984 period. Persistence, experiment 1, experiment 2, and experiment 4 all versus experiment 3 are shown in figures D1 through D4, respectively. The a, b, c associated with figures D1 through D4 relate to sub-areas of the total region shown in figure 45. The figures for the warm-side sub-region are denoted a, for the frontal sub-region as b, and the cold-side sub-region as c. The statistical tables D1 through D4 provide relevant statistical measures corresponding to figures D1 through D4. Again the a, b, c represent warm, frontal, and cold sub-regions. Figure D5 represents RMSD temperature versus depth for the various experiments relative to experiment 3. This figure is for the frontal region alone.

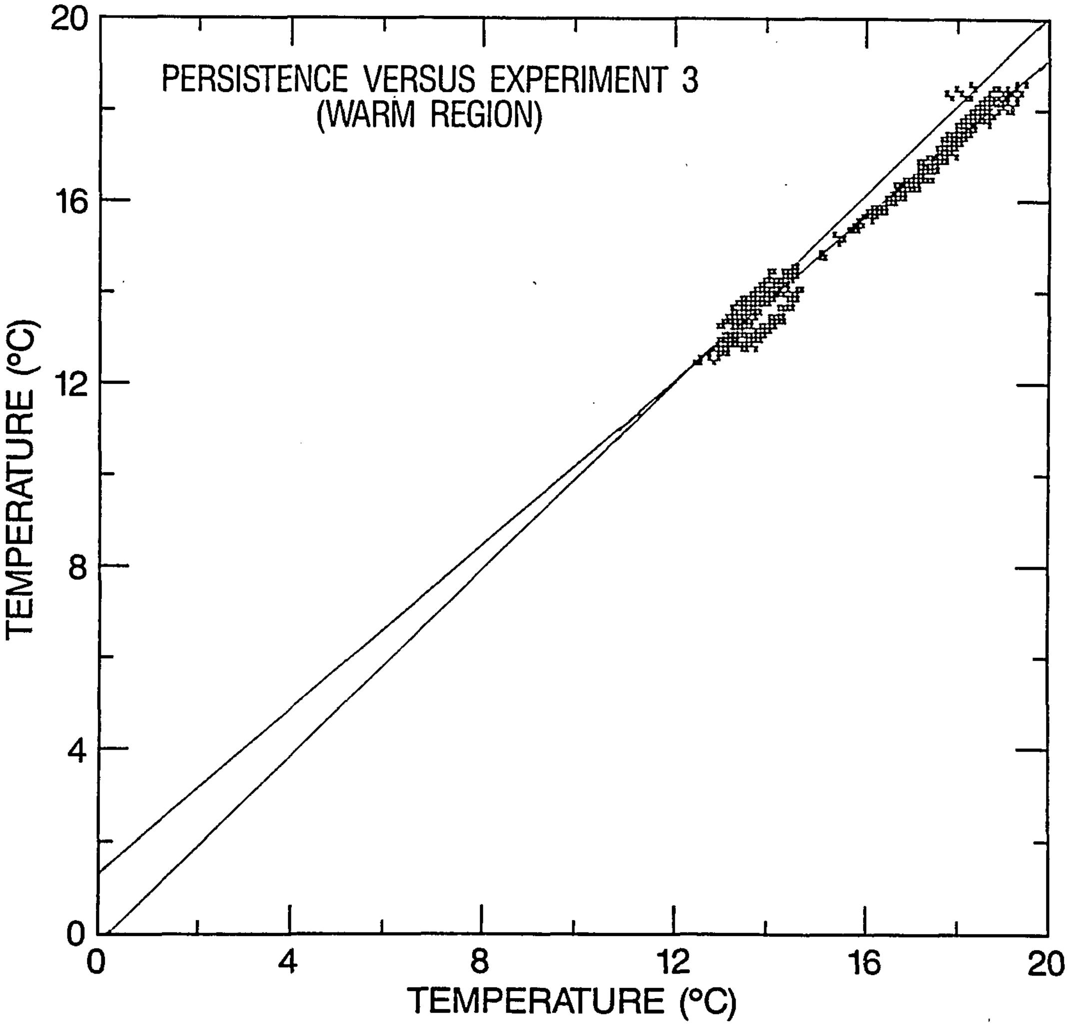

Figure D1a. Scatter plot of TAU 72 SST (°C) forecasts covering May 8 - June 4, 1984, for persistence vs. experiment 3 (warm side).

TABLE D1a STATISTICAL SUMMARY:
WARM REGION, TAU 72 SST (°C),
PERSISTENCE VS. EXPERIMENT 3

	PERSISTENCE	EXPERIMENT 3
NUMBER OF POINTS (N)	977	977
MEAN ($\overline{P}$, $\overline{O}$)	15.37	15.79
95% CONFIDENCE BOUNDS	(15.25, 15.48)	(15.65, 15.91)
STANDARD DEVIATION	1.88	2.12
95% CONFIDENCE BOUNDS	(1.85, 1.92)	(2.08, 2.16)

....

MEAN DEVIATION	-0.42
RMS DEVIATION (RMSD)	0.56
95% CONFIDENCE BOUNDS	(0.55, 0.58)
SYSTEMATIC RMS DEVIATION ($RMSD_s$)	0.49
UNSYSTEMATIC RMS DEVIATION ($RMSD_u$)	0.28
INDEX OF AGREEMENT (d_2)	0.98
95% CONFIDENCE BOUNDS	(0.98, 0.98)
LINEAR REGRESSION LINE	Y = 0.88X + 1.50

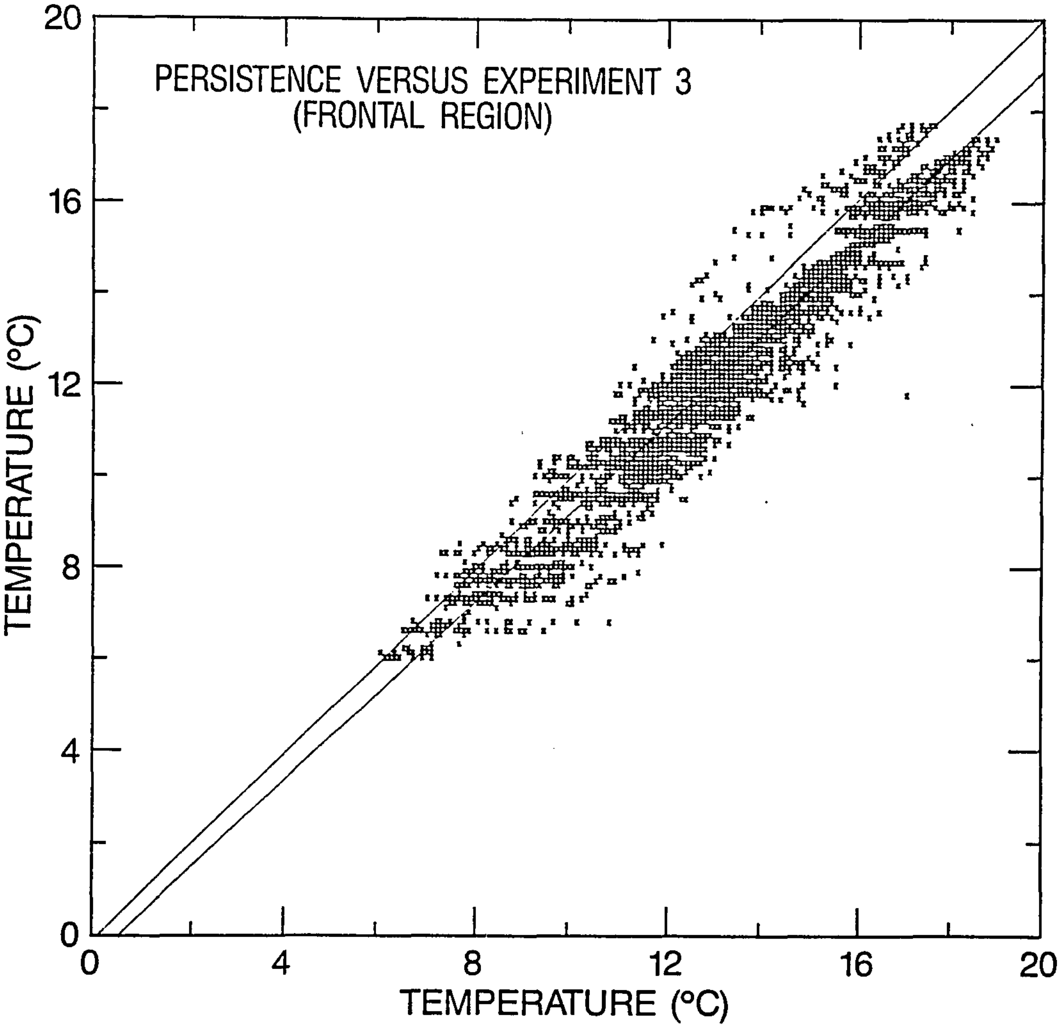

Figure D1b. Scatter plot of TAU 72 SST (°C) forecasts covering May 8 - June 4, 1984, for persistence vs. experiment 3 (frontal region).

TABLE D1b STATISTICAL SUMMARY:
FRONTAL REGION, TAU 72 SST (°C),
PERSISTENCE VS. EXPERIMENT 3

	PERSISTENCE	EXPERIMENT 3
NUMBER OF POINTS (N)	4125	4125
MEAN $(\bar{P}, \bar{O})$	12.10	13.00
95% CONFIDENCE BOUNDS	(12.02, 12.17)	(12.92, 13.06)
STANDARD DEVIATION	2.53	2.51
95% CONFIDENCE BOUNDS	(2.48, 2.58)	(2.46, 2.56)

....

MEAN DEVIATION	-0.89
RMS DEVIATION (RMSD)	1.14
95% CONFIDENCE BOUNDS	(1.12, 1.16)
SYSTEMATIC RMS DEVIATION $(RMSD_s)$	0.90
UNSYSTEMATIC RMS DEVIATION $(RMSD_u)$	0.70
INDEX OF AGREEMENT (d_2)	0.95
95% CONFIDENCE BOUNDS	(0.95, 0.95)
LINEAR REGRESSION LINE	$Y = 0.97X - 0.45$

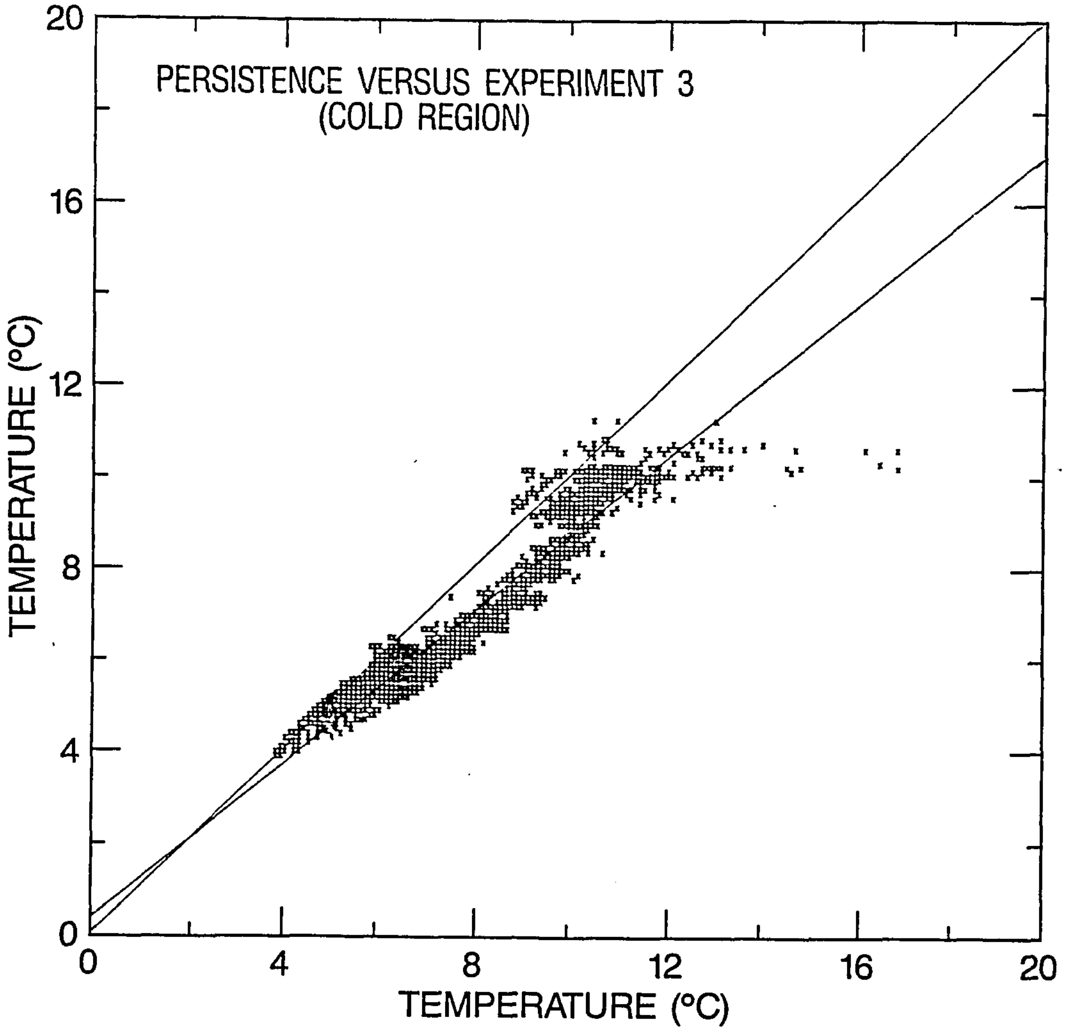

Figure D1c. Scatter plot of TAU 72 SST (°C) forecasts covering May 8 - June 4, 1984, for persistence vs. experiment 3 (cold side).

TABLE D1c STATISTICAL SUMMARY: COLD REGION, TAU 72 SST (°C), PERSISTENCE VS. EXPERIMENT 3

	PERSISTENCE	EXPERIMENT 3
NUMBER OF POINTS (N)	2648	2648
MEAN ($\overline{P}$, $\overline{O}$)	7.03	8.04
95% CONFIDENCE BOUNDS	(6.95, 7.10)	(7.96, 8.12)
STANDARD DEVIATION	1.79	2.05
95% CONFIDENCE BOUNDS	(1.76, 1.83)	(1.99, 2.09)

……

MEAN DEVIATION	-1.01
RMS DEVIATION (RMSD)	1.20
95% CONFIDENCE BOUNDS	(1.17, 1.23)
SYSTEMATIC RMS DEVIATION ($RMSD_s$)	1.06
UNSYSTEMATIC RMS DEVIATION ($RMSD_u$)	0.56
INDEX OF AGREEMENT (d_2)	0.91
95% CONFIDENCE BOUNDS	(0.90, 0.91)
LINEAR REGRESSION LINE	$Y = 0.83X + 0.34$

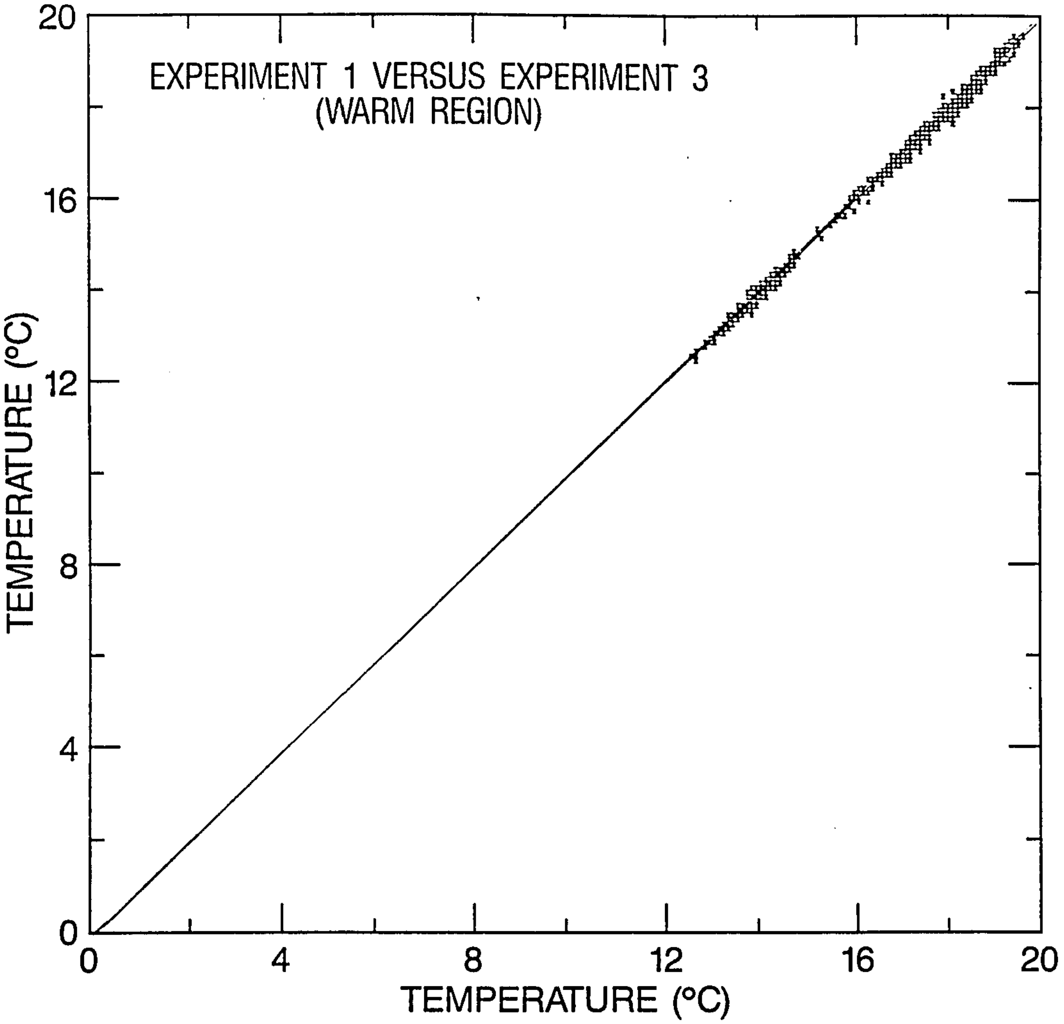

Figure D2a. Scatter plot of TAU 72 SST (°C) forecasts covering May 8 - June 4, 1984, for experiment 1 vs. experiment 3 (warm side).

TABLE D2a STATISTICAL SUMMARY:
WARM REGION, TAU 72 SST (°C),
EXPERIMENT 1 VS. EXPERIMENT 3

	EXPERIMENT 1	EXPERIMENT 3
NUMBER OF POINTS (N)	977	977
MEAN $(\bar{P}, \bar{O})$	15.71	15.79
95% CONFIDENCE BOUNDS	(15.57, 15.83)	(15.65, 15.91)
STANDARD DEVIATION	2.11	2.12
95% CONFIDENCE BOUNDS	(2.07, 2.15)	(2.08, 2.16)

....

MEAN DEVIATION	-0.08
RMS DEVIATION (RMSD)	0.13
95% CONFIDENCE BOUNDS	(0.13, 0.14)
SYSTEMATIC RMS DEVIATION ($RMSD_s$)	0.08
UNSYSTEMATIC RMS DEVIATION ($RMSD_u$)	0.10
INDEX OF AGREEMENT (d_2)	1.00
95% CONFIDENCE BOUNDS	(1.00, 1.00)
LINEAR REGRESSION LINE	Y = 0.99X + 0.03

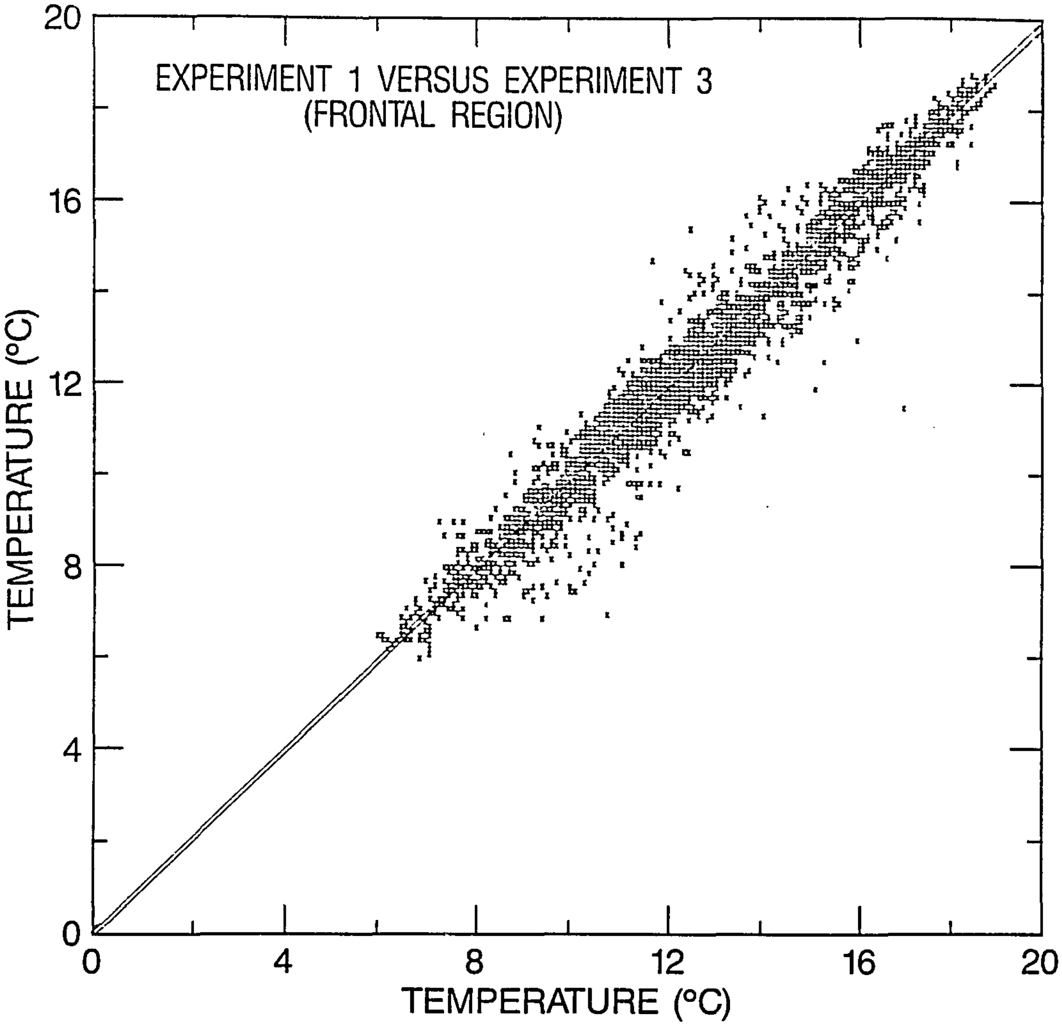

Figure D2b. Scatter plot of TAU 72 SST (°C) forecasts covering May 8 - June 4, 1984, for experiment 1 vs. experiment 3 (frontal region).

TABLE D2b STATISTICAL SUMMARY: FRONTAL REGION, TAU 72 SST (°C), EXPERIMENT 1 VS. EXPERIMENT 3

	EXPERIMENT 1	EXPERIMENT 3
NUMBER OF POINTS (N)	4125	4125
MEAN ($\overline{P}$, $\overline{O}$)	12.83	13.00
95% CONFIDENCE BOUNDS	(12.76, 12.89)	(12.92, 13.06)
STANDARD DEVIATION	2.56	2.51
95% CONFIDENCE BOUNDS	(2.50, 2.61)	(2.46, 2.56)

....

MEAN DEVIATION	-0.17
RMS DEVIATION (RMSD)	0.56
95% CONFIDENCE BOUNDS	(0.53, 0.58)
SYSTEMATIC RMS DEVIATION ($RMSD_s$)	0.17
UNSYSTEMATIC RMS DEVIATION ($RMSD_u$)	0.53
INDEX OF AGREEMENT (d_2)	0.99
95% CONFIDENCE BOUNDS	(0.99, 0.99)
LINEAR REGRESSION LINE	Y = 1.00X - 0.12

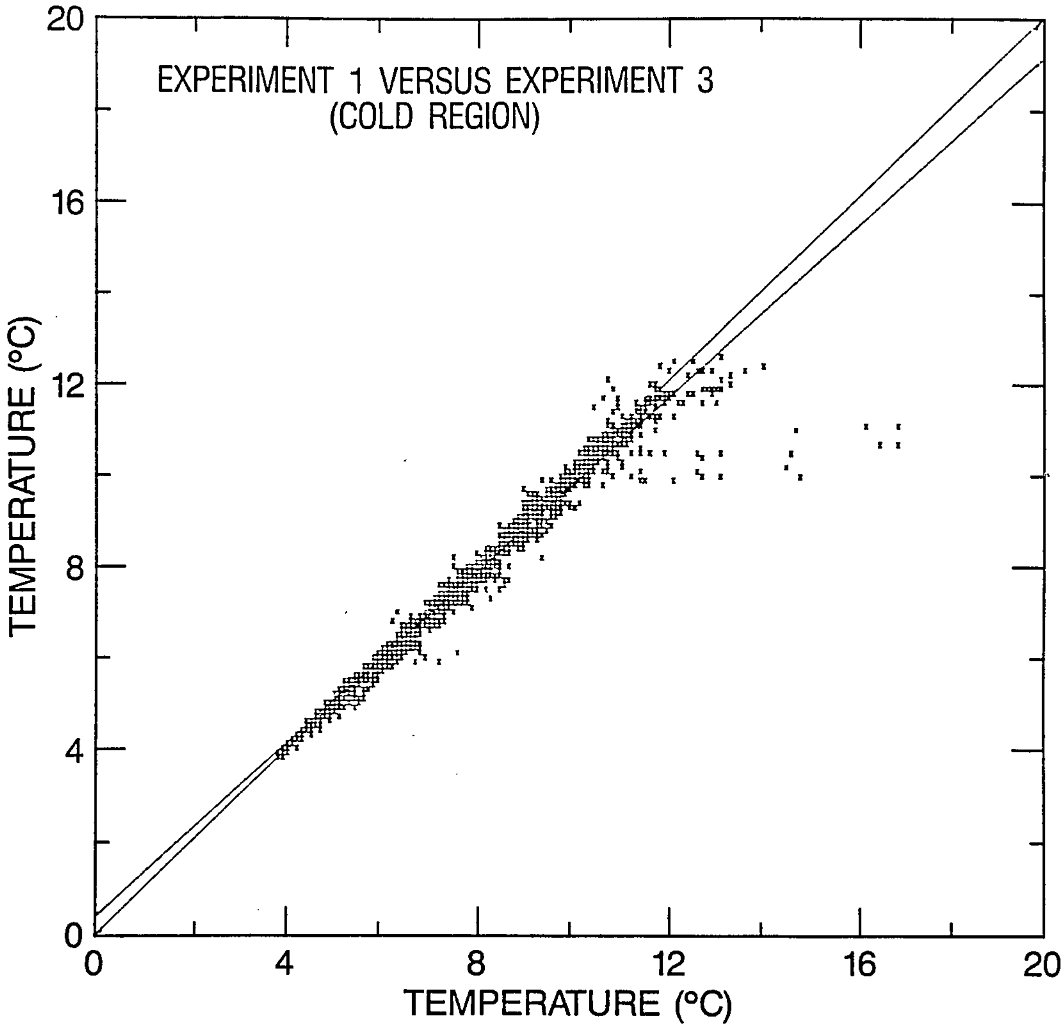

Figure D2c. Scatter plot of TAU 72 SST (°C) forecasts covering May 8 - June 4, 1984, for experiment 1 vs. experiment 3 (cold side).

TABLE D2c STATISTICAL SUMMARY:
COLD REGION, TAU 72 SST (°C),
EXPERIMENT 1 VS. EXPERIMENT 3

	EXPERIMENT 1	EXPERIMENT 3
NUMBER OF POINTS (N)	2648	2648
MEAN $(\bar{P}, \bar{O})$	7.92	8.04
95% CONFIDENCE BOUNDS	(7.84, 7.99)	(7.96, 8.12)
STANDARD DEVIATION	1.95	2.05
95% CONFIDENCE BOUNDS	(1.91, 1.98)	(1.99, 2.09)

....

MEAN DEVIATION	-0.12
RMS DEVIATION (RMSD)	0.40
95% CONFIDENCE BOUNDS	(0.33, 0.46)
SYSTEMATIC RMS DEVIATION (RMSD_s)	0.18
UNSYSTEMATIC RMS DEVIATION (RMSD_u)	0.36
INDEX OF AGREEMENT (d_2)	0.99
95% CONFIDENCE BOUNDS	(0.99, 0.99)
LINEAR REGRESSION LINE	$Y = 0.94X + 0.39$

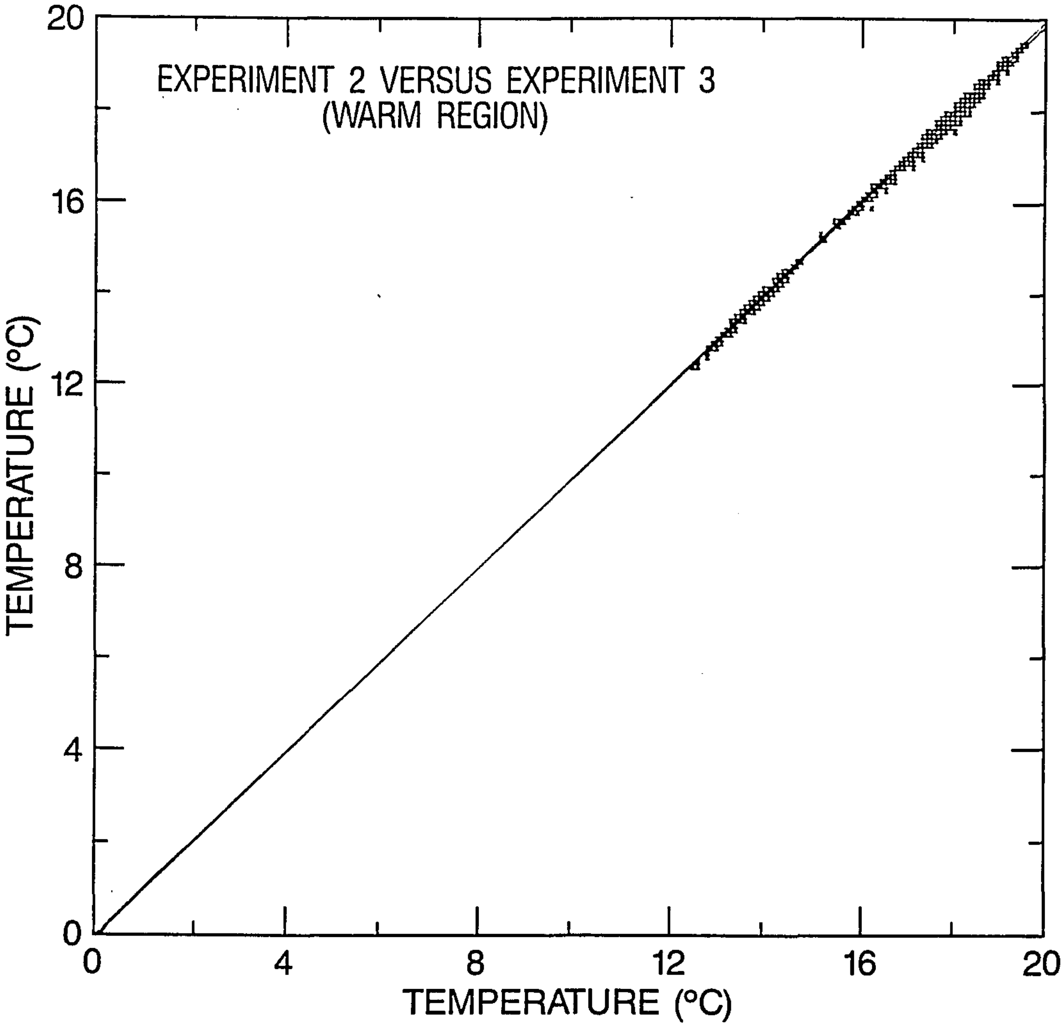

Figure D3a. Scatter plot of TAU 72 SST (°C) forecasts covering May 8 - June 4, 1984, for experiment 2 vs. experiment 3 (warm side).

TABLE D3a STATISTICAL SUMMARY:
WARM REGION, TAU 72 SST (°C),
EXPERIMENT 2 VS. EXPERIMENT 3

	EXPERIMENT 2	EXPERIMENT 3
NUMBER OF POINTS (N)	977	977
MEAN ($\overline{P}$, $\overline{O}$)	15.72	15.79
95% CONFIDENCE BOUNDS	(15.58, 15.84)	(15.65, 15.91)
STANDARD DEVIATION	2.11	2.12
95% CONFIDENCE BOUNDS	(2.07, 2.14)	(2.08, 2.16)

....

MEAN DEVIATION	-0.07
RMS DEVIATION (RMSD)	0.12
95% CONFIDENCE BOUNDS	(0.11, 0.12)
SYSTEMATIC RMS DEVIATION ($RMSD_s$)	0.07
UNSYSTEMATIC RMS DEVIATION ($RMSD_u$)	0.09
INDEX OF AGREEMENT (d_2)	1.00
95% CONFIDENCE BOUNDS	(1.00, 1.00)
LINEAR REGRESSION LINE	Y = 0.99X + 0.06

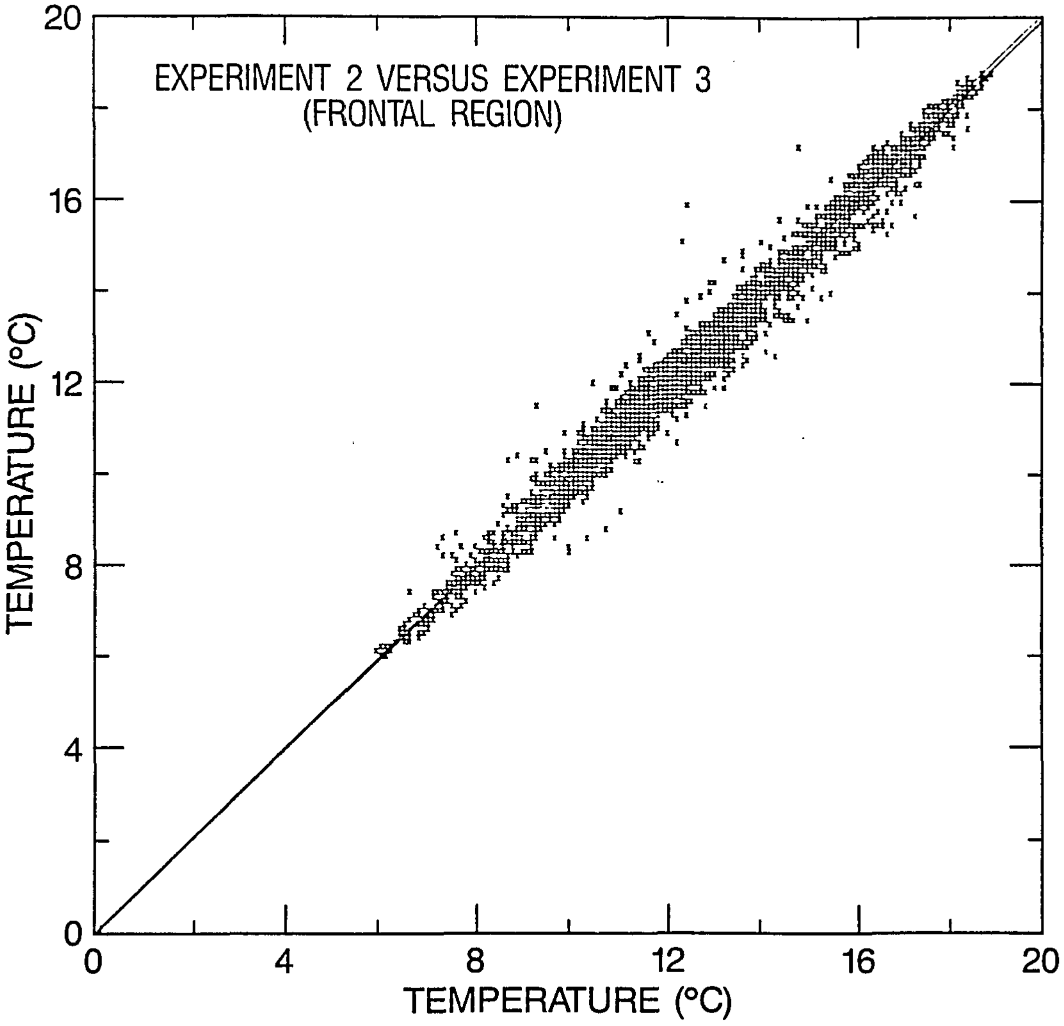

Figure D3b. Scatter plot of TAU 72 SST (°C) forecasts covering May 8 - June 4, 1984, for experiment 2 vs. experiment 3 (frontal region).

TABLE D3b STATISTICAL SUMMARY:
FRONTAL REGION, TAU 72 SST (°C),
EXPERIMENT 2 VS. EXPERIMENT 3

	EXPERIMENT 2	EXPERIMENT 3
NUMBER OF POINTS (N)	4125	4125
MEAN ($\bar{P}$, $\bar{O}$)	12.88	13.00
95% CONFIDENCE BOUNDS	(12.81, 12.95)	(12.92, 13.06
STANDARD DEVIATION	2.52	2.51
95% CONFIDENCE BOUNDS	(2.46, 2.57)	(2.46, 2.56)

....

MEAN DEVIATION	-0.11
RMS DEVIATION (RMSD)	0.38
95% CONFIDENCE BOUNDS	(0.36, 0.39)
SYSTEMATIC RMS DEVIATION ($RMSD_s$)	0.11
UNSYSTEMATIC RMS DEVIATION ($RMSD_u$)	0.36
INDEX OF AGREEMENT (d_2)	0.99
95% CONFIDENCE BOUNDS	(0.99, 0.99)
LINEAR REGRESSION LINE	Y = 0.99X - 0.03

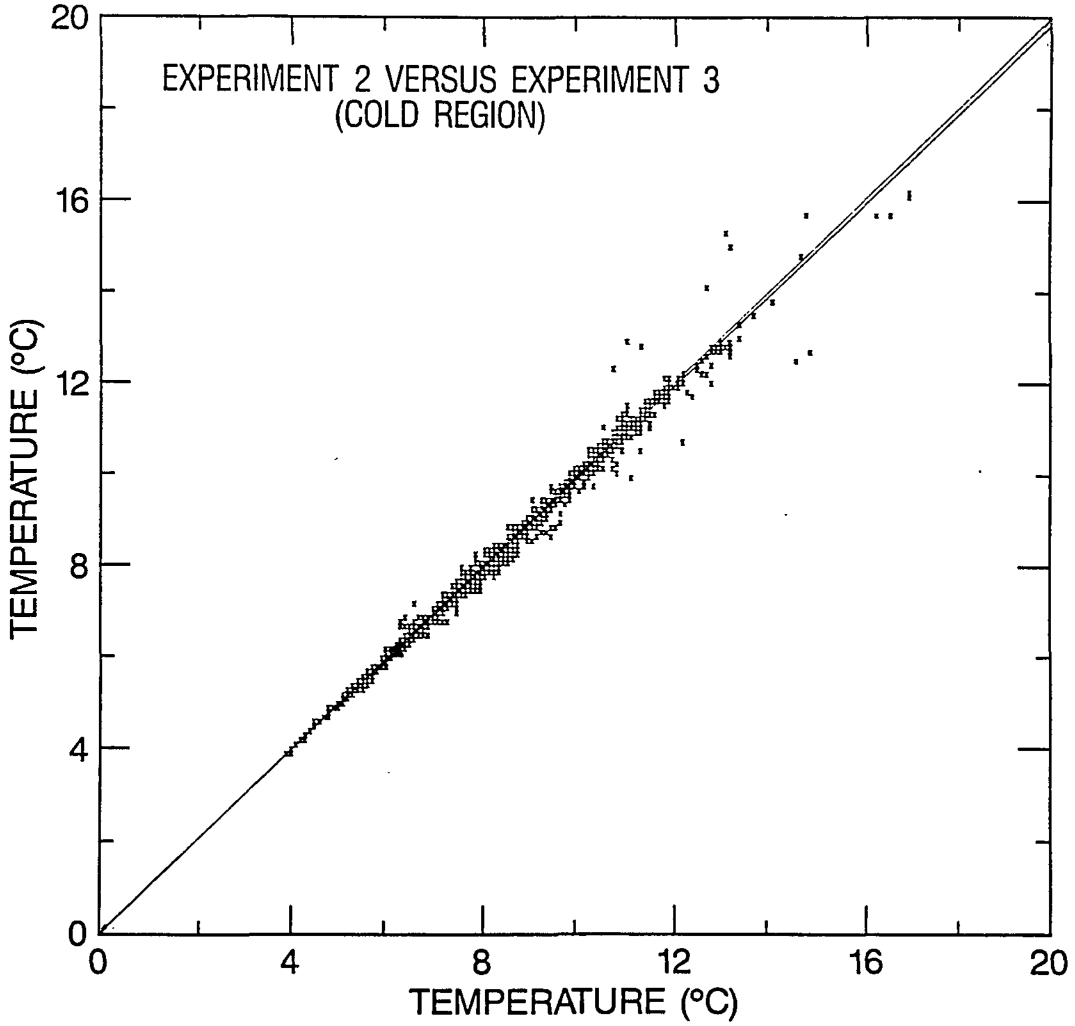

Figure D3c. Scatter plot of TAU 72 SST (°C) forecasts covering May 8 - June 4, 1984, for experiment 2 vs. experiment 3 (cold side).

TABLE D3c STATISTICAL SUMMARY: COLD REGION, TAU 72 SST (°C), EXPERIMENT 2 VS. EXPERIMENT 3

	EXPERIMENT 2	EXPERIMENT 3
NUMBER OF POINTS (N)	2648	2648
MEAN ($\bar{P}$, $\bar{O}$)	7.99	8.04
95% CONFIDENCE BOUNDS	(7.91, 8.06)	(7.96, 8.12)
STANDARD DEVIATION	2.03	2.05
95% CONFIDENCE BOUNDS	(1.98, 2.08)	(1.99, 2.09)
MEAN DEVIATION	-0.05	
RMS DEVIATION (RMSD)	0.17	
95% CONFIDENCE BOUNDS	(0.15, 0.20)	
SYSTEMATIC RMS DEVIATION ($RMSD_s$)	0.05	
UNSYSTEMATIC RMS DEVIATION ($RMSD_u$)	0.17	
INDEX OF AGREEMENT (d_2)	1.00	
95% CONFIDENCE BOUNDS	(1.00, 1.00)	
LINEAR REGRESSION LINE	$Y = 0.99X + 0.03$	

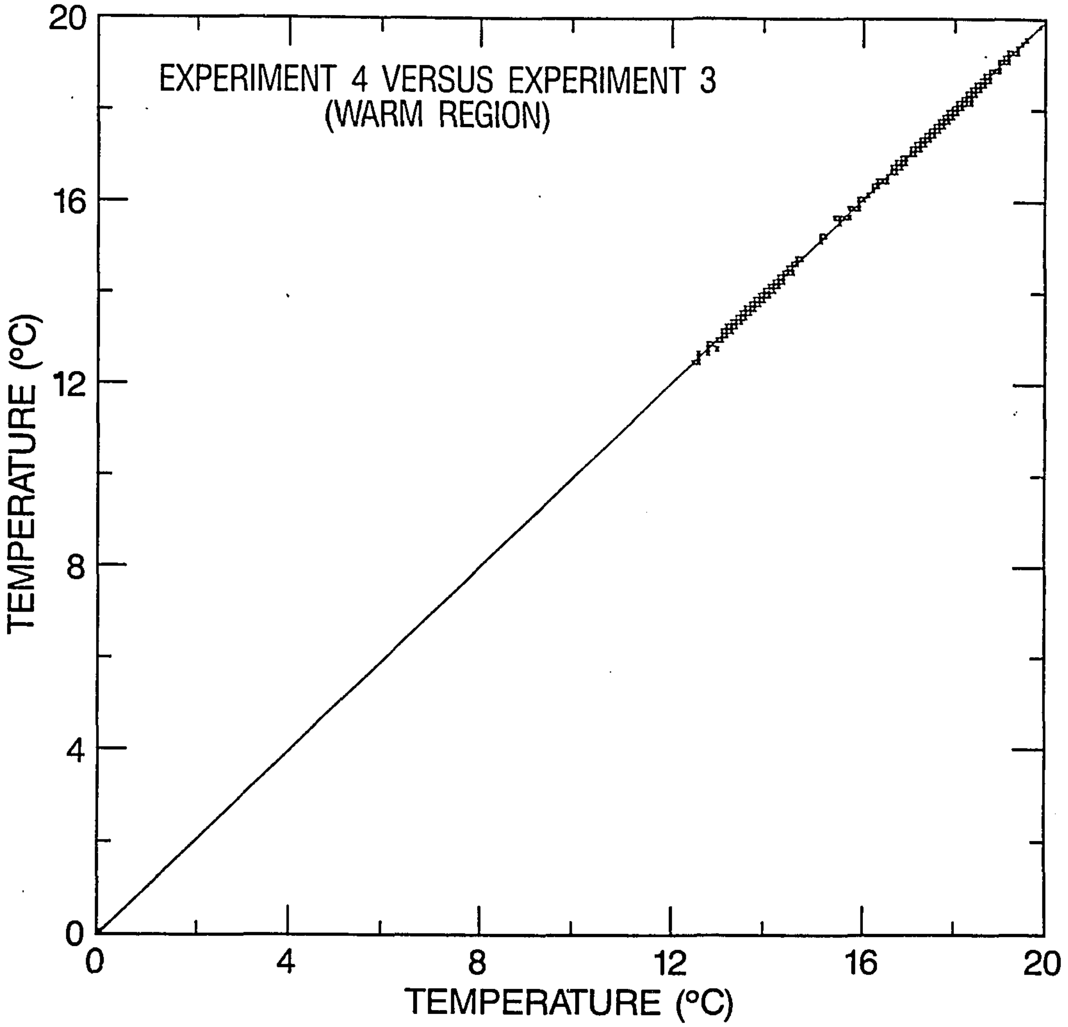

Figure D4a. Scatter plot of TAU 72 SST (°C) forecasts covering May 8 - June 4, 1984, for experiment 4 vs. experiment 3 (warm side).

TABLE D4a STATISTICAL SUMMARY: WARM REGION, TAU 72 SST (°C), EXPERIMENT 4 VS. EXPERIMENT 3

	EXPERIMENT 4	EXPERIMENT 3
NUMBER OF POINTS (N)	977	977
MEAN ($\overline{P}$, $\overline{O}$)	15.79	15.79
95% CONFIDENCE BOUNDS	(15.66, 15.91)	(15.65, 15.91)
STANDARD DEVIATION	2.12	2.12
95% CONFIDENCE BOUNDS	(2.08, 2.16)	(2.08, 2.16)

....

MEAN DEVIATION	0.01
RMS DEVIATION (RMSD)	0.06
95% CONFIDENCE BOUNDS	(0.05, 0.06)
SYSTEMATIC RMS DEVIATION ($RMSD_s$)	0.01
UNSYSTEMATIC RMS DEVIATION ($RMSD_u$)	0.06
INDEX OF AGREEMENT (d_2)	1.00
95% CONFIDENCE BOUNDS	(1.00, 1.00)
LINEAR REGRESSION LINE	Y = 0.99X + 0.03

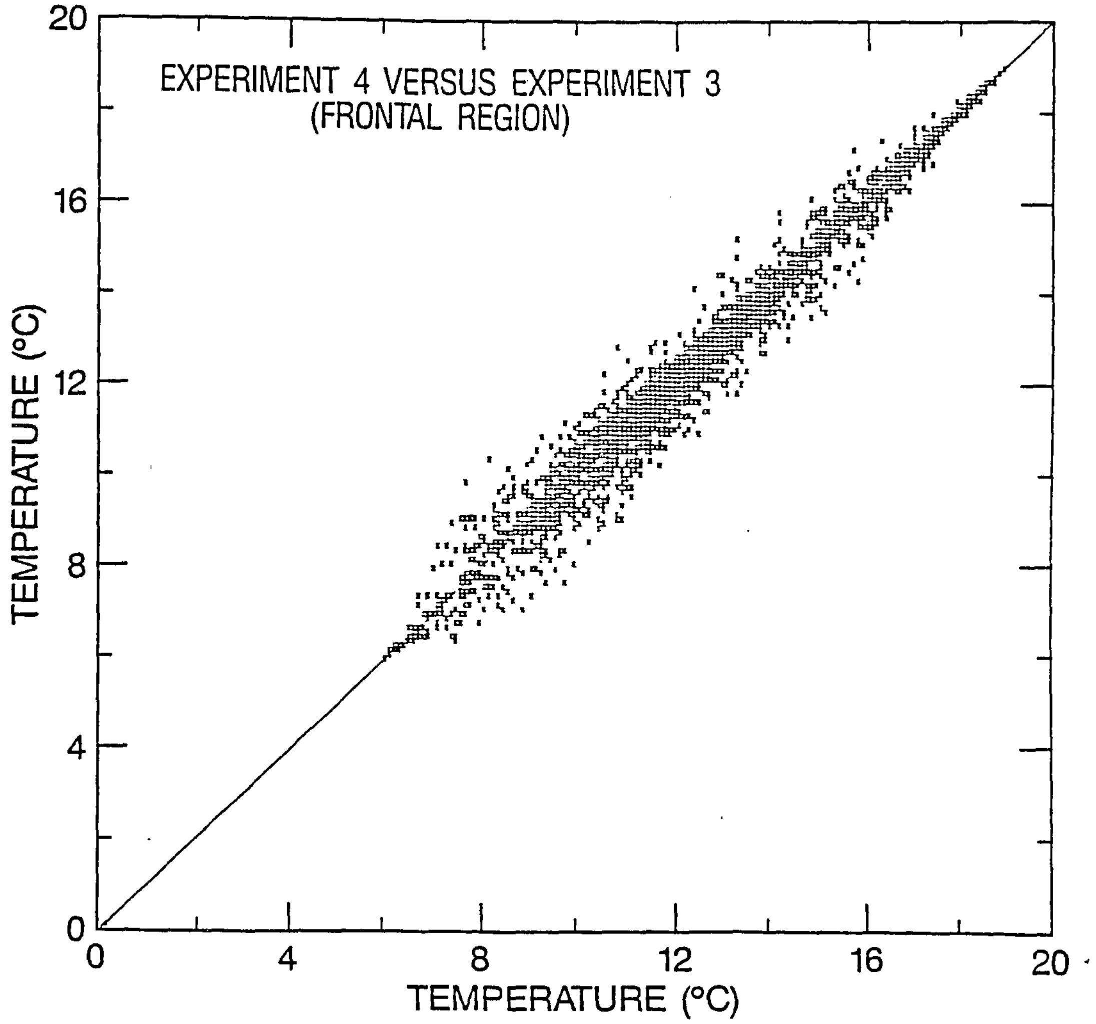

Figure D4b. Scatter plot of TAU 72 SST (°C) forecasts covering May 8 - June 4, 1984, for experiment 4 vs. experiment 3 (frontal region).

TABLE D4b STATISTICAL SUMMARY: FRONTAL REGION, TAU 72 SST (°C), EXPERIMENT 4 VS. EXPERIMENT 3

	EXPERIMENT 4	EXPERIMENT 3
NUMBER OF POINTS (N)	4125	4125
MEAN ($\bar{P}$, $\bar{O}$)	12.99	12.99
95% CONFIDENCE BOUNDS	(12.91, 13.06)	(12.92, 13.06)
STANDARD DEVIATION	2.54	2.51
95% CONFIDENCE BOUNDS	(2.48, 2.59)	(2.46, 2.56)

……

MEAN DEVIATION	-0.01
RMS DEVIATION (RMSD)	0.39
95% CONFIDENCE BOUNDS	(0.38, 0.41)
SYSTEMATIC RMS DEVIATION ($RMSD_s$)	0.01
UNSYSTEMATIC RMS DEVIATION ($RMSD_u$)	0.39
INDEX OF AGREEMENT (d_2)	0.99
95% CONFIDENCE BOUNDS	(0.99, 0.99)
LINEAR REGRESSION LINE	Y = 1.00X + 0.02

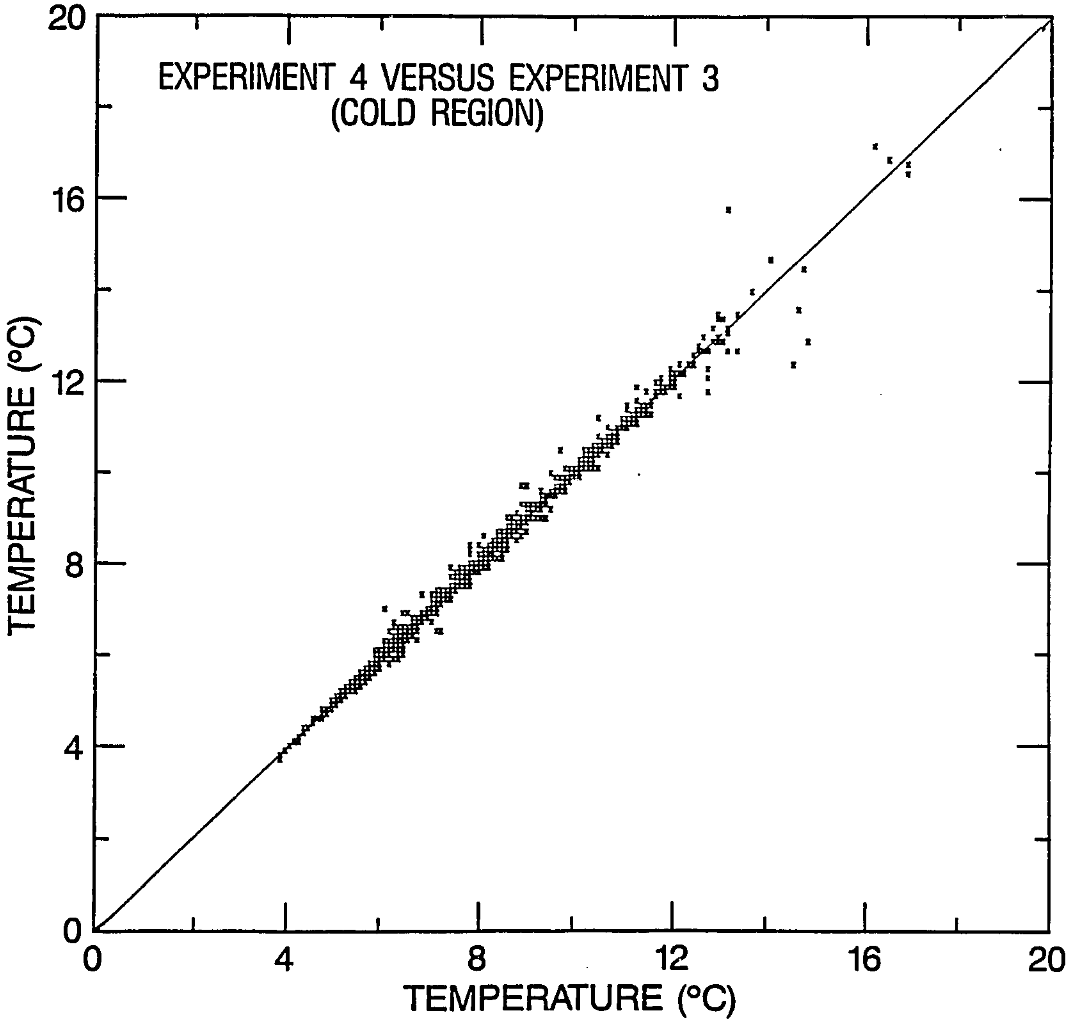

Figure D4c. Scatter plot of TAU 72 SST (°C) forecasts covering May 8 - June 4, 1984, for experiment 4 vs. experiment 3 (cold side).

TABLE D4c STATISTICAL SUMMARY: COLD REGION, TAU 72 SST (°C), EXPERIMENT 4 VS. EXPERIMENT 3

	EXPERIMENT 4	EXPERIMENT 3
NUMBER OF POINTS (N)	2648	2648
MEAN ($\overline{P}$, $\overline{O}$)	8.05	8.04
95% CONFIDENCE BOUNDS	(7.97, 8.12)	(7.96, 8.12)
STANDARD DEVIATION	2.05	2.05
95% CONFIDENCE BOUNDS	(1.99, 2.09)	(1.99, 2.09)

MEAN DEVIATION	0.01
RMS DEVIATION (RMSD)	0.13
95% CONFIDENCE BOUNDS	(0.11, 0.16)
SYSTEMATIC RMS DEVIATION ($RMSD_s$)	0.01
UNSYSTEMATIC RMS DEVIATION ($RMSD_u$)	0.13
INDEX OF AGREEMENT (d_2)	1.00
95% CONFIDENCE BOUNDS	(1.00, 1.00)
LINEAR REGRESSION LINE	$Y = 1.00X + 0.02$

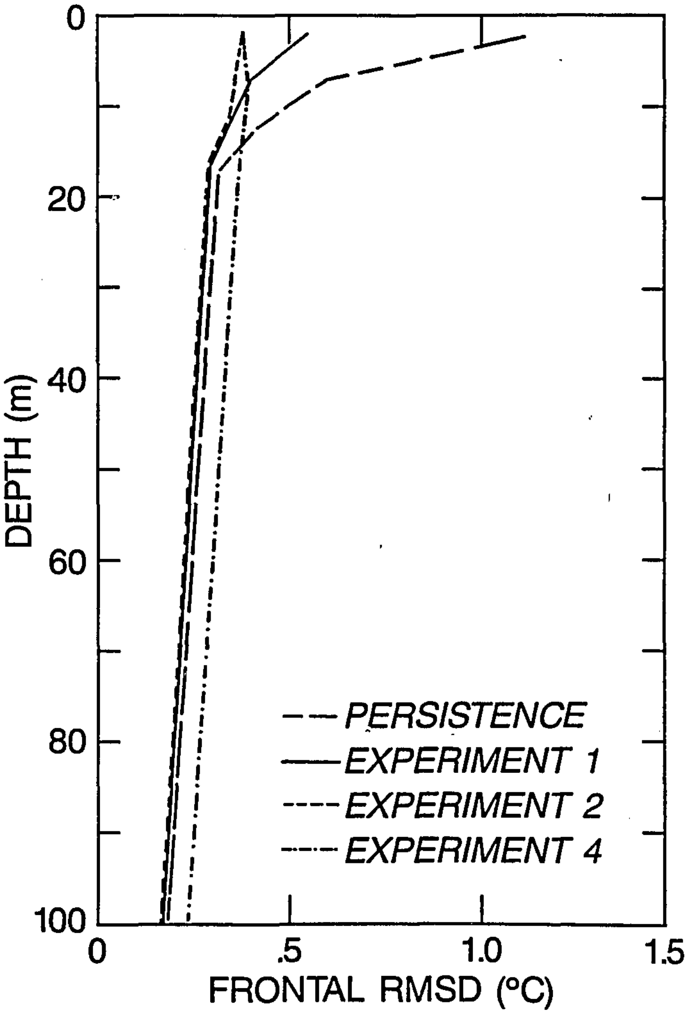

Figure D5. RMSD temperature (°C) vs. depth (m) for TAU 72 forecasts of persistence, experiment 1, experiment 2, and experiment 4, all vs. experiment 3, May 8 - June 4, 1984, (frontal region).

VITA

John M. Harding, Jr.
Rt. 2 Box 670
Lacombe, LA 70445
December 1987

Major Professional Experience:

Oceanographer (Numerical modeling, air/sea interaction), Naval Ocean Research and Development Activity, NSTL, MS 39529, 1976-present.

Oceanographer (Air/sea interaction, numerical modeling), Naval Environmental Prediction Research Facility, Monterey, CA 93943, 1973-1976.

Oceanographer (Data collection and analysis), Southern California Coastal Water Research Project, El Segundo, CA 90245, 1972-1973.

Education:

PhD., (Marine Sciences), December 1987, Louisiana State University, Baton Rouge, LA.

M.S., (Marine Science), December 1971, University of California at San Diego, La Jolla, CA.

B.S., (Physics), May 1970, University of Miami, Coral Gables, FL.

Personal:

Born:	September 1, 1948
Married:	October 27, 1974
Spouse:	Therese Marie Walsh
Children:	Ventana Therese (7), Soquel Elana (5), Jevon Janelle (2)
Hobbies:	Reading, volleyball, bicycling, home and auto maintenance and repair.

DOCTORAL EXAMINATION AND DISSERTATION REPORT

Candidate: John M. Harding, Jr.

Major Field: Marine Sciences

Title of Dissertation: THE ROLE OF HORIZONTAL PROCESSES IN UPPER-OCEAN PREDICTION: A FORECAST SIMULATION IN THE SEA OF JAPAN

Approved:

Wm. J. Wiseman Jr.
Major Professor and Chairman

William Coyle
Dean of the Graduate School

EXAMINING COMMITTEE:

Dorothy Pashley

Robert L. Thomas

Stephen P. Murray

Harry H. Roberts

Date of Examination:

November 23, 1987